Structure and Kinetics of the PTEN Tumor Suppressor: Investigation of Solution and Membrane-Associated States

by

Siddharth Subhash Shenoy

Submitted in partial fulfillment of the
requirements for the degree of
Doctor of Philosophy
at
Carnegie Mellon University
Department of Physics
Pittsburgh, Pennsylvania 15213

Thesis Committee:
Mathias Lösche (Chair)
Kris Dahl
Markus Deserno
Frederick Lanni

May, 2012

Abstract

Cancer is an umbrella term for a class of diseases all characterized by uncontrolled cell growth. In 2008, the average person had a 20% probability of being diagnosed with cancer before the age of 75 and a 11% chance of dying from it [1]. There are two categories of genes whose alteration can result in cancer: 1) oncogenes that promote cell growth and 2) tumor-suppressor genes that inhibit cell division and survival. *PTEN* is the second-most frequently mutated gene in human cancer [2] after *p53*, which in turn is mutated in half of all tumors [3]. While PTEN has a protein phosphatase capacity, it fulfills its cancer protective role through its ability to dephosphorylate the lipid $PI(3,4,5)P_3$, which in turn shuts down the PI3K/Akt signaling pathway thereby downregulating cell growth. Despite its critical role in preventing aberrant cell proliferation, there is no structural information available on membrane-bound PTEN. The crystal structure of a highly truncated membrane-free PTEN mutant was determined [4], but the deleted N-terminal and C-terminal tails have postulated membrane-association and regulatory roles, respectively.

Since PTEN's regulatory function has been postulated to be membrane-mediated, it is crucial to identify the binding mechanism and the contribution of various lipid species to the overall kinetics. In this thesis, we first describe a novel biomimetic construct called a tethered bilayer lipid membrane (tBLM) which allows for the simultaneous characterization of the bilayer by multiple techniques while allowing for an exquisite control of lipid composition. To validate the biological relevance of tBLMs, we visualized their optical homogeneity using fluorescence microscopy (FM), quantified the defect-density using electrochemical impedance spectroscopy (EIS) and the lipid diffusivity using two-photon fluorescence correlation spectroscopy (2P-FCS). We formulated a protocol that allowed for the preparation of defect-free planar bilayers which were able to reproduce the fluidity of free-standing membranes (such as lipid vesicles) without compromising on long-term stability (the issue with black lipid membranes) while decoupling the proximal (to the substrate) leaflet from the distal leaflet (the issue with solid-supported lipid bilayers).

We then proceeded to quantify the binding affinities of *wt* PTEN, an autism-related mutant H93R PTEN, a Cowden syndrome-related mutant C124S PTEN and the truncated crystal structure PTEN mutant to the anionic lipids phosphatidylserine (PS), phosphatidylinositol (4,5)-bisphosphate $[PI(4,5)P_2]$ and phosphatidylinositol (3,4,5)-trisphosphate $[PI(3,4,5)P_3]$ individually, as well as to membranes composed of biologically-relevant mixtures of these lipids. We show

that the membrane-association of PTEN is very sensitive to lipid composition. It had earlier been determined that PTEN has a very weak affinity for the zwitterionic phosphatidylcholine (PC) lipids [$K_d > 500$ µM] [5]. *wt* PTEN is initially attracted to the membrane through interactions with PS lipids [K_d=22.0±0.5 µM; B_{max}=155±3 ng/cm^2]. This is then followed by specific association with PI(4,5)P$_2$ lipids [K_d=0.4±0.1 µM; B_{max}=23±1 ng/cm^2] which allows for the efficient dephosphorylation of the PI(3,4,5)P$_3$ catalytic substrate [K_d=2.4±0.2 µM]. We also observed that *wt* PTEN shows an order of magnitude stronger affinity to membranes containing both PS and PI(4,5)P$_2$ [K_d=0.04±0.01 µM] indicating a cooperative binding effect. The H93R PTEN mutation is spatially separated from the PI(4,5)P$_2$-binding module (PBM), the CBR3 PS-binding motif in the C2 domain as well as the active site. Yet, it exhibits a 4-fold strengthened affinity to PS-containing membranes [K_d(H93R)=3.1±0.3 µM], a 3-fold weakened affinity to PI(4,5)P$_2$-containing membranes [K_d(H93R)=1.3±0.2 µM] and a 75% reduced phosphatase activity [6] with respect to the *wt*. The catalytically inactive C124S mutation allows us to show that PTEN's association with PI(4,5)P$_2$ and PI(3,4,5)P$_3$ is independent and non-competitive [K_d(PI(4,5)P$_2$) = 0.32±0.03 µM; K_d(PI(3,4,5)P$_3$)=0.12±0.03 µM; [K_d(PI(4,5)P$_2$:PI(3,4,5)P$_3$=1:1) = 0.13±0.01 µM], indicating distinct binding sites. The truncated PTEN mutant has a stronger association to PS lipids [2.5≤K_d(truncated)≤4.9 µM] compared to *wt* PTEN due to the increase in net charge of the protein by +14 as a result of the deletions and the loss of any unfavorable interactions between the tail and the body of the protein. We also observe a two-fold decreased affinity to PI(4,5)P$_2$-bearing membranes compared to *wt* PTEN [K_d(truncated)=0.77±0.07 µM], likely due to the absence of six residues from the PI(4,5)P$_2$ binding module (PBM).

The SPR binding measurements serve a dual purpose of quantifying PTEN's membrane association as well as identifying suitable conditions for performing neutron reflectivity (NR) measurements to determine the structure of membrane-bound PTEN. We studied four systems: H93R PTEN bound to a PS-bearing membrane, *wt* bound to a PS-bearing membrane, *wt* PTEN bound to a PS+PI(4,5)P$_2$-bearing membrane and the truncated PTEN mutant bound to a PS+PI(4,5)P$_2$-bearing membrane. The NR data was fit using the conventional slab/box model [7] as well as the new continuous distribution model that was recently developed by our group [8]. All four protein neutron scattering length density (nSLD) profiles are distinct, implying unique membrane-bound states. Both *wt* PTEN bound states show a 60 Å extension of the protein along the bilayer normal while the H93R bound state is more compact at an extension of just 45 Å. We suggest that this is primarily due to the C-terminal tail being located distal to the membrane for the *wt* PTEN, unlike for H93R PTEN, although the H93R point mutation could also result in a conformational change in the core domains of the protein. In all cases, there is minimal penetration of the protein into the

lipid headgroups indicating an interfacial association of PTEN with the lipid bilayer.

We estimated the orientation of membrane-bound PTEN using the SASSIE [9] conformational generator in combination with Euler angle rotational analysis. Assuming that the core domains of the protein are unchanged from the crystal structure, *wt* PTEN binds to PS at an angle given by $(\theta, \phi) = (30°, 30°)$ while *wt* PTEN binds to membranes containing both PS and PI(4,5)P$_2$ at an angle given by $(\theta, \phi) = (10°, 300°)$ where $(\theta, \phi) = (0°, 0°)$ corresponds to the proposed membrane binding orientation of the protein, as predicted by the crystal structure [4]. This analysis fails when applied to the H93R PTEN NR data, likely indicating a deviation in the secondary structure of the mutant from the crystal structure.

Finally, we performed complementary all-atom molecular dynamic (MD) simulations which allowed us to study the molecular-level details of PTEN's equilibrium conformation(s), both in solution as well as in a membrane-bound state, while using the experimental results as a source of validation. The association of PTEN with a PS-bearing membrane results in a conformational change of the protein which provides the active site with easier access to the PI(3,4,5)P$_3$ catalytic substrate. The C-terminal tail of membrane-bound PTEN is in a relatively compact conformation and is located distal to the membrane, making minimal contacts with the body of the protein, as suggested by the NR data. However, the tail is extended in solution, allowing it to associate with the CBR3 PS-binding motif of the C2 domain, thereby obstructing membrane association. While this is only one of the conformations that the tail can adopt, the PEST phosphorylation sites on the C-terminal tail are spatially adjacent to Lysines on the C2 domain. Consequently, multiple phosphorylations of the C-terminal tail could lock the protein in a 'closed' state where the tail interacts with the PS-binding sites, thereby excluding the possibility of membrane-association [10]. This implies the phosphorylation of the C-terminal tail is a plausible mechanism for PTEN regulation.

In combination, these results from a broad spectrum of investigations provide an entirely new perspective on the activation and regulation of the PTEN tumor suppressor. The detailed molecular picture that arises is urgently needed to help define future research investigation into PTEN's tumor suppressor role and aid in the search for pharmaceutical targets to counteract the adverse impact of *PTEN* mutations. They also provide a reference structure for a lipid phosphatase in its active state on a thermally disordered, in-plane fluid membrane. We showcase the ability of seemingly innocuous point mutations to disrupt the membrane-association process through a combination of altered interactions and conformational changes. Our data supports a regulatory role for the disordered C-terminal tail, based on its ability to defy the structure-function paradigm by interfering with PTEN's ability to bind to the lipid membrane, thereby reducing its catalytic activity.

Acknowledgments

The research presented in this thesis is the culmination of six years of hard work that would not have been possible without the collaborative environment that exists at Carnegie Mellon. First and foremost, I would like to thank my advisor, Mathias Lösche. By offering me a fellowship before I joined CMU, he showed that he had confidence in my abilities – something that has never waivered. With his years of experience, he knew the importance of working on multiple projects to maximize the probability of success. Every project I have worked on has been intellectually challenging and exciting and this has fed my passion for the subject. Mathias was always available to discuss the status of my work and provided me with all the resources I needed to be successful. He made me the scientist I am today and for that I will forever be grateful.

I want to thank Arne Gericke and Alonzo Ross for inviting us to join their existing collaboration focused on studying the PTEN tumor suppressor. They were a wealth of knowledge and afforded me the opportunity to make a significant contribution to our understanding of the protein and the link between seemingly innocuous point mutations and disease.

In order to be successful, I had to make use of a variety of complementary techniques, both experimental and computational. Frank Heinrich and Prabhanshu Shekhar aided me with neutron reflectivity measurements and the subsequent data evaluation. Agnieszka Kalinowski taught me how to perform surface plasmon resonance measurements. Radu Moldovan trained me to use the fluorescence microscopy and fluorescence correlation spectroscopy setups in our lab. Haw Zan Goh helped me with electrochemical spectroscopy measurements. Joseph Curtis taught me the basics of molecular dynamics simulations and Hirsh Nanda was an integral part of designing, running and analyzing our PTEN simulations. The members of my thesis committee: Kris Dahl, Markus Deserno and Fred Lanni are brilliant scientists who challenged me to do my best, suggested different ways of looking at a problem, were full of new ideas and experiments for me to explore and always made time for me when I needed their advice.

Our department is fortunate to have a wonderful support staff in the form of Donna Thomas, Chuck Gitzen, Al Brunk, Hilary Homer, Gary Wilkin and Pat Carr, among others and I am grateful for their help and assistance.

I had a wonderful graduate school experience thanks to all the warm and friendly people I met in the Burgh. In particular, I would like to thank Garima Jain, Meera Ramachandran, Venkat Krishnamurthi, Nishtha Srivastava, Luxmi Dabas, Michelle Ntampaka, Reshma Ramadurai, Tristan Bereau, Ryan Booth, Eric

Evarts and all the members of the Lösche and Deserno research groups.

I have had excellent teachers and professors throughout my career from Sharjah Indian School to the University of Texas at Austin to Carnegie Mellon. At each step, I had mentors who nurtured my scientific curiosity and guided me on the path that has brought me to where I am today. For all that and more, I am ever grateful to them.

I will never be able to appropriately thank my parents and my sister for all they have done for me. I had a wonderful childhood in a loving home. My parents always wanted the best for my sister and me and made a lot of sacrifices to ensure that we got a high quality education without the accompanying financial debt that most students are burdened with.

And last, but my no means the least, I want to thank Ashwini Aroskar – my best friend, the love of my life and my wife. Meeting her was the best thing that happened to me at Carnegie Mellon. She is my pillar of strength and has supported me through my Ph.D., during good times and when things were rough. I dedicate this thesis to her.

List of Publications

Chapter 4:

Shenoy S, Moldovan R, Fitzpatrick J, Vanderah D, Deserno M and Lösche M. *In-Plane Homogeneity and Lipid Dynamics in Tethered Bilayer Lipid Membranes (tBLMs)*. Soft Matter. 2010; 6: 1263-1274.

Chapters 5 and 7:

Shenoy S, Shekhar P, Heinrich F, Daou M-C, Gericke A, Ross A and Lösche M. *Membrane Association of the PTEN Tumor Suppressor: Molecular Details of the Protein-Membrane Complex from SPR Binding Studies and Neutron Reflection*. PLoS ONE. 2012; 7(4): e32591

Chapter 9:

Shenoy S, Nanda H and Lösche M. *Membrane Association of the PTEN Tumor Suppressor: Electrostatic Interaction with Phosphatidylserine-Containing Bilayers and Regulatory Role of the C-Terminal Tail*. J. Mol. Biol. Submitted.

Contents

List of Tables

List of Figures

Nomenclature

$1 - PE$ One Photon Excitation

$2 - PE$ Two Photon Excitation

βME β-mercaptoethanol or 2-mercaptoethanol

$\chi^2/ChiSq$ Chi Square Goodness of Fit

AND/R Advanced Neutron Diffractometer/Reflectometer

ASD Autism Spectrum Disorders

B_{max} Change in SPR Resonance Angle at Saturation

BLM Bilayer Lipid Membrane / Black Lipid Membrane

$CHARMM$ Chemistry at HARvard Molecular Mechanics

$CHOL$ Cholesterol

CPE Constant Phase Element

CS Cowden Syndrome

D Diffusion Coefficient

DLS Dynamic Light Scattering

$DOPC$ 1,2-dioleoyl-sn-glycero-3-phosphocholine

$DOPS$ 1,2-dioleoyl-sn-glycero-3-phospho-L-serine

$DPhyPC$ 1,2-diphytanoyl-sn-glycero-3-phosphocholine

$DPPC$ 1,2-dipalmitoyl-sn-glycero-3-phosphocholine

$DPPI(3,4,5)P_3$ PtdIns-(3,4,5)-P_3 (1,2-dipalmitoyl)

$DPPI(4,5)P_2$ PtdIns-(4,5)-P_2 (1,2-dipalmitoyl)

$dtBLM$ Densely Tethered Bilayer Lipid Membrane

EIS Electrochemical Impedance Spectroscopy

$FC16$ 29-hexadecyloxy-3,6,9,12,15,18,21,24,27,31-decaoxaheptatetracontan-1-thiol

FCS Fluorescence Correlation Spectroscopy

FM Fluorescence Microscopy

$FTIR$ Fourier Transform Infrared Spectroscopy

$HC18$ 20-(Z-octadec-9-enyloxy)-3,6,9,12,15,18,22-heptaoxatetracont-31-ene-1-thiol

K_d Equilibrium Dissociation Constant

k_{off} Off-Rate

k_{on} On-Rate

KI Potassium Iodide

$LRPE$ Lissamine Rhodamine Phosphatidyl-Ethanolamine

MD Molecular Dynamics

$MMAC1$ Mutated in Multiple Advanced Cancers

n Refractive index

$NaCl$ Sodium Chloride

$NAMD$ Not Another Molecular Dynamics package

$NCNR$ NIST Center for Neutron Research

NR Neutron Reflectivity/Reflectometry

$nSLD$ Neutron Scattering Length Density

OS Osmotic Shock

PBM PI(4,5)P$_2$ Binding Motif

PDZ Post synaptic density protein/Drosophila disc large tumor suppressor/Zonula occludens-1 protein

$PEST$ Proline, Glutamic Acid, Serine, Threonine

$PI(3,4,5)P_2$ L-α-phosphatidylinositol-3,4,5-trisphosphate

$PI(4,5)P_2$ L-α-phosphatidylinositol-4,5-bisphosphate

$PTEN$ Phosphatase and Tensin Homologue Deleted on Chromosome Ten

$RMSD$ Root-Mean-Square Deviation

RSE Rapid Solvent Exchange

SAM Self-Assembled Monolayer

SPR Surface Plasmon Resonance

$stBLM$ Sparsely Tethered Bilayer Lipid Membrane

$tBLM$ Tethered Bilayer Lipid Membrane

$TEP1$ TGF-regulated and Epithelial cell-enriched Phosphatase 1

$v.f.$ Volume Fraction

VF Vesicle Fusion

VMD Visual Molecular Dynamics

$WC14$ 20-tetradecyloxy-3,6,9,12,15,18,22 -heptaoxahexatricontane-1-thiol

Chapter 1

Introduction

1.1 PTEN

Phosphatase and tensin homologue deleted on chromosome ten (*PTEN*) is a tumor suppressor located at chromosome 10q23 which often exhibits mutations and deletions. In fact, *PTEN* is considered to be the second most commonly mutated gene in human cancer, after *p53* [2].

In 1997, while hunting for a tumor suppressor on chromosome 10, Li et al. noticed that a genetic alteration that occurs at high frequency in a variety of human tumors is loss of heterozygosity (LOH) at 10q23 [11]. They isolated the gene and subsequent sequence analysis of the open reading frame showed a protein tyrosine phosphatase domain and a 175 amino acid region that showed homology with chicken tensin. This led them to conclude that the gene may be a tumor suppressor that operates by antagonizing protein tyrosine kinases and hence they named it *PTEN*. In the same year, Steck et al. independently isolated a gene which they termed as *MMAC1* (Mutated in Multiple Advanced Cancers 1) [12]. They too noticed significant homology between *PTEN* and protein phosphatases as well as to tensin and auxilin. Also in 1997, Li et al. identified a gene they called *TEP1* (TGF-regulated and epithelial cell-enriched phosphatase) while screening cDNA libraries in the search for human protein tyrosine phosphatases [13]. *PTEN*, *MMAC1* and *TEP1* all proved to be the same gene.

PTEN, the gene, encodes for PTEN, the protein, which is a dual-specificity phosphatase as it can dephosphorylate tyrosine-, threonine- and serine-phosphorylated proteins (see equation 1.1), as well as being a lipid phosphatase specific for the D3-position of the inositol ring and dephosphorylates PI(3,4,5)P$_3$ to PI(4,5)P$_2$ (see reaction 1.2) [14]. The corresponding enzymatic reactions are as follows:

$$\text{Phosphoprotein} + \text{H}_2\text{O} \Rightarrow \text{Protein} + \text{Phosphate} \tag{1.1}$$

$$\text{PI(3,4,5)P}_3 + \text{H}_2\text{O} \Rightarrow \text{PI(4,5)P}_2 + \text{Phosphate} \tag{1.2}$$
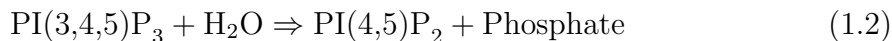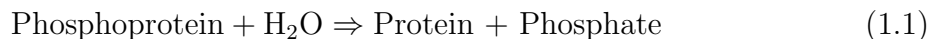
PTEN negatively regulates the PI3K-Akt/PKB pathway through its lipid phosphatase activity (see section 1.3) and the MAPK pathway through its protein phosphatase activity. PTEN is expressed in all adult human tissues including the brain, heart, lungs, liver and the pancreas. Apart from *wt* PTEN, we also consider H93R PTEN which is an autism related mutant that has the same secondary structure as *wt* PTEN but has significantly reduced enzyme activity [6] as well as C124S which is a Cowden syndrome related mutant that is catalytically inactive and is unable to inhibit the formation of focal adhesions [15]. We aim to quantify and compare the binding affinities of *wt* PTEN, H93R PTEN and the truncated PTEN (used to determine the crystal structure) to lipid bilayers and to correlate them with structural changes in the protein.

1.2 Sequence and Crystal Structure

Figure 1.1: PTEN Primary Structure. PTEN consists of a PI(4,5)P_2 binding module (PBM), a phosphatase domain (PD), a C2 domain, two Phosphorylation sites (PEST) and a PDZ binding motif.

Figure 1.1 shows the primary structure of PTEN. The protein consists of a 14 residue (1-14) N-terminal PI(4,5)P_2 binding module (PBM), followed by a 171 residue (15-185) phosphatase domain that includes the Cys-71 and Cys-124 that form the catalytic site, a 166 residue (186-351) C2 domain (named for its homology with a domain in protein kinase C) that is responsible for calcium independent membrane association [4] via a CBR3 (Calcium binding region 3) motif (residues 255-280) and a long 52 residue (352-403) C-terminal tail that consists of two phosphorylation 'PEST' (Proline, Glutamic Acid, Serine, Threonine) sites and a PDZ (post synaptic density protein/Drosophila disc large tumor suppressor/zonula occludens-1 protein) binding motif for interaction with other proteins. The C-terminal tail was shown to be necessary for maintaining protein stability [16]. The PDZ domain was shown to associate with MAGI2 and MAGI3 (membrane-associated guanylate kinase inverted) proteins which enhances the ability of low concentrations of PTEN to inhibit Akt and the removal of the PDZ domain adversely affects PTEN's ability to regulate Akt [17, 18]. C124S PTEN is an enzymatically inactive mutant and a truncated version consisting of residues 1-377 is rescued from rapid degradation by

Figure 1.2: Truncated PTEN. The amino acid sequences excluded from the crystal structure of PTEN are highlighted in red.
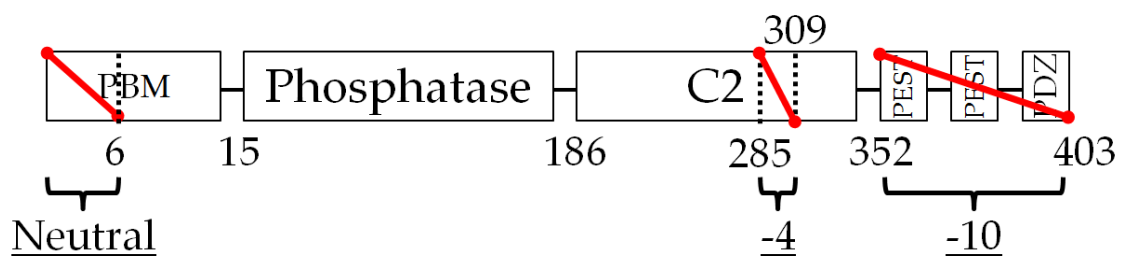
Figure 1.3: Effect of Truncation. The truncated PTEN used to determine the X-Ray crystal structure has a net positive charge of 14 as compared to *wt* PTEN.

the return of the PDZ domain to the C-terminal [17]. All this hints at an important role for the C-terminal tail in enhancing PTEN's stability.
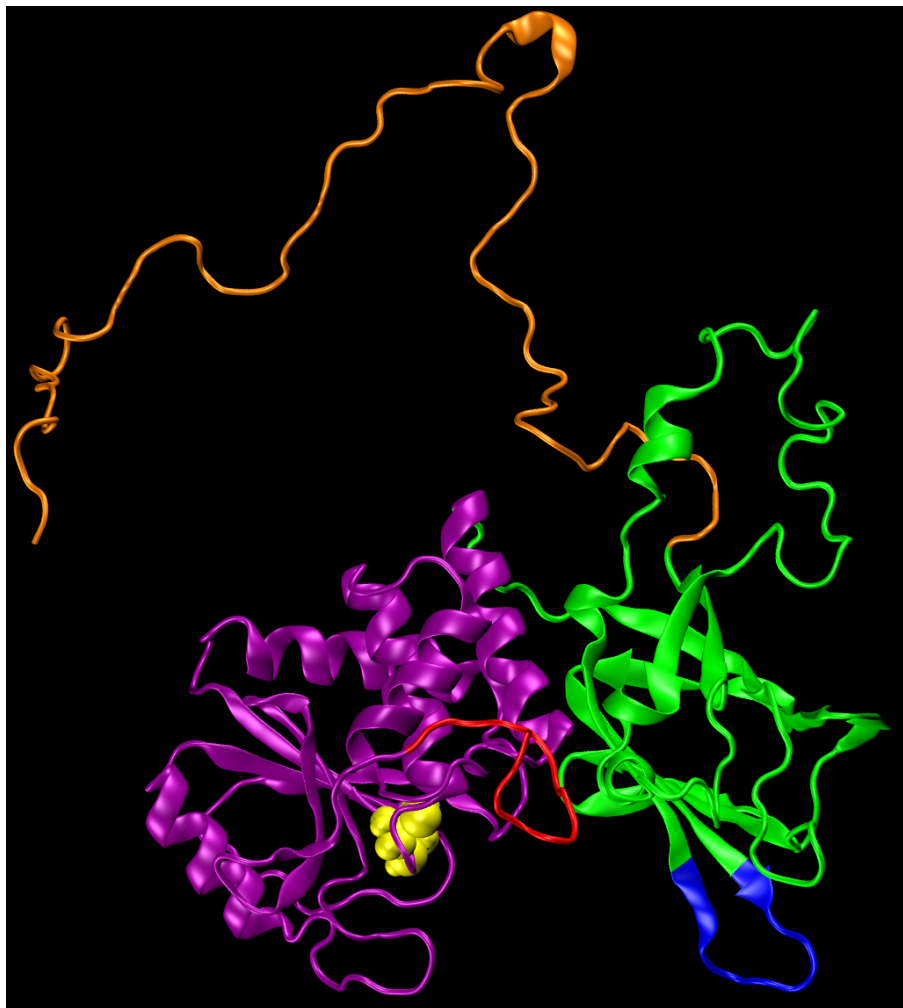
Figure 1.4: PTEN Tertiary Structure. PI(4,5)P$_2$ binding module (red), phosphatase domain (purple), active site (yellow), C2 domain (green), CBR3 PS-binding motif (blue) and the disordered C-terminal tail (orange).

The 2.1 Å crystal structure of human PTEN bound to L(+)-tartrate was determined in 1999 [4]. However, 20% of the residues (80 of the 403) were not included due to their highly disordered nature (see figure 1.2). As a result, the truncated protein has a net charge difference of +14 as compared to *wt* PTEN (see figure 1.3). This could enhance the electrostatic interaction of the truncated crystal structure PTEN to anionic lipids in the bilayer. The coordinates of an additional 16 residues could not be determined. A tertiary structure of the full-length protein is shown in figure 1.4. PTEN has an enlarged active site (CX5R motif, residues 124-130),

as compared to other protein phosphatases, that Lee et al. suggest is needed to accommodate the larger PI(3,4,5)P$_3$ lipid [4]. The structure also shows that the phosphatase domain (PD) and C2 domain are tightly linked via a large interface [4], hinting at the role the C2 domain's membrane association may play in optimizing the protein's orientation to facilitate the catalytic activity of the PD. The C2 domain has a CBR3 (calcium binding region 3) loop that consists of five lysines and two hydrophobic residues (a leucine and a methionine) and the mutation of four of the lysines to alanines results in a complete loss in membrane binding [4].

1.3   PI3K-PTEN Phosphorylation Switch
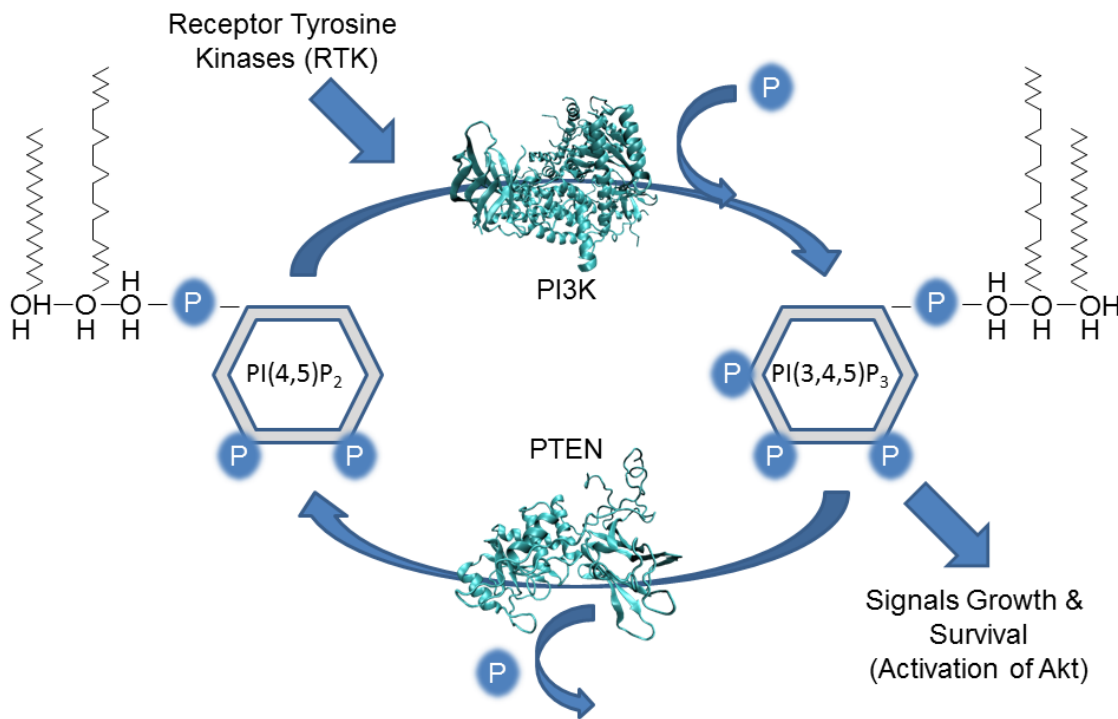
Figure 1.5: PI3K-PTEN Phosphorylation Switch. PI3K phosphorylates PI(4,5)P$_2$ to PI(3,4,5)P$_3$, signaling cell growth and survival. PTEN dephosphorylates PI(3,4,5)P$_3$ back to PI(4,5)P$_2$, fulfilling its tumor suppressor role.

When PTEN was first discovered in 1997, its similarity to tyrosine phosphatases led to the assumption that PTEN's primary function was as a protein phosphatase. However, it had a very low efficiency and it was only later that its lipid phosphatase

role and the PI(3,4,5)P$_3$ substrate were identified [14]. PTEN is an antagonist for the PI3K-Akt/PKB signaling pathway as shown in figure 1.5. The PI3K pathway is evolutionarily conserved from yeast to humans [19]. Growth factors activate PI3K, leading to the phosphorylation of PI(4,5)P$_2$ to PI(3,4,5)P$_3$, which is an important intracellular second messenger. PI(3,4,5)P$_3$ is responsible for the translocation of Akt to the membrane by binding to its pleckstrin homology (PH) domain. This is followed by a conformational change in Akt that results in its phosphorylation and subsequent activation [20]. Akt is a serine/threonine kinase that controls cell growth, size, survival and mRNA translation [21]. PTEN shuts off that signaling pathway by dephosphorylating PI(3,4,5)P$_3$ back to PI(4,5)P$_2$, thereby signaling cells to stop dividing or even controlled cell death (apoptosis) when necessary.

PTEN is a crucial tumor suppressor for the following reasons [22]:

1. No other phosphatase can duplicate PTEN's function, as the inactivation of PTEN deregulates both the upstream and downstream pathways of PI3K [20].

2. The PTEN/PI3K-Akt pathway is a critical signaling pathway for tumorigenesis.

3. PTEN has multiple interactions with p53, which is the only protein more commonly mutated in human cancer than PTEN, and has been shown to result in an increase in p53's stability [23], although it is unclear how this occurs.

1.4 Regulation of PTEN

1.4.1 Transcriptional Regulation

Over the last decade, several transcription factors that regulate PTEN expression have been identified, thereby dissipating the notion that PTEN was constitutively expressed [24]. PTEN is upregulated by early growth regulated transcription factor 1 (EGR1) [25], peroxisome proliferator-activated receptor γ (PPARγ) [26], the tumor suppressor p53 [27], human sprouty homolog 2 (SPRY2) [28], the cytokine resistin [29] as well as several phytoestrogens [30]. On the other hand, mitogen-activated protein kinase kinase-4 (MKK4) [31], transforming growth factor (TGF)β [32, 33] and proto-oncogenic transcription factor JUN [34] negatively regulate PTEN transcription.
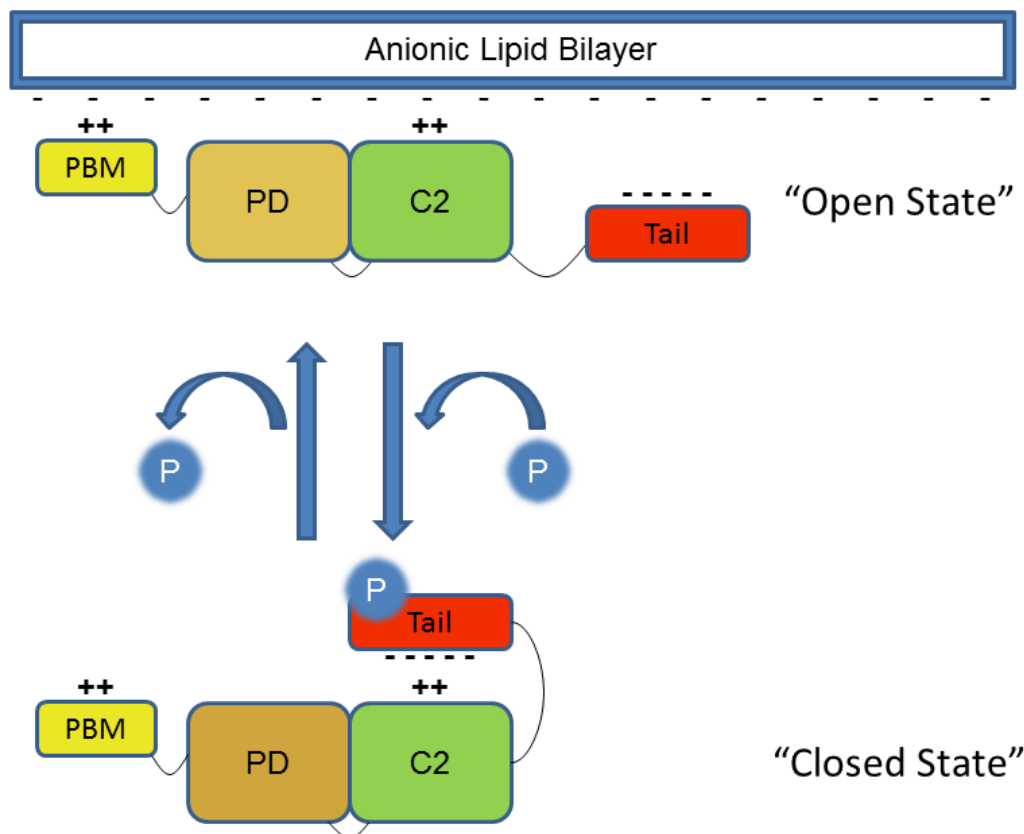
Figure 1.6: Proposed Regulation of PTEN. When PTEN is in the 'Open' state, the C2 domain is accessible for binding to anionic lipids. If the PEST sites on the C-terminal tail are phosphorylated, PTEN is proposed to go into a 'Closed' state where the tail interacts with the C2 domain, thereby obstructing membrane association and forcing it to remain in the cytosol.

1.4.2 Post-Transcriptional Regulation

Phosphorylation

PTEN has a long, disordered C-terminal tail that was too disordered to be crystallized. While there is little structural information available, there have been efforts to investigate a functional role for PTEN. In a groundbreaking paper, Vazquez et al. [16] discovered two key functions for the C-terminal tail:

1. **The tail is required for PTEN stability.** A 1-353 PTEN mutant was expressed which had a half-life that was reduced four-fold in comparison to *wt* PTEN [16]. This was also accompanied by an increase in PTEN activity and the C-terminal tail has subsequently been associated with an inhibitory function [16]. This leads to a model where the full-length *wt* PTEN is in a stable

but inactive state. Upon activation, it is prone to quicker degradation, thereby acting as a regulatory mechanism preventing excessive dephosphorylation of $PI(3,4,5)P_3$.

2. **The tail is required for PTEN phosphorylation.** Nearly 30% of the C-terminal tail is made up of serines or threonines that are potential phosphorylation sites. Not surprisingly, the 1-353 PTEN mutant results in a significant reduction in the total PTEN phosphorylation [16]. There are two consecutive PEST sites along the C-terminal tail: residues 350-375 and 379-386 [35]. Through a series of single, double, triple and quadruple point mutations, it was discovered that Ser370 is almost always phosphorylated in combination with Ser380, Thr382, Thr383 and Ser385 [16]. Mutating all five of these residues results in a dramatic decrease in steady-state levels of PTEN but an increase in its catalytic activity [16]. It was independently shown that mutating Ser385 to an alanine increases catalytic activity *in vitro* and PTEN association with the plasma membrane *in vivo* [36]. It is unclear how the tail is phosphorylated *in vivo* and how it is regulated. *In vitro*, casein kinase 2 (CK2) (targets Ser370 and Ser385), glycogen synthase kinase 3β (GSK3β) (targets Ser362 and Thr366) and protein interacting to the C-terminus-1 (PICT-1) (targets Ser380) have been identified as possible kinases of the C-terminal tail [37, 38, 39, 40], although it has also been suggested that PTEN may even engage in auto-phosphorylation. Apart from the PEST sites mentioned earlier, residues Ser229, Thr232, Thr319 and Thr321 can be phosphorylated by the rho-associated protein kinase (ROCK), resulting in enhanced localization of PTEN to the plasma membrane [41].

This has resulted in the model of membrane association [10] shown in figure 1.6. The C2 domain is electrostatically attracted to anionic lipids in the membrane. The PBM then binds to $PI(4,5)P_2$, which may provide selective targeting of PTEN to the inner leaflet of the plasma membrane which is relatively enriched in $PI(4,5)P_2$, and finally the active site dephosphorylates $PI(3,4,5)P_3$. If the C-terminal tail is phosphorylated at the PEST sites, the protein goes into a 'closed' state with the C-terminal tail preventing the C2 domain from associating with the membrane.

More recently, it was shown for the first time that the C-terminal tail interacts with the CBR3 motif of the C2 domain (residues 255-280) [36]. However, if the five basic lysines in the stretch were mutated to alanines, there was no change in the interaction indicating a non-electrostatic mode of association [36]. In addition, a phosphomimic peptide consisting of residues 368-390 from the C-terminal tail with serines 370, 380 and 385 changed to aspartic acid and threonines 382 and 383 changed to glutamic acid was able to significantly inhibit catalytic activity *in vitro* and membrane localization *in vivo* [36].

PTEN can also inhibit the migration of human glioma cells independent of its lipid phosphatase activity [42]. It was shown that G129E PTEN, which only lacks

lipid phosphatase activity, was able to control cell migration as long as threonine 383 was dephosphorylated [42]. Both the phosphorylated version of G129E and the lipid and protein phosphatase inactive mutant C124S did not show a similar effect [42]. While the connection between dephosphorylation and activity is consistent with earlier experiments and the 'open' and 'closed' states of PTEN, the requirement for protein phosphatase activity as well has led to speculation that PTEN can dephosphorylate itself [43]. This is not unprecedented as PTEN has already been shown to dephosphorylate other protein substrates such as FAK (PTK2) [44], albeit weakly.

Ubiquitination

Lys13 and Lys289 are conserved ubiquitination sites in PTEN and this discovery led to the search for E3 ligases [45]. Subsequently, the Hect domain E3 ubiquitin ligase Nedd4-1 was identified as a mediator of the mono- and polyubiquitination of PTEN [46].

Acetylation and Oxidation

The catalytic activity of PTEN can be negatively regulated by acetylation of Lys125 and Lys128 by the nuclear histone acetyltransferase p300/CBP-associated factor (PCAF) [47]. PTEN can also be downregulated by the formation of a disulfide bond between the catalytic Cys124 with Cys71 by reactive oxygen species (ROS) [48, 49, 50, 51].

Interaction with Other Proteins

PTEN has a three amino acid PDZ binding motif that allows PTEN to interact with other proteins, which in turn can regulate PTEN's membrane localization, thereby affecting its ability to dephosphorylate $PI(3,4,5)P_3$. PTEN can be recruited to the membrane by Na^+/H^+ exchanger regulatory factor (NHERF) adaptor proteins NHERF1 and NHERF2; membrane-associated guanylate kinase inverted (MAGI) proteins MAGI1b, MAGI2 and MAGI3 as well as microtubule associated serine/threonine kinase 3 (MAST3) and syntrophin associated serine/threonine kinase (SAST) [24]. Many of these interactions can be negatively regulated by phosphorylation of the C-terminal tail [16, 52, 53]. Since PTEN binding to the membrane is in the millisecond timescale [54], these interactions don't have to be long-lived to have an impact on the levels of $PI(3,4,5)P_3$.

1.5 Nuclear PTEN

PTEN was initially assumed to be a purely cytosolic protein [4, 55] leading to the focused research described above. In 1999, the first evidence of nuclear PTEN and

a possible tumor suppressor role emerged [56, 57, 58, 59]. However, such work was often criticized for the use of poor quality antibodies and the results were designated as artifacts [60]. Today, there is a large body of work supporting the existence of nuclear PTEN leading to investigations of its function and the method of import from the cytoplasm.

It is unclear whether PTEN enters the nucleus through diffusion [61] or active transport [62, 63], with evidence of both in different systems. PTEN has been shown to possess putative nuclear localization signals (NLS) sequences as well as several nuclear exclusion motifs (in the phosphatase domain, C2 domain and the C-terminal tail) [62, 64]. It was also shown that the K289E Cowden-syndrome related mutation is catalytically active but is unable to localize to the nucleus [45]. K289 is monoubiquitinated by the E3 ligase neural precursor cell expressed, developmentally downregulated 4-1 (NEDD4-1) in the cytoplasm, thereby allowing for nuclear import.

Given the presence of PI(4,5)P$_2$, PI(3,4,5)P$_3$, PI3K, PDK1 and AKT in the nucleus as well, it is natural to assume that the primary function of nuclear PTEN is its lipid phosphatase activity. This view has been challenged by the discovery that nuclear PI(3,4,5)P$_3$ is not sensitive to PTEN catalysis [65]. It is uncertain how nuclear PTEN performs its tumor suppressor function if not through the Akt signaling pathway. Recent work has focused on identifying near targets for nuclear PTEN. The nuclear proto-oncogene MSP58 was recently shown to bind to nuclear PTEN in a lipid phosphatase independent manner and the C-terminal tail was shown to play an important role [66]. PTEN also interacts with the nuclear histone acetyltransferase PCAF and p300/CBP with the latter promoting acetylation of p53 to counteract damage to DNA [47, 67].

1.6 Role of PI(4,5)P$_2$ in the Regulation of PTEN Enzymatic Activity

The N-terminal tail of PTEN is disordered, yet it has been implicated in specific association with PI(4,5)P$_2$. Since PTEN 10-353 retains its activity [16] and mutating Lys13 or Arg14 reduces the efficiency of PI(3,4,5)P$_3$ hydrolysis, both in the presence and absence of PI(4,5)P$_2$, the N-terminal tail residues 1-14 have been termed as the PI(4,5)P$_2$ binding module (PBM) [Soluble PI(3,4,5)P$_3$: [4, 68]; Membrane-bound PI(3,4,5)P$_3$: [69, 70]]. There are three models that have been proposed to explain the role of PTEN association with PI(4,5)P$_2$ in regulating the catalytic activity of PTEN [71]. In the first [72, 73], the PI(4,5)P$_2$ binding module (PBM) is believed to obstruct the binding of the active site to PI(3,4,5)P$_3$. Upon association of the PBM with PI(4,5)P$_2$, the active site is now made accessible thereby enhancing the enzymatic activity. In the second [70], binding of PI(4,5)P$_2$ to the PBM helps orient the protein in a catalytically favorable configuration. And finally, the third

model [5, 68] suggests that there is an allosteric conformational change in the PBM upon binding to PI(4,5)P$_2$ that is the cause for enhanced activity. It has to be noted that these three models are not mutually exclusive and it may be the case that a combination of all three occurs.

1.7 Non-Tumor Suppressor Roles of PTEN

The loss of PTEN has been shown to lead to a significant number of breaks of double-stranded DNA, implicating both cytoplasmic and nuclear PTEN in a role that attempts to preserve the integrity of genomic material, the mechanism of which is still being debated [74, 75].

PTEN regulates cell migration with the ability to both induce [76, 77, 78] and inhibit it [15, 42]. In fact, there are instances where PTEN inhibits migration through its effect on the PI3K signaling pathway but in a lipid phosphatase independent manner, once again bringing up the possibility of a currently unknown mechanism [15, 42].

PTEN also plays opposing roles in stem cell renewal. Loss of PTEN has been shown to result in the loss of hematopoietic stem cells (HSCs) [79, 80]. Conversely, in the nervous system the loss of PTEN results in the proliferation of neural stem cells [78, 81].

1.8 PTEN Mutations

Mutations of and amino acid deletions within PTEN often adversely impact its enzymatic activity thereby resulting in uncontrolled cell growth and proliferation leading to cancer. PTEN has been linked to prostate [82] and colorectal carcinomas [83]; breast [84], brain, prostate [85], endometrial [86] and lung cancer [87] as well as glioblastoma [88]. While most of these PTEN associations were observed for advanced stage tumors [60], in the endometroid subtype of endometrial cancer (EEC) PTEN is mutated in 20% of cases with hyperplasias (the precancerous lesions) [89, 90, 91, 92] and 37-51% of overall cases [92, 93, 94]. The loss of both copies of the *PTEN* gene in mice results in death during embryogenesis [95]. However, it has also been shown that PTEN is functionally haploinsufficient since the loss of even a single allele of the *PTEN* gene can result in cancerous tumors in mice [96].

Apart from its association with human cancer, PTEN mutations are also observed in the development of benign formation of disorganized masses in tissues called hamartomas. PTEN hamartoma tumor syndromes (PHTS) include Cowden syndrome (CS), Bannayan-Riley-Ruvalcaba syndrome, Proteus syndrome and Proteus-like syndrome. 80% of patients with Cowden syndrome exhibit inherited mutations in the PTEN gene which can lead to an increased risk of breast, thyroid and other cancers [97].

Figure 1.7: PTEN Mutants. The location of the H93R mutation is highlighted in red and the C124S mutation in yellow. The H93R mutation is located ~ 10 Å from the active site. Both mutations are spatially separated from the PBM (in purple) and the CBR3 PS-binding motif of the C2 domain (in orange).

It has been proposed that there is a continuum of functional PTEN losses through a combination of events such as genetic mutations, transcriptional repression, post-translational modification, epigenetic silencing and aberrant localization [98]. Towards the high end of this gradation, corresponding to total loss of PTEN expression, p53 signaling can result in cellular senescence thereby halting the spread of the cancer [98].

Autism is a neurodevelopmental disorder with symptoms that include a severe impairment of communication and social interaction. Most cases of autism and autism spectrum disorders (ASD) are due to multiple genetic factors [99]. A large body of evidence implicates the role of PTEN mutations in certain autism patients with macrocephaly [100, 101, 102, 103, 104, 105, 106, 107].

In this work, we focus on the H93R autism-related missense mutation – a point mutation that affects a single nucleotide resulting in the expression of an arginine instead of a histidine, located near the phosphatase active site (see figure 1.7). Circular dichroism data shows that the secondary structure of H93R PTEN is indistinguishable from that of *wt* PTEN [6] indicating that the mutant folds properly. H93R PTEN has a 75% reduction in phosphatase activity as seen in *in vivo* experiments [4, 6] and the slight increase in alpha-helical content upon binding to PI(4,5)P$_2$ that was observed for wt PTEN [5] is no longer observed [6]. The H93 residue is highly evolutionarily conserved [101]. A H93Y mutation was reported in a patient with CS and macrocephaly [108] that abolished phosphatase activity [109]. Computational analysis predicts the H93R mutation will increase hydrophilicity [101], thereby raising the likelihood that the residue is exposed to the solvent and hence the membrane.

1.9 Objectives

The proper functioning of PTEN is critical to maintaining the normal growth and survival of cells. It's catalytic activity is mediated by a rich and complex interaction with the lipid cell membrane. In spite of the importance of its regulatory behavior, little progress has been made in understanding the molecular basis of PTEN's interaction with the cell membrane and the ability of seemingly innocuous point mutations to disrupt the mechanism of membrane association.

Specific Aim 1: To identify the factors that affect PTEN's association with the lipid membrane; the mechanistic difference between association to PS and PI(4,5)P$_2$ and the role of the disordered N-terminal and C-terminal tails.

1. Quantify and compare the binding affinity of *wt* PTEN with the autism related H93R PTEN, the Cowden syndrome related C124S PTEN and the truncated PTEN to lipid bilayers.

2. Quantify and compare the contribution of the anionic lipids PS, PI(4,5)P$_2$ and PI(3,4,5)P$_3$ to the membrane binding kinetics.

3. Identify the cause of the apparent specificity of the N-terminal tail for PI(4,5)P$_2$ and not PI(3,4)P$_2$, PI(3,5)P$_2$ or PI(3,4,5)P$_3$.

4. Determine the stoichiometry of PTEN (*wt* and mutants) to PS and PI(4,5)P$_2$.

Specific Aim 2: Investigate the equilibrium structure of *wt* PTEN and the mutants in solution as well as in a membrane bound state.

1. Determine the equilibrium structure of full-length *wt* PTEN in solution, including the residues that were truncated during the determination of the crystal structure.

2. Investigate the impact of the point mutations in H93R PTEN and C124S PTEN on the structure of PTEN.

3. Determine the effect of binding to membranes bearing PS, PI(4,5)P$_2$ and both PS and PI(4,5)P$_2$ on the conformation of *wt* PTEN.

4. Determine the residues that contribute to membrane association, the mechanism of the interaction and their relative strengths.

5. Calculate the orientation of membrane-bound PTEN as a function of lipid composition and PTEN species.

6. Identify the equilibrium conformation and location of the disordered N-terminal and C-terminal tails, both in solution as well as when bound to a membrane.

1.10 Outline

We will first describe the development and characterization of a novel biomimetic lipid membrane system called the tethered bilayer lipid membrane (tBLM) that was used to quantify PTEN's membrane interactions. This was achieved by measuring the defect-density of the bilayer using electrochemical impedance spectroscopy (EIS) and the fluidity of lipids using two-photon fluorescence correlation spectroscopy (2P-FCS). In order to quantify protein binding, we conducted surface plasmon resonance (SPR) experiments on a custom-built setup. This allowed us to calculate the dissociation constant of *wt* PTEN and various mutants to the anionic lipids PS, PI(4,5)P$_2$ and PI(3,4,5)P$_3$ while ensuring the high quality of the lipid membranes by simultaneously performing EIS on the same sample. We then performed neutron reflectivity measurements to determine the structure of membrane-bound PTEN under physiological conditions and the impact of binding on the properties of the membrane. Finally, we carried out all-atom molecular dynamic simulations to complement the experimental results by providing molecular-level details of PTEN's structure and behavior, both in solution and while associating with a lipid membrane.

Chapter 2

Materials and Sample Preparation

2.1 Chemicals

20-tetradecyloxy-3,6,9,12,15,18,22-heptaoxahexatricontane-1-thiol (WC14), 29-hexadecyloxy-3,6,9,12,15,18,21,24,27,31-decaoxaheptatetracontan-1-thiol (FC16) and 20-(Z-octadec-9-enyloxy)-3,6,9,12,15,18,22-heptaoxatetracont-31-ene-1-thiol (HC18) were synthesized, purified and characterized by Dr. D. J. Vanderah at the IBBR as described in [110]. βME was purchased from Sigma-Aldrich (St. Louis, MO) and distilled before use. 200-proof Ethanol was purchased from Pharmco-Aaper (Philadelphia, PA). Sodium Chloride (S271-1), Sodium Phosphate Monobasic Monohydrate (S369-1), HEPES (BP310-500), Chloroform (C606-1), Methanol (A452SK-4), Sulfuric Acid (A298-212), Sodium Hydroxide (S318-1) and Hydrochloric Acid (A144S) were used as received from Fisher Scientific (Pittsburgh, PA). Hellmanex II was purchased from Hellma GmbH (Mullheim, Germany), EDTA from Acros Organics (118432500; Morris Plains, NJ) and Nochromix from Godax Laboratories (19-010; Cabin John, MD). Ultrapure water was obtained from a Millipore (Billerica, MA) UHQ reagent grade water purification system. D_2O (99.9% isotope purity) was used as received from Cambridge Isotopes Laboratory (Andover, MA). For the SPR experiments, n=1.52 refractive index matching liquid was obtained from Cargille Labs (Cedar Grove, NJ).

2.2 Lipids

The phospholipids, DOPC: 1,2-dioleoyl-sn-glycero-3-phosphocholine; DOPS: 1,2-dioleoyl-sn-glycero-3-phospho-L-serine; LRPE: 1,2-dioleoyl-sn-glycero-3-phosphoethanolamine-N-(lissamine rhodamine B sulfonyl); cholesterol purified from ovine wool and brain PI(4,5)P$_2$: L-α-phosphatidylinositol-4,5-bisphosphate were used as supplied in powder form from Avanti Polar Lipids (Birmingham, AL). DPPI(4,5)P$_2$: phosphatidylinositol-(4,5)-P$_2$ (1,2-dipalmitoyl) and DPPI(3,4,5)P$_3$:

phosphatidylinositol-(3,4,5)-P_3 (1,2-dipalmitoyl) were used as supplied in powder form from Cayman Chemical (Ann Arbor, MI). 5 mg/ml solutions of lipids were prepared. DOPC was dissolved in ethanol; DOPS and cholesterol were dissolved in chloroform and the phosphoinositol phosphates were dissolved in a mixture of chloroform:methanol:water = 20:9:1.

2.3 Proteins

2.3.1 PTEN Expression and Purification

Human PTEN with a six-histidine tag at the C-terminus was expressed in Escherichia coli BL21(DE3) bacteria by Marie-Claire Daou and Dr. Alonzo Ross at the University of Massachusetts medical school as described in [5]. The H93R and C124S mutations were introduced using a Quick-Change site-directed mutagenesis kit (Stratagene, La Jolla, CA). The plasmid of the truncated PTEN used to determine the crystal structure [4] was provided by Dr. N. R. Leslie (University of Dundee). The protein was purified with a HisTrap HP kit (GE Healthcare) and then further purified with a Superdex 200 16/60 column followed by a MonoQ 5/5 anion-exchange column. Phosphatase activity was verified as described in [68].

2.3.2 Dialysis

Prior to performing physio-chemical characterization, the protein was ultracentrifuged using an Eppendorf Centrifuge 5415 (Hauppauge, NY) at 13200 rpm (16100 rcf) for 10 minutes. The protein was dialyzed overnight in the appropriate buffer (see 2.4) using a Slide-A-Lyzer dialysis cassette (66370; Thermo Scientific). The protein was then ultracentrifuged once again for 10 minutes and the supernatant was used for experiments.

2.4 Buffers

For PTEN work and bilayer preparation by rapid solvent exchange (see section 2.5.3), the buffer used was 100 mM NaCl + 10 mM HEPES + 1 mM EDTA + 1 mM βME at pH 7. For bilayer preparation by osmotic shock vesicle fusion (see section 2.5.3), vesicles were prepared in 500 mM NaCl + 10 mM HEPES at pH 7 and subsequently ruptured by dilution into the RSE buffer.

2.5 Preparation of Tethered Bilayer Lipid Membranes

2.5.1 Carrier Substrates for tBLMs

For SPR and EIS experiments, self-assembled monolayers (SAMs) were prepared on 3"×1"×1 mm microscope slides (12-544-1; Fisherfinest, Fisher Scientific) while for FCS and NR experiments SAMs were prepared on 3" diameter [100] silicon wafers (thickness = 380 ± 25 μm) from Silicon Quest International (Santa Clara, CA).

2.5.2 Substrate and SAM Preparation

Silicon wafers and glass slides were cleaned with an aqueous solution of Hellmanex (5% by volume) and then immersed in Nochromix solution (85 g of Nochromix crystals per 2.5 L of sulfuric acid) for 15 minutes. Both steps were followed by excessive rinsing with ultrapure water and a second rinse with 200-proof ethanol. They were then blown dry with nitrogen gas (99.995% pure). The substrates were then placed in a high-energy magnetron sputtering instrument (ATC Orion; AJA International Inc., North Scituate, MA). Once the pressure in the chamber reached 1.5×10^{-7} Torr, the substrates were coated with chromium (~ 20 Å) and gold (~ 150 Å for NR and ~ 450 Å for all other experiments) as described below:

1. Turn the sample rotation speed knob to the maximum setting.

2. Turn on the compressor, start the flow of argon gas by pressing 'Gas1' on the touchscreen and set the flow-rate to 10.0.

3. Increase the chamber pressure to 3.0×10^{-3} Torr by rotating the handle on the side of the magnetron.

4. Make sure the selected gun is 'Gun1' and press the 'DC On' button on the touchscreen.

5. Once the formation of a plasma has been achieved wait for the ramp time and the delay time to elapse, then open the chromium shutter by pressing 'SH1'.

6. Once the required deposition time has elapsed, press the 'SH1' button again to close the chromium shutter.

7. When the ramp down has completed, press 'Gas1' to turn off the argon gas flow.

8. Reduce the chamber pressure as much as possible by rotating the handle in the direction opposite to step 3.

17

9. Wait for the chamber pressure to drop back to 1.5×10^{-7} Torr.

10. Start the argon gas flow by pressing 'Gas1' on the touch-screen.

11. Ensure the argon gas flow-rate is exactly 10.0.

12. Increase the chamber pressure to 3.0×10^{-3} Torr by rotating the handle on the side of the magnetron.

13. Select 'Gun2' and press the 'DC On' button on the touchscreen.

14. Once plasma has been acquired and the ramp time and delay time have elapsed, press the 'SH2' button to open the gold shutter.

15. When the required deposition time has elapsed, press the 'SH2' button again to close the gold shutter.

16. Once the ramp down has completed, press 'Gas1' to turn off the argon gas flow.

17. Reduce the chamber pressure as much as possible by rotating the handle in the direction opposite to step 3.

18. Turn off the wafer rotation, turn off the compressor and the vacuum pump and close the side valve completely.

19. Once the chamber has attained atmospheric pressure, open it and extract the wafer, then place a freshly cleaned wafer inside and start the vacuum pump.

20. Once the chamber pressure has reached 10^{-3} Torr, open the valve closed in step 18.

Using an in-house X-ray reflectometer (Bruker AXS, Germany) and an ellipsometer, the sputtering parameters were optimized to achieve an RMS roughness of ~ 5 Å and a thickness variation of less than 3% [110].

Fresh gold-coated substrates were incubated overnight in a 0.2 mM ethanolic mixture of tether-lipid (WC14, FC16 or HC18) and βME at the specified molar ratio (usually tether:βME=30:70). The SAMs were then rinsed with 200-proof ethanol, dried with nitrogen and used within 24 hours of preparation.

2.5.3 Bilayer Completion

Once a substrate with a SAM has been prepared, there are 2 ways of completing the bilayer:

Rapid Solvent Exchange (RSE)

In this technique of bilayer preparation first described in [111], SAMs were incubated with a 5 mg/ml solution of phospholipids for $\sim$ 5 minutes. The surplus lipids in this highly concentrated solution near the SAM were then rapidly displaced with an excess of aqueous buffer while care was taken not to introduce any air bubbles that could result in an incomplete bilayer. Bilayers composed purely of zwitterionic lipids were prepared at room temperature while bilayers with anionic lipids were prepared by heating the sample cell, the lipids and the buffer to $\sim$ 45 ℃. In the latter case, the bilayer was kept at $\sim$ 45 ℃ for a further 10 minutes following the RSE and was then allowed to cool to room temperature at which it was maintained for the rest of the experiment. The bilayer was allowed to equilibrate for at least one hour before any physio-chemical measurements were performed. RSE requires the use of cholesterol for preparation of complete bilayers with an anionic component greater than 10 mol% (Niepa, Shenoy and Lösche, unpublished EIS data).

Osmotic Shock Vesicle Fusion

In this technique of bilayer preparation, 300 µl of 5 mg/ml lipid solution is transferred to a glass test tube and dried in a vacuum oven. The lipid film is resuspended in pentane, dried overnight under the hood, resuspended in a high salt (500 mM NaCl) aqueous buffer (see section 2.4) and sonicated for an hour. The lipid suspension is then extruded with an Avanti Mini-Extruder (Avanti Polar Lipids, Alabaster, AL) using 23 passes through a 100 nm pore-size nuclepore polycarbonate track-etched membrane (800309; Whatman, Kent, UK) to produce unilamellar vesicles. SAMs are incubated with these unilamellar vesicles at $\sim$ 45 °C for at least an hour. The vesicle solution is gently diluted and rinsed away with an excess of low salt (100 mM NaCl) aqueous buffer. This 5-fold difference in salt concentration results in the osmotic rupturing of the vesicles and the production of complete bilayers (see section 4.3.3). Cholesterol is not needed to prepare anionic lipid bilayers even if the anionic component accounts for up to 30 mol% of the mixture.

Chapter 3

Experimental Techniques

3.1 Fluorescence Correlation Spectroscopy (FCS)

3.1.1 Background

FCS was developed in the 1970s [112, 113, 114] and is a single-molecule technique that may be used to determine the concentration and diffusion coefficient of fluorophores in a sample. Unlike other optical techniques where the time-averaged fluorescence is the main signal and fluctuations are a source of noise that needs to be minimized, the fluctuations are the measured quantity in FCS. The technique became mainstream once it was combined with a confocal setup [115].

3.1.2 Two-Photon Excitation (2-PE)

In 1-PE, a fluorophore absorbs a photon whose energy is equal to the gap between the ground state and the excited state. However, excitation can also take place by the absorption of two (2-PE) (or even three photons) of lower energy, as theoretically predicted by Maria Göppert-Mayer [116]. Multi-photon excitation is a quantum mechanically forbidden process, as the initial photon excites the molecule to a virtual intermediate state that is not an eigenstate of the system, but can still occur with a very low probability. In practice, the two photons in 2-PE need to absorbed within a femtosecond of each other [117] (see figure 3.1). High-power pulsed lasers are used in order to increase the probability of the occurrence of this event. While it would appear that taking two photons of twice the wavelength (and hence half the energy) needed for one-photon excitation (1-PE) would suffice, due to the complex selection rules this is rarely the case with some dyes requiring more than and others requiring less than double the 1-PE excitation wavelength.

 2-PE has several advantages over 1-PE:

1. The probability of two photons being simultaneously absorbed increases with the square of the intensity. This results in a sub-femtoliter excitation volume
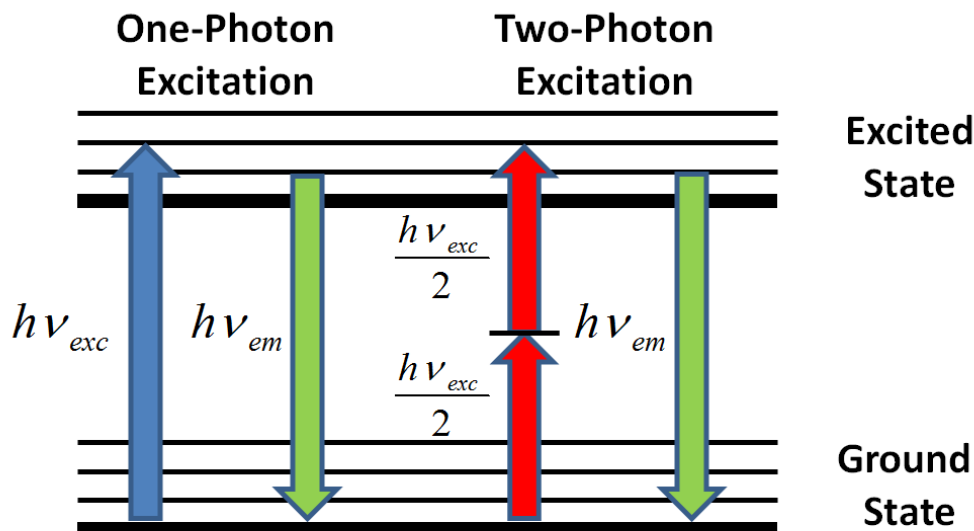
Figure 3.1: One-Photon (Linear) Excitation vs. Two-Photon (Non-Linear) Excitation. In standard 1P excitation, a fluorophore absorbs a photon and goes into an excited state. Following internal relaxation, the molecule returns to its ground state (not necessarily the zero vibrational state) emitting a photon of slightly lower energy (and hence frequency) than that of the incoming photon ($\nu_{exc} > \nu_{em}$). In 2P excitation, a fluorophore absorbs two photons, each of approximately half the energy required for 1P excitation.

that eliminates any out-of-focus excitation and photodamage as well as the need for pinholes that are used in 1-PE to filter fluorescence not from the focal plane, thereby simplifying the experiment.

2. For dyes that have a 1-PE excitation wavelength in the visible range of the spectrum, the corresponding 2-PE wavelengths are usually in the infrared, resulting in greatly decreased photodamage to biological samples.

3. 2-PE also gives the user the option of performing two-color FCS, where two different dyes with the same excitation wavelength but different emission wavelengths are excited with a single laser beam.

3.1.3   Brief Synopsis of FCS Theory

A detailed description of the theoretical concepts behind FCS can be found in [117]. A summary of the key concepts shall be presented below.
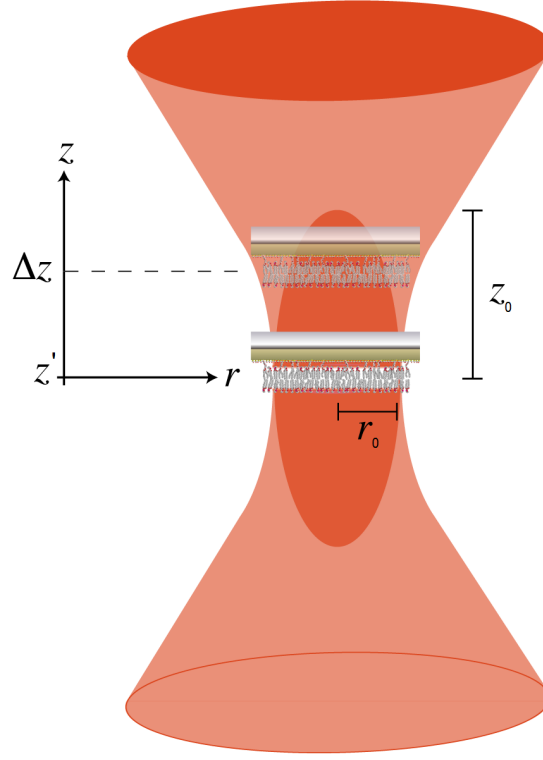
Figure 3.2: The FCS sample placed in a Gaussian focal volume with dimensions r_0 and z_0 with z' corresponding to the beam waist and Δz being the displacement in the z-scan methodology.

Assume a laser beam that illuminates a spot of local intensity $I(\mathbf{r})$ at a wavelength that matches the excitation wavelength of a given fluorophore of very low concentration (nM to μM) that is diffusing in the sample.

The fluorescence signal $F(\tau)$ detected in a short period of time $\Delta\tau$ depends on the intensity $I(\mathbf{r})$ as well as the density of labeled molecules $C(\mathbf{r},\tau)$, and is given by:

$$F(\tau) = \Delta\tau Q \int \mathrm{d}^3 r I(\mathbf{r}) C(\mathbf{r},\tau) \tag{3.1}$$

where Q is a constant that is determined by experimental details and the time-averaged value of $F(\tau)$ is given by:

$$\langle F(\tau) \rangle = \frac{1}{T} \int_0^T F(\tau)\, d\tau \tag{3.2}$$

FCS measures the fluctuations of the fluorescence signal which are defined as:

$$\delta F(\tau) = F(\tau) - \langle F(\tau) \rangle \tag{3.3}$$

22

where $\delta F(\tau)$ arises due to fluctuations in $C(\mathbf{r}, \tau)$ within the focal volume which can similarly be expressed as:

$$\delta C(\mathbf{r}, \tau) = C(\mathbf{r}, \tau) - \langle C(\mathbf{r}, \tau) \rangle \tag{3.4}$$

From equations 3.1 and 3.3, we get:

$$\delta F(\tau) = \Delta \tau Q \int \mathrm{d}^3 r I(\mathbf{r}) \delta C(\mathbf{r}, \tau) \tag{3.5}$$

The normalized autocorrelation function $G(\tau)$ is defined as:

$$G(\tau) = \frac{\langle \delta F(0).\delta F(\tau) \rangle}{\langle F(\tau) \rangle^2} \tag{3.6}$$

and can be expressed in terms of $I(\mathbf{r})$ and $C(\mathbf{r}, \tau)$ using equation 3.5 as:

$$G(\tau) = \frac{(Q \Delta \tau)^2}{\langle F(\tau) \rangle} \int \mathrm{d}^3 r \int \mathrm{d}^3 r' I(\mathbf{r}) I(\mathbf{r}') \langle \delta C(\mathbf{r}, 0) \delta C(\mathbf{r}', \tau) \rangle \tag{3.7}$$

Given free diffusion of the fluorophores, the diffusion equation for $\delta C(\mathbf{r}, \tau)$ is given by:

$$\frac{\partial}{\partial t} \delta C(\mathbf{r}, \tau) = D \Delta \delta C(\mathbf{r}, \tau) \tag{3.8}$$

Given the following 3D Fourier transform relations:

$$\tilde{f}(k) = \frac{1}{(2\pi)^{3/2}} \int \mathrm{d}^3 r f(\mathbf{r}) e^{i\mathbf{k}.\mathbf{r}} \tag{3.9}$$

$$f(r) = \frac{1}{(2\pi)^{3/2}} \int \mathrm{d}^3 k \tilde{f}(\mathbf{k}) e^{-i\mathbf{k}.\mathbf{r}} \tag{3.10}$$

equation 3.8 can be Fourier transformed to give the differential equation:

$$\frac{\partial}{\partial t} \delta \tilde{C}(\mathbf{k}, \tau) = -D k^2 \delta \tilde{C}(\mathbf{k}, \tau) \tag{3.11}$$

which has the solution:

$$\delta \tilde{C}(\mathbf{k}, \tau) = \delta \tilde{C}(\mathbf{k}, 0) e^{-D k^2 \tau} \tag{3.12}$$

Taking the Fourier transform of $\delta C(\mathbf{r}', \tau)$ and using equation 3.12, we get:

$$\delta C(\mathbf{r}', \tau) = \frac{1}{(2\pi)^3} \int \mathrm{d}^3 k \int \mathrm{d}^3 r e^{-D k^2 \tau} e^{i\mathbf{k}.(\mathbf{r}'' - \mathbf{r})} \tag{3.13}$$

Given that the density fluctuations at different positions are uncorrelated and that the local variance is proportional to the mean:

$$\langle \delta C(\mathbf{r}, 0) \delta C(\mathbf{r}'', 0) \rangle = \langle C(\mathbf{r}, \tau) \rangle \delta(\mathbf{r} - \mathbf{r}'') \tag{3.14}$$

From equations 3.13 and 3.14, we get:

$$\langle \delta C(\mathbf{r}, 0) \delta C(\mathbf{r}', \tau) \rangle = \frac{\langle C(\mathbf{r}, \tau) \rangle}{(2\pi)^3} \int d^3 k e^{-Dk^2\tau} e^{i\mathbf{k}.(\mathbf{r}-\mathbf{r}')} \tag{3.15}$$

Combining this with equation 3.7, we get:

$$G(\tau) = \frac{(Q\Delta\tau)^2}{\langle F(\tau) \rangle} \langle C(\mathbf{r}, \tau) \rangle \int d^3 k |\tilde{I}(\mathbf{k})|^2 e^{-Dk^2\tau} \tag{3.16}$$

If the laser is tightly focused, the beam spot $I(\mathbf{r})$ can be approximated by a three-dimensional Gaussian that decays to $1/e^2$ at r_0 and z_0 in the direction normal and radial to the excitation intensity, respectively (see figure 3.2):

$$I(\mathbf{r}) = e^{-2\frac{x^2+y^2}{r_0^2}} . e^{-2\frac{z^2}{z_0^2}} \tag{3.17}$$

Therefore, the effective focal volume, V_{eff}, is given by:

$$V_{\text{eff}} = \pi^{3/2} r_0^2 z_0 \tag{3.18}$$

Let $\langle N \rangle$ be the time-averaged number of fluorescent molecules diffusing in the focal volume. Its relation to the time-averaged concentration $\langle C \rangle$ ($\langle C \rangle \equiv \langle C(\mathbf{r}, \tau) \rangle$), by:

$$\langle N \rangle = V_{\text{eff}} \langle C \rangle \tag{3.19}$$

Combining equations 3.16, 3.17, 3.18 and 3.19 we get the autocorrelation function for a single freely diffusing species in three-dimensions:

$$G_{3D}(\tau) = \frac{1}{\langle N \rangle} \frac{1}{1 + \frac{\tau}{\tau_D}} \frac{1}{\sqrt{1 + \left(\frac{r_0}{z_0}\right)^2 \frac{\tau}{\tau_D}}} \tag{3.20}$$

where τ_D is the characteristic diffusion time.

For two-dimensional diffusion (see figure 3.3), equation 3.20 reduces to:

$$G_{2D}(\tau) = \frac{1}{\langle N \rangle} \frac{1}{1 + \frac{\tau}{\tau_D}} \tag{3.21}$$

Both $\langle N \rangle$ and τ_D can be determined by fitting the experimental data to the appropriate autocorrelation function. The diffusion coefficient, D, can then be calculated by:

$$D = \frac{r_0^2}{4p\tau_D} \tag{3.22}$$

where $p=1$ for 1-PE and $p=2$ for 2-PE.

r_0 and z_0 are usually calibrated by measuring the autocorrelation function for a dye with a known diffusion coefficient in medium with a given viscosity.
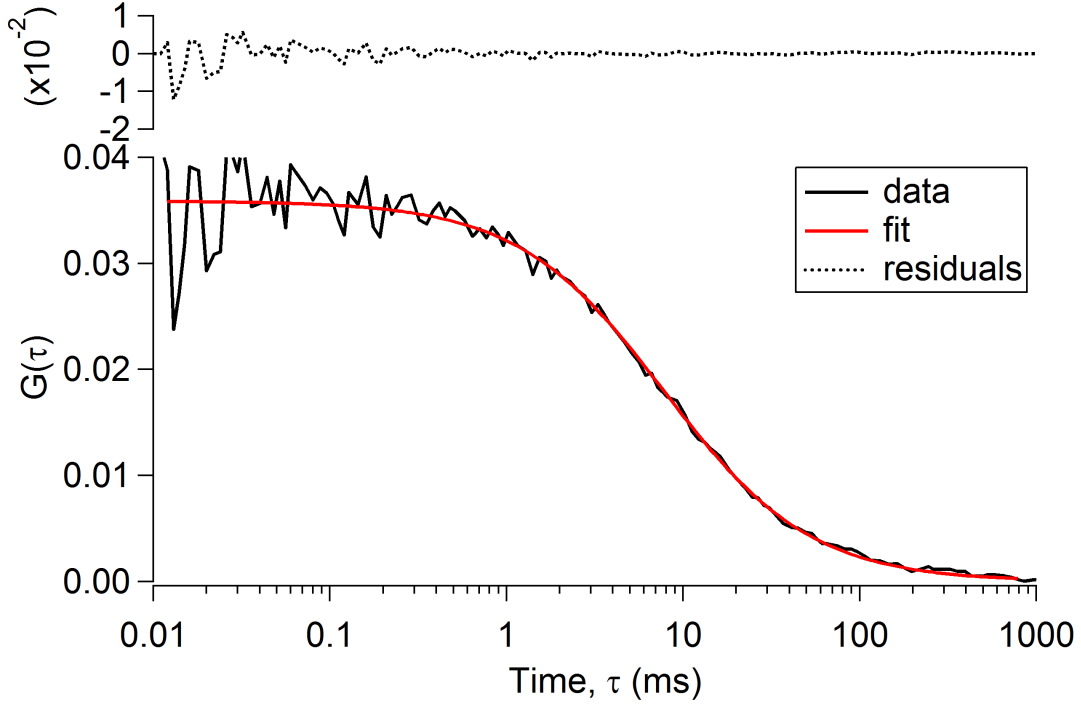
Figure 3.3: Autocorrelation function of the fluorescence from an ensemble of fluorophores that are confined to diffuse in 2D.

3.1.4 z-Scan FCS

Equation 3.22 is only valid if the sample is located at the beam waist, $z = z'$. For a sample not located at the beam waist (see figure 3.2), the beam cross-section increases as [118]:

$$r = r_0 \sqrt{1 + \frac{\lambda^2 (\Delta z)^2}{\pi^2 n^2 r_0^4}} \tag{3.23}$$

where Δz is the difference between the sample position and the beam waist, λ is the laser wavelength and n is the refractive index of the medium.

Combining equations 3.22 and 3.23, we get [119]:

$$\tau_D = \frac{r_0^2}{4pD} \left(1 + \frac{\lambda^2 (\Delta z)^2}{\pi^2 n^2 r_0^4} \right) \tag{3.24}$$

'z-scan FCS' is a technique where one scans the laser focus across the sample in a series of well-calibrated displacements along the bilayer normal z and measures the apparent diffusion time at each of these positions (see figure 3.4). A fit of the data to equation 3.24 gives r_0 and D without the need for calibrating r_0 or z_0. In the work reported here, multiple z-scan experiments were performed to achieve
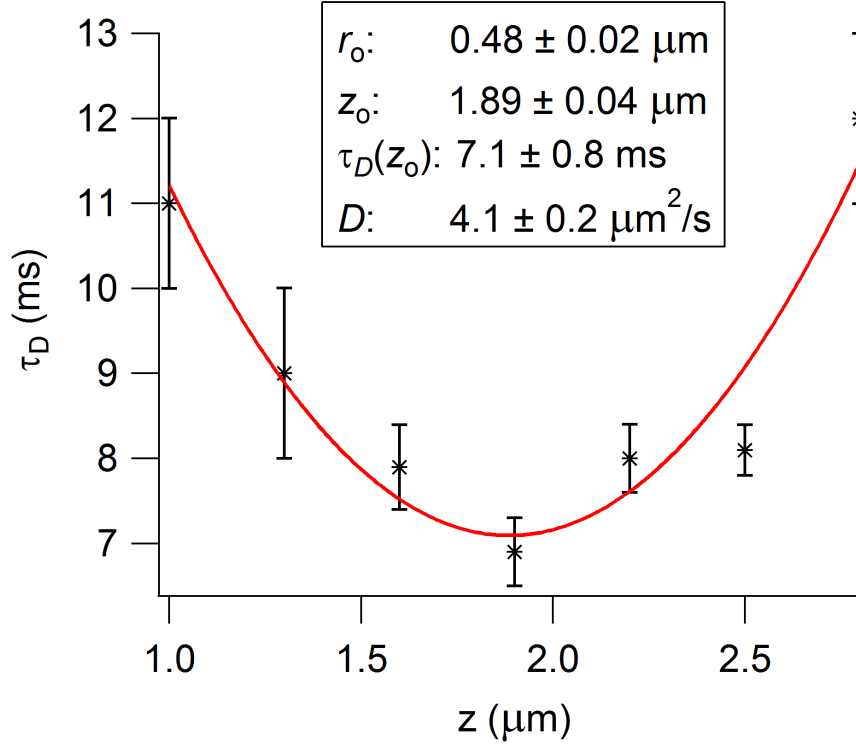
Figure 3.4: z-**Scan FCS:** A fit to the apparent diffusion time corresponding to seven displacements of the sample in 300 nm steps along the z direction.

statistically significant data and an averaged D was calculated using a maximum likelihood estimator defined in section 3.1.5 below (see figure 3.5).

3.1.5 Averaging z-Scans

FCS measurements on tBLMs can have two sources of error that are independent of each other [120]:

1. Variability in sample preparation – both locally in terms of micro-heterogeneity in the tBLM and also globally between different tBLMs.

2. Variance from the Levenberg-Marquardt fit of the experimental data due to random and/or systematic errors.

Let us describe the variability in sample preparation by a variance, σ^2, and the variance from the experimental fit by σ_i^2. If there is a large number of statistically independent deviations from the mean, they are both Gaussian in their distribution and the probability density of obtaining a diffusion coefficient D_i during a measurement i is also a Gaussian, $\Gamma(D_i - D, \sigma_i^2 + \sigma^2)$, with a mean D and variance $\sigma_i^2 + \sigma^2$.
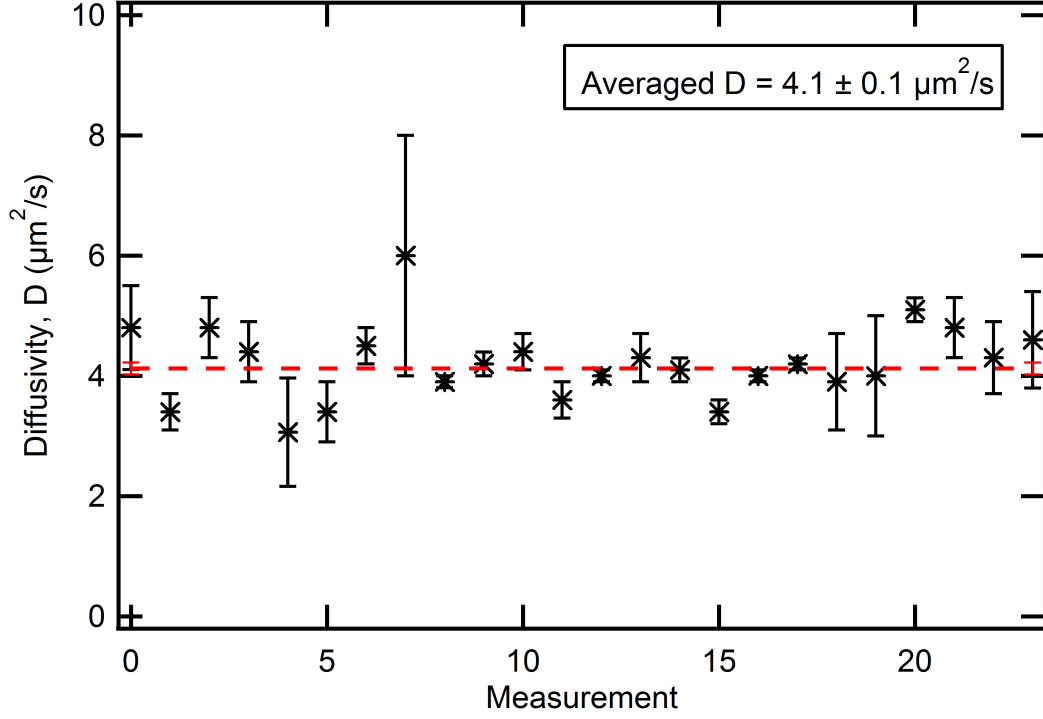
Figure 3.5: Averaged z-Scan: The average of 24 independent z-scan measurements.

The likelihood of measuring diffusion coefficients $D_1, D_2, ..., D_N$ with respective fitting errors $\sigma_1^2, \sigma_2^2, ..., \sigma_N^2$ in N measurements is given by the function:

$$L(\{D_i\}, \{\sigma_i\}; D, \sigma^2) = \prod_{i=1}^{N} \Gamma(D_i - D, \sigma_i^2 + \sigma^2) \qquad (3.25)$$

D and σ^2 can be treated as maximum-likelihood estimators that maximize L. So the following conditions must hold:

$$\frac{\partial L}{\partial D} = 0 \Rightarrow D(\sigma^2) = \sum_{i=1}^{N} \frac{D_i}{\sigma_i^2 + \sigma^2} \Big/ \sum_{i=1}^{N} \frac{1}{\sigma_i^2 + \sigma^2} \qquad (3.26)$$

$$\frac{\partial L}{\partial \sigma^2} = 0 \Rightarrow \sum_{i=1}^{N} \frac{(D_i - D)^2 - (\sigma_i^2 + \sigma^2)}{\sigma_i^2 + \sigma^2} = 0 \qquad (3.27)$$

Plugging equation 3.26 into equation 3.27 we get an equation that can be solved for σ^2. Inserting this value for σ^2 into equation 3.26, we can calculate the mean diffusion coefficient D.

The error in D can be calculated from error propagation and is given by:

$$(\delta D)^2 = \sum_{i=1}^{N} \frac{\partial D}{\partial D_i}(\partial D_i)^2 = \sum_{i=1}^{N} \frac{\partial D}{\partial D_i}(\sigma_i^2 + \sigma^2) \tag{3.28}$$

Using equation 3.26 in equation 3.28 and keeping only the first term (see [120] for details) we get an equation for the error in D:

$$\frac{1}{(\delta D)^2} = \sum_{i=1}^{N} \frac{1}{\sigma_i^2 + \sigma^2} \tag{3.29}$$

This analysis shows that considering only the variance from the experimental fit is a worst-case estimate of the error in the measured value of the diffusion coefficient. By accounting for variability in sample preparation, the estimate of errors in the diffusion coefficient values will yield results that are considerably smaller. In the special case where all the σ_i^2 terms are zero, equations 3.26 and 3.27 simplify to give the standard maximum-likelihood estimators for the mean and variance of a distribution when N data points have been measured. Similarly, equation 3.29 also reduces to $\Delta D \approx \sigma/\sqrt{N}$ when the σ_i^2 terms are zero.

3.1.6 Instrumentation

We used a custom-built two-photon FCS system consisting of a Verdi 10 W continuous wave diode-pumped solid-state (DPSS) laser (λ=532 nm) that pumps a Mira 900F mode-locked titanium-sapphire laser (125 fs pulse-width, 76 MHz repetition rate, 1.8 W at λ=780 nm) from Coherent (Santa Clara, CA). The output wavelength from the Mira can be tuned between 700 nm and 980 nm. 840 nm is used for exciting the Lissamine-Rhodamine dyed lipids. A neutral density filter is used to attenuate the infrared laser's output to between 5-10 mW before it enters the reflector turret of an Axiovert 200M inverted microscope (Carl Zeiss, Jena, Germany). The light then passes through a dichroic mirror (750dcspxr; Chroma Technologies, Rockingham, VT) and is focused using a 63× 1.2 NA C-Apochromat water immersion lens (Carl Zeiss) corrected for the coverslip thickness (0.14-0.18 mm). The excited fluorescence is epi-collected, passed through a bandpass filter (et575/50m-2p, Chroma Technologies, Rockingham, VT), focused via the microscope tube lens, re-collimated via an achromatically corrected doublet lens, split into two beams with a 50:50 beam splitter cube (Thorlabs, NJ) and is then focused via two achromatically corrected doublet lenses onto two separate avalanche photodiode detectors (SPCM-AQR14, Perkin-Elmer, Fremont, CA). The signal from the detectors are then sent to a hardware correlator (5000EPP; ALV, Langen, Germany) where they can be correlated or cross-correlated.
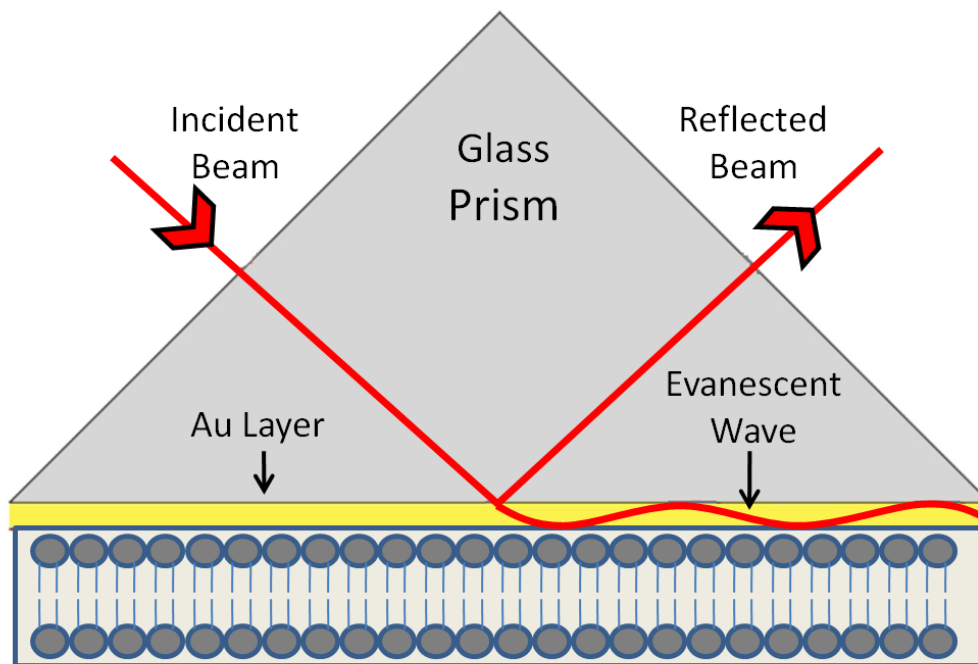
Figure 3.6: Kretschmann configuration for coupling laser light to a metal surface with the use of a prism in order to excite an evanescent surface plasmon wave in the metal.

3.2   Fluorescence Microscopy (FM)

3.2.1   Instrumentation

FM experiments were performed on an $Axiotech^{\mathrm{vario}}$ epifluorescence microscope from Carl Zeiss (Jena, Germany). A Zeiss filter set was used consisting of a BP510-560 excitation filter, an FT580 beam splitter and a LP590 emission filter. A Zeiss water Achroplan (20× 0.5 NA) objective lens was used along with a C9100 EM-CCD camera from Hamamatsu (Hamamatsu City, Japan) for high sensitivity fluorescence imaging of bilayers with the LRPE labeled lipid used as a probe.

3.3   Surface Plasmon Resonance (SPR)

3.3.1   Background

Surface plasmons are evanescent electromagnetic waves generated by the oscillation of free electrons in a metal with the intensity dropping exponentially as a function of

distance from the metal/dielectric or metal/vacuum interface. As a result, surface plasmons are very sensitive to changes in the refractive index at the interface – a property that is harnessed for high signal to noise binding measurements. In order to excite these surface plasmons, a laser is commonly used such that both the energy and momentum of the incoming photons match simultaneously with those of the surface plasmons. The Kretschmann configuration (see figure 3.6) is a standard method of achieving this coupling where a thin metal film is in direct contact with a glass prism of high refractive index. Only an electric field with a component perpendicular to the interface (or parallel to the plane of propagation, called p-polarized) can produce oscillations of the surface plasmons. Light passes through the prism, reflects off the metal film and is detected with a photodetector. While metals such as silver and chromium can be used, gold is the preferred choice due to it's biological (many proteins denature on silver surfaces) and chemical inertness. Above a critical incidence angle, the condition of total internal reflection is met and an evanescent wave is formed at the gold/dielectric interface. This excites the surface plasmons and results in a reduction in intensity of reflected light at the photodetector (see figure 3.7). This critical angle is a function of the refractive index (n) of the dielectric which changes upon an adsorption process, for example when protein ($n_{protein}$=1.41) replaces the buffer (n_{buffer}=1.33) adjacent to a biomimetic interface (see figure 3.8).

3.3.2 Theory

A detailed description of the theory that describes the properties of surface plasmons and surface plasmon resonance is available in the literature and in standard textbooks (such as [121, 122]). A brief overview is given below.

Total Internal Reflection

Take the situation of a plane wave from a laser traveling from a high refractive index glass prism (n_h) to a low refractive index buffer medium (n_l). Snell's law defines a 'critical' angle θ_c as

$$\sin \theta_c = \frac{n_l}{n_h} \tag{3.30}$$

where light incident at an angle greater than θ_c undergoes total internal reflection. Below θ_c, most of the light is transmitted but as one approaches θ_c the reflectivity (the ratio of the intensities of reflected and incident light) increases towards a maximum value of 1.

Above an incident angle of θ_c, an evanescent wave is formed at the interface where the electric field component normal the to the surface has a decay length l

30
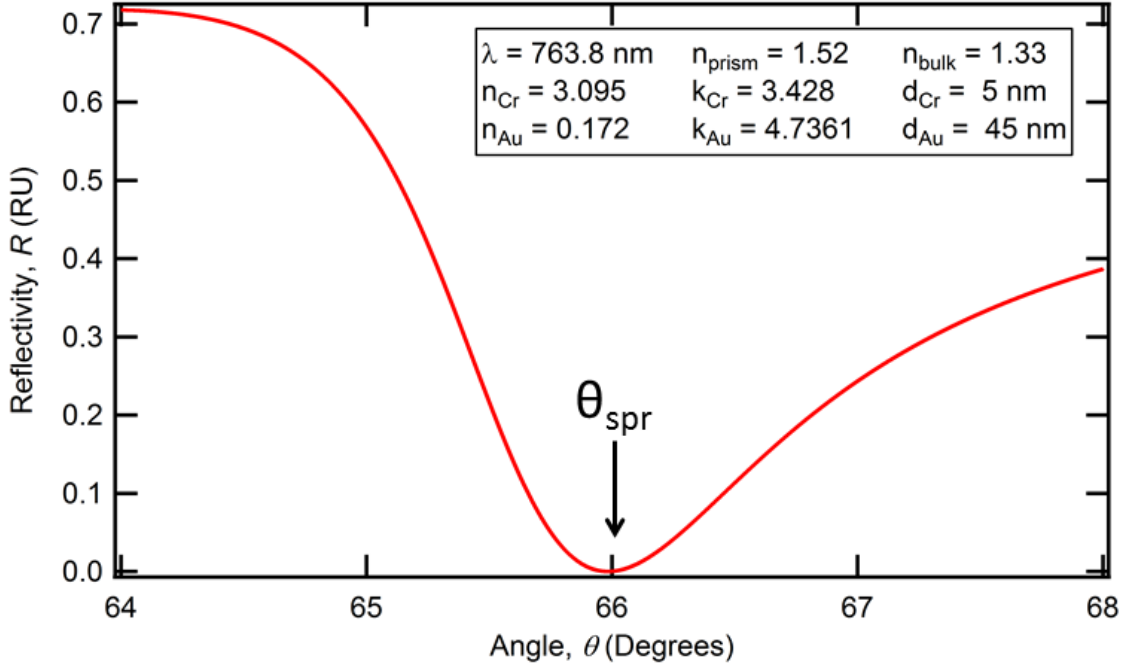
Figure 3.7: Reflectivity as a function of incident laser beam angle for a 50 Å layer of chromium followed by a 450 Å layer of gold deposited on a glass slide in contact with a prism in the Kretschmann configuration. There is perfect energy and momentum matching between the incoming photons and the surface plasmons at an incident angle of θ_{SPR} (the 'SPR resonance angle').

given by [121]:

$$l = \frac{\lambda}{2\pi\sqrt{(n.sin\theta)^2 - 1}} \tag{3.31}$$

In the next section, we will describe the theory behind the generation of evanescent surface plasmon waves in metals which results in a dramatic amplification of the the intensity of the waves [123], thereby allowing for their use as a probe of changes in the dielectric at the interface.

Surface Plasmons

Consider an interface at $z=0$ between a semi-infinite metal and a dielectric medium in the xy-plane with complex frequency-dependent dielectric functions given by:

$$\tilde{\epsilon}_m = \epsilon'_m + i\epsilon''_m \tag{3.32}$$

$$\tilde{\epsilon}_d = \epsilon'_d + i\epsilon''_d \tag{3.33}$$
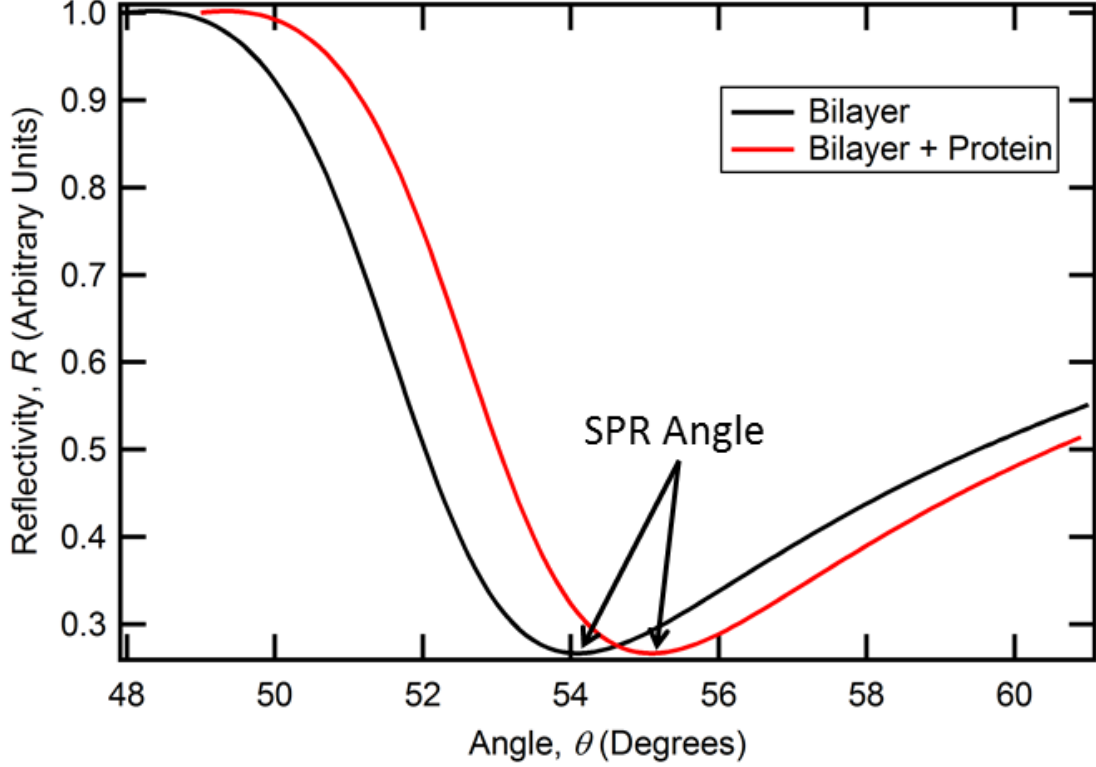
Figure 3.8: The SPR resonance angle is very sensitive to the refractive index of the dielectric medium at the gold interface. The binding of a small amount of protein to a bilayer would result in a shift in the SPR resonance angle to larger values.

and their respective refractive indices are given by:

$$n_m = \sqrt{|\epsilon'_m|} \tag{3.34}$$

$$n_d = \sqrt{|\epsilon'_d|} \tag{3.35}$$

where $n_m > n_d$.

In order to excite surface plasmons, a surface charge density σ needs to be induced by a component of the dielectric displacement $\vec{D}$ normal to the interface ($\vec{z}$) [121]:

$$\left(\vec{D}_2 - \vec{D}_1\right).\vec{z} = 4\pi\sigma \tag{3.36}$$

As mentioned earlier, only p-polarized light possesses an electric field component normal to the surface. The electric field $\vec{E}$ and magnetic H-field $\vec{H}$ of the resulting surface-bound electromagnetic wave have the general form ($\vec{A}$):

$$\vec{A}_m = \vec{A}_{m0}e^{i\left(\vec{k}_{xm}\vec{x}+\vec{k}_{zm}\vec{z}-\omega t\right)}, z < 0 \tag{3.37}$$

$$\vec{A}_d = \vec{A}_{d0}e^{i\left(\vec{k}_{xd}\vec{x}+\vec{k}_{zd}\vec{z}-\omega t\right)}, z > 0 \tag{3.38}$$

where $\vec{k}_{xm}$ and $\vec{k}_{xd}$ are the wavevectors in the x-direction, $\vec{k}_{zm}$ and $\vec{k}_{zd}$ are the wavevectors in the z-direction and ω is the angular frequency.

Maxwell's equations state:

$$\nabla.\vec{E} = 0 \tag{3.39}$$

$$\nabla.\vec{H} = 0 \tag{3.40}$$

$$\nabla \times \vec{E} + \frac{1}{c}\frac{\partial \vec{H}}{\partial t} = 0 \tag{3.41}$$

$$\nabla \times \vec{H} - \frac{\epsilon}{c}\frac{\partial \vec{E}}{\partial t} = 0 \tag{3.42}$$

where c is the speed of light and ϵ is the dielectric constant of the medium.

At the interface,

$$E_{xm} = E_{xd} \tag{3.43}$$

$$H_{ym} = H_{yd} \tag{3.44}$$

From equation 3.43, we get:

$$k_{xm} = k_{xd} \equiv k_x \tag{3.45}$$

And from equations 3.37 and 3.42, we get:

$$k_{zm}H_{ym} = \frac{\omega}{c}\epsilon'_m E_{xm} \tag{3.46}$$

$$k_{zd}H_{yd} = -\frac{\omega}{c}\epsilon'_d E_{xd} \tag{3.47}$$

the nontrivial solution to which is given by:

$$\frac{k_{zm}}{k_{zd}} = -\frac{\epsilon'_m}{\epsilon'_d} \tag{3.48}$$

Consequently, not only is $|\epsilon'_m| > |\epsilon'_d|$, but ϵ'_m and ϵ'_d must be of opposite sign. Equations 3.41, 3.42, 3.46 and 3.47 can be combined to give:

$$k_m^2 + k_{zd}^2 = \left(\frac{\omega}{c}\right)\epsilon_d \tag{3.49}$$

From equations 3.48 and 3.49, we get the dispersion relation for surface plasmons at a metal/dielectric interface:

$$k_{sp} = \frac{\omega}{c}\sqrt{\frac{\epsilon_m.\epsilon_d}{\epsilon_m + \epsilon_d}} \tag{3.50}$$

where $k_{sp} \equiv k_x$ is the wave vector of the surface plasmons parallel to the metal/dielectric interface, ω is the angular frequency and c is the speed of light,

ϵ_m is the dielectric constant of the metal and ϵ_d is the dielectric constant of the dielectric medium.

The dispersion relation for the photons propagating in the dielectric medium is given by:

$$k_{ph} = \frac{\omega}{c}\sqrt{\epsilon_d}\sin(\theta) \qquad (3.51)$$

where k_{ph} is the wave vector of the photons parallel to the metal/dielectric interface.

At $\theta = \theta_{\mathrm{spr}}$, $k_{sp} = k_{ph}$ which allows for the determination of θ_{spr} from equations 3.50 and 3.51:

$$sin(\theta_{\mathrm{spr}}) = \frac{1}{\sqrt{\epsilon_d}}\sqrt{\frac{\epsilon_m.\epsilon_d}{\epsilon_m + \epsilon_d}} \qquad (3.52)$$

Therefore θ_{spr} is the 'SPR resonance angle' at which there is a minimum in the intensity of reflected light due to matching of the photon and plasmon wave vectors.

3.3.3 Monitoring Kinetics with SPR

There are two different modes to characterize the changes in the SPR curve as a function of time:

Changes in Reflectivity

In this technique, the change in light reflection at a fixed angle is monitored (see figure 3.9). The angle is usually chosen to be smaller than the SPR resonance angle along the near linear portion such that it is highly sensitive to changes in the reflectivity. Changes in reflectivity at a fixed angle are assumed to be proportional to changes in the index of the dielectric, which is not strictly the case [122]. This technique is generally implemented in a fixed-angle setup (see section 3.3.4) where the SPR resonance angle cannot be tracked in real time.

Changes in the SPR Resonance Angle

In this technique, changes in the SPR resonance angle as a function of time are monitored (see figure 3.10). This is the preferred method of quantifying binding kinetics and is used in both a fan-shaped and an angle-scanning experimental configuration (see section 3.3.4).

3.3.4 SPR Beam Configurations

Given the Kretschmann configuration, there are three types of beam optics that can be used [122], the selection of which impacts the way the SPR curve is monitored.
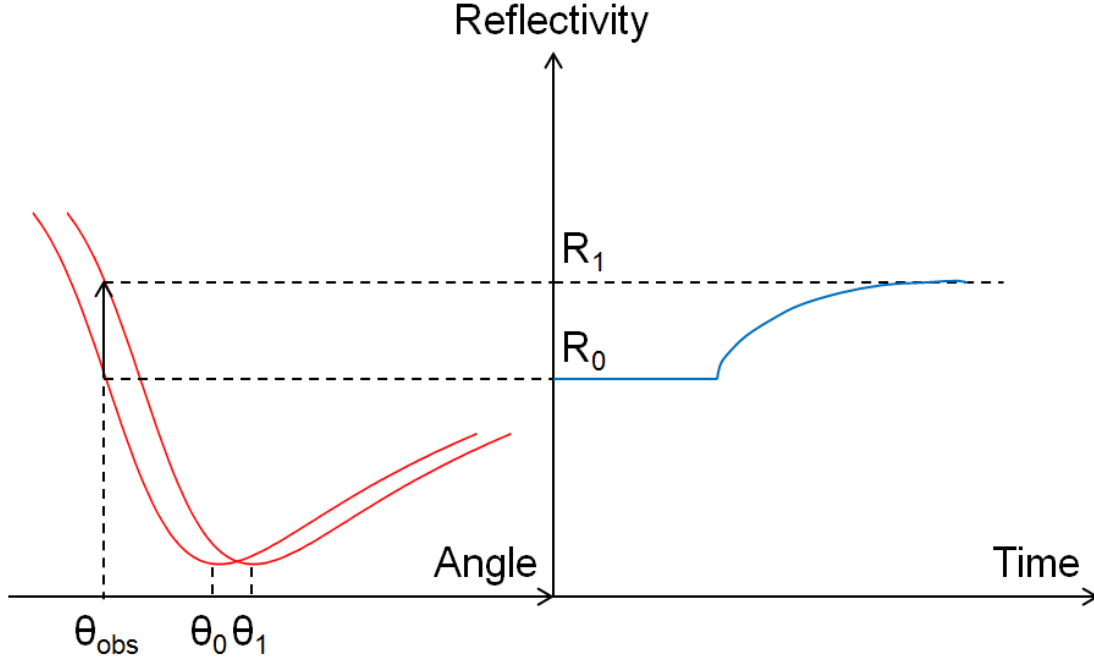
Figure 3.9: One approach to monitor the change in the SPR resonance angle is to follow the change in reflectivity at a fixed angle (θ_{obs}). If the fixed angle remains in the linear portion of the curve, it is assumed that the change in reflectivity at this angle (R_1-R_0) is proportional to the change in the SPR resonance angle (θ_1-θ_0).

Fan-Shaped

In this configuration, the apex of a converging beam of p-polarized light is located at the surface of the prism and the reflected diverging beam is focused onto a detector (see figure 3.11). This allows for the simultaneous measurement of the reflectivity off the metal film at various angles and therefore the determination of SPR resonance angle over a range of incident angles without the need for any moving parts.

Fixed-Angle

In this configuration, the reflectivity is measured for a given incident angle (see figure 3.12). Usually the reflectivity at different incident angles is measured to locate the SPR resonance angle as well as the linear portion of the curve that is most sensitive to changes in the reflectivity. The incident angle is then fixed to the middle of the linear portion and reflectivity changes at that angle are monitored and are assumed to be linearly proportional to changes in the SPR resonance angle (see section 3.3.3).
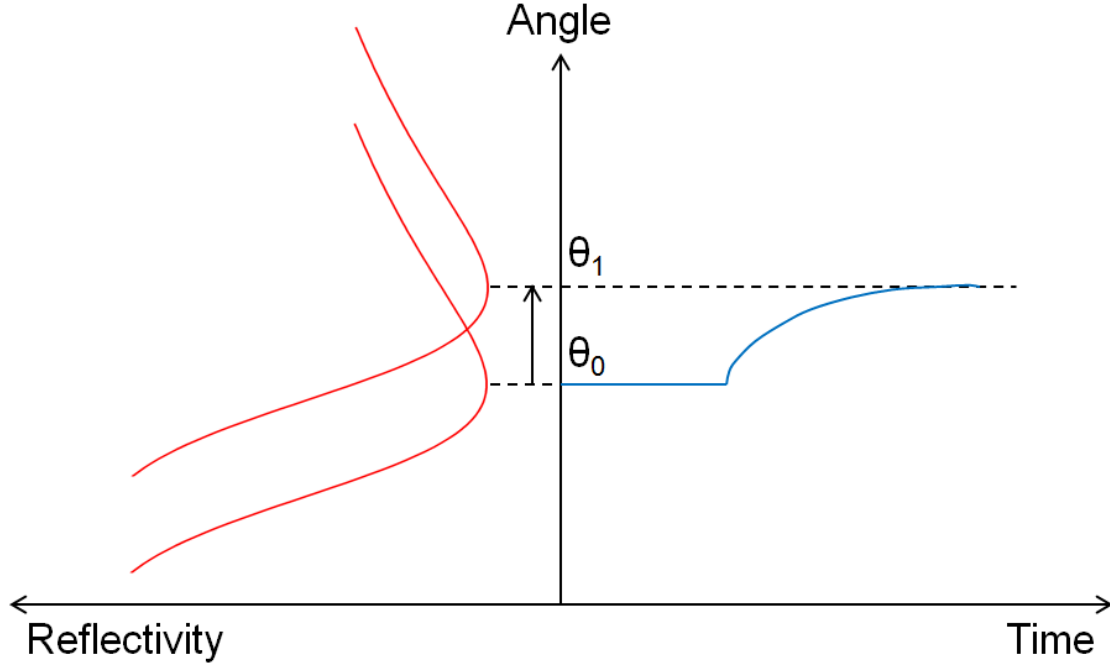
Figure 3.10: The accurate way of monitoring the change in the SPR resonance angle (θ_1-θ_0) is by fitting the reflectivity curve in real-time to determine the instantaneous SPR resonance angle.

Angle-Scanning

This configuration is a compromise between the fan-shaped and fixed-angle setups. While the reflectivity can only be measured for a given angle, the angle is quickly scanned over a certain range to provide near real-time monitoring of the SPR resonance angle (see figure 3.13). This allows for plotting of the changes in the SPR resonance angle (as is done in the fan-shaped setup) as opposed to changes in the reflectivity at a given angle (as is done for the fixed-angle setup).

3.3.5 Instrumentation

We used a custom-built SPR instrument from SPR Biosystems (Germantown, MD). It uses the Kretschmann configuration where a glass slide coated with a thin film of gold ($\sim$ 450 Å) is coupled to a prism. A Superluminescent Light Emitting Diode (SLED) (EXS7510 from Exalos AG, Switzerland) at λ=763.8 nm is used to excite surface plasmons in the gold film. The illuminated sample area is 10 mm×100 μm with the former being along the direction perpendicular to propagation. The signal is detected using a Hamamatsu (Hamamatsu City, Japan) Digital CCD (C10990) which has 250 lines of 1024 pixels with 25 μm resolution. In standard single channel measurement mode, all 250 lines are binned into one line of 1024 pixels. The system
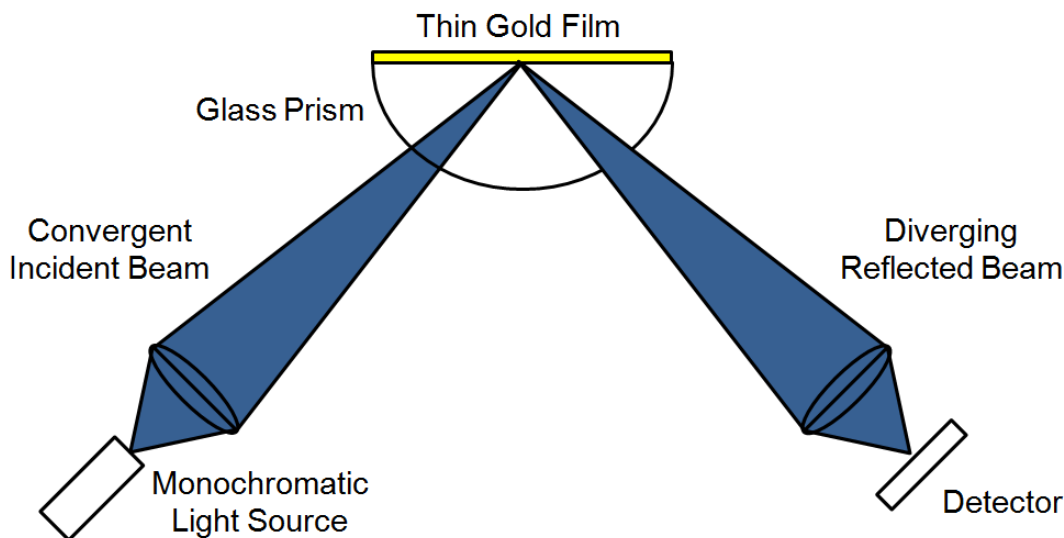
Figure 3.11: Fan-shaped beam configuration which allows for the simultaneous use of multiple incident angles.

has a temporal resolution of 0.1 s with a sensitivity of 5×10^{-7} response units (RU; 1 RU∼1 pg of adsorbed protein per mm^2) or better. The dynamic range by refractive index is n=1.33 to n=1.41. A Wavelength Electronics (Bozeman, MT) temperature controller (LFI-3751) is used with a range from ambient to 50 °C with 0.005 °C resolution. The non-flow cell is composed of a Teflon cylinder of 6 mm diameter with a volume of 1 ml. An IKA (Wilmington, NC) RW11 overhead stirrer is used in order to accelerate protein binding to lipid bilayers. The instrument was designed in such a way as to allow simultaneous SPR and EIS measurements on a given sample. The hardware is accompanied by a software package, SPR Aria, written by SPR Biosystems that allows for acquisition and real-time viewing of the data.

3.3.6 Raw Data

During a measurement, two sets of data are generated. The first is the reflectivity as a function of pixels on the detector (see figure 3.7). This is the standard SPR reflectivity curve whose minimum is the SPR resonance angle that corresponds to the critical angle at which there is perfect energy and momentum matching between the incoming photons and the surface plasmons (as described in section 3.3.2). The second data set represents the SPR binding/interaction kinetics as it plots the SPR resonance angle as a function of time (see figure 3.14). The SPR Aria software performs a polynomial fit of the reflectivity curve with user-defined pixel ranges, polynomial order and time interval between subsequent re-fits of the reflectivity curve. The standard time interval used is 0.2 s. i.e., Every 0.2 seconds, the SPR
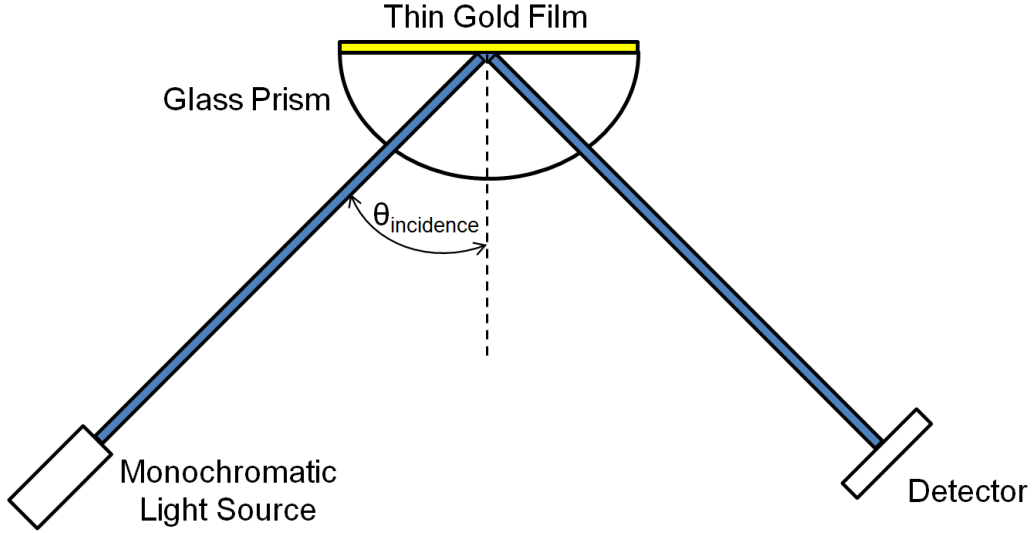
Figure 3.12: Fixed-angle configuration where the reflectivity is measured at a single angle of incidence ($\theta_{\text{incidence}}$).

reflectivity curve is fit to obtain the SPR resonance angle at that instant in time which is then used to follow the kinetics.

3.3.7 Quantitative Analysis

Reflectivity Profile

The SPR reflectivity profile can be analyzed using an N-layer Fresnel model. Each layer is parameterized by a thickness d and a complex refractive index:

$$\tilde{n} = n + ik \tag{3.53}$$

where n and k are the real and imaginary components of the refractive index $\tilde{n}$.

The angular-dependent ratio of the intensity of reflected light to incident p-polarized light for the Kretschmann configuration was determined by Hansen [124]. The equations were exported to the Igor Pro software package (Wavemetrics, Portland, OR) and were used to both generate theoretical reflectivity profiles (given substrate parameters) as well as to fit experimental reflectivity curves to obtain the substrate parameters.

Binding Kinetics

The SPR Aria software calculates the absolute value of the SPR resonance angle as a function of time as described in section 3.3.6. In a standard binding assay,
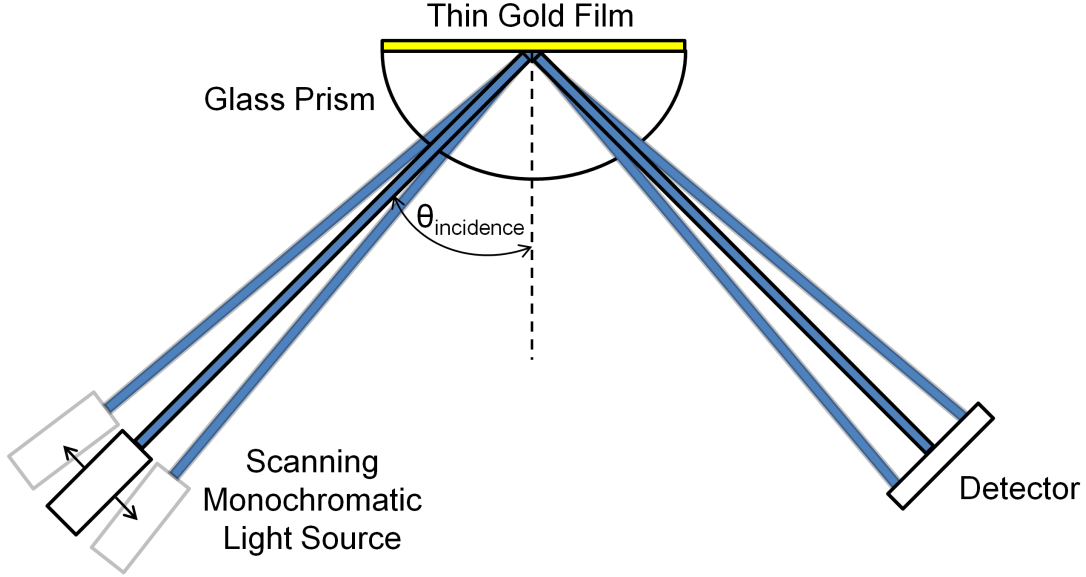
Figure 3.13: Angle-scanning configuration where the angle of incidence ($\theta_{\mathrm{incidence}}$) can be scanned across a range of angles to provide the entire reflectivity curve in a step-wise manner.

a given concentration of protein is added to a stable bilayer. An increase in the SPR resonance angle is due to an increase in refractive index at the bilayer/buffer interface which can be attributed to protein binding to the bilayer (the standard value for $n_{protein}$ is 1.41, n_{lipid} is 1.5 and n_{bulk} is 1.33). Once the SPR resonance angle ceases to change, equilibrium has been attained. A higher concentration of protein is then added and the process is repeated (typical protein concentrations range from 10 nM to 50 μM).

Assuming the binding of an analyte A (protein) to a ligand B (lipid), a 1:1 Langmuir bimolecular model (an analyte molecule binding to a single ligand molecule) can be written as:

$$A + B \underset{k_{\mathrm{off}}}{\overset{k_{\mathrm{on}}}{\rightleftharpoons}} AB \tag{3.54}$$

If the concentration of the bound complex at saturation is given by $[AB]_{\mathrm{max}}$, we get:

$$[B] = [AB]_{\mathrm{max}} - [AB] \tag{3.55}$$

The following rate equations can be derived:

$$Association: \ \frac{d[AB]}{dt} = k_{\mathrm{on}}[A][B] - k_{\mathrm{off}}[AB] \tag{3.56}$$

$$Dissociation: \ \frac{-d[AB]}{dt} = k_{\mathrm{off}}[AB] \tag{3.57}$$

39
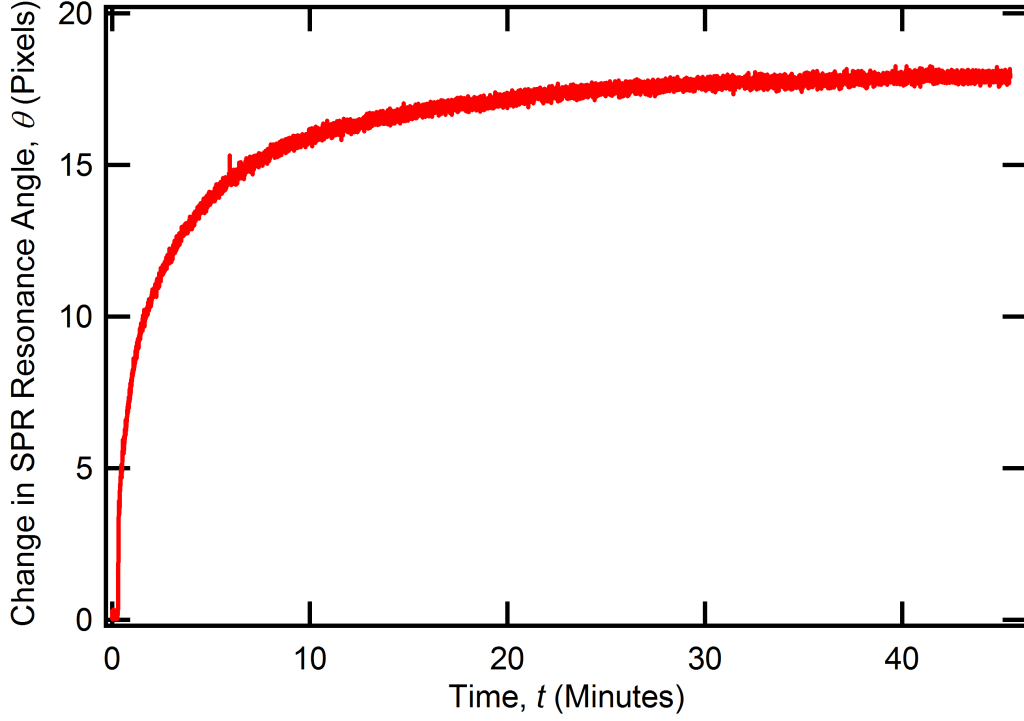
Figure 3.14: A standard SPR binding kinetics curve that shows the increase in the SPR resonance angle (in pixels) as a function of time, depicting the binding of protein to a lipid bilayer. The measurement is stopped once equilibrium has been achieved as indicated by a constant SPR resonance angle.

where the association phase is during the addition of protein to the bilayer and the dissociation phase begins once unadsorbed protein in the bulk is flushed away.

At equilibrium,

$$k_{\text{on}}[A][B] = k_{\text{off}}[AB] \tag{3.58}$$

This allows us to define the equilibrium association and dissociation constant, K_a and K_d respectively, as:

$$K_a = \frac{[AB]}{[A][B]} = \frac{k_{\text{on}}}{k_{\text{off}}} \tag{3.59}$$

$$K_d = \frac{[A][B]}{[AB]} = \frac{k_{\text{off}}}{k_{\text{on}}} \tag{3.60}$$

Combining equations 3.55 and 3.56 we get:

$$\frac{dR}{dt} = k_{\text{on}}c_0(B_{\text{max}} - R) - k_{\text{off}}R \tag{3.61}$$

where we assume the SPR response, R, scales linearly with $[AB]$; $B_{\max}$ is the saturation SPR response and $c_0 = [A]$.

The analytical solution for 3.61 is given by:

$$
\begin{aligned}
R &= \frac{k_{\text{on}} c_0 B_{max}}{k_{\text{on}} c_0 + k_{\text{off}}} [1 - e^{-(k_{\text{on}} c_0 + k_{\text{off}})t}] \\
&= R_0 [1 - e^{-(k_{\text{on}} c_0 + k_{\text{off}})t}]
\end{aligned} \tag{3.62}
$$

The analytical solution for 3.57 is given by:

$$
R = R_0 e^{-k_{\text{off}} t} \tag{3.63}
$$

where R_0 is the SPR response at dissociation time zero.

If R_{eq} is the equilibrium response for a given c_0, equation 3.61 becomes:

$$
\frac{dR}{dt} = k_{\text{on}} c_0 (B_{\max} - R_{\text{eq}}) - k_{\text{off}} R_{\text{eq}} = 0 \tag{3.64}
$$

Equation 3.64 can be solved for R_{eq} to give:

$$
R_{eq} = \frac{c_0 B_{\max}}{c_0 + K_d} \tag{3.65}
$$

where K_d is the equilibrium dissociation constant (defined in equation 3.60) as shown in figure 3.15.

In the case of two independent and non-competitive binding sites with dissociation constants K_{d1} and K_{d2} and saturated SPR resonance angle change given by $B_{\max 1}$ and $B_{\max 2}$, respectively, equation 3.65 is modified to give:

$$
R_{eq} = \frac{c_0 B_{\max 1}}{c_0 + K_{d1}} + \frac{c_0 B_{\max 2}}{c_0 + K_{d2}} \tag{3.66}
$$

Estimation of K_d in Cases of Insufficiently High Concentration

The equilibrium binding constant (K_d) can be determined with high precision if the highest concentration of protein used in the SPR experiment is 1-2 orders of magnitude greater than the K_d. However, if the highest concentration is 'sufficiently' greater than the K_d (as determined by the size of the uncertainties in K_d compared to its mean value), it is possible to develop a criterion to estimate its value and define confidence limits.

Let us consider the specific example of truncated PTEN association with PS-bearing membranes where we were limited to a maximum protein concentration of 3 µM due to aggregation. The 3 µM concentration corresponds to an experimentally measured change in the SPR resonance angle of 34.0 ± 0.2 pixels (as compared to the baseline bilayer signal). We artificially added a 10 µM data point and varied
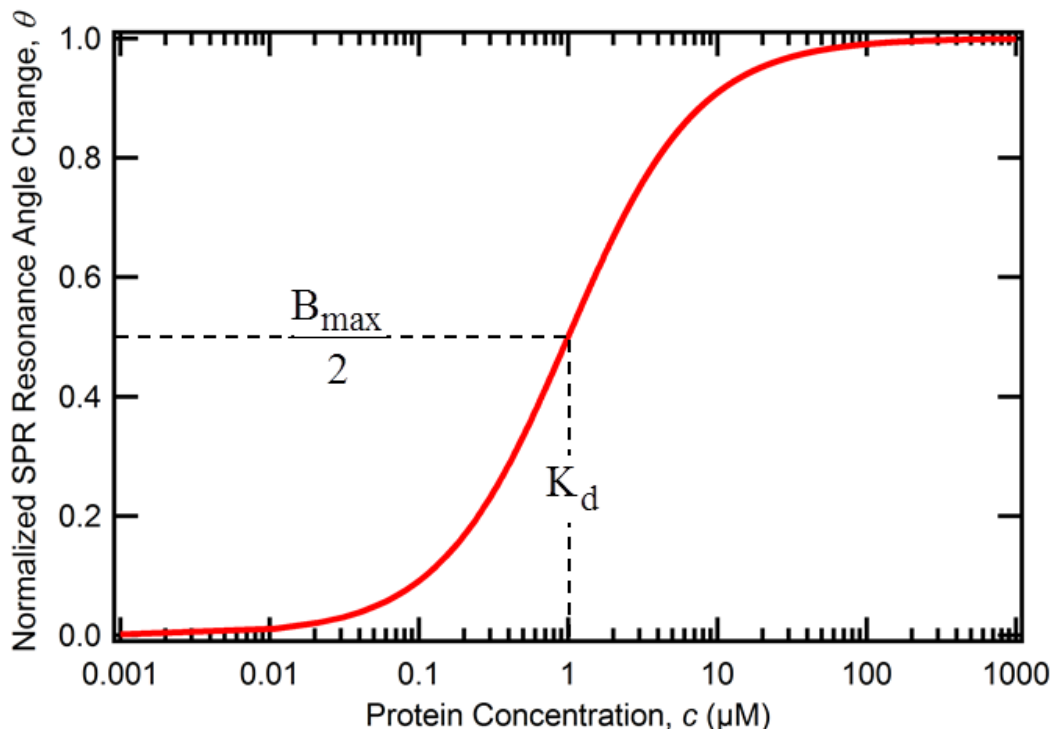
Figure 3.15: Equilibrium analysis of the binding kinetics data involves fitting the change in SPR resonance angle as a function of protein concentration to a sigmoidal function whose two parameters are the equilibrium dissociation constant (K_d) and saturation SPR resonance angle change (B_{max}), which is an estimate of the number of available binding sites.

its corresponding SPR resonance angle change from 30 pixels to 100 pixels, both significantly larger than the 0.2 pixel standard deviation, in 1 pixel increments. We then fit each data set (consisting of the 5 experimentally determined points + 1 artificial data point) to determine the K_d and the χ^2 of the fit (see figure 3.16).

To sufficiently account for the concentration and pixel change uncertainties associated with the experimental data points, a Monte-Carlo resampling method was used [125]. Using the experimental uncertainties of each data point, 1000 statistically independent data sets were generated any of which could have occurred given the statistical uncertainties. For each of the 1000 data sets, we varied the pixel change for the 10 μM concentration from 30 pixels to 100 pixels and calculated the K_d and χ^2 in each case. We then averaged the K_d and χ^2 values for a given pixel change across all 1000 fits and plotted them (see figure 3.17). The smallest χ^2 of 10.7 corresponds to a K_d of 3.3 μM. Using one standard deviation, we are able to set bounds on the K_d from 2.5 μM to 4.9 μM.

In this example, we had used an artificial data point with a concentration (3 μM)
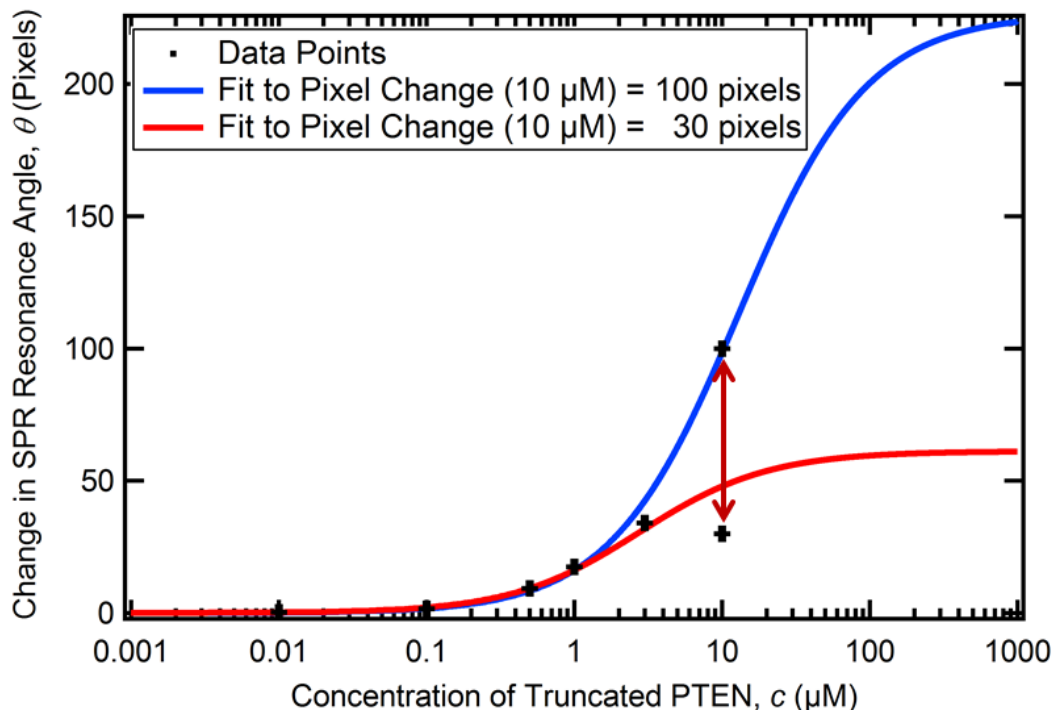
Figure 3.16: The SPR resonance angle change for the 10 μM truncated PTEN concentration was varied from 30 to 100 pixels (maroon arrow). The red curve shows the fit to the data if the 30 pixel value is used and the blue curve if the 100 pixel value is used.

approximately three times larger than the average K_d. We repeated this calculation with the data point at a concentration of 100 μM and a pixel change varied between 50 and 200 pixels. The bounds on K_d obtained were very similar to the earlier result, illustrating that as long as the concentration of the artificial data point is above a certain threshold, the bounds on K_d are stable. The reason we did not directly pick a high concentration for the artificial data point is that the larger the concentration, the larger the pixel change range that has to be explored and the more intensive the calculation that needs to be performed. We suggest picking a concentration 3-5 times larger than the highest concentration used in the experiment and calculating the bounds on K_d. However, time and resources permitting, we strongly encourage repeating the procedure for a concentration an order of magnitude larger than the one initially chosen to ensure that there is no discrepancy between the results.
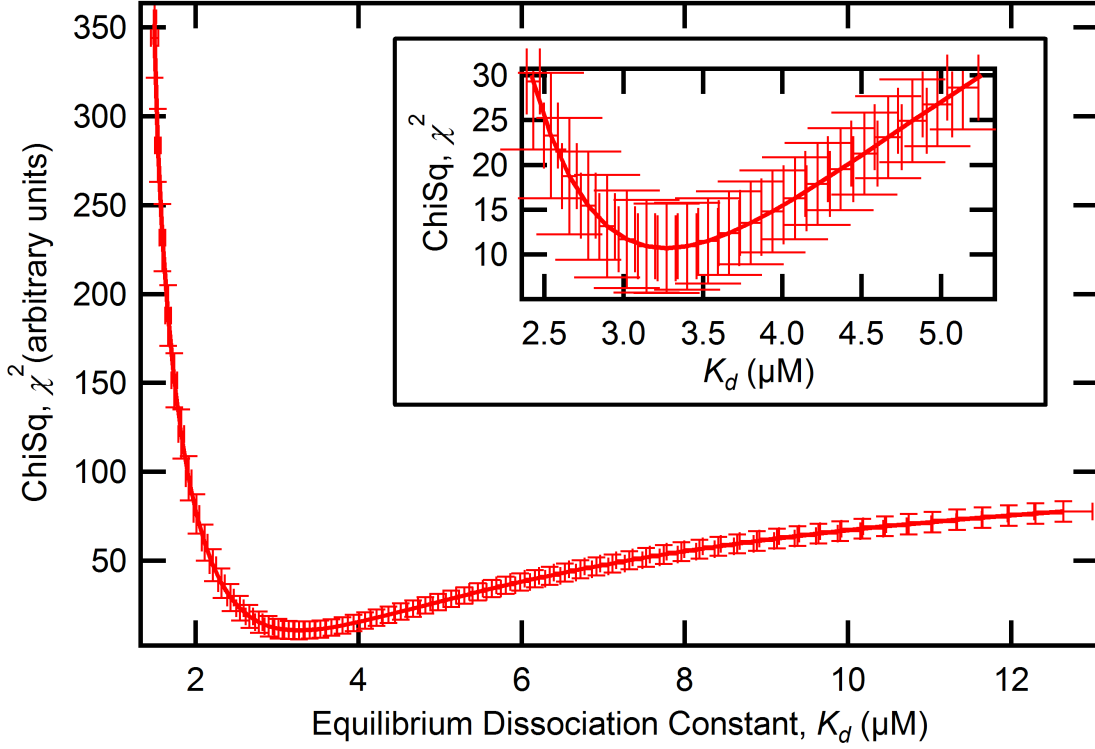
Figure 3.17: A plot of χ^2 and K_d, averaged over 1000 Monte-Carlo resampled data sets, as the pixel change for the 10 μM concentration is varied from 30 to 100 pixels. **Inset:** A zoomed in version focusing on the minimum χ^2 region.

3.3.8 Calibration

Conversion between Pixels and Degrees

Standard SPR reflectivity curves are plots of the reflectivity as a function of incidence angle in degrees. As our SPR uses a fan-design, it samples a range of incidence angles simultaneously. However, the angles are reported as pixels on the detector and a conversion factor from pixels to degrees needs to be calculated for comparison of the data to the literature. This was accomplished by using glycerol:water mixtures of known refractive index on slides of known gold and chromium thickness thereby allowing for a comparison between the SPR resonance angle in pixels (experimental) and the SPR resonance angle in degrees (theoretical) [126].

While the refractive index of glycerol:water mixtures are commonly tabulated in the literature and in handbooks, we were unable to find any corresponding to λ=763.8 nm. Weighting the refractive index of water and glycerol by the respective volume fractions has been shown to be a bad estimate of the refractive index of the mixture [127]. Instead, we resorted to weighting the water and glycerol components

by their respective mass fractions.

At λ=763.8 nm, the refractive index of pure glycerol is 1.46716 [128] and that of water is 1.32972 [129]. Glycerol:water mixtures were prepared ranging from 0% glycerol (by volume) to 10% glycerol in 1% increments. The mass-weighted refractive indices of these mixtures are given in Table 3.1.

Table 3.1: Mass-weighted refractive index of glycerol:water mixtures.

Amount of Glycerol (% by volume)	Refractive Index (n)
0	1.32972
1	1.33145
2	1.33317
3	1.33488
4	1.33658
5	1.33828
6	1.33996
7	1.34164
8	1.34330
9	1.34496
10	1.34661

Using the Fresnel model, we can fit the SPR reflectivity curve to obtain the refractive index and thickness of each layer of dielectric medium on the glass prism. For the substrate used in this calibration measurement, the parameters are given in Table 3.2.

Table 3.2: Substrate parameters where n and k are the real and imaginary parts of the complex refractive index, respectively.

Substrate	n	k	Thickness (nm)
Glass Slide	1.52	-	-
Chromium	3.095	3.428	5
Gold	0.172	4.7361	44

Based on the substrate parameters (Table 3.2) and the refractive index of the glycerol:water solution (Table 3.1), the expected SPR resonance angle in degrees can be calculated. These values are given in Table 3.3.

From the data in Table 3.1 and Table 3.3, we get the following conversion relation:

$$\Delta n = 105.8 \pm 0.2 \text{ degrees} \tag{3.67}$$

45

Table 3.3: Theoretical SPR resonance angle (in degrees) for a given glycerol:water mixture on the given substrate.

Amount of Glycerol (% by volume)	SPR Resonance Angle (in degrees)
0	65.9751
1	66.1537
2	66.3327
3	66.5117
4	66.6910
5	66.8716
6	67.0512
7	67.2322
8	67.4123
9	67.5937
10	67.7753

This gives us a relation connecting the change in refractive index and the corresponding SPR resonance angle in degrees. In order to calculate the conversion factor between refractive index change and the SPR resonance angle in pixels, we performed 3 calibration experiments [detailed in Tables 3.4, 3.5 and 3.6].

Table 3.4: Calibration Experiment 1: Experimental SPR resonance angle (in pixels) for a given glycerol:water mixture on the given substrate.

Amount of Glycerol (% by volume)	SPR Resonance Angle (in pixels)
0	292.640 ± 0.002
2	348.703 ± 0.004
4	410.500 ± 0.004
6	462.840 ± 0.004
8	510.260 ± 0.003
10	542.790 ± 0.004

From Table 3.4 we get:

$$\Delta\,1\,\text{Pixel} = (6.11 \pm 0.08) \times 10^{-5}\Delta n \tag{3.68}$$

From Table 3.5 we get:

$$\Delta\,1\,\text{Pixel} = (6.47 \pm 0.06) \times 10^{-5}\Delta n \tag{3.69}$$

Table 3.5: Calibration Experiment 2: Experimental SPR resonance angle (in pixels) for a given glycerol:water mixture on the given substrate.

Amount of Glycerol (% by volume)	SPR Resonance Angle (in pixels)
0	287.650 ± 0.004
1	308.880 ± 0.001
2	334.280 ± 0.001
3	361.160 ± 0.005
4	389.060 ± 0.002
5	423.910 ± 0.004

Table 3.6: Calibration Experiment 3: Experimental SPR resonance angle (in pixels) for a given glycerol:water mixture on the given substrate.

Amount of Glycerol (% by volume)	SPR Resonance Angle (in pixels)
1	273.030 ± 0.004
2	296.700 ± 0.004
3	327.730 ± 0.004
4	368.760 ± 0.004
5	396.740 ± 0.004

From Table 3.6 we get:

$$\Delta\, 1\, \text{Pixel} = (6.4 \pm 0.3) \times 10^{-5} \Delta n \tag{3.70}$$

Averaging equations 3.68, 3.69 and 3.70, we get the relation:

$$\Delta\, 1\, \text{Pixel} = (6.3 \pm 0.1) \times 10^{-5} \Delta n \tag{3.71}$$

From equations 3.67 and 3.71, we get the relation:

$$\Delta\, 1\, \text{Pixel} = 0.0067 \pm 0.0001\, \text{degrees} \tag{3.72}$$

Given the SPR resonance angle in pixels, we can calculate the absolute SPR resonance angle in degrees as:

$$\text{SPR angle(degrees)} = (63.97 \pm 0.03) + (0.0067 \pm 0.0001) \times \text{SPR angle(pixels)} \tag{3.73}$$

Relation between SPR Resonance Angle and Protein Layer Thickness and Surface Density

The Fresnel model can be used to fit the refractive index and thickness of a lipid bilayer atop the thin gold film on the glass slide. However, fitting a protein layer

atop a bilayer atop a substrate has such a high number of parameters that an accurate fit of the parameters is nearly impossible. Instead, it is easier to calculate a conversion factor between SPR resonance angle change and protein thickness (or surface density) as observed by comparing the reflectivity curve corresponding to the bilayer with that for the bilayer with protein.

The relation between protein thickness and surface density is given by [130]:

$$\Gamma = \frac{d_{protein}(n_{protein} - n_{bulk})}{dn/dc} \tag{3.74}$$

where Γ is the surface density, $d_{protein}$ is the thickness of the protein layer, $n_{protein}$ is the refractive index of the protein, n_{bulk} is the refractive index of the bulk buffer and dn/dc is the change in refractive index of the protein as a function of protein concentration.

The standard value for $n_{protein}$ is 1.41, n_{lipid} is 1.5 and n_{bulk} is 1.33. $dn/dc = 0.187 \pm 0.003$ ml/g was calculated for Bovine Serum Albumin (BSA) [130]. Plugging these values into Equation 3.74, we get:

$$\Gamma = 4.3 * d_{protein} \text{ ng/cm}^2 \tag{3.75}$$

where $d_{protein}$ is in Angstroms.

If we assume the same substrate parameters as in Table 3.2, there are 3 ways to model a tethered bilayer lipid membrane (tBLM) in a slab model:

1. Single slab model: We can consider the PEG layer (tethers+βME), the lipid chains and the headgroups as a single slab with a thickness of 55 Å and n=1.5.

2. Double slab model: Treat the PEG layer and the lipid chains as a slab of 45 Å thickness and n=1.5 and the distal headgroups as a slab of 10 Å thickness and n=1.417 (assuming 50% lipid and 50% water by volume).

3. Triple slab model: Treat the PEG layer as a slab of 15 Å thickness and n=1.442 (65% PEG and 35% water), the lipid chains as a slab of 30 Å thickness and n=1.5 and finally the distal headgroups as a slab of 10 Å thickness and n=1.417 (assuming 50% lipid and 50% water by volume).

For each model, we can plot a theoretical curve of the neat bilayer and then add increasing amounts of protein of n=1.41. We can then plot the SPR resonance angle as a function of protein layer thickness. We did this for all three models and also for model 1 assuming 30 nm of gold instead of the standard 45 nm to test the effect of the thickness of gold (see figure 3.18).

In all four cases, the slope obtained was approximately 20 nm/degree. This means that a change in the SPR resonance angle of the reflectivity profile between
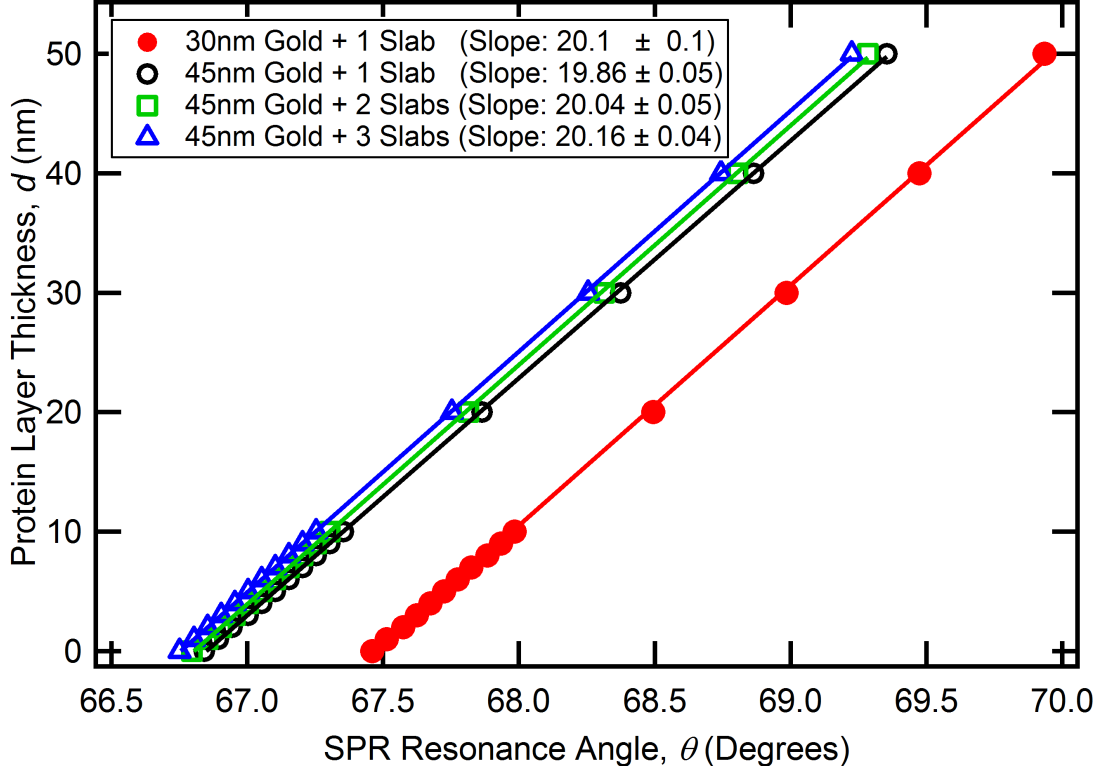
Figure 3.18: Effect of protein thickness on the SPR resonance angle (degrees) for different substrate thicknesses and modeling approaches.

the bilayer and bilayer+protein corresponds to the addition of a 20 nm protein layer. Given the conversion relation between pixels and degrees (Equation 3.72), we get:

$$\Delta \ 1 \text{ pixel} \Rightarrow \Delta d_{protein} = 0.134 \text{ nm} \tag{3.76}$$

i.e., A 1 pixel increase in the SPR resonance angle corresponds to the addition of 0.134 nm of protein.

$$\Delta \ d_{protein} = 1 \text{ nm} \Rightarrow \Delta \text{SPR Angle} = 7.5 \text{ pixels} \tag{3.77}$$

i.e., The addition of a 1 nm layer of protein corresponds to an increase in the SPR resonance angle by 7.5 pixels.

Combining equations 3.75 and 3.76, we get the relation:

$$\Delta \ 1 \text{ pixel} \Rightarrow \Delta \Gamma = 5.8 \text{ ng/cm}^2 \tag{3.78}$$

i.e., A 1 pixel increase in the SPR resonance angle corresponds to an increase in protein surface density by 5.8 ng/cm^2.

It has to be noted that the calculations to derive these conversions assume that there is a homogeneous layer of protein with constant refractive index adsorbed onto
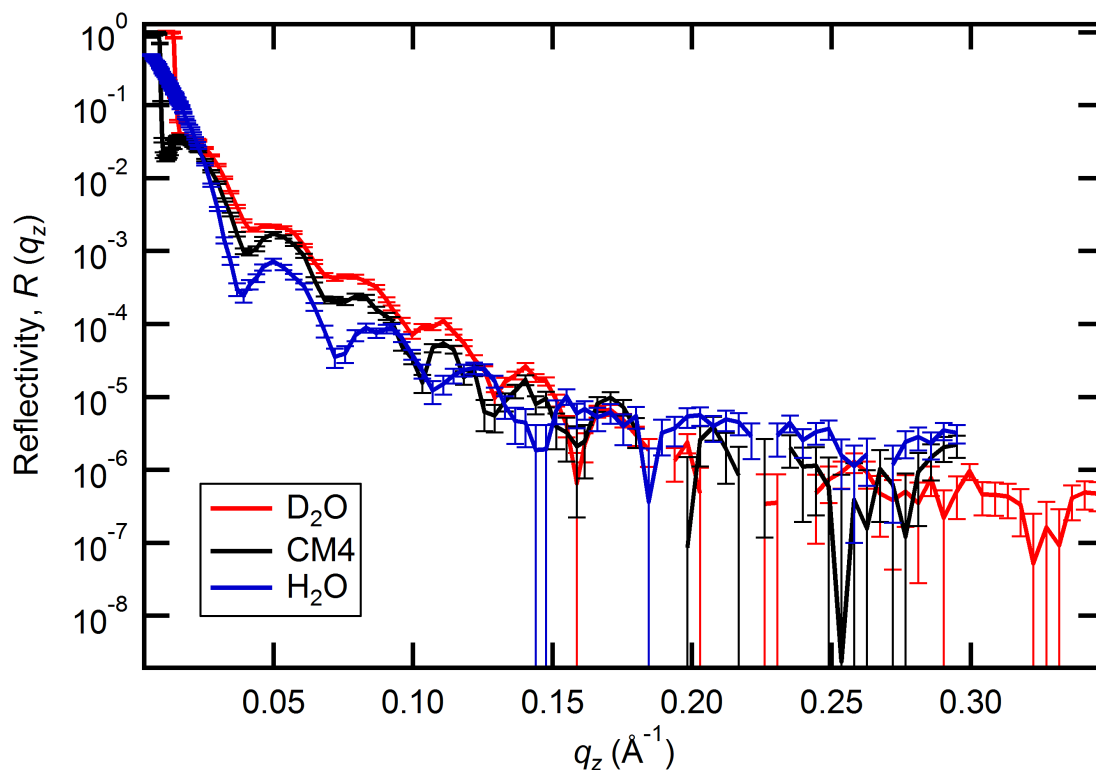
Figure 3.19: Reflectivity profile for a tBLM in D_2O, CM4 and H_2O based buffers.

the bilayer. Consequently, they do not distinguish between a sparse layer of protein with a large average thickness and a dense layer of protein with smaller average thickness. A priori knowledge of the size of the protein and its extent along the bilayer normal can aid in this regard – parameters that can be quantified using techniques such as dynamic light scattering (DLS) and neutron reflectometry (NR), for example.

3.4 Neutron Reflectometry (NR)

3.4.1 Background

NR is a diffraction technique that provides nanometer-scale detail of the structure of thin films oriented perpendicular to the interface. It involves the measurement of the reflected intensity as a function of the normal component of the neutron momentum transfer vector, q_z, (see figure 3.19) which is given by:

$$q_z = \frac{4\pi}{\lambda}\sin(\theta) \tag{3.79}$$

50
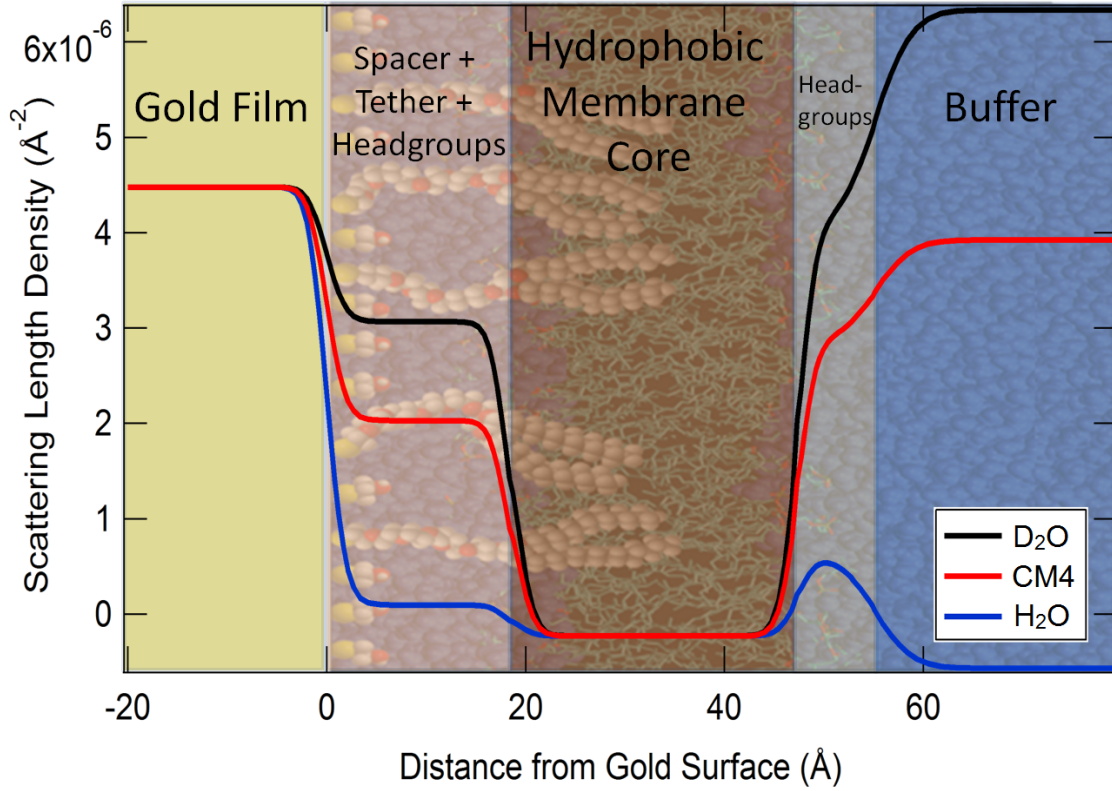
Figure 3.20: Neutron scattering length density (nSLD) profile of a tBLM in three different isotopic contrasts. The perfect overlap in the three curves corresponds to the absence of buffer in the hydrophobic core of the membrane indicating a defect-free membrane.

where z is the direction normal to the interface, λ is the wavelength of the collimated neutron beam and θ is the incident angle (which is equal to the reflected angle).

Since neutrons only interact with the nuclei of atoms, the neutron reflectivity data can be fit to obtain the the neutron scattering length density (nSLD) which is characteristic of a given material (see figure 3.20). Although NR requires a large intensity to achieve sufficient statistical quality in the reflectivity data, the energy of neutrons used is in the meV range and not the eV range, as is the case for X-Ray reflectivity. Consequently, NR results in drastically reduced radiation damage as the energy of the individual neutrons is insufficient to break bonds. NR is also sensitive to different isotopes which allows for enhanced contrast by the use of isotopic substitution. In these experiments, the buffers are prepared in H_2O, D_2O and mixtures of the two (see figure 3.20) which allows for multiple measurements on the same physical sample, thereby improving the quality and reliability of the data analysis.
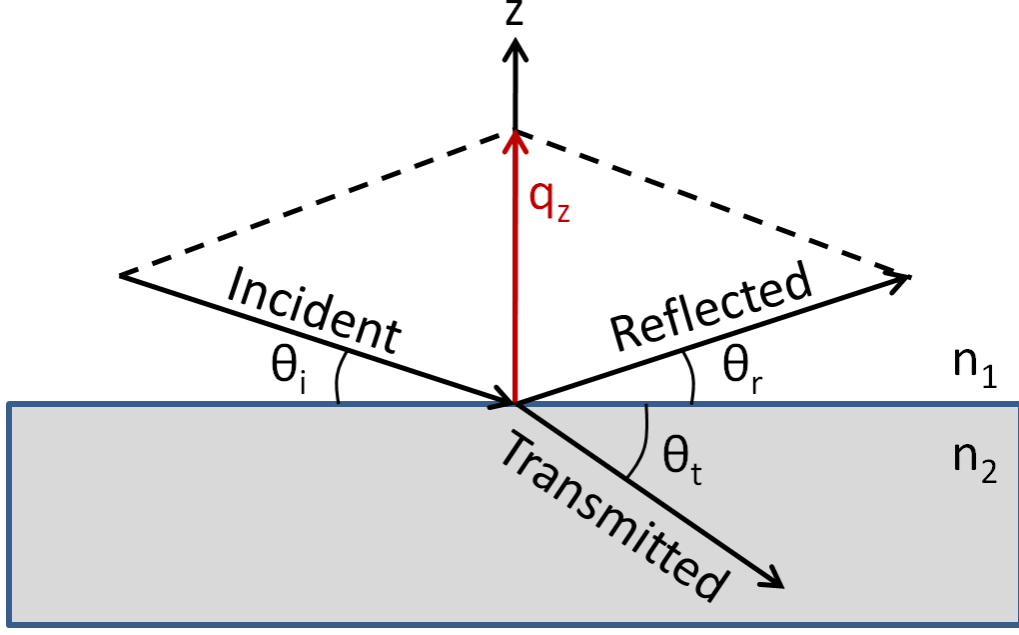
Figure 3.21: Specular Reflectivity: A visual of the reflectivity geometry showing the incident, reflected and transmitted waves along with the critical wave vector q_z.

3.4.2 Theory

A thorough description of the theory and applications of NR can be found in [131]. An overview of the essential concepts is given below.

The neutron refractive index of a medium is given by:

$$n = 1 - \frac{\lambda^2 N_d b}{2\pi} + \frac{i\lambda N_d \sigma_a}{4\pi} \tag{3.80}$$

where λ is the neutron wavelength, N_d is the atomic number density, b is the coherent scattering length and σ_a is the adsorption cross-section.

The neutron scattering length density, ρ, is given by:

$$\rho = N_d b \tag{3.81}$$

For most materials, $\sigma_a = 0$. Combining this with equation 3.81, equation 3.80 reduces to:

$$n \approx 1 - \frac{\lambda^2 \rho}{2\pi} \tag{3.82}$$

At the interface between two media (see figure 3.21), if the incoming wave is reflected in a single direction then the reflection is termed as 'specular' and the law

of reflection ($\theta_i = \theta_r$) applies. Snell's law gives us the relation:

$$n_1\cos(\theta_i) = n_2\cos(\theta_t) \tag{3.83}$$

Assuming medium 1 is air (n_1=1), then the condition for total external reflection is given by:

$$\theta_t = 0 \Rightarrow \cos(\theta_c) = n \tag{3.84}$$

where θ_c is the critical angle below which all incident neutrons are reflected and $n = n_2$.

θ_c is sufficiently small that the first term in the Taylor expansion can be used to approximate $\cos(\theta_c)$. Then, equations 3.82 and 3.84 can be combined to give:

$$\theta_c = \sqrt{\frac{\rho}{\pi}}\lambda \tag{3.85}$$

The critical neutron momentum transfer wave vector, q_c, is given by:

$$q_c = \frac{4\pi\sin(\theta_c)}{\lambda} = 4\sqrt{\pi\rho} \tag{3.86}$$

The reflected and transmitted amplitudes can be calculated from the classical Fresnel equation and are given by:

$$r = \frac{\sin(\theta_i) - n\sin(\theta_t)}{\sin(\theta_i) + n\sin(\theta_t)} \tag{3.87}$$

$$t = \frac{2\sin(\theta_i)}{\sin(\theta_i) + n\sin(\theta_t)} \tag{3.88}$$

Equation 3.87 can be rewritten in terms of the surface-normal components of the momentum transfer vectors, $q_{z,i}$, as:

$$r = \frac{q_{z,1} - q_{z,2}}{q_{z,1} + q_{z,2}} \tag{3.89}$$

The $q_{z,i}$ terms can written in terms of q_c as:

$$q_{z,i}^2 = q_z^2 - q_c^2 \tag{3.90}$$

where $q_z = \frac{4\pi}{\lambda}\sin(\theta_i)$.

The reflectivity, R, which is the experimentally measurable parameter is given by:

$$R = rr^* \tag{3.91}$$

where r^* is the complex conjugate of the reflected amplitude (r).
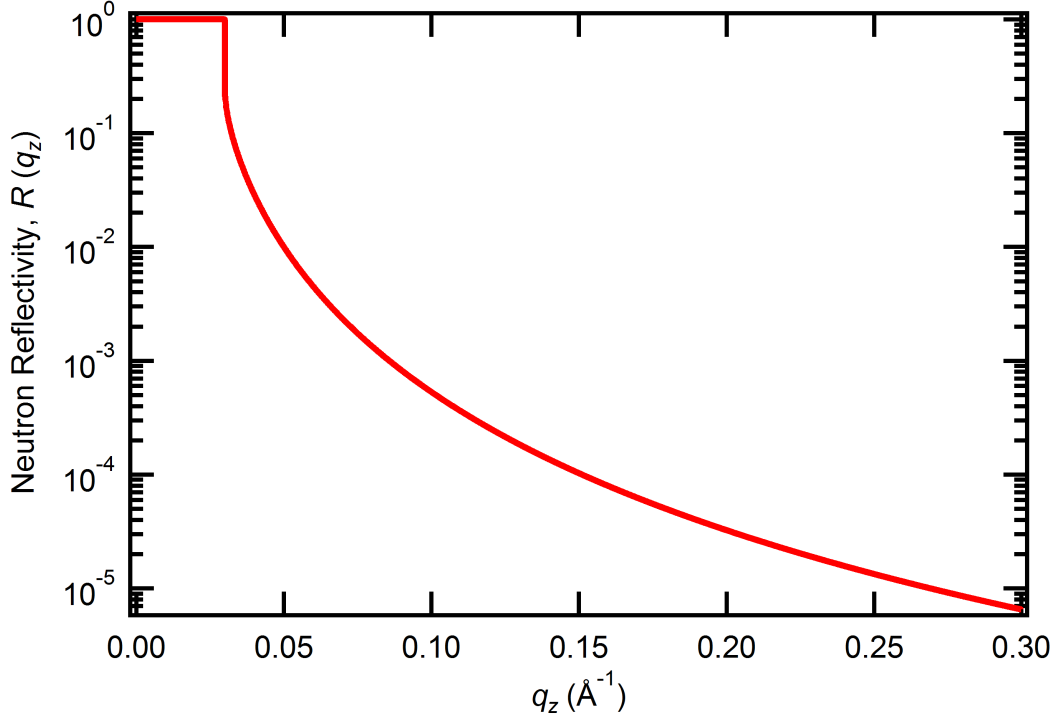
Figure 3.22: Fresnel Reflectivity: The reflectivity profile for an interface with q_c=0.03 Å^{-1}.

Combining equations 3.89, 3.90 and 3.91, we get:

$$R(q) = \left[\frac{1 - \sqrt{1 - (\frac{q_c}{q_z})^2}}{1 + \sqrt{1 - (\frac{q_c}{q_z})^2}}\right]^2 \tag{3.92}$$

For a perfectly flat and sharp interface, the reflectivity profile (from equation 3.92) is shown in figure 3.22 where q_c was chosen to be 0.3 Å^{-1}. For $q_z \leq q_c$, R=1 implying total external reflection.

We can now consider the case of a typical reflectivity sample which consists of m discrete layers (see figure 3.23) with the semi-infinite 0th layer being the aqueous buffer and the semi-infinite $(m+1)^{th}$ layer being the substrate.

The reflectivity amplitude between the $(m-1)^{th}$ and the mth layer is given by:

$$r'_{m-1,m} = \frac{r_{m-1,m} + r_{m,m+1}e^{2i\beta_m}}{1 + r_{m-1,m}r_{m,m+1}e^{2i\beta_m}} \tag{3.93}$$
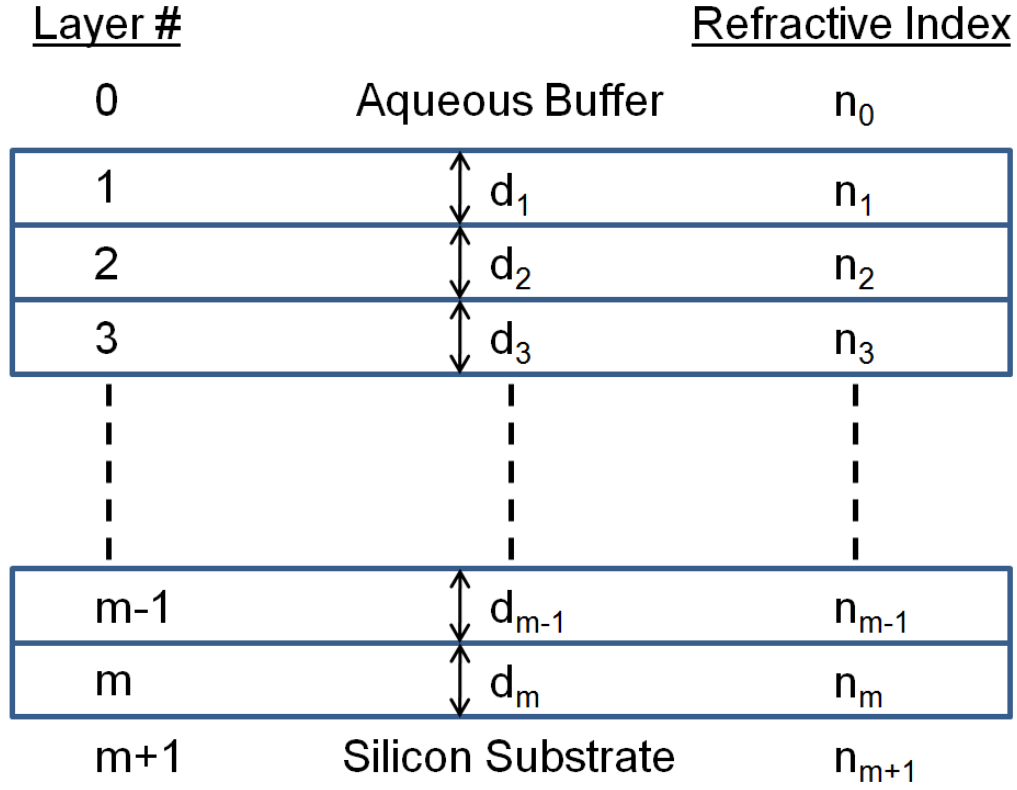
Figure 3.23: Slab model view of a typical reflectivity sample consisting of m layers of thickness d_i and refractive index n_i.

where:

$$r_{i,j} \;=\; \frac{n_i \sin(\theta_i) - n_j \sin(\theta_j)}{n_i \sin(\theta_i) + n_j \sin(\theta_j)} \quad \textbf{and} \tag{3.94}$$

$$\beta_m \;=\; \frac{2\pi}{\lambda} n_m d_m \sin\theta \tag{3.95}$$

The reflected amplitude for the sample, r, is calculated by first computing the reflected amplitude, $r_{m+1,m}$, between the bottom most two layers, m and $m+1$ (using equation 3.93). This value is then used to calculate $r_{m,m-1}$ and the process is repeated till we calculate $r_{0,1}$. Finally, the reflectivity for the sample is given by plugging $r_{0,1}$ into equation 3.91 [132].

3.4.3 NR Data Acquisition

NR measurements were performed on the AND/R (λ=5 Å) and NG1 (λ=4.75 Å) monochromatic, horizontal geometry reflectometers at the NIST Center for Neutron

Research (NCNR) in Gaithersburg, MD. The flow-cell allowed for the in situ change of isotopic contrast, thereby allowing for measurements on the exact same footprint on the sample. In a standard experiment, the same sample is measured in three isotopic contrasts: H_2O, D_2O and CM4 (a mixture of 2 parts D_2O and 1 part H_2O by volume) over a q_z range of 0.008 to 0.25 Å^{-1}. The typical coherence length is about 10 μm longitudinal and 1 μm transverse to the beam. To ensure sufficient statistics were acquired, three measurements of two hours each were performed. The flow-cell was maintained at 25 °C for the course of the experiment. A microfluidic pump (MP5 with MP-X controller, Bartels Mikrotechnik, GmbH) was used for protein work to enhance the rate of binding kinetics.

3.4.4 NR Data Analysis

Neutron reflectivity data consists of the reflectivity as a function of momentum transfer. While changes in the sample can be identified by differences in the neutron reflectivity profile, the real power of NR becomes apparent once the underlying substructure of the sample is modeled in a way that allows for the determination of physical parameters such as thickness, density, etc. Since NR data is typically not of high enough spatial resolution to justify the modeling of individual molecules, the components are usually grouped in some predefined manner. The standard method of analyzing NR data is using the 'slab' or 'box' model [7]. However, we have recently developed a 'continuous distribution' model which models the spatial distribution of individual molecular groups and utilizes information about the molecular composition and connectivity of the sample, thereby enhancing the precision and reliability of the fit parameters [8]. Both models are implemented in the ga_refl software package developed at NCNR [133] and are briefly described below. The software performs a constrained fit of multiple data sets with shared parameters between the different files. The reflectivity profile was calculated from the substrate parameters using an optical matrix based on Parratt's recursion algorithm [132]. It uses a genetic algorithm alternated with a simplex amoeba algorithm [125]. The quality of the fit is analyzed by χ^2 obtained from a Levenberg-Marquardt non-linear least-squares fit.

Slab Model Data Analysis

In the slab model, each material at the interface is treated as a slab characterized by a thickness, roughness and nSLD. A typical slab model consists of the following sequence of layers along the interface normal: (semi-infinite) silicon wafer, silicon oxide (SiOx), chromium (Cr), gold (Au), the hydrated tether and spacer region, the proximal and distal leaflets of the bilayer, the distal lipid headgroups, the protein (if any) and finally the (semi-infinite) bulk solvent (see figure 3.20).
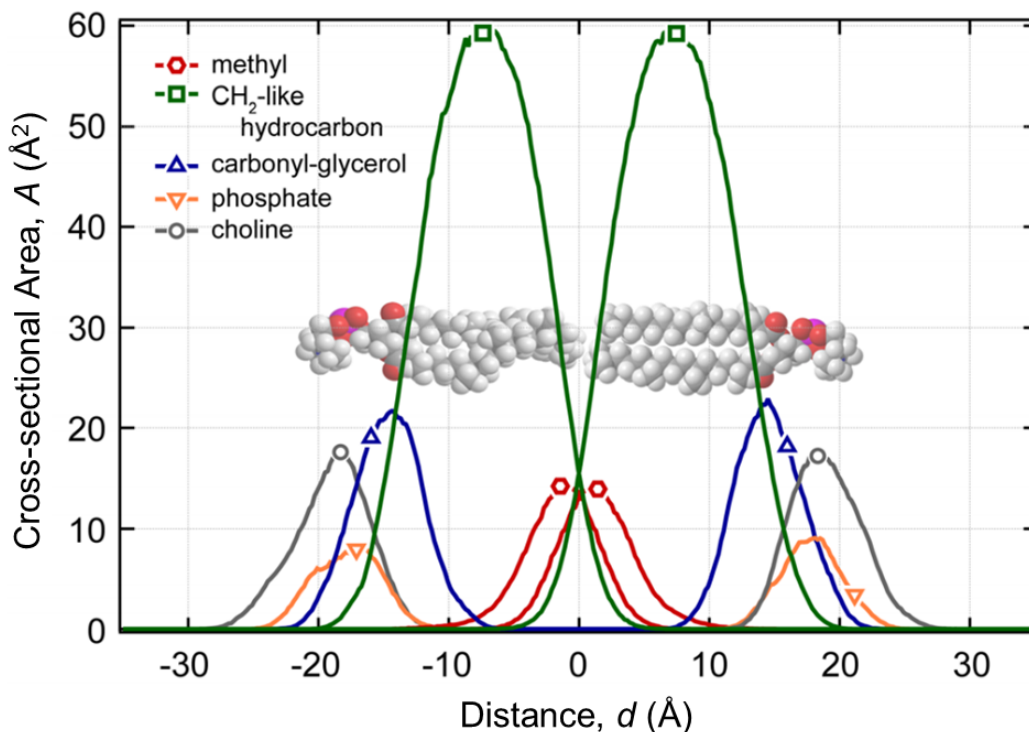
Figure 3.24: Continuous Distribution Model: Visualization of DMPC phospholipids in a bilayer as modeled by the continuous distribution NR data analysis model (Figure from [8]).

Continuous Distribution Model Data Analysis

While the slab model is widely used in the analysis of reflectometry data, it does have some limitations:

- **Inability to describe the partial overlap of different molecular components:** Each distinct component of the sample is assigned to a different slab, implying a sharp demarcation of its extent. This precludes the possibility that the constituents of two or more different slabs inter-mix. For instance, when a protein incorporates into a bilayer, apart from a bilayer slab and a protein slab there is also a region where both lipids and protein co-exist and interact with one another.

- **Unrealistic parameterization of complex molecular architectures and their interfaces:** Since an instantaneous change of the neutron scattering length density (nSLD) from one slab to another is unphysical, standard implementations of the slab model utilize error functions with a width determined by the global roughness parameter to navigate this transition. While this is

57

an improvement over a step function, it still does not reproduce the smooth transition based on the underlying distribution of molecules. Also, a single global roughness parameter does not account for variations in the thermal and compositional disorder of each interface. Consequently, components that are much smaller or more broadly distributed than the width of the slab they have been assigned may not be properly accounted for.

The next-generation of reflectometry analysis models will need to overcome these shortcomings of the venerable slab model without necessitating the utilization of a large number of free model parameters which would result in an 'overfitting' of the data [134]. The continuous distribution model [8] is successful in achieving the right balance by modeling each component as the sum of two error functions and using known volumetric information and knowledge of the underlying chemical structure and connectivity. For instance, a phospholipid is modeled as consisting of methyl, CH_2-like hydrocarbon, carbonyl-glycerol, phosphate and choline groups (see figure 3.24). While it may appear that a large number of parameters will be required, the use of chemical constraints, such as two lipid tails always being associated with a single headgroup, allow us to realistically parameterize the sub-molecular groups without the expense of additional parameters. As a result, we are able to access parameters such as the density of tether lipid and βME on the gold substrate as well as the contribution of phospholipids and tether lipids to the proximal (to the substrate) leaflet that could not be determined with the slab model. We are also able to estimate parameters such as the area per lipid and bilayer thickness with much higher precision than was earlier possible.

The distribution of the protein normal to the bilayer was parameterized using Catmull-Rom splines [135] which were constrained to be single-peaked. A parameter representing the position of the support point of the spline closest to the membrane was varied, allowing the protein profile to penetrate the lipid headgroup region.

3.4.5 Monte-Carlo Resampling

To determine the confidence intervals and correlations between the various fit parameters, a Monte-Carlo resampling procedure [125] implemented in ga_refl was used. Using the statistical errors of the individual data points obtained from a single fit (detailed above), a large number (typically 1000) of statistically independent data sets are generated. Each of these synthetic reflectivity profiles are fit using the same model to produce parameters corresponding to an nSLD profile that could have occurred, given the uncertainty associated with the experimental data [136]. This allows us to calculate the values and uncertainties of the fit parameters in a bias-free manner. All the nSLD profiles obtained from the Monte-Carlo resampling procedure are plotted on an 'nSLD vs. z' graph thereby allowing for a visualization of the deviation of the various fits from the median profile (see figure 3.25).
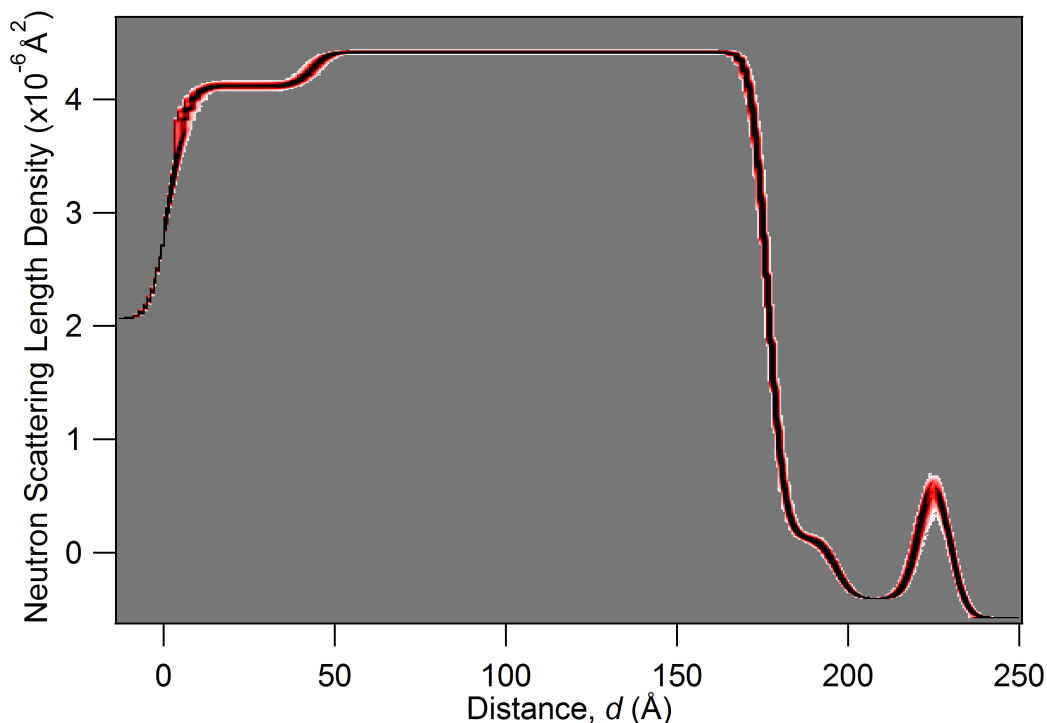
Figure 3.25: Monte-Carlo Resampling: The overlap of the nSLD profile from 1000 monte carlo fits of a given reflectivity data set for a tBLM in H_2O.

3.5 Electrochemical Impedance Spectroscopy (EIS)

3.5.1 Introduction and Theory

EIS is a technique that enables the measurement of the electrical properties of materials and their interfaces and is sensitive to any parameter that alters the conductivity of the system [137]. In the experiments we performed, the electrical stimulus $[V(t)]$ applied was a voltage (V_0) over a certain frequency (ω) range and the phase shift (θ) and amplitude (I_0) of the resulting current $[I(t)]$ were measured.

$$
\begin{aligned}
V(t) &= V_0 \sin(\omega t) & (3.96) \\
I(t) &= I_0 \sin(\omega t + \theta) & (3.97)
\end{aligned}
$$

The response of a passive element of capacitance C in the sample is given by:

$$
I(t) = C \frac{dV(t)}{dt} \tag{3.98}
$$

The response of an element of inductance L in the sample is given by:

$$V(t) = L\frac{dI(t)}{dt} \tag{3.99}$$

Taking the Fourier transform of equations 3.98 and 3.99 we get equations 3.100 and 3.101, respectively.

$$I(\omega) = [i\omega C]V(\omega) \tag{3.100}$$

$$I(\omega) = \frac{V(\omega)}{[i\omega L]} \tag{3.101}$$

where $i \equiv \sqrt{-1}$.

We can therefore define Ohm's law as:

$$V(\omega) = I(\omega)Z(\omega) \tag{3.102}$$

where Z is the impedance and $Z(\omega) = \frac{1}{[i\omega C]}$ for a capacitor and $Z(\omega) = i\omega L$ for an inductor. The admittance, Y, is defined as the inverse of the impedance.

3.5.2 Constant-Phase Elements (CPEs)

Real-life systems are not always well approximated by ideal circuit elements, such as resistors and capacitors, due to possible heterogeneities in the electrical properties of the underlying material. The idea of a CPE was first introduced by Fricke [138] and is a component that models the behavior of an imperfect capacitor.

$$Z_{CPE} = \frac{1}{CPE(i\omega)^{\alpha}} \tag{3.103}$$

where CPE is the CPE coefficient and $0 \leq \alpha \leq 1$, where $\alpha{=}0$ describes an ideal resistor and $\alpha{=}1$ describes an ideal capacitor.

3.5.3 Equivalent Circuit Model

The equivalent circuit model used in this work for a SAM is depicted in figure 3.26 and that for a tBLM is depicted in figure 3.27. The buffer is modeled with a resistance R_{sol} and the stray capacitance of the cell and the wiring is modeled as C_{stray}. The SAM is modeled as a RC circuit with the capacitance-like behavior captured by CPE_{SAM} and the resistance by R_{def}. The tBLM is modeled as a CPE in parallel with a resistor and CPE. R_{def} represents the resistance of the bilayer, CPE_{tBLM} the capacitance-like behavior of the bilayer and CPE_{def} the capacitance-like behavior of defects in the bilayer. For details, please refer [110].
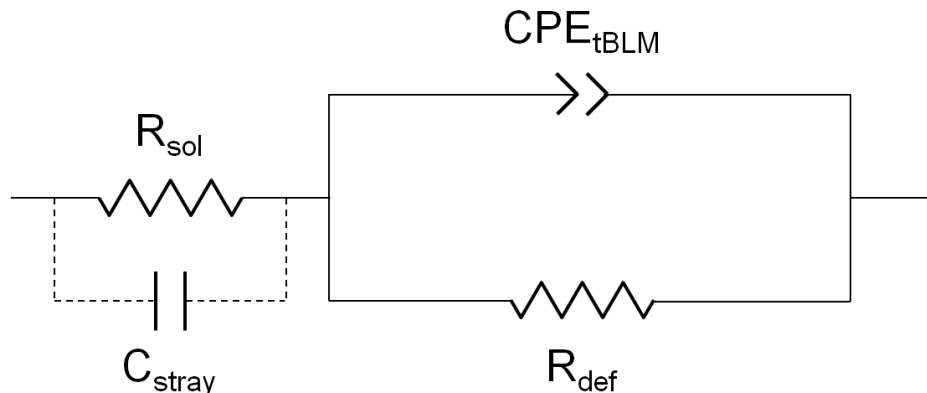
Figure 3.26: Equivalent circuit model for a SAM.
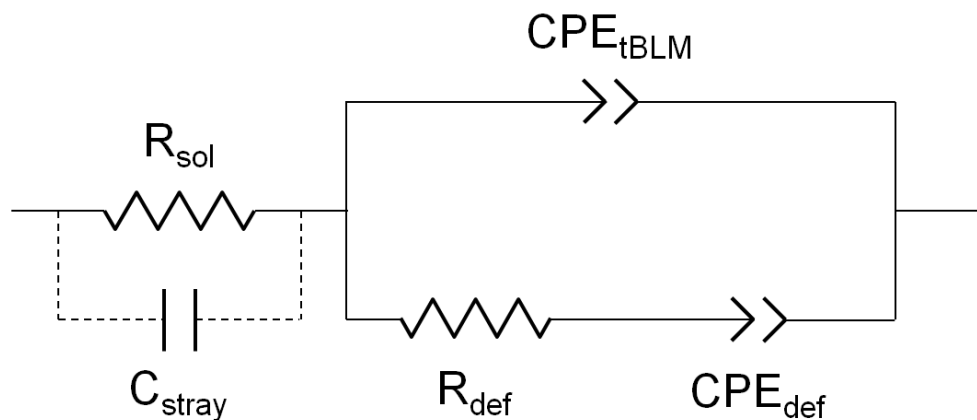
Figure 3.27: Equivalent circuit model for a tBLM.

3.5.4 Cole-Cole Plots and Data Evaluation

EIS data is viewed as a plot of C' vs. C'', where $C = C' + iC''$ is the frequency-dependent capacitance of the electrode (see figure 3.28). This is referred to as a Cole-Cole (or Nyquist) plot and was first described in [139]. For an ideal membrane capacitor with α=1 on a surface electrode, the shape of the data is a semi-circle. For α<1, a tail representing the resistive component appears at low frequencies (high capacitance). The intersection of the semi-circle with the C' axis gives the value of C' ($C' \sim 3\ \mu F$ for a SAM, $C' \sim 0.2\ \mu F$ for a tBLM) and the length of the tail scales with the defect density [110].

Copper contrast was used to measure the surface area, A, in the EIS cell geometry
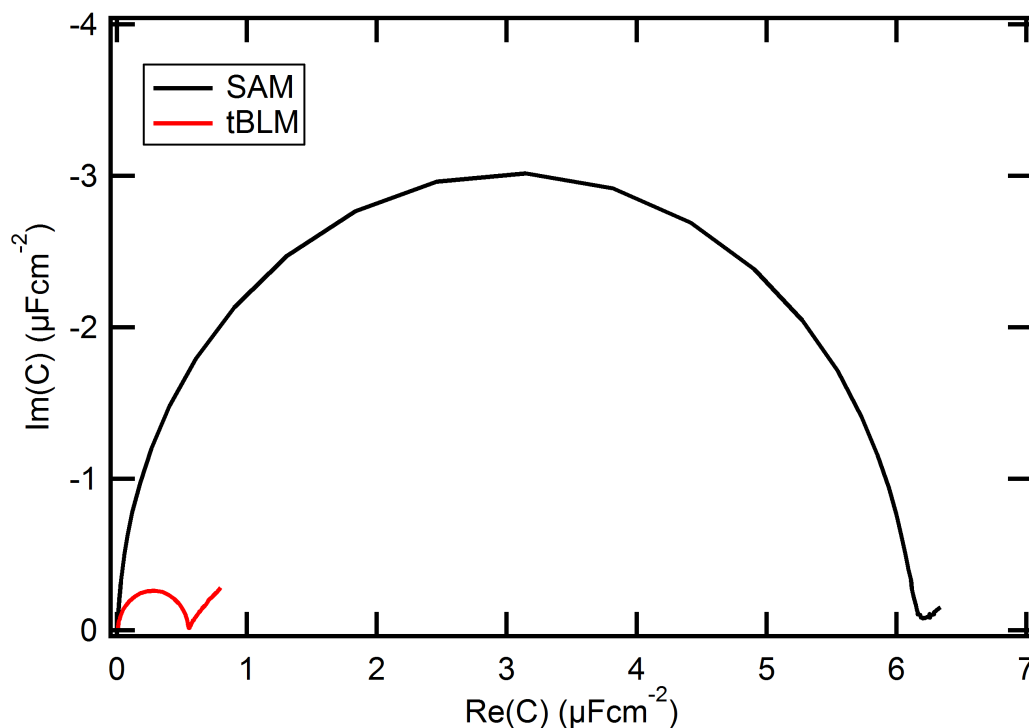
Figure 3.28: EIS Cole-Cole Plot for a SAM and a tBLM.

$(A \sim 0.33 \text{ cm}^2)$ and this value was used to normalize the data to allow comparison with experiments in the literature. The data was fit using the Levenberg-Marquardt algorithm in the ZView software (Scribner Associates, Southern Pines, NC) to obtain a χ^2 parameter to evaluate the goodness of the fit.

3.5.5   Sample Cell

A custom-designed Teflon EIS cell was used which consists of six distinct electrochemical wells (volume ~ 400 µl) on a single gold coated silicon wafer or glass slide. Viton O-rings are used to ensure a tight seal between the Teflon well and the gold and define the area (0.33 cm^2) over which the EIS measurement is averaged.

3.5.6   Instrumentation

EIS experiments were performed using a Solartron (Farnborough, UK) 1287A potentiostat and a 1260 frequency analyzer. EIS data was acquired and modeled using ZPlot and ZView respectively (Scribner Associates, Southern Pines, NC). Spectra were measured between a frequency range of 1 Hz to 100000 Hz with ten logarithmically distributed data points per decade. The thin (~ 450 Å) gold film on a glass

slide or silicon wafer served as the working electrode. A Microelectrodes (Bedford, NH) M-401F saturated silver-silver chloride $[Ag|AgCl|NaCl_{(aq,sat)}]$ microelectrode was used at the reference electrode. A 0.25 mm diameter platinum wire (99.9% purity, Sigma-Aldrich) coiled around the barrel of the reference electrode served as the auxiliary electrode. The microelectrode was inserted into the EIS cell with care taken to separate it's tip from the working electrode by 2-3 mm. EIS measurements were carried out using a 10 mV AC at 0 V bias versus the reference electrode.

Chapter 4

Development of a Novel Membrane Mimic

4.1 Introduction

The intrinsic complexity of cell membranes makes it difficult to characterize their structure and study the interactions that take place in extracellular and intracellular spaces in quantitative terms using biophysical techniques. This need for simplicity has driven the development of artificial biomimetic membranes. There are different kinds of model membranes that have been designed over the years and a brief overview is given below.

4.1.1 Langmuir Monolayers

One of the simplest membrane mimics is the Langmuir monolayer which consists of a mono-molecular thick layer of lipids at the air-water interface and is commonly used to simulate the outer leaflet of the cell membrane. Lipids, like other surface active agents (surfactants), are 'amphiphilic' since they consist of both a hydrophobic and a hydrophilic component, thereby trapping them at the air-water interface.

While Benjamin Franklin performed the first scientific investigation of the effect of a monolayer of oil on water [140], it was Irving Langmuir in 1917 who provided evidence for the single-molecule nature of such a film and quantified the pressure-area relationships of various molecules on water [141]. The controlled preparation and characterization of monolayers are achieved on a 'Langmuir trough', usually made of chemically inert materials such as Teflon. The lipid is dissolved in a volatile solvent that is insoluble in water (usually chloroform) and is added to a 'semi-infinite' pure water reservoir (usually of thickness 5 mm) in a drop-wise manner such that the solvent is allowed to fully evaporate before the next drop is added.

Given a solution, every molecule experiences attractive forces from the surrounding molecules which cancel out for a molecule in the bulk due to spherical symmetry.
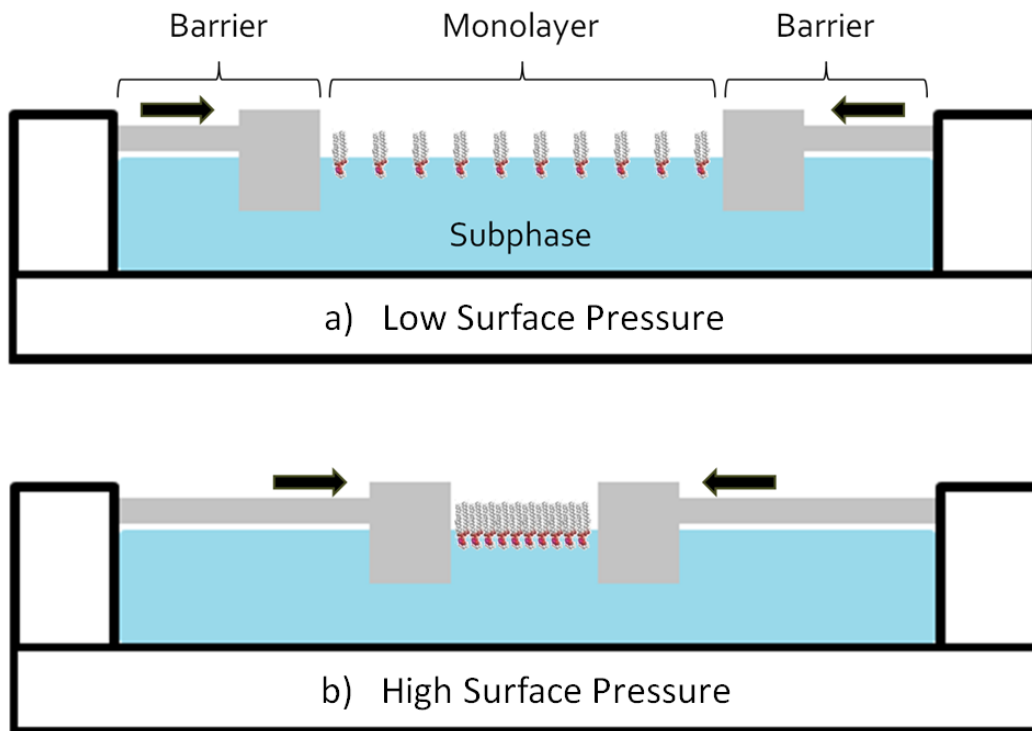
Figure 4.1: Lipids spread at the air-water interface form a monolayer with their hydrophilic heads hydrated by water and the hydrophobic tails exposed to the air. In a Langmuir trough, the area per lipid of the monolayer (and hence the surface pressure) can be controlled by compressing barriers, thereby allowing access to different phases of the system.

However for a molecule at an interface, say a water molecule at the air-water interface, there is a net cohesive force pulling it into the bulk. This is why droplets of water try to form a spherical shape, thereby minimizing the surface area and hence the 'surface tension' they experience. The reduction in surface tension is called surface pressure with both having the same units of mN/m and:

$$\text{Surface Tension} + \text{Surface Pressure} = \text{Constant} \tag{4.1}$$

where the constant is the absolute surface tension of the liquid (72.8 mN/m at STP for water).

The troughs are equipped with hydrophilic barriers (such as Delrin) used to expand or compress the area occupied by the lipids (see figure 4.1). This allows for the precise control of the surface pressure, which in turn allows for the exploration of different phases (gas, fluid, gel, etc.) of the lipid system [142].

A measurement of the surface pressure as a function of area is called a 'compression isotherm' and is distinct for every lipid. The binding of protein to lipids in a
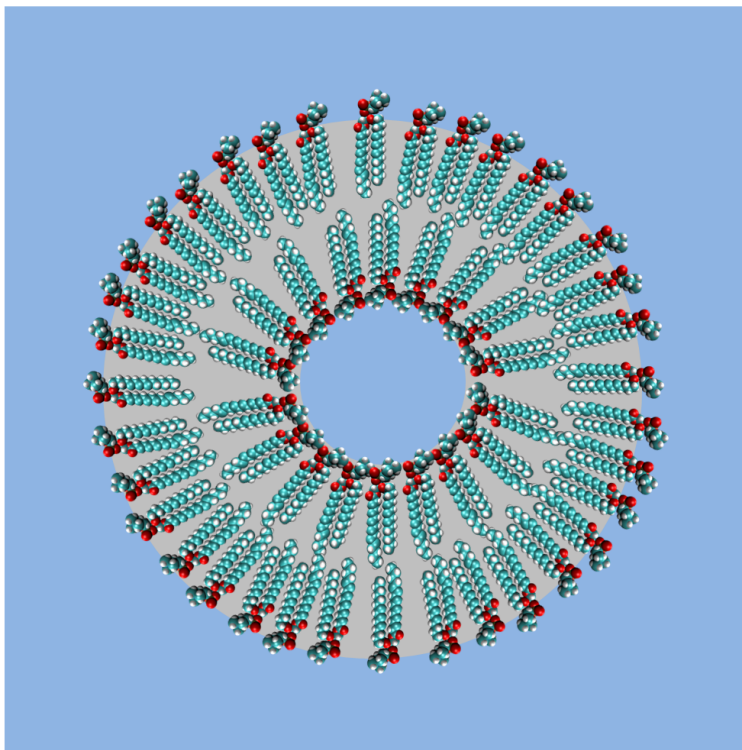
Figure 4.2: A unilamellar vesicle of DPPC where a single bilayer in a spherical shape separates the contents of the vesicle from the bulk solvent.

certain phase can be studied by injecting protein into the subphase and monitoring the resultant change in surface pressure [143, 144, 145]. The use of fluorescent lipids and/or proteins allows for the visualization of the system under observation [146, 147]. Langmuir was also the first person to demonstrate a technique for transferring a monolayer onto a solid substrate [148]. Katharine Blodgett extended his work to show that multilayers could be transferred sequentially by techniques now known as 'Langmuir-Blodgett' and 'Langmuir-Schafer' [149].

4.1.2 Vesicles

The most common model bilayer is the unilamellar vesicle (see figure 4.2). It is a spherical assembly of lipids that can form naturally due to the hydrophobic effect, given a certain minimum concentration (referred to as the critical micelle concentration or CMC). In a physiological context, vesicles play many important roles in material transport in (endocytosis) and out (exocytosis) of cells. They are classified based on the number of lipid layers as well as their size. If they are separated from the buffer by one lipid bilayer (the minimum) they are called unilamellar, else they are called multilamellar. Unilamellar vesicles that are a few 10s of nanometers in
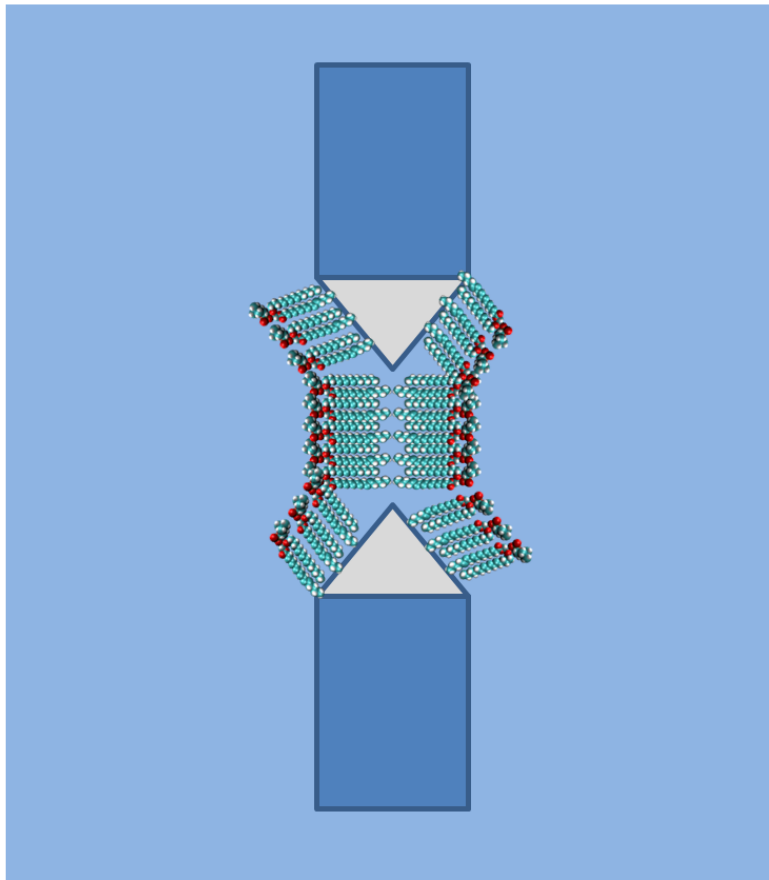
Figure 4.3: Black lipid membranes (BLMs) are prepared by 'painting' a lipid mixture across an aperture forming a bilayer. They appear 'black' in visible light due to destructive interference between light reflected from the two leaflets.

size are called small unilamellar vesicles (SUVs), those that are a few microns in size are called large unilamellar vesicles (LUVs) and those that are 100s of microns in size or larger are called giant unilamellar vesicles (GUVs).

4.1.3 Planar Bilayers

Free-Standing

There are several situations where a planar bilayer aids in the characterization of the membrane, such as in resistance and capacitance measurements or X-ray and neutron reflectivity experiments. One of the first planar bilayer models was the black lipid membrane (BLM) where a lipid solution in an appropriate solvent is spread across an aperture a few microns in size (see figure 4.3) [150]. As such membranes are only a few nanometers in thickness and light reflected from one leaflet destructively
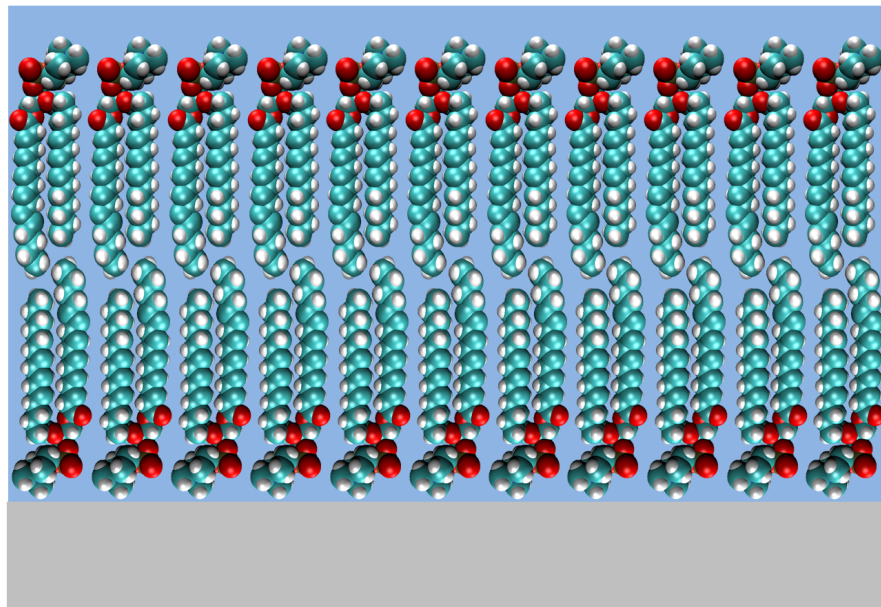
Figure 4.4: A supported lipid bilayer (SLB) formed directly on a hydrophilic substrate with only a small layer of water molecules separating the proximal lipid headgroups from the surface of the support.

interferes with light reflected from the other leaflet, they cannot be seen using visible light and hence appear 'black' [151]. While they are optimal in configuration for electrochemical measurements, they are very hard to prepare at sufficiently large sizes and are highly unstable.

Supported

Supported bilayer lipid membranes (SBLMs) or supported lipid bilayers (SLBs) are model systems where the proximity of the bilayer to a solid substrate lends it stability (see figure 4.4) [152]. Unfortunately, the diffusivity of lipids in this membrane system is substantially lower than in free membranes due to coupling between the substrate and the proximal (to the substrate) leaflet as well as between the proximal and distal leaflets [153]. The close association of the proximal leaflet to the substrate also inhibits the incorporation of trans-membrane peptides.

4.2 Tethered Bilayer Lipid Membranes (tBLMs)

tBLMs are resilient biomimetic systems where the bilayer is covalently anchored to a substrate by means of a hydrophilic oligomer (see figure 4.5). Just as in the case of a SBLM, the bilayer is stabilized by its proximity to the substrate. However,
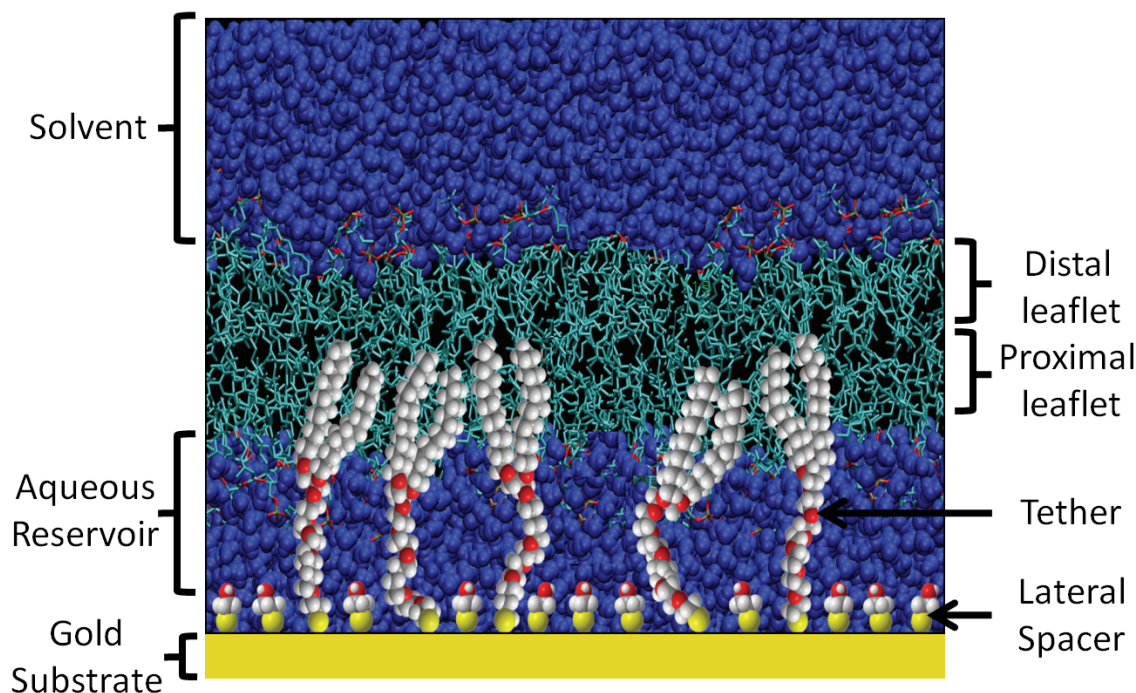
Figure 4.5: Visual of a Sparsely Tethered Bilayer Lipid Membrane (stBLM). The lipid bilayer is tethered to a gold substrate via lipid-like molecules that consist of a thiol molecule, a poly-ethyleneoxide stretch and alkyl chains. A submembrane aqueous reservoir is formed between the gold substrate and the proximal leaflet whose contents can be exchanged by changing the bulk solvent. Hydrophilic spacer molecules (βME) are used to modulate the density of the tether molecules.

the tethers allow for the formation of a nanometer-thick submembrane aqueous reservoir [110]. As a result, tBLMs can be exploited to investigate protein-membrane interactions at the molecular length-scale, even if the protein is transmembrane. The proximal leaflet is either composed of both tether and lipid molecules or pure tether. The distal leaflet is always composed purely of the phospholipids used to complete the bilayer. In principle, tBLMs can be prepared in a wide-range of geometries, as long as the surface is gold-coated and solvent accessible, since they are created from a self-assembly process in solution. In this work, the tBLMs have a planar geometry to make them more practical and amenable to characterization techniques such as neutron reflectivity (NR) and electrochemical impedance spectroscopy (EIS).

4.2.1 Dense Tethering vs. Sparse Tethering

The hydrophilic anchor can be chemisorbed to the gold surface as a pure compound [figure 4.6 (a)] resulting in the formation of a densely tethered bilayer (dtBLM)

a) Densely Tethered   b) Sparsely Tethered
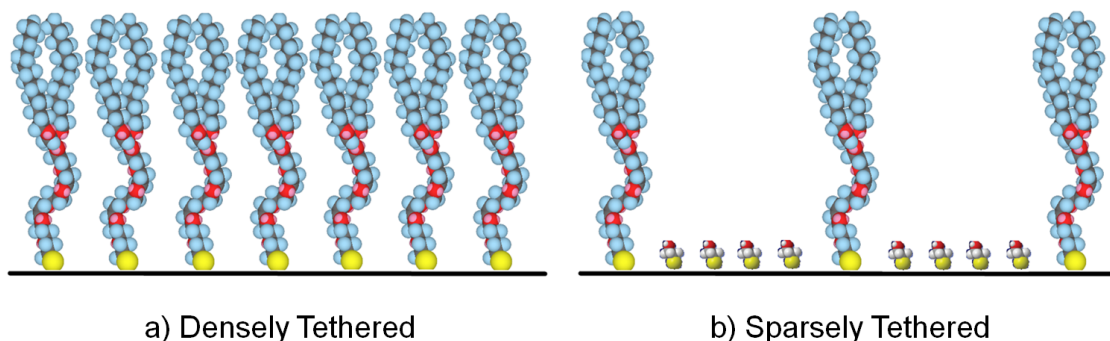
Figure 4.6: The SAM used to prepare a tBLM can be classified either as a) Densely tethered: where the proximal leaflet of the bilayer (dtBLM) is composed solely of tether molecules or b) Sparsely tethered: where hydrophilic βME molecules are used to laterally dilute the tether density. Consequently, the proximal leaflet of the bilayer (stBLM) is composed of both tether and lipid molecules.

where the inner leaflet is lipid-free. Alternatively, the tether can be laterally diluted [figure 4.6 (b)] by the use of small hydrophilic thiol spacer molecules (βME, for example) to form a sparsely tethered bilayer (stBLM). This flexibility in controlling the composition of the proximal leaflet is useful as the appropriate system can be chosen, based on the application at hand. For instance, a stBLM would be used to study transmembrane proteins while a dtBLM would be used to create a bilayer with fluorescently labeled lipids exclusively in the distal leaflet.

4.2.2 Variety of Lipid Tethers

There are three kinds of lipid tethers that were synthesized by our collaborator Dr. Vanderah (NIST) and used in this work: WC14 [110], FC16 [154] and HC18 (see figure 4.7). WC14 and HC18 have a Hexa(ethylene oxide) sequence while FC16 has a Nona(ethylene oxide) sequence. WC14 has dimyristoyl chains, FC16 has dipalmitoyl chains and HC18 has dioleoyl chains. While WC14 and HC18 are approximately the same length, FC16 is approximately 6 Å longer.

4.3 Homogeneity and Fluidity of tBLMs

4.3.1 Introduction

tBLMs are a versatile biomimetic system that are resilient under experimental manipulation and are amenable to a variety of characterization techniques and therefore can be used to gain insight into a range of different biological processes and interactions. However, all this is conditional on the system being able to reproduce charac-
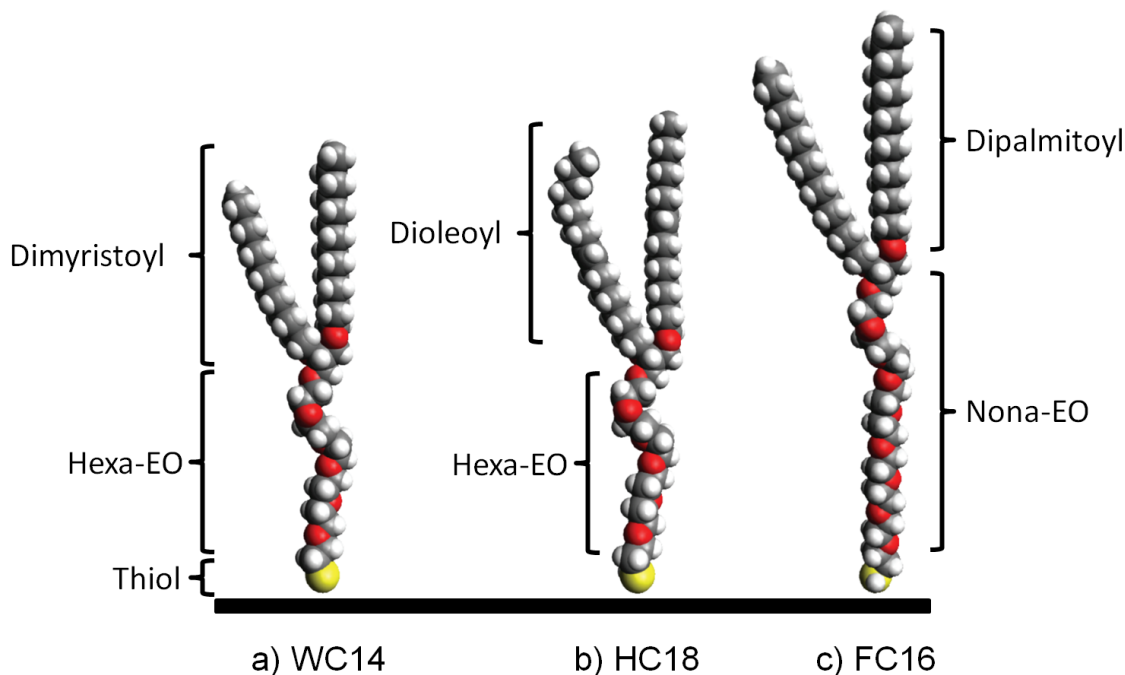
Figure 4.7: Comparison of the three lipid tethers used in this work: a) WC14, b) HC18 and c) FC16 ('EO'≡Ethylene Oxide).

teristics of in-vivo membranes that are relevant to the problem being investigated. For the purpose of this body of work, it was crucial that the tBLMs prepared were homogeneous and that lipids in tBLMs had a fluidity that was comparable to lipids in unsupported and free systems such as vesicles. In order to determine whether this was the case, fluorescence microscopy (FM) was used to check the optical homogeneity, electrochemical impedance spectroscopy (EIS) was used to ensure preparation of low defect-density membranes and fluorescence correlation spectroscopy (FCS) was used to quantify the diffusivity of lipids in the tBLMs.

4.3.2 Optical Homogeneity

Optical homogeneity is one of the hallmarks of a defect-free artificial lipid bilayer composed of a single lipid (or multiple lipids that are known to coexist in a single phase). Consequently, a large amount of time was devoted to using FM to ensure that the tBLM formation protocols guaranteed the reproducible preparation of high-quality bilayers. Figure 4.8 (a) shows the FM micrograph of a DOPC densely tethered bilayer (dtBLM) prepared on a WC14 SAM (with no βME) and figure 4.8 (b) shows the micrograph for a DPhyPC sparsely tethered bilayer (stBLM) prepared on a WC14:βME=30:70 SAM. They are representative of typical tBLMs illustrating the high-quality, optically homogeneous nature of tBLMs used in this
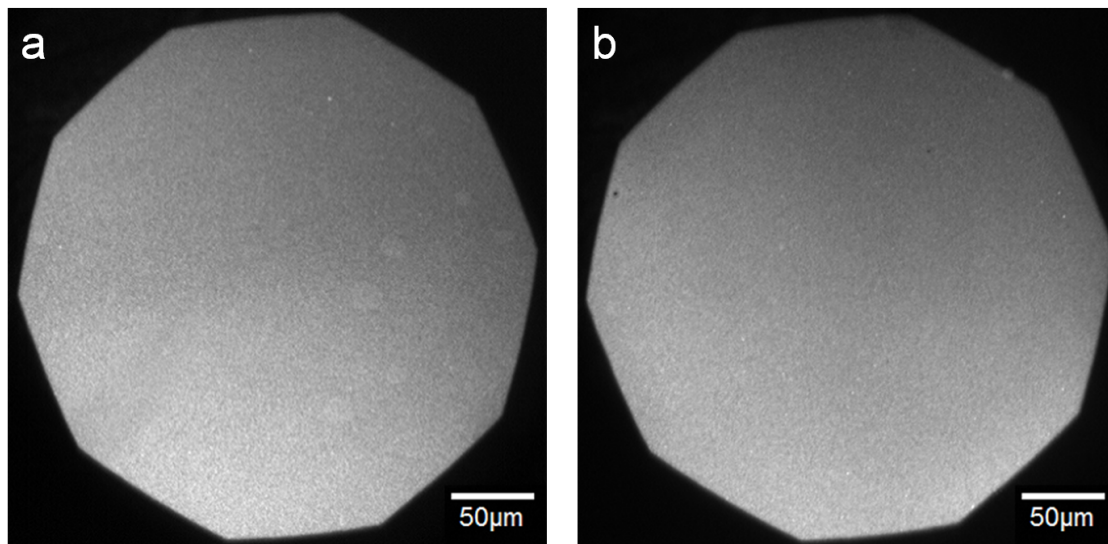
Figure 4.8: Optically homogeneous FM images of a) DOPC on a WC14 dtBLM and b) DPhyPC on a WC14:βME=30:70 stBLM. The concentration of LRPE is 0.06 mol% with respect to the unlabeled lipid. The original image was linearly enhanced to improve contrast.

work. Defects are usually caused by turbulent flow of buffer along the substrate or the introduction of air bubbles during the rapid solvent exchange used to complete the SAM to form a tBLM.

4.3.3 Electrical Resistance

Background

As discussed in section 4.1, there are different systems that can be used to model a lipid membrane. An important test of any membrane mimic is its low defect density and resistance to ion transport. Electrochemical impedance spectroscopy (EIS) (see section 3.5 for details) was used to characterize the electrically insulating nature of the tBLMs to ensure high quality lipid membranes are used in the experimental assays. Prior work done in our group [110] has established the criteria for homogeneous and defect-free bilayers.

Correlation Between Optical Homogeneity and Electrical Insulation

By combining EIS with FM, we were able to correlate the optical homogeneity of tBLMs with their electrically insulating properties. Figure 4.9 shows Nyquist plots based on EIS data for two independently prepared DOPC dtBLMs on the FC16 tether system along with the corresponding fluorescence images. 0.06 mol%
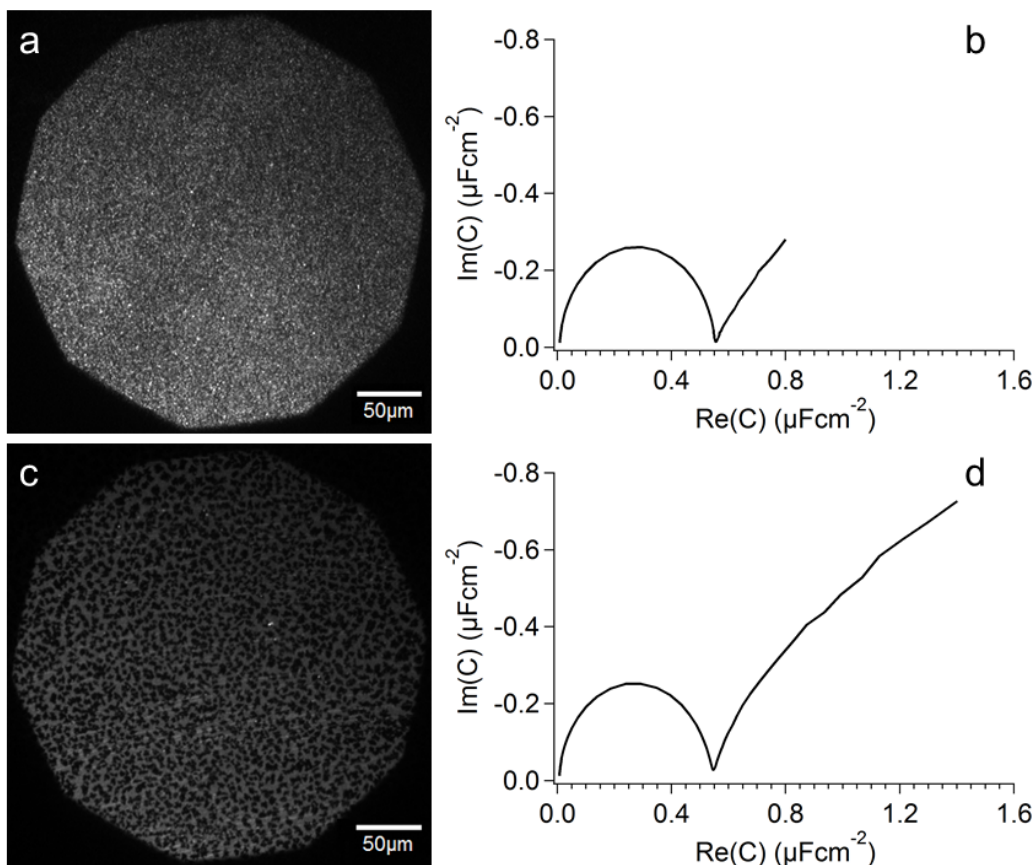
Figure 4.9: Correlation Between Optical Homogeneity and Electrical Insulation. Both FM images (a) and (c) correspond to DOPC bilayers prepared on 100% FC16 dtBLMs with 0.06 mol% LRPE. Uncontrolled differences in the bilayer preparation led to differences in their optical homogeneity and correspond to differences in their insulating properties, as indicated by EIS measurements shown in (b) and (d).

LRPE was used as a fluorescent probe of the homogeneity of the bilayers. While the two bilayers were prepared using an identical protocol, the flow pattern of the rapid solvent exchange is hard to reproduce which results in minor differences in the quality of individual bilayers. The bilayer in figure 4.9 (a) is optically homogeneous and the corresponding EIS spectrum in figure 4.9 (b) shows a short tail indicating a high resistance (R=1.3 ± 0.1 MΩ cm^2) and correspondingly a low defect-density. On the other hand, the bilayer in figure 4.9 (c) shows some inhomogeneities which are accompanied by a longer tail in the EIS spectrum in figure 4.9 (d) and nearly an order of magnitude lower resistance (R=0.29 ± 0.01 MΩ cm^2). Since these correlations are difficult to obtain on a routine basis, we have established a tBLM quality threshold of 50 KΩ cm^2.

Characterization of Cholesterol-Free tBLMs Prepared by Vesicle Fusion

Table 4.1: EIS measurement of tBLMs with varying amounts of anionic lipids prepared by standard vesicle fusion where the vesicle incubation and rinse buffers have an identical salt concentration.

DOPC (%)	DOPS (%)	Run	Time After Bilayer Preparation	Capacitance ($\times 10^{-7}$F)	Resistance ($\times 10^5 \Omega$)
100	0	1	+1 hour	3.01±0.02	1.64±0.03
			+2 hour	3.11±0.03	1.96±0.09
			Overnight	3.13±0.04	1.2±0.1
		2	+1 hour	2.88±0.03	1.10±0.03
			+2 hour	2.94±0.03	1.42±0.06
			Overnight	2.95±0.04	0.87±0.07
95	5	1	+1 hour	3.05±0.03	0.59±0.01
			+2 hour	3.18±0.05	0.78±0.04
			Overnight	3.43±0.06	0.65±0.04
		2	+1 hour	2.97±0.01	1.02±0.01
			+2 hour	3.17±0.03	1.20±0.04
			Overnight	3.36±0.05	0.97±0.04
90	10	1	+1 hour	2.88±0.02	0.388±0.006
			+2 hour	2.94±0.03	0.325±0.005
			Overnight	2.99±0.02	0.312±0.005
		2	+1 hour	3.04±0.02	0.84±0.01
			+2 hour	3.03±0.02	1.64±0.03
			Overnight	3.13±0.04	1.06±0.05
85	15	1	+1 hour	6.12±0.02	0.087±0.004
			+2 hour	6.23±0.08	0.147±0.004
			Overnight	9.12±0.07	0.150±0.003
		2	+1 hour	2.96±0.04	0.121±0.002
			+2 hour	3.03±0.03	0.396±0.009
			Overnight	3.50±0.07	0.72±0.05
80	20	1	+1 hour	5.5±0.3	0.039±0.002
			+2 hour	5.84±0.07	0.115±0.002
			Overnight	8.9±0.1	0.32±0.02
		2	+1 hour	5.1±0.03	0.186±0.002
			+2 hour	4.80±0.02	0.352±0.004
			Overnight	5.74±0.07	0.91±0.03
					Continued on the next page

Table 4.1 – Continued from the previous page

DOPC (%)	DOPS (%)	Run	Time After Bilayer Preparation	Capacitance ($\times 10^{-7}$F)	Resistance ($\times 10^{5}\Omega$)
75	25	1	+1 hour	3.5±0.2	0.017±0.001
			+2 hour	4.1±0.2	0.042±0.002
			Overnight	5.6±0.2	0.105±0.005
		2	+1 hour	4.3±0.2	0.026±0.001
			+2 hour	4.2±0.1	0.034±0.001
			Overnight	4.7±0.3	0.057±0.003

As was mentioned in section 2.5.3, cholesterol facilitates the preparation of high quality tBLMs with an anionic lipid component exceeding 10 mol% using the rapid solvent exchange technique. In order to prepare cholesterol-free anionic tBLMs and to get a better control of the percentage of PS incorporated into the bilayer, the vesicle fusion technique (described in section 2.5.3) was used and the data is shown in Table 4.1. An 'ideal' bilayer has a resistance in excess of 100 kΩ cm^2 and a bilayer with resistance less than 50 kΩ cm^2 is not suitable for use in experiments. Above 10 mol% PS, the resistance is on the order of 10 kΩ cm^2 or lower. We also see an increase in capacitance with an increase in mol% of PS indicating a thinning of the bilayer. Once we reach 25 mol% PS, the resistance is on the order of 5 kΩ cm^2 which is an order of magnitude leakier than the quality threshold.

Table 4.2: EIS measurement of tBLMs prepared by osmotic shock vesicle fusion where SAMs are incubated with 30 nm vesicles in a high salt buffer for 1 hour before being rinsed off with a low salt buffer.

DOPC (%)	DOPS (%)	Run	Time After Bilayer Preparation	Capacitance ($\times 10^{-7}$F)	Resistance ($\times 10^{5}\Omega$)
70	30	1	+1 hour	4.20±0.07	0.074±0.001
			+2 hour	4.15±0.04	0.105±0.002
			Overnight	3.89±0.04	0.430±0.007
		2	+1 hour	3.73±0.08	0.180±0.005
			+2 hour	3.73±0.06	0.205±0.005
			Overnight	3.56±0.08	0.138±0.004

We then attempted to prepare bilayers using the osmotic shock vesicle fusion technique (described in Section 2.5.3). Table 4.2 shows EIS data of tBLMs prepared by incubating HC18:βME=30:70 SAMs with a 5 mg/ml solution of 30 nm

DOPC:DOPS = 70:30 vesicles in a 500 mM salt buffer. After an hour of incubation, the vesicles were rinsed off using a 100 mM salt buffer. The resulting osmotic stress on the vesicles causes them to rupture thereby completing the tBLM. The bilayers have an average resistance of 20 kΩ cm^2 which is an improvement over bilayers of the same lipid composition prepared by rapid solvent exchange, but is still below the quality threshold.

Table 4.3: EIS measurement of tBLMs prepared by osmotic shock vesicle fusion where SAMs were incubated with 100 nm vesicles for 1 hour. Measurement 1 was prepared by rinsing off the vesicles with a 100 mM salt buffer, while measurement 2 was prepared by rinsing off the vesicles with DI water followed by the 100 mM salt buffer.

DOPC (%)	DOPS (%)	Run	Time After Bilayer Preparation	Capacitance ($\times 10^{-7}$F)	Resistance ($\times 10^{5}\Omega$)
70	30	1	+1 hour	3.42$\pm$0.04	1.00$\pm$0.03
			+2 hour	3.36$\pm$0.04	1.65$\pm$0.06
			Overnight	3.22$\pm$0.03	1.54$\pm$0.04
		2	+1 hour	3.74$\pm$0.04	0.69$\pm$0.01
			+2 hour	3.71$\pm$0.04	0.91$\pm$0.02
			Overnight	3.58$\pm$0.04	0.71$\pm$0.02

Since vesicles with a larger diameter have an increased propensity to rupture under an osmotic pressure difference (from the Young-Laplace equation), we shifted from using 30 nm vesicles to 100 nm vesicles. Table 4.3 shows EIS data of tBLMs prepared by incubating HC18:βME=30:70 SAMs with a 5 mg/ml solution of 100 nm DOPC:DOPS = 70:30 vesicles in a 500 mM salt buffer. After an hour, the vesicles were rinsed off the substrate using a 100 mM salt buffer. The bilayers have a resistance of 100 kΩ cm^2 or higher and are stable overnight.

To test the effect of incubation time on bilayer quality, we prepared bilayers where the SAM was incubated with 100 nm vesicles overnight instead of one hour (see Table 4.4). The bilayers are, on average, the same quality as those prepared with a one hour incubation indicating that the extra time need not be expended, at least when a 5 mg/ml concentration of vesicles is used.

Table 4.4: EIS measurement of tBLMs prepared by osmotic shock vesicle fusion using 100 nm vesicles incubated overnight on the SAM. Measurement 1 was prepared by rinsing off the vesicles with a 100 mM salt buffer, while measurement 2 was prepared by rinsing off the vesicles with DI water followed by the 100 mM salt buffer.

DOPC (%)	DOPS (%)	Run	Time After Bilayer Preparation	Capacitance ($\times 10^{-7}$F)	Resistance ($\times 10^{5}\Omega$)
70	30	1	+1 hour	3.32±0.04	1.28±0.04
			+2 hour	3.34±0.04	1.44±0.05
			Overnight	3.54±0.07	2.0±0.1
		2	+1 hour	3.43±0.04	0.58±0.02
			+2 hour	3.47±0.04	0.68±0.02
			Overnight	3.40±0.04	0.60±0.02

Table 4.5: EIS measurement of tBLMs with varying amounts of anionic lipids prepared by osmotic shock vesicle fusion using 100 nm vesicles incubated on the SAM for 1 hour.

DOPC (%)	DOPS (%)	Run	Time After Bilayer Preparation	Capacitance ($\times 10^{-7}$F)	Resistance ($\times 10^{5}\Omega$)
100	0	1	+1 hour	3.46±0.06	0.63±0.03
			+2 hour	3.19±0.04	0.56±0.02
			Overnight	3.55±0.07	0.54±0.02
95	5	1	+1 hour	3.22±0.06	1.7±0.2
			+2 hour	3.01±0.04	1.7±0.1
			Overnight	3.41±0.05	1.44±0.09
		2	+1 hour	2.93±0.05	1.2±0.2
			+2 hour	2.82±0.02	1.3±0.1
			Overnight	3.13±0.04	1.5±0.1
90	10	1	+1 hour	3.21±0.08	1.0±0.2
			+2 hour	3.11±0.04	1.4±0.1
			Overnight	3.65±0.07	1.4±0.1
		2	+1 hour	3.01±0.05	1.01±0.06
			+2 hour	3.08±0.04	1.16 ±0.05
			Overnight	3.55±0.09	0.66±0.04
					Continued on the next page

77

Table 4.5 – Continued from the previous page

DOPC (%)	DOPS (%)	Run	Time After Bilayer Preparation	Capacitance ($\times 10^{-7}$F)	Resistance ($\times 10^5 \Omega$)
85	15	1	+1 hour	2.63±0.09	0.38±0.08
			+2 hour	2.70±0.05	0.67±0.06
			Overnight	2.90±0.06	0.59±0.05
		2	+1 hour	2.64±0.03	1.47±0.07
			+2 hour	2.59±0.02	1.64±0.06
			Overnight	2.74±0.05	1.17±0.06
80	20	1	+1 hour	3.02±0.07	1.4±0.1
			+2 hour	2.86±0.05	1.19±0.08
			Overnight	3.15±0.07	1.01±0.07
		2	+1 hour	2.74±0.08	1.5±0.1
			+2 hour	2.71±0.04	1.39±0.08
			Overnight	2.96±0.06	0.88±0.04
75	25	1	+1 hour	2.93±0.05	1.8±0.1
			+2 hour	2.77±0.05	1.3±0.1
			Overnight	2.95±0.07	0.87±0.08
		2	+1 hour	2.94±0.07	1.24±0.09
			+2 hour	2.91±0.06	1.23±0.08
			Overnight	3.44±0.08	0.82±0.04
70	30	1	+1 hour	3.42±0.04	1.00±0.03
			+2 hour	3.36±0.04	1.65±0.06
			Overnight	3.22±0.03	1.54±0.04

Finally, a series of measurements were performed to test the quality of DOPC:DOPS bilayers ranging from 100:0 to 70:30 using 100 nm vesicles incubated for one hour and using the osmotic shock vesicle fusion technique (see Table 4.5). No matter what mol% of PS was used, the bilayers were of high quality and stable for at least 24 hours, thereby making them amenable for protein-membrane binding assays.

4.3.4 Quantifying the Fluidity of tBLMs

The in-plane fluidity of model membranes is an important property as it determines the molecular interactions that can be characterized and the extent to which protein reconstitution can be pursued. It has been shown that the diffusivity of lipids in solid-supported bilayers, where the bilayer is physisorbed to a mica or glass surface, is substantially lower than in free membranes [153]. Failure to decouple the proximal leaflet from the substrate results in the freezing out of lipid kinetics which can alter dynamics in the distal leaflet. As a result, a crucial step to validate the usefulness

of the tBLM system is to measure the fluidity of these bilayers and to compare them with free membranes. We used z-scan FCS (see section 3.1.4) to measure the diffusivity of fluorescently labeled lipids (LRPE) in the tBLMs. 0.003 mol% LRPE was used to minimize the impact of the fluorophore on the properties of the bilayer.

As described earlier, in dtBLMs mobile lipids are restricted to the distal leaflet. Consequently, a probe of the diffusivity of labeled fluorophores in a dtBLM will yield the fluidity of lipids solely in the distal leaflet. However, similarly prepared stBLMs consist of labeled lipids in both proximal and distal leaflets. As a result, the measured diffusion coefficient would represent a fluidity averaged over both leaflets. Bearing this in mind, let us examine the FCS diffusion data and the conclusions that can be drawn.

Fluidity of tBLMs vs. Other Model Membrane Systems

Table 4.6: Comparison of the fluidity of lipids in tBLMs with that of lipids in GUVs.

WC14	GUV	GUV
7.1±0.3 µm^2/s (Distal Leaflet)	7.8±0.8 µm^2/s [153]	6.3±0.2 µm^2/s [155]

We compared the fluidity of lipids in the distal leaflet of DOPC tBLMs with those in giant unilamellar vesicles (GUVs), described in the literature (see Table 4.6). The tBLM system compares very favorably, showing that a tethered membrane system can be prepared with a fluidity that is indistinguishable from that of free vesicles. This validates the model system as we have gained structural stability without compromising on lipid diffusivity. We performed an analysis of the fluidity of tBLMs as a function of tether length, tether density, lipid type and cholesterol composition.

Effect of Tether Length and Tether Density

z-scan FCS experiments were performed on both the WC14 and FC16 tethers using the sparsely tethered (stBLM, tether:βME=30:70) and densely tethered (dtBLM, no βME) architectures (see Table 4.7). We observed three results where the chemistry of surface ligation had a significant impact on membrane fluidity:

1. **dtBLMs have higher apparent fluidity than stBLMs:** As mentioned earlier, labeled lipids in stBLMs are present in both proximal and distal leaflets. Lipids in the proximal leaflet have a reduced diffusivity due to obstruction from the tethers which in turn reduces the apparent diffusivity of

Table 4.7: Diffusivity of lipids in DOPC bilayers prepared on WC14 and FC16 tethers in stBLM and dtBLM configurations.

Tether	Sparsely Tethered (stBLM)	Densely Tethered (dtBLM)
WC14	4.1±0.1 $\mu m^2/s$	7.1±0.3 $\mu m^2/s$
FC16	3.6±0.2 $\mu m^2/s$	5.4±0.2 $\mu m^2/s$

stBLMs. Since lipids are primarily restricted to the distal leaflet in dtBLMs, there is no hindered diffusion to lower the averaged diffusivity, thereby explaining why dtBLMs appear to be more fluid than stBLMs.

2. **WC14 stBLMs are more fluid than FC16 stBLMs:** When measuring the diffusivity of lipids in an stBLM, we are measuring an 'apparent' diffusion coefficient with contributions from fluorescently labeled lipids in both the proximal and distal leaflets. FC16 has a longer oligo(ethyleneoxide) linker (n=9 repeats for FC16 vs. n=6 for WC14) and polymethylene chains (16 carbons for FC16 vs. 14 carbons for WC14). It is well known that an increase in the hydrophobic chain length results in enhanced van der Waals interactions between the chains. For instance, the addition of two methylenes to DMPC resulting in DPPC increases the chain melting temperature by $\sim$ 20 °C. In analogy, it must be assumed that the longer alkyl chains in FC16, compared to WC14, result in tighter packing in the proximal leaflet. This is expected to reduce the diffusivity of lipids in the proximal leaflet and hence will result in the measurement of a lower apparent diffusivity of the stBLM.

3. **WC14 dtBLMs are more fluid than FC16 dtBLMs:** In the case of dtBLMs, it is assumed that the proximal leaflet is composed solely of tether molecules in which case the only contribution to the measured diffusivity would be from the distal leaflet. In such a situation, both WC14 and FC16 dtBLMs should have an identical distal leaflet composition and hence the same diffusion coefficient. Surprisingly, the FCS data shows that WC14 dtBLMs have a higher diffusivity than their FC16 counterparts. There are two possible scenarios that would explain this result:

    (a) The longer tethers in FC16, which played a role in reducing the fluidity of FC16 stBLMs, also increase the inter-leaflet coupling thereby decreasing the fluidity of lipids in the outer leaflet. Lipopolymers are "amphiphiles of conic shape" [156] with the hydrocarbon chains being bulkier than ethyleneoxide anchor. It has been hypothesized that an increase in chains length can result in a more pronounced conical shape, thereby increasing

80
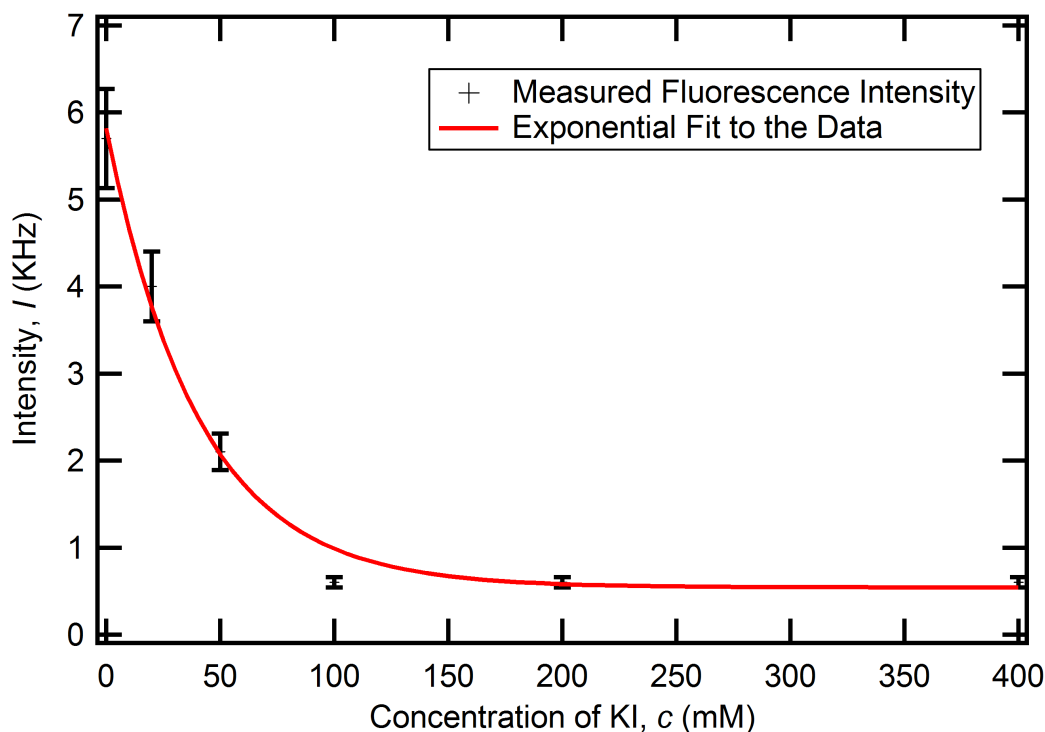
Figure 4.10: Quenching of 0.003 mol% LRPE in a DOPC WC14 dtBLM by the addition of Potassium Iodide (KI).

the lateral stress, especially at high tether density [156]. This can enhance the propensity for self-aggregation and/or protrusion of the tethers, resulting in tether-induced deformation of the bilayer around 'pinning sites' and inter-leaflet coupling of obstructed lipid diffusion [156].

(b) Our assumption that the proximal leaflet is devoid of lipids is incorrect. If there is some residual intercalation of phospholipids into the proximal leaflet, their hindered diffusion would lower the apparent diffusivity, thereby explaining the observed result. This is feasible as the longer linker and alkyl chains in FC16 could result in a more flexible SAM, thereby allowing for the possibility of lipid incorporation into the proximal leaflet during bilayer completion [120].

Proximal vs. Distal Leaflet Diffusivity

A z-scan FCS measurement of diffusion in an stBLM produces an averaged diffusivity of both leaflets. Measuring a dtBLM allows us to calculate the diffusion coefficient of lipids primarily located in the distal leaflet because they are the majority of mobile lipids in the beam focus. In order to measure the fluidity of lipids in

Table 4.8: Comparison of the diffusivity of DOPC lipids in the proximal and distal leaflets of tBLMs prepared on WC14 SAMs.

Tether	Proximal Leaflet (stBLM + 100mM KI)	Distal Leaflet (dtBLM)
WC14	2.0 ± 0.2 µm^2/s	7.1 ± 0.3 µm^2/s

the proximal leaflet, we need some way to mask the fluorescence from lipids in the distal leaflet. Potassium iodide (KI) has been identified as a membrane-impermeable quencher of LRPE in the distal leaflet [157]. A calibration curve (see figure 4.10) was measured where the fluorescence intensity was plotted as a function of increasing amounts of KI added to a DOPC dtBLM consisting of 0.003 mol% LRPE. Based on this data, 100 mM KI was identified as the minimum amount needed to quantitatively quench fluorescence from the distal leaflet.

A DOPC stBLM with 0.003 mol% LRPE was prepared and 100 mM KI was added to the bulk buffer. By performing z-scan FCS experiments, we measured a diffusion coefficient for proximal leaflet lipids of 2.0 ± 0.2 µm^2/s (see table 4.8). Given that the diffusion coefficient of distal leaflet lipids is 7.1 ± 0.3 µm^2/s, the apparent diffusion coefficient of an stBLM of 4.1 ± 0.1 µm^2/s can therefore be interpreted as an average of the individual diffusivities of each leaflet.

Rapid Solvent Exchange vs. Vesicle Fusion

Table 4.9: Comparison of the fluidity of DOPC stBLMs prepared by rapid solvent exchange and by vesicle fusion.

Tether	Rapid Solvent	Vesicle Fusion
WC14	4.1 ± 0.1 µm^2/s	4.2 ± 0.5 µm^2/s

As described in section 2.5.3, we pursued two avenues for completing the bilayer on a SAM: rapid solvent exchange and vesicle fusion. While the former protocol is easier to execute, it limits the amount of anionic lipid that can be incorporated into the bilayer without the use of cholesterol and also the final lipid composition does not necessarily reflect the composition in the ethanolic solvent. As we saw in section 4.3.3, osmotic shock vesicle fusion allows for the preparation of high quality, defect-free bilayers. We performed z-scan FCS experiments to compare the fluidity of DOPC bilayers prepared using both these techniques (see Table 4.9). The

diffusion coefficient of lipids in both cases are comparable, justifying the use of either technique in preparing tBLMs.

Effect of Lipid Chain: DOPC vs. DPhyPC

Table 4.10: Comparison of the fluidity of DOPC stBLMs and DPhyPC stBLMs.

Tether	DOPC stBLM	DPhyPC stBLM
WC14	4.1±0.1 µm^2/s	3.1±0.6 µm^2/s
FC16	3.6±0.2 µm^2/s	2.5±0.3 µm^2/s

So far, all the diffusion data described concerned tBLMs composed of DOPC. We also studied the effect of lipids chains on bilayer fluidity. We compared DOPC and DPhyPC stBLMs on both the WC14 and FC16 tether systems (see Table 4.10). We see that lipids in DPhyPC bilayers diffuse systematically slower than those in DOPC bilayers. It is well known that there is better packing of lipid chains in DPhyPC than in DOPS due to the absence of disorder introduced by unsaturation. The branching in DPhyPC also results in increased van der Waals interactions. Consequently, it is natural that the denser packing of lipid chains in a DPhyPC bilayer results in a lower lipid diffusivity, compared to a DOPC bilayer.

Effect of Charged Lipids and Cholesterol

Table 4.11: Comparison of the fluidity of stBLMs prepared on the WC14 tether using DOPS and cholesterol.

Lipid Composition	Diffusivity
DOPC	4.1±0.1 µm^2/s
DOPC:DOPS = 95:5	4.5±0.4 µm^2/s
DOPC:DOPS = 80:20	3.3±0.2 µm^2/s
DOPC:DOPS:CHOL = 80:20:5	3.5±0.2 µm^2/s
DOPC:DOPS:CHOL = 80:20:30	2.3±0.1 µm^2/s

Finally, we studied the effect of charged headgroups and cholesterol on bilayer fluidity (see Table 4.11). There are two main points to note:

1. The addition of small amounts (5%) of DOPS has no measurable affect on bilayer fluidity. However, when 20% of the bilayer is composed of anionic

lipid, the label diffusivity decreases by about 20%. We suggest that the mutual repulsion of charged headgroups at high DOPS concentration leads to an obstruction of free Brownian motion. While this effect might occur even at small DOPS concentrations, its impact on non-DOPS lipids such as the labeled species used as a reporter molecule may only be noticeable experimentally at a sufficiently high concentration.

2. The addition of small amounts (5%) of cholesterol has a minor affect on bilayer fluidity. However, when 30% cholesterol is incorporated into the bilayer, there is a 30% drop in lipid diffusivity. This condensing effect is a well known phenomenon where cholesterol aids in the tighter packing and suppression of conformations of lipid chains in fluid, disordered membranes [158, 159, 160, 161, 162].

4.4 Discussion

The pursuit of the mechanisms governing biomolecular processes and interactions involving the lipid membrane launched efforts to engineer a new and versatile bilayer mimic – one whose composition can be tuned while providing a stable platform amenable to a multitude of characterization techniques. Tethered bilayer lipid membrane (tBLMs) are the latest attempt at fulfilling this mission by building on the successes of supported lipid bilayers (SLBs) while trying to avoid the loss in lipid mobility due to contact with the substrate. Prior to investing time and effort pursuing protein-membrane investigations using tBLMs, it was important to validate their physical properties with respect to free lipid bilayers, such as vesicles. We aimed to do just that through a three-pronged approach using fluorescence microscopy (FM), electrochemical impedance spectroscopy (EIS) and fluorescence correlation spectroscopy (FCS).

FM micrographs of tBLMs using 0.06 mol% of fluorescently labeled lipids (LRPE) allowed us to visually confirm their optical homogeneity and identify telltale signs of improper rapid solvent exchange during tBLM preparation. In particular, we recognized the importance of controlled laminar flow of buffer along the substrate in order to avoid the formation of micro-heterogeneities and defects. By performing EIS and FM measurements on the same tBLM samples, we were able to correlate the insulating property of bilayers with their optical homogeneity. EIS is a very sensitive technique that allows for the precise determination of the defect density of a given bilayer. This allowed us to implement a quality control protocol where tBLMs had to possess a minimum defect resistance of 50 kΩ cm^2 in order to be considered for further characterization and use in biochemical assays.

However, a defect-free tBLM only validates the preparation protocol and does not, *a priori,* warrant the suitability of the membrane as a mimic of fluid, free-

standing lipid bilayers. FCS allowed us to probe the fluidity of each leaflet of the tBLM and the effect of tether length, tether density, lipid saturation, anionic composition and cholesterol as an additive. The lipids in the distal leaflet of a tBLM are comparable in diffusivity to lipids in GUVs verifying the ability of tBLMs to satisfy both the stability and fluidity characteristics required of model membranes. Lipids in the proximal leaflet are hindered in their motion due to presence of tether molecules which lowers the apparent diffusivity of stBLMs in which the diffusion of labels in both leaflets cannot be discriminated.

The longer alkyl chains in FC16 result in an enhanced van der Waals interaction and tighter packing of lipids in tBLMs, thereby lowering the fluidity of lipids in both the proximal and distal leaflets. Similarly, the absence of unsaturation in DPhyPC lipids allows for the preparation of tBLMs with a smaller diffusion coefficient. The addition of anionic lipids, such as DOPS at high concentration in a dual-component membrane with zwitterionic lipids, also results in a lower diffusivity due to the impact of hindered DOPS diffusion on the surrounding lipids. Cholesterol is known to condense otherwise fluid bilayers resulting in a better packing of lipid chains and headgroups thereby reducing membrane fluidity – a result that holds for tBLMs.

In summary, we have validated the use of tBLMs to mimic the properties of free standing bilayers while offering the ability to prepare resilient, planar membranes that can be simultaneously characterized by a variety of biophysical techniques, while allowing for a precise control of lipid composition. We have also established the groundwork for probing the interaction of the PTEN tumor suppressor with the plasma membrane, which will constitute the remainder of the research described here.

Chapter 5

Interaction Strength of PTEN to tBLMs

5.1 Introduction

The plasma membrane mediates PTEN's regulatory function through complex interactions with the anionic lipids PS (the primary anionic lipid component of the plasma membrane), PI(4,5)P$_2$ (the major PIP component) and PI(3,4,5)P$_3$ (the catalytic substrate). In order to understand the mechanism by which PTEN performs it regulatory function and its disruption following mutations, it is critical to quantify the effect of various molecular factors on the membrane association of PTEN. This was achieved by performing high sensitivity (with respect to refractive index changes) SPR measurements of *wt* PTEN and several mutants (H93R PTEN, C124S PTEN and the truncated crystal structure PTEN) to sparsely tethered bilayer membranes (stBLMs) of varying lipid composition using the HC18:βME=30:70 self-assembled monolayer (SAM). The zwitterionic lipid DOPC was the majority component in each case as it is one of the primary components of the plasma membrane. It has been shown that the affinity of PTEN for DOPC bilayers is very weak ($K_d > 500$ μM) [5]. 5 mol% cholesterol was added to membranes containing greater than 10 mol% anionic lipid to ensure the preparation of a defect-free ($> 95\%$ surface coverage) bilayer. At this low concentration, no impact of cholesterol on PI(4,5)P$_2$ lateral distribution has been observed (Gericke and Jiang, unpublished data).

stBLMs provide us with the unique ability to exquisitely control the lipid composition of membranes while ensuring the reproducible preparation of defect-free bilayers. The ability to simultaneously perform electrochemical impedance spectroscopy (EIS) and surface plasmon resonance (SPR) measurements on the same physical sample allows for a quality control protocol to be implemented that guarantees binding assays are only performed on the highest grade bilayers.

Commercial SPR setups utilize carboxymethylated dextran chips as substrates

to study protein binding kinetics. These do not allow for any quantitative measurements of bilayer completeness to be performed. As a result, strong non-specific interactions to the chip can bias the measured data, providing inaccurate estimates of the dissociation constant. Traditionally, reference channels are used to quantify non-specific interactions and subtract their contribution from the data measured in the main channel. This only works if the non-specific affinity is weaker than the specific interaction, which need not be the case. This was highlighted in the only publication [163] prior to our work that used SPR to quantify PTEN association with lipid membranes. While the work was very comprehensive and compared the affinity of *wt* PTEN with several mutants, the dissociation constants obtained were three orders of magnitude smaller than those obtained by other methods [5, 164]. Apart from incomplete lipid coverage, the other contributor to an inaccurate binding constant could be the use of kinetic binding analysis – calculating K_d by measuring K_{off} and K_{on} and taking their ratio. This methodology can underestimate the dissociation constant by one to three orders of magnitude compared to equilibrium binding methods such as sedimentation analysis and isothermal titration calorimetry [165]. Performing equilibrium binding analysis in a flow cell is prohibitive due to the large amount of protein needed to achieve saturation. In the SPR work presented above, we used a non-flow cell with a stirring apparatus to achieve the ideal balance of small protein volumes and accurate kinetic measurements.

The SPR binding data provides us with two quantitative measures of the interaction being studied: 1) The equilibrium binding constant, K_d in μM, which quantifies the affinity. i.e., gives a measure of the protein concentration at which the amount of adsorbed protein reaches half the saturation value in the Langmuir model and 2) The shift in the SPR resonance angle at infinite analyte concentration, B_{max} in ng/cm^2, which quantifies the amount of adsorbed material. The master table summarizes all the measured SPR data which will be described in detail below.

5.2 *wt* PTEN Binding Kinetics

5.2.1 Binding to PS

wt PTEN has a moderate affinity for PS lipids with K_d=11.9±0.4 μM to DOPC:DOPS = 70:30 lipid bilayers (see table 5.1 and figure 5.1). This is roughly consistent with prior work [5] reporting a K_d of 22.0±0.5 μM, given the difference in bilayer systems (planar stBLMs in this work vs. spherical vesicles [5]) and methodology (SPR in this work vs. Tryptophan fluorescence quenching assays [5]). With a B_{max} of 155±3 ng/cm^2, PS fulfills its proposed role as the attractor of PTEN to the plasma membrane through electrostatic interactions with basic residues, primarily in the CBR3 motif in the C2 domain (see chapter 1 for details).

		PC:PS (+ chol)	PC:PI(4,5)P$_2$	DPPC: DPPI(4,5)P$_2$	PC:PS:PI(4,5)P$_2$ (+ chol)	PC: PI(3,4,5)P$_3$	PC:PI(4,5)P$_2$:PI(3,4,5)P$_3$
wt PTEN	system	70:30	99.3:0.7 / 97.8:2.2 / 96.3:3.7	96.3:3.7	69.7:29:1.3 / 68.8:28.6:2.6	97.9:2.1	96.4:1.8:1.8
	K_d (μM)	11.9 ± 0.4	0.4 ± 0.1	1.9 ± 0.3	**a:** 0.04 ± 0.01 / **b:** > 5	2.4 ± 0.2	1.0 ± 0.1
	B_{max} (ng/cm^2)	155 ± 3	23 ± 1 / 26 ± 1 / 71 ± 2	73 ± 2	**a:** 22 ± 1 / **a:** 29 ± 12 / **b:** > 174	145 ± 23	93 ± 35
C124S PTEN	system	70:30	97.8:2.2	n.d.	n.d.	97.9:2.1	98:1.8:0.2 / 98:1:1 / 98:0.2:1.8
	K_d (μM)	2.9 ± 0.3	0.32 ± 0.03	n.d.	n.d.	0.12 ± 0.03	0.26 ± 0.01 / 0.13 ± 0.01 / 0.12 ± 0.01
	B_{max} (ng/cm^2)	273 ± 17	99 ± 17	n.d.	n.d.	191 ± 17	127 ± 2 / 152 ± 1 / 218 ± 2
H93R PTEN	system	70:30	97.8:2.2	n.d.	68.8:28.6:2.6	n.d.	n.d.
	K_d (μM)	3.1 ± 0.3	1.3 ± 0.2	n.d.	0.7 ± 0.1		
	B_{max} (ng/cm^2)	162 ± 17	64 ± 6		191 ± 23		
trunc'd PTEN	system	70:30	97.8:2.2	n.d.	68.8:28.6:2.6	n.d.	n.d.
	K_d (μM)	2.5 … 4.9	0.77 ± 0.07	n.d.	0.9 ± 0.2		
	B_{max} (ng/cm^2)	348 … 563	81 ± 3		325 ± 35		

Master Table: A comprehensive listing of SPR data for *wt* PTEN, C124S PTEN, H93R PTEN and the truncated PTEN binding to tBLMs composed of PS, PI(4,5)P$_2$, PI(3,4,5)P$_3$ and mixtures of the three lipids.

Table 5.1: SPR binding data for *wt* PTEN association with lipid membranes composed of PS, PI(4,5)P$_2$, PI(3,4,5)P$_3$ and mixtures of the three lipids.

System	Composition	K_d (µM)	B_{max} (ng/cm^2)
PC:PS:chol	70:30:5	11.9±0.4	155±3
PC:PI(4,5)P$_2$	99.3:0.7	0.4±0.1	23±1
	97.8:2.2	0.4±0.1	26±1
	96.3:3.7	0.4±0.1	71±2
DPPC:DPPI(4,5)P$_2$	96.3:3.7	1.9±0.3	73±2
PC:PS:PI(4,5)P$_2$: **chol**	69.7:29:1.3:5	**a:** 0.04±0.01	**a:** 22±1
		b: >5	**b:** >174
	68.8:28.6:2.6:5	**a:** 0.04±0.01	**a:** 29±12
		b: >5	**b:** >174
PC:PI(3,4,5)P$_3$	97.9:2.1	2.4±0.2	145±23
PC:PI(4,5)P$_2$: **PI(3,4,5)P$_3$**	96.4:1.8:1.8	1.0±0.1	93±35

5.2.2 Binding to PI(4,5)P$_2$

We observe a 30 fold stronger affinity of *wt* PTEN to PI(4,5)P$_2$ than to PS with $K_d^{PI(4,5)P_2}$=0.4±0.1 µM (see table 5.1 and figure 5.1). For a physiologically relevant PI(4,5)P$_2$ concentration of 0.7 mol%, we see a low B_{max} of 23±1 ng/cm^2. This further reinforces the distinct role of PS and PI(4,5)P$_2$ in membrane association with the weak PTEN-PS interactions drawing large amounts of PTEN to the bilayer which is subsequently followed by strong specific interactions of PTEN with PI(4,5)P$_2$. It has been shown that the N-terminal PI(4,5)P$_2$ binding domain is specific for PI(4,5)P$_2$ and shows a weak affinity for PI(3,4)P$_2$, PI(3,5)P$_2$ and PI(3,4,5)P$_3$ [5], unlike the behavior of proteins like MARCKS where the interaction is merely electrostatic [166]. The ability of an intrinsically disordered region of PTEN to locate and specifically bind to PI(4,5)P$_2$ is intriguing and something we hope to address in our structural investigations, both experimental and computational.

5.2.3 Binding to PS:PI(4,5)P$_2$

The SPR data for *wt* PTEN binding to membranes containing both PS and PI(4,5)P$_2$ is the only instance where the equilibrium binding analysis clearly indicated a concentration dependence with two distinct K_ds (see figure 5.1). If PTEN bound to PS and PI(4,5)P$_2$ in a non-competitive and independent manner, we would
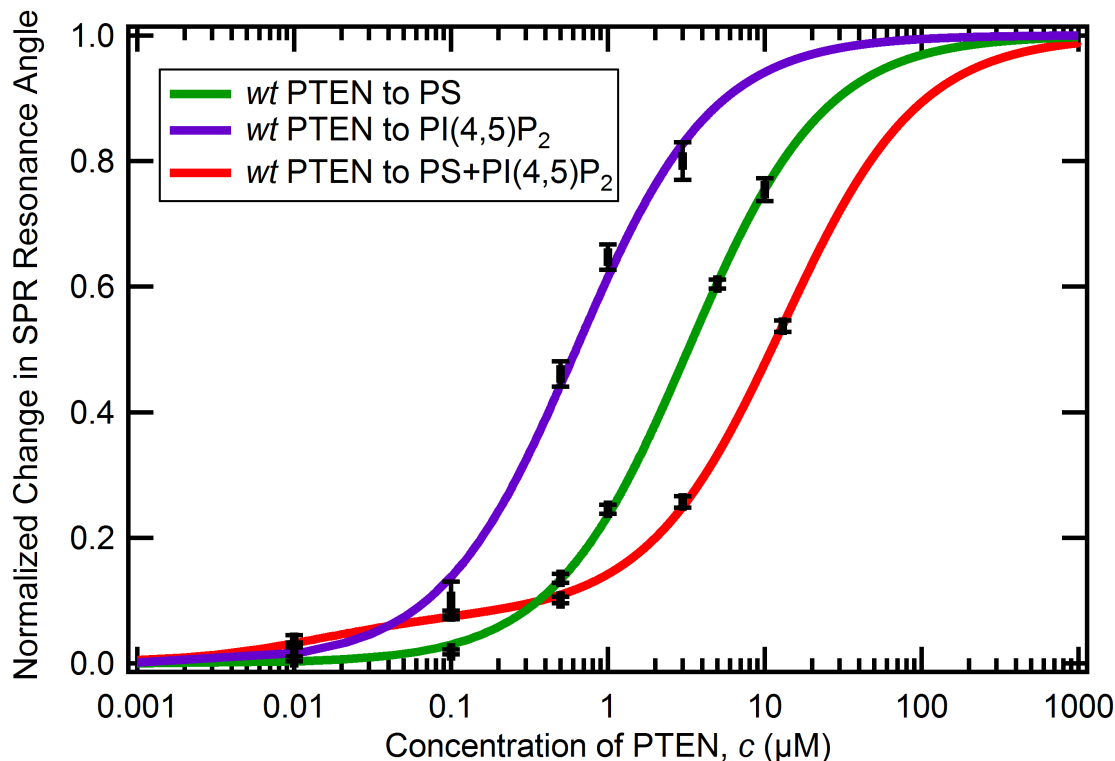
Figure 5.1: Equilibrium binding analysis of *wt* PTEN to PS-, PI(4,5)P$_2$- and PS+PI(4,5)P$_2$-bearing lipid bilayers, assuming a 1:1 Langmuir model. While the curves corresponding to association with PS (green) and PI(4,5)P$_2$ (purple) are unimodal, the curve for association to membranes containing both PS and PI(4,5)P$_2$ lipid species (red) cannot be fit with a 1:1 Langmuir model.

expect the K$_d$s obtained from the bimodal fit to match the K$_d$s for PTEN to the individual lipids. However, we observe an affinity that is increased by an order with K$_{d_1}$=0.04±0.01 µM as compared to K$_d^{PI(4,5)P_2}$=0.4±0.1 µM (see table 5.1). This is indicative of a cooperative binding effect where PS and PI(4,5)P$_2$ synergistically bind to *wt* PTEN. The weaker binding constant obtained from the bimodal fit, K$_{d_2}$, could not be precisely measured due to a lack of high-concentration data but a lower bound of 5 µM can be set.

5.2.4 Binding to DPPI(4,5)P$_2$

It has been assumed in the literature that the stoichiometry of *wt* PTEN:PI(4,5)P$_2$ bound complexes is 1:1. We tested this assumption by comparing the K$_d$ for *wt* PTEN binding to PI(4,5)P$_2$ in a fluid phase bilayer and in a gel phase bilayer. If the stoichiometry is indeed 1:1, then the binding constants obtained in the two situations should be identical. This is because the average PI(4,5)P$_2$-PI(4,5)P$_2$ dis-
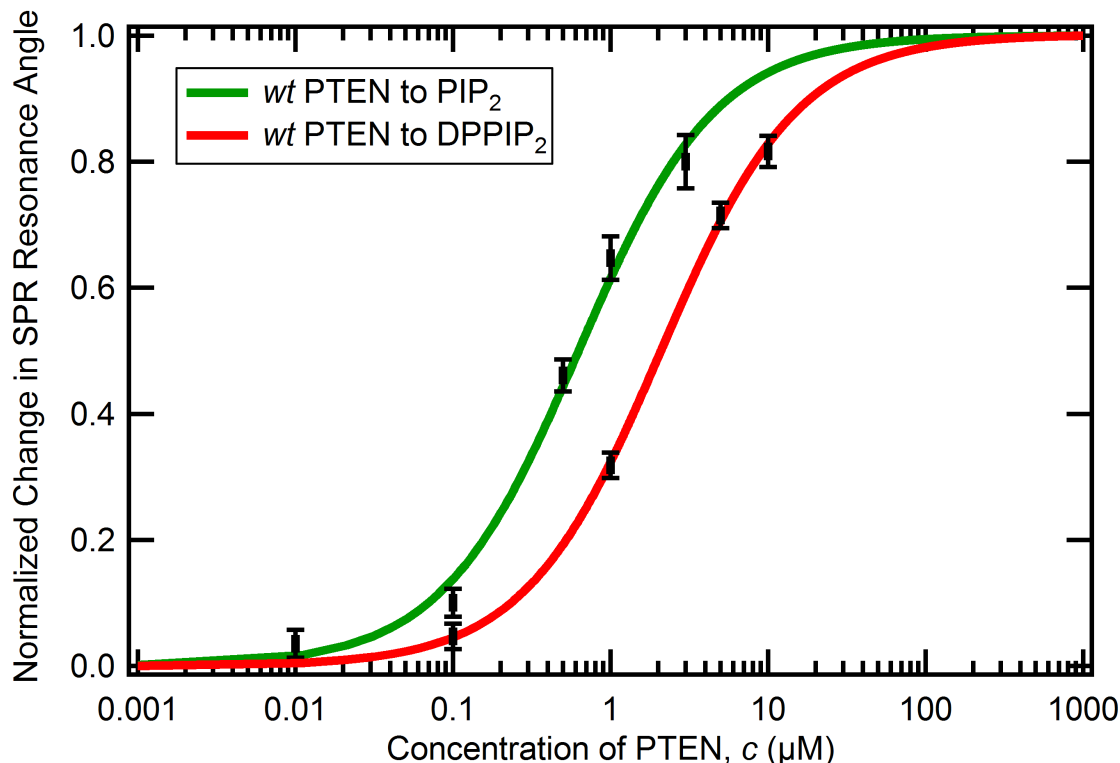
Figure 5.2: The effect of bilayer phase on the dissociation constant of *wt* PTEN to PI(4,5)P$_2$-bearing lipid membranes. The green and red curves correspond to the equilibrium binding analysis of *wt* PTEN to PI(4,5)P$_2$-bearing bilayers that are in the fluid and gel phase, respectively.

tance is larger than the dimensions of the protein, therefore requiring the lipid to diffuse in the plane of the bilayer in order to satisfy a multi-lipid-per-protein stoichiometry. All the aforementioned binding data were obtained using lipids with unsaturated chains which results in a fluid phase membrane at room temperature. To test the binding stoichiometry, we performed a set of experiments with lipids that had saturated dipalmitoyl chains that have a gel to fluid transition temperature above room temperature [T$_m$(DPPC)=41 °C]. We observed a 5-fold decreased affinity of PTEN to PI(4,5)P$_2$ in a gel phase bilayer as opposed to a fluid phase bilayer [K$_d^{PI(4,5)P_2}$(fluid)=0.4±0.1 μM vs. K$_d^{PI(4,5)P_2}$(gel)=1.9±0.3 μM] (see table 5.1 and figure 5.2). This indicates a stoichiometry that deviates from the 1:1 Langmuir model. In a gel phase bilayer, the two orders of magnitude lower lipid diffusivity adversely impacts PTEN's ability to attract multiple PI(4,5)P$_2$, thereby adversely impacting its binding constant. It is unclear if multiple PI(4,5)P$_2$ lipids are simultaneously bound to the PI(4,5)P$_2$ binding module (PBM) or if there are indeed multiple PI(4,5)P$_2$ binding sites located across the protein. We hope to address this
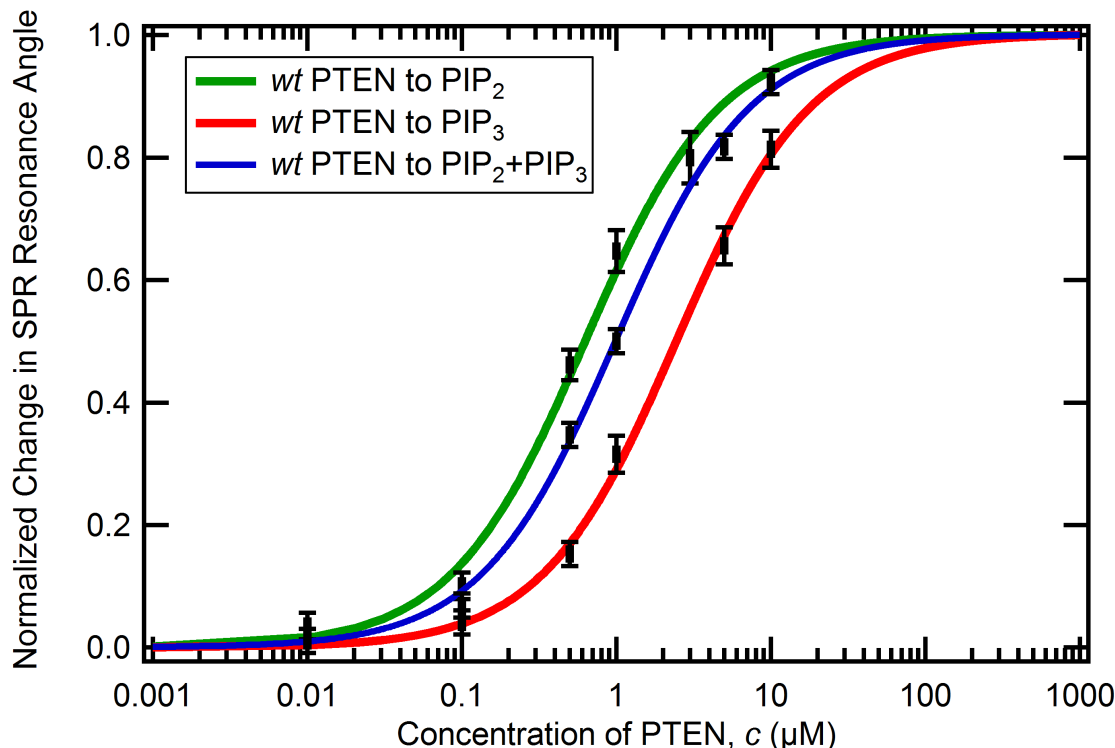
Figure 5.3: Equilibrium binding analysis of *wt* PTEN to lipid bilayers composed of $PI(4,5)P_2$ (green), $PI(3,4,5)P_3$ (red) and both $PI(4,5)P_2$ and $PI(3,4,5)P_3$ (blue). We see that the binding to the two lipid species is independent and non-competitive.

issue with our *in silico* work described in chapter 9. Determining the exact stoichiometry experimentally is complicated by the observation, through fluorescence experiments, that PTEN association can result in the clustering of $PI(4,5)P_2$ (Gericke et al., unpublished data). This precludes the use of standard techniques such as isothermal titration calorimetry (ITC), due to the difficulty in disentangling the enthalpy of aggregation from the enthalpy of association.

5.2.5 Binding to $PI(3,4,5)P_3$ and $PI(4,5)P_2{:}PI(3,4,5)P_3$

We also studied the interaction of *wt* PTEN to $PI(3,4,5)P_3$, its catalytic substrate (see table 5.1 and figure 5.3). We obtained K_ds of 2.4 ± 0.2 µM for *wt* PTEN to $PI(3,4,5)P_3$ and 1.0 ± 0.1 µM for *wt* PTEN to stBLMs with equal amounts of $PI(4,5)P_2$ and $PI(3,4,5)P_3$. Since *wt* PTEN is catalytically active, we cannot exclude the possibility that PTEN converts $PI(3,4,5)P_3$ to $PI(4,5)P_2$ during the experiment. As a result, we consider the K_d obtained from the interaction of the catalytically inactive C124S PTEN mutant to $PI(3,4,5)P_3$ (see section 5.4.2) as a more reliable measure than the *wt* PTEN experiments.

5.3 H93R PTEN Binding Kinetics

Table 5.2: SPR binding kinetics data for H93R PTEN association with lipid membranes composed of PS, PI(4,5)P$_2$ and both PS and PI(4,5)P$_2$.

System	Composition	K_d(μM)	B_{max}(ng/cm^2)
PC:PS:chol	70:30:5	3.1±0.3	162±17
PC:PI(4,5)P$_2$	97.8:2.2	1.3±0.2	64±6
PC:PS:PI(4,5)P$_2$:chol	68.8:28.6:2.6:5	0.7±0.1	191±23

H93R PTEN is a mutant that exhibits markedly decreased phosphatase activity [6], as compared to *wt* PTEN, even though the mutation is spatially separated by 10 Å from the active site, as per the crystal structure (see section 1.8 for more details). This may be due, in large part, to an altered membrane association which we sought to probe with the following SPR experiments.

5.3.1 Binding to PS, PI(4,5)P$_2$ and PS:PI(4,5)P$_2$

H93R PTEN exhibits a 4-fold increased affinity to PS-containing membranes [K_d(H93R)=3.1±0.3 μM; K_d(*wt*)=11.9±0.4 μM] but a 3-fold decreased affinity to PI(4,5)P$_2$-containing membranes [K_d(H93R)=1.3±0.2 μM; K_d(*wt*)=0.4±0.1 μM] (see table 5.2). This is surprising as the H93R mutation is in the phosphatase domain (PD) while the PS and PI(4,5)P$_2$-binding sites are believed to be located in the C2 domain and the PI(4,5)P$_2$ binding module (PBM), respectively. When we study H93R PTEN association with membranes containing both PS and PI(4,5)P$_2$ lipids, we get a K_d of 0.7±0.1 μM (see table 5.2). Although this is 2-fold stronger than the affinity of H93R PTEN to PI(4,5)P$_2$ alone, there is clearly an abolition of the cooperative binding we observed for *wt* PTEN.

All these results, together with the lowered phosphatase activity, are part of a large body of evidence suggesting that PTEN is a very plastic protein. Point mutations that are spatially separated from the membrane binding domains by tens of Ångstroms are still able to alter the protein's association with the membrane. These changes in activity and binding affinities may well be accompanied by conformation changes, as described by the structure-function paradigm, which we hope to study with the neutron reflectivity experiments described in section 7.

Table 5.3: SPR binding kinetics data for C124S PTEN association with lipid membranes composed of PS, PI(4,5)P$_2$, PI(3,4,5)P$_3$ and both PI(4,5)P$_2$ and PI(3,4,5)P$_3$.

System	Composition	K_d(µM)	B_{max}(ng/cm^2)
PC:PS:chol	70:30:5	2.9±0.3	273±17
PC:PI(4,5)P$_2$	97.8:2.2	0.32±0.03	99±17
PC:PI(3,4,5)P$_3$	97.9:2.1	0.12±0.03	191±17
PC:PI(4,5)P$_2$: PI(3,4,5)P$_3$	98:1.8:0.2	0.26±0.01	127±2
	98:1:1	0.13±0.01	152±1
	98:0.2:1.8	0.12±0.01	218±2

5.4 C124S PTEN Binding Kinetics

In C124S PTEN, the mutation of an active-site cysteine results in a complete loss of phosphatase activity (see section 1.8 for more details). We used this catalytically inactive mutant to study the interaction of PTEN to the PI(3,4,5)P$_3$ substrate, as well as to the PC and PI(4,5)P$_2$ lipids, for comparison with *wt* PTEN.

5.4.1 Binding to PS and PI(4,5)P$_2$

The mutation in the active-site results in an unexpected 4-fold increased affinity for PS-containing membranes, similar to the H93R mutation [K_d(C124S)=2.9±0.3 µM; K_d(*wt*)=11.9±0.4 µM] (see table 5.3). There is only a minor change in the strength of the association with PI(4,5)P$_2$, indicating that this mutation, unlike H93R, does not affect the PI(4,5)P$_2$ binding module [K_d(C124S)=0.32±0.03 µM; K_d(*wt*)=0.4±0.1 µM] (see table 5.3).

5.4.2 Binding to PI(3,4,5)P$_3$

As described in section 5.2.5, the catalytically inactive C124S PTEN provides us with the perfect opportunity to quantify the interaction of PTEN with PI(3,4,5)P$_3$, without its subsequent dephosphorylation as a result of PTEN's catalytic activity. C124S PTEN has a 3-fold stronger affinity for PI(3,4,5)P$_3$ [K_d=0.12±0.03 µM] (see table 5.3) than for PI(4,5)P$_2$ [K_d=0.32±0.03 µM] – a value that is 20-fold stronger than the dissociation constant we obtained for *wt* PTEN association with PI(3,4,5)P$_3$ [K_d=2.4±0.2 µM], reaffirming our concern that the *wt* PTEN data was compromised due to the protein's catalytic activity.

5.4.3 Binding to PI(4,5)P$_2$:PI(3,4,5)P$_3$

To examine the possibility that PTEN has common binding sites for associating with both PI(4,5)P$_2$ and PI(3,4,5)P$_3$, we measured the affinity of C124S PTEN to membranes with three different compositions: PI(4,5)P$_2$:PI(3,4,5)P$_3$ = 1.8:0.2, 1:1 and 0.2:1.8 (see table 5.3). If the binding constants to the dual anionic species range between those of the individual binding constants (as the relative proportions of the two PIP components are varied), then we have proof of independent association of PTEN to PI(4,5)P$_2$ and PI(3,4,5)P$_3$.

When the system is dominated by PI(4,5)P$_2$ [PI(4,5)P$_2$:PI(3,4,5)P$_3$=1.8:0.2], the dissociation constant [K$_d$=0.26±0.01 µM] is comparable to the value obtained for binding to PI(4,5)P$_2$ individually [K$_d$=0.32±0.03 µM]. Similarly, when PI(3,4,5)P$_3$ is the majority component [PI(4,5)P$_2$:PI(3,4,5)P$_3$=0.2:1.8] the affinity [K$_d$=0.12±0.01 µM] is identical for association solely to PI(3,4,5)P$_3$ [K$_d$=0.12±0.03 µM]. When PI(4,5)P$_2$:PI(3,4,5)P$_3$=1:1, the interaction is dominated by the association to PI(3,4,5)P$_3$ as evidenced by a K$_d$ of 0.13±0.01 µM. This is consistent with an independent and non-competitive association of PTEN to PI(4,5)P$_2$ and PI(3,4,5)P$_3$.

5.5 Truncated PTEN Binding Kinetics

Table 5.4: SPR binding kinetics data for truncated PTEN association with lipid membranes composed of PS, PI(4,5)P$_2$ and both PS and PI(4,5)P$_2$.

System	Composition	K$_d$(µM)	B$_{max}$(ng/cm^2)
PC:PS:chol	70:30:5	2.5-4.9	348-563
PC:PI(4,5)P$_2$	97.8:2.2	0.77±0.07	81±3
PC:PS:PI(4,5)P$_2$:chol	68.8:28.6:2.6:5	0.9±0.2	325±35

Unlike the H93R PTEN and C124S PTEN disease-related mutants, the truncated PTEN is an artificial construct that was suitable for crystallization and subsequent structural determination by X-Ray crystallography [4]. Binding assays with this mutant would serve the dual purpose of studying the role of the disordered segments of the protein in membrane association as well as establishing concentrations and conditions amenable for subsequent neutron reflectivity experiments.

5.5.1 Binding to PS, PI(4,5)P$_2$ and PS:PI(4,5)P$_2$

The truncated PTEN mutant was prone to aggregation at high protein concentrations (> 3 µM), thereby limiting the concentration range over which we could

perform the SPR measurements. While this prevented a precise determination of the dissociation constant for truncated PTEN association with PS, we were able to set lower and upper bounds using the methodology described in section 3.3.7. Similar to the H93R PTEN and C124S PTEN mutants, the truncated PTEN exhibits a 3-fold strengthened association to PS-containing membranes as compared to *wt* PTEN [$2.5 \leq K_d$(truncated)≤ 4.9 μM; $K_d(wt)=11.9\pm0.4$ μM]. The truncation of a loop in the C2 domain and the entire C-terminal tail increases the net charge of the protein by +14. Combined with the loss of unfavorable interactions where the tail physically occludes membrane association, the two effects may explain the enhanced affinity of the truncated PTEN to PS lipids.

The truncated PTEN mutant is missing the first 6 residues of the $PI(4,5)P_2$ binding module (PBM). Consequently, it is not surprising to observe a 2-fold reduced affinity of the truncated mutant to $PI(4,5)P_2$ containing membranes, as compared to *wt* PTEN [K_d(truncated)$=0.77\pm0.07$ μM; $K_d(wt)=0.4\pm0.1$ μM]. This is consistent with other work strongly suggesting that residues 1-14 play a dominant role in the interaction [68, 16], hence earning them the title '$PI(4,5)P_2$ binding module'. Similar to H93R PTEN, we see the loss of the synergistic binding to membranes containing both PS and $PI(4,5)P_2$ lipids ($K_d^{PS+PI(4,5)P_2}= 0.9\pm0.2$ μM).

5.6   Discussion

Cytosolic PTEN performs a critical tumor suppressor function through interactions with the inner leaflet of the plasma membrane. It is believed that there are different pools of PTEN, only a small fraction of which can associate with the membrane at any given time [167]. One of the keys to understanding PTEN's regulation and activation, as well as its loss of catalytic activity upon mutation, is quantifying the contribution of individual anionic lipid species to the overall binding affinity.

We compared the binding affinities of *wt* PTEN, H93R PTEN, C124S PTEN and a truncated PTEN to the anionic lipids PS, $PI(4,5)P_2$ and $PI(3,4,5)P_3$, both individually as well as in mixtures. *wt* PTEN has the weakest affinity for PS while all the mutants exhibit a 3-fold stronger association. For the truncated PTEN, this can be explained by the increased positive charge of the protein, relative to the *wt*, and the absence of conformations where the C-terminal tail obstructs membrane binding. Both *wt* and C124S PTEN show the strongest affinity for $PI(4,5)P_2$. The truncated PTEN is missing a portion of the N-terminal $PI(4,5)P_2$ binding module (PBM) which could be the reason for its 2-fold decreased affinity. *wt* PTEN is also unique in the synergistic binding it displays for membranes containing both the PS and $PI(4,5)P_2$ anionic lipids. This cooperative effect is absent for all the mutants we studied and, together with H93R PTEN's deviation from the behavior of the *wt* in every respect, is a strong indicator of the plasticity of PTEN wherein point mutations spatially separated from key binding sites can still have a dramatic

impact upon membrane association.

By observing a 5-fold decreased affinity of *wt* PTEN to PI(4,5)P$_2$ in a gel phase bilayer, as opposed to a fluid phase bilayer, we have evidence that suggests that the stoichiometry of PTEN binding to PI(4,5)P$_2$ is not 1:1, as is currently assumed to be the case. It is unclear if the additional PI(4,5)P$_2$ lipids also bind to the PBM or if there are additional binding sites located elsewhere along the protein-membrane interface. As the experimental determination of the stoichiometry is difficult to determine, we have turned to molecular dynamics simulations to provide an *in silico* estimation of the stoichiometry (see chapter 9).

The catalytically inactive C124S PTEN mutant afforded us the opportunity to measure the affinity of PTEN for PI(3,4,5)P$_3$ without the constant dephosphorylation of PI(3,4,5)P$_3$ to PI(4,5)P$_2$ adversely affecting the experimental results. C124S PTEN exhibits a 3-fold stronger affinity for PI(3,4,5)P$_3$ than for PI(4,5)P$_2$ and the binding to each occurs in a non-competitive and independent manner, as is evident from binding assays to membranes containing both lipid species.

Our body of work provides quantitative experimental validation of a model of PTEN association wherein PTEN is initially electrostatically attracted to the PS lipids in the membrane which, despite their weak affinity, are able to draw a large amount of PTEN to the membrane interface by virtue of their significant membrane composition ($\sim$ 30 mol% of the inner leaflet of the plasma membrane is composed of PS) and their ability to alter the electrostatic potential experienced by PTEN in solution. This then allows for the PBM to specifically locate and bind to PI(4,5)P$_2$, which accounts for less than 1 mol% of the membrane. Finally, with both tether points anchoring the protein to the membrane, the catalytic site binds and dephosphorylates its substrate PI(3,4,5)P$_3$ to PI(4,5)P$_2$, thereby fulfilling its tumor suppressor function by shutting of the Akt pathway that signals cell growth and survival.

Chapter 6

Analysis of the Binding Kinetics

6.1 Introduction

In chapter 5.2.4, we examined the impact of bilayer fluidity on the association of *wt* PTEN to PI(4,5)P$_2$. Equilibrium analysis of the SPR data provided us with a dissociation constant for *wt* PTEN binding to a gel phase bilayer bearing PI(4,5)P$_2$ that was 5-fold larger than for a fluid phase bilayer bearing PI(4,5)P$_2$. This led us to conclude that the stoichiometry of PTEN association with PI(4,5)P$_2$ was not 1:1. However, this is only half the story. Equilibrium analysis focuses on the start and end points of the protein binding kinetics and ignores the path the kinetics follow in between. A closer examination of the data revealed marked differences in the binding kinetics as well.

6.2 The 'Overshoot' Effect

Figure 6.1 (A) depicts the binding kinetics observed in a standard SPR experiment. When a given concentration of protein is added to the SPR cell, the reflectivity minimum (SPR resonance angle, in pixels) increases by an amount proportional to the density of membrane-bound protein. If we examine the time course, there is a sharp increase in the pixel count followed by saturation as the association reaction reaches an equilibrium. As long as there is no alteration in the state of the system, the signal remains steady and unchanged.

If we examine the kinetics of PTEN association with a PC:PI(4,5)P$_2$ membrane, be it that of the *wt* or any mutant other than C124S PTEN, we see something very different [see figure 6.1 (B)]. Up to a characteristic concentration of 0.5 µM, the kinetics follows the expected time course. Above this concentration, once protein is added to the cell the SPR minimum increases and reaches a maximum within 15 minutes. Unlike in the standard situation, the signal is no longer steady in the long time limit. Instead, we see an exponential decrease similar to what we would
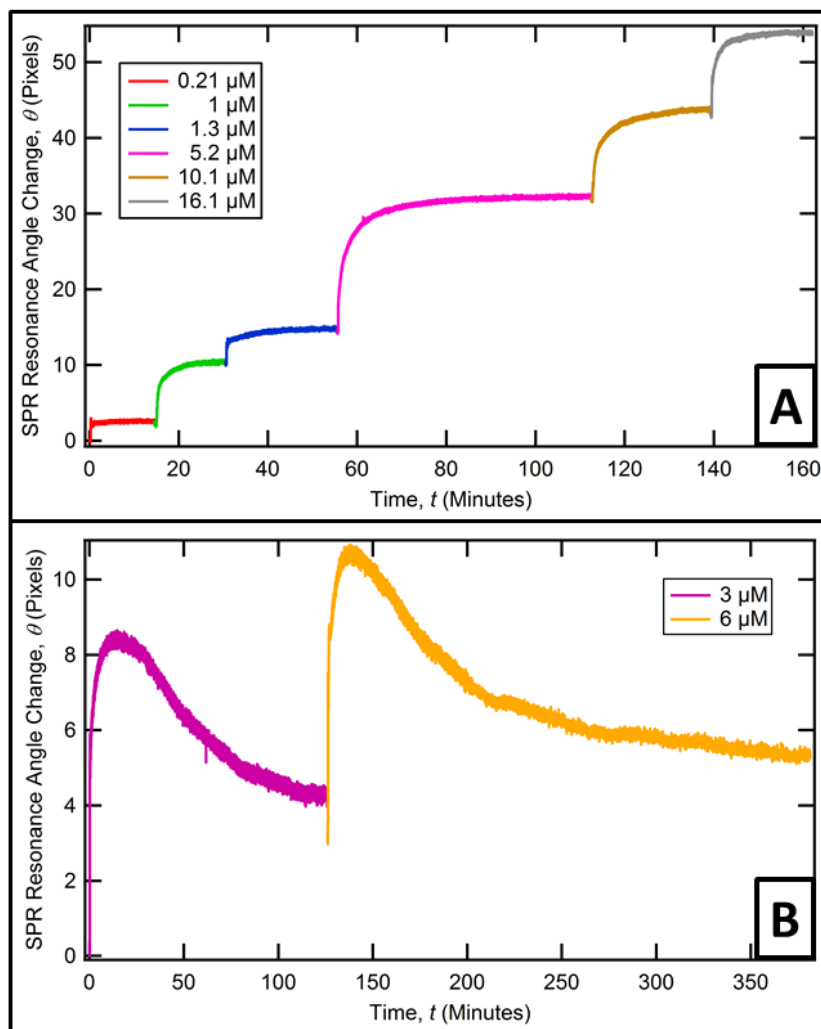
Figure 6.1: SPR Binding Kinetics: (A) Standard SPR binding curves where the addition of a given concentration of protein to the cell containing the bilayer is accompanied by a quick increase in the SPR resonance angle, followed by saturation. (B) When we measure the binding of *wt* PTEN, H93R PTEN or truncated PTEN to PI(4,5)P$_2$, we see normal binding curves up to a characteristic concentration, usually 0.5 μM. Above that concentration, once protein is added the kinetics initially follows the same rise and saturation behavior but is followed by an exponential decay in the value of the SPR angle.

observe with a rinse of the cell that removes non-specifically bound protein. Upon adding a higher concentration, we once again observe the same 'overshoot' behavior of an increase in the SPR angle to a maximum, followed by an exponential decay to a level equal to or higher than the previous baseline.

If we move from a binary PC:PI(4,5)P$_2$ system to a ternary PC:PS:PI(4,5)P$_2$

99
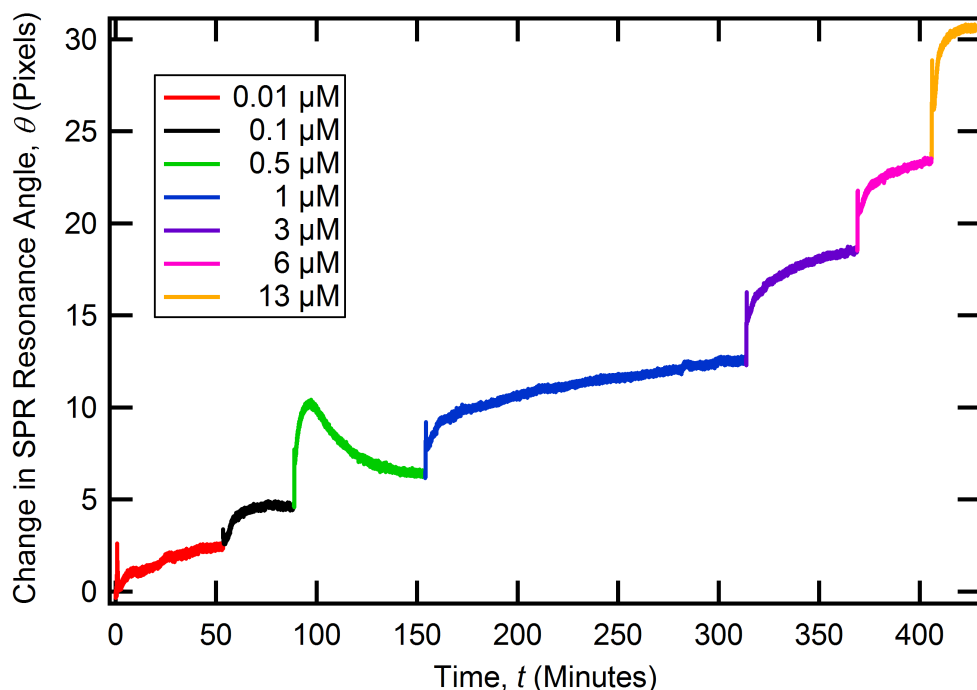
Figure 6.2: Binding kinetics time-course for *wt* PTEN association with a PC:PS:PI(4,5)P$_2$ lipid bilayer. We see normal binding kinetics at every step of the measurement, except for the characteristic 0.5 μM concentration.

system, we observe something unique (see figure 6.2). At protein concentrations below 0.5 μM, we observe normal binding kinetics. Upon adding the 0.5 μM protein sample, we see the overshoot effect. And above that concentration, we once again observe normal binding kinetics. It appears as though binding to PI(4,5)P$_2$ dominates in the low protein concentration regime (due to the stronger affinity) while binding to PS dominates in the high concentration regime. In fact, if this data is fit to a two-component binding model, the larger K$_d$ is consistent with the K$_d$ for *wt* PTEN association with a PC:PS membrane.

Finally, if we study the kinetics of *wt* PTEN association with a DPPC:DPPI(4,5)P$_2$ bilayer that is in a gel phase at room temperature, we see normal binding kinetics with no overshoot effect (see figure 6.3).

6.3   Discussion

Each piece of data presented above showcases a different facet of this complicated interaction process. It is worth noting that this data is unlikely to be reproduced by any commercial SPR setup due to the long timescales involved. i.e., the use of an SPR instrument that constantly flows protein over the bilayer for 15 minutes
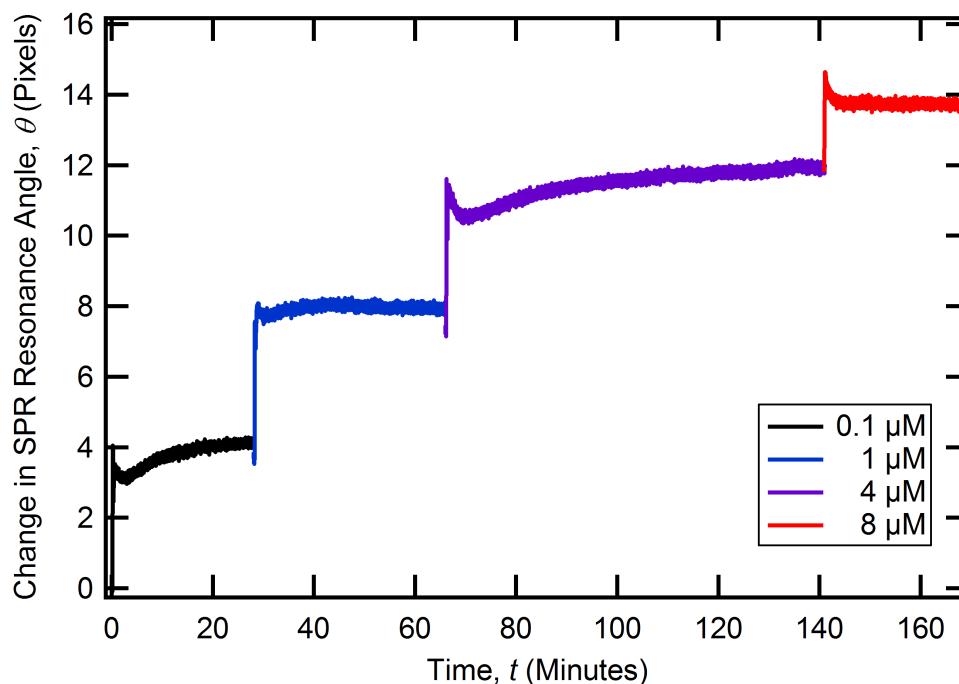
Figure 6.3: *wt* PTEN association with gel-phase membranes containing PI(4,5)P$_2$ display standard binding kinetics with no sign of the overshoot effect.

would use a prohibitorily large volume of protein. Any model that tries to explain the experimentally observed binding kinetics has to address the following questions:

1. What is the underlying molecular mechanism that results in the overshoot?

2. What is special about the 0.5 μM characteristic concentration at which the overshoot effect is first observed?

3. Why do subsequent concentrations above 0.5 μM also result in an overshoot in the PC:PI(4,5)P$_2$ binary system?

4. Why do subsequent concentrations above 0.5 μM NOT result in an overshoot in the PC:PS:PI(4,5)P$_2$ ternary system?

5. Why is the overshoot not observed in the DPPC:DPPI(4,5)P$_2$ system?

6. Why is the overshoot not observed for C124S PTEN binding to PI(4,5)P$_2$?

Before we attempt to build a model, let us examine the conclusions that can be drawn from the data and standard models that could explain the observations:

1. **Protein aggregation model:** A decrease in the value of the SPR reflectivity minimum (SPR resonance angle) is due to a drop in the refractive index of

material at the interface. Naively, this would imply that the overshoot effect corresponds to a loss of material from the interface, most likely that of the bound protein. One explanation would be a PI(4,5)P$_2$-promoted aggregation of PTEN that results in aggregates unbinding from the bilayer and returning to the bulk. However, given that the K$_d$ of *wt* PTEN to PI(4,5)P$_2$ is 0.4 µM, the newly available binding site would be quickly bound by a non-aggregated PTEN. This would continue till all the protein was aggregated and consequently no protein would ever be bound to the bilayer at any concentration, in the long time scale. Also, no detectable aggregation has been experimentally observed and protein can be re-used from experiment to experiment with no shift in the characteristic overshoot concentration to lower values. This strongly suggests that the aggregation model is not an accurate description of the overshoot binding kinetics.

2. **PI(4,5)P$_2$ extraction model:** Another explanation would be that PTEN binds to PI(4,5)P$_2$ and pulls it out of the bilayer. This would increase the defect density of the bilayer, which is not observed experimentally. More importantly, this would mean that the number of available binding sites would keep dropping. But once we observe the overshoot effect and add a higher concentration, the signal returns to the previous baseline (or slightly higher) indicating no decrease in the number of available binding sites. Consequently, this model too is inconsistent with the experimental observations.

3. **Role of lipid-lipid interactions:** The fact that the fluidity of the bilayer dictates whether the overshoot effect is observed or not is a very powerful criteria that rules out many plausible mechanisms. It suggests that instead of focusing on protein-protein interactions (such as in the aggregation model) or protein-lipid interactions (such as in the PI(4,5)P$_2$ extraction model) we need to base the model on lipid-lipid interactions and their alteration upon protein association.

6.4 Stoichiometry-Based Overshoot Model

Based on all of the data, both in terms of binding kinetics and equilibrium data analysis, we have devised the following model that best explains the observations. At a low concentration of PTEN added to a PI(4,5)P$_2$-bearing membrane, there is both singly-bound and multiply-bound PTEN [see figure 6.4 (A)]. As we increase the concentration of protein, the competition for PI(4,5)P$_2$ results in the ejection of singly-bound PTEN [see figure 6.4 (B)]. Eventually, every PTEN molecule is bound to multiple PI(4,5)P$_2$ lipids, at a yet to be determined stoichiometry. This explains both the overshoot effect as well as the existence of a stable level that the SPR
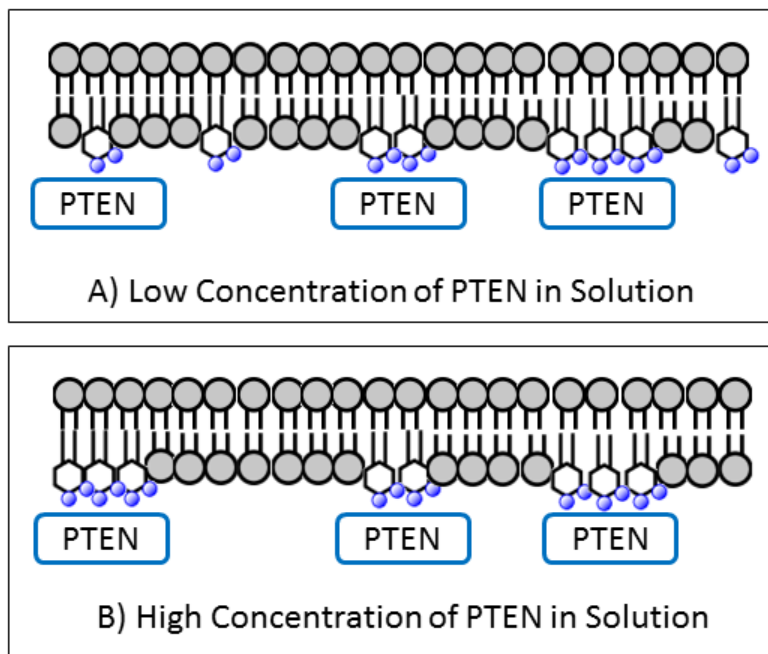
Figure 6.4: Overshoot Hypothesis for a Fluid Bilayer: (A) At low concentrations of PTEN in solution, there are singly-bound and multiply-bound $PI(4,5)P_2$ molecules. (B) But as the concentration of PTEN is increased, multiply-bound PTEN dominate the binding landscape.

resonance angle returns to, upon the addition of subsequent protein concentrations above the characteristic 0.5 μM.

If the system is a gel-phase bilayer, then at both low [see figure 6.5 (A)] and high [see figure 6.5 (B)] concentrations we only have singly-bound PTEN to $PI(4,5)P_2$. This is because the low diffusivity of lipids in the membrane prevents a PTEN molecule from drawing/attracting multiple $PI(4,5)P_2$ towards it, at least on the timescale of the experiment. This explains the absence of the overshoot effect in the $DPPC:DPPI(4,5)P_2$ system.

Depending on the stoichiometry, there could be multiple bound states. For example, if the stoichiometry of PTEN to $PI(4,5)P_2$ is 1:3, we could have 1:1, 1:2 and 1:3 bound PTEN, apart from free PTEN in solution, with interconversion rates between all four of these states. Any increase in the stoichiometry can make the model very complicated, very quickly.

A simple model would assume a saturation stoichiometry of 1:2. If F represents free PTEN in solution, P an unbound $PI(4,5)P_2$ lipid, B a 1:1 PTEN:$PI(4,5)P_2$ bound state and D a 1:2 PTEN:$PI(4,5)P_2$ bound state, the mathematical model
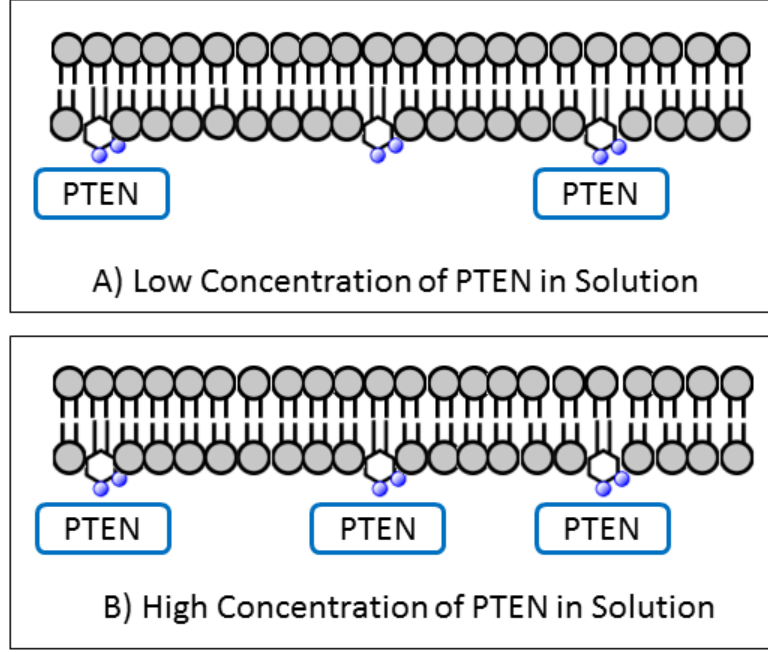
Figure 6.5: Overshoot Hypothesis for a Gel Phase Bilayer: At (A) low or (B) high concentrations of PTEN in solution, there is only singly-bound PI(4,5)P$_2$ as the slow diffusivity of lipids prevents any PTEN-driven aggregation or domain-formation.

that describes the system is as follows:

$$F + P \underset{k_b'}{\overset{k_b}{\rightleftharpoons}} B \tag{6.1}$$

where a free PTEN molecule binds to a free PI(4,5)P$_2$ lipid to form a singly-bound state and

$$B + B \underset{k_d'}{\overset{k_d}{\rightleftharpoons}} D + F \tag{6.2}$$

where two singly-bound states combine to form a doubly-bound state thereby ejecting a free PTEN molecule from the protein-bilayer interface.

Figure 6.6 depicts the ability of this model to reproduce the overshoot on the same timescales as is experimentally observed. Initially, PTEN binds in a 1:1 fashion with PI(4,5)P$_2$. Once singly-bound PTEN is formed, doubly-bound PTEN is slowly produced. At some critical time point, dependent on the initial concentrations and the four interconversion rates, the concentration of singly bound PTEN begins to drop exponentially, increasing the amount of PTEN in solution. Even though doubly-bound PTEN is continuously being produced, its contribution to the refractive index at the interface is less than that of PTEN singly-bound to the same

104
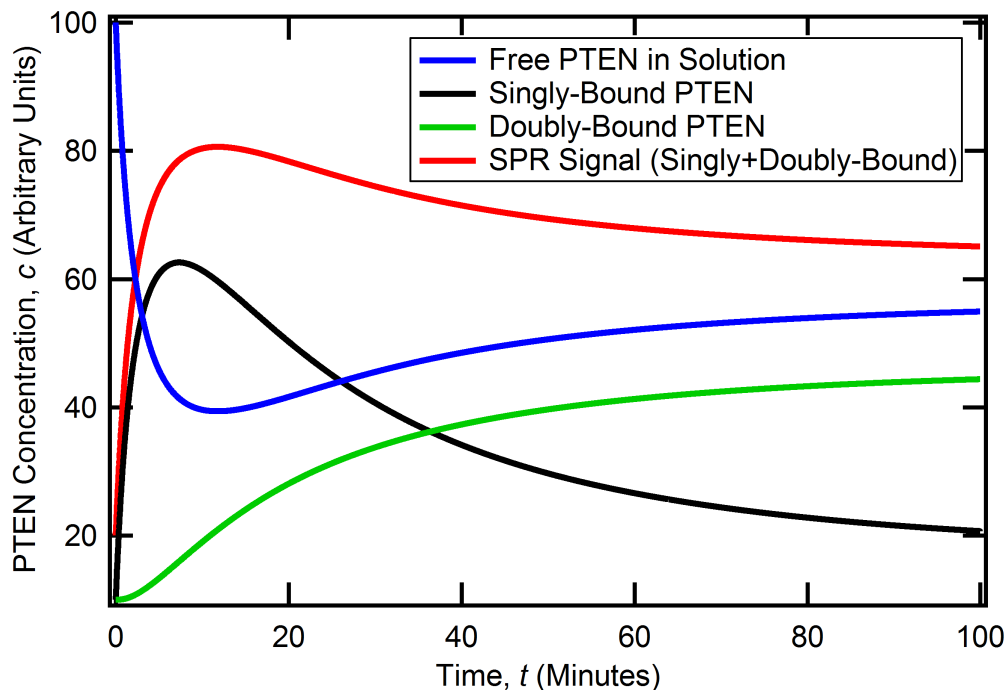
Figure 6.6: Overshoot Kinetics Model: It is possible to recreate the binding kinetics we observe during the overshoot effect with a simple model that assumes that PTEN can bind up to two PI(4,5)P$_2$ molecules. Assuming some initial conditions, we can model the concentration of PTEN in solution (blue), singly-bound PTEN (black), doubly-bound PTEN (green) as well as the observed SPR signal which is the net protein bound to the membrane (the sum of the singly-bound and doubly-bound contributions, shown in red).

number of PI(4,5)P$_2$ lipids. Therefore, the sum of the singly-bound and doubly-bound PTEN populations, which is what the SPR detects, also drops exponentially producing the overshoot effect, though at a rate that is lower than that of singly-bound PTEN alone.

We caution that this model may not be unique in its ability to describe the overshoot effect and the simplistic 1:2 PTEN:PI(4,5)P$_2$ stoichiometry that was assumed could underestimate the true binding ratio. In fact, we were unable to determine an appropriate combination of rate constants that allowed for multiple overshoots to occur. But we are confident that the overshoot effect is a real physical phenomenon and not an experimental artifact. Our model provides one possible mechanism for PTEN binding to PI(4,5)P$_2$ and we are currently seeking means of verifying it independently. We are also performing all-atom MD simulations of *wt* PTEN binding to a PC:PS:PI(4,5)P$_2$ membrane (as described in chapter 9) with the aim to determine the stoichiometry of PTEN bound to PI(4,5)P$_2$.

Chapter 7

Neutron Reflectivity Analysis of Membrane-Associated PTEN

7.1 Introduction
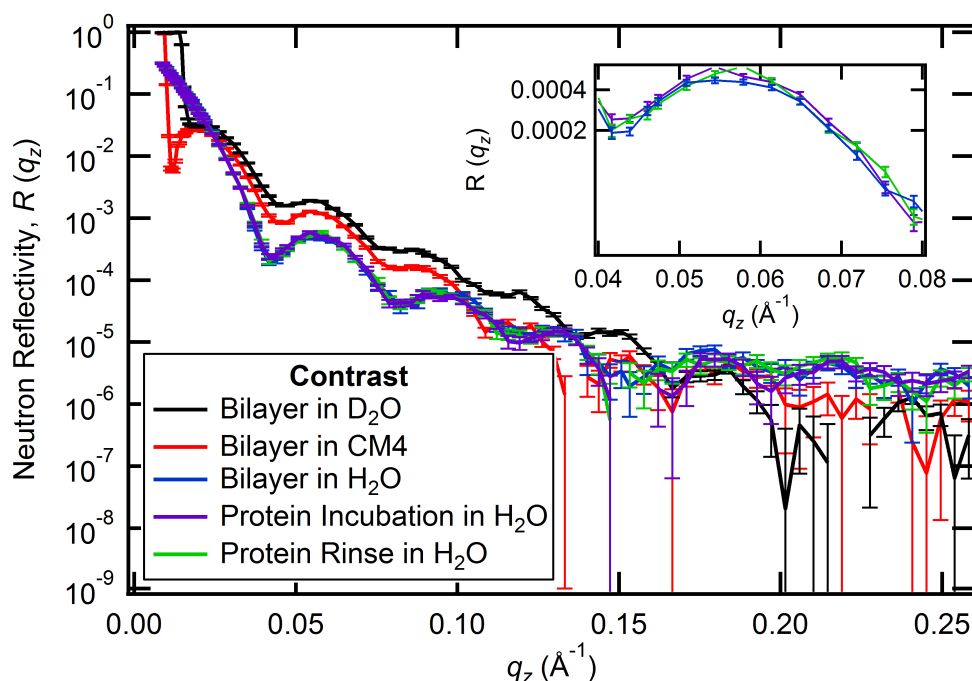
Figure 7.1: Neutron reflectivity profiles for H93R PTEN bound to a DOPC:DOPS:CHOL=70:30:3 HC18 stBLM. **Inset:** A close-up of the water scans to show the contribution of bound PTEN.

The crystal structure of a truncated PTEN mutant is our only insight into the

three-dimensional folded structure of the protein in solution [4]. No structure for membrane-bound PTEN exists. Our lab has perfected the technique of performing neutron reflectivity measurements on planar stBLMs to ascertain the structural properties of the bilayer, before and after the addition of protein, as well as that of protein bound to the membrane, irrespective of the penetration depth of the protein into the membrane [8, 110, 136, 164, 168, 169, 170, 171, 172]. While the primary goal of the SPR kinetic measurements was to quantify the affinity of PTEN with various anionic lipid species and the impact of mutations on these interactions, they also served to define the optimal conditions under which neutron reflectivity measurements of the PTEN-membrane system could be performed. With this information, we studied four systems: 1) H93R PTEN bound to PS, 2) *wt* PTEN bound to PS, 3)*wt* PTEN bound to PS+PI(4,5)P$_2$ and 4) the truncated crystal structure mutant bound to PS+PI(4,5)P$_2$. The results of these structural investigations are described below.

7.2 Neutron Reflectivity Measurements

7.2.1 H93R PTEN Bound to PS
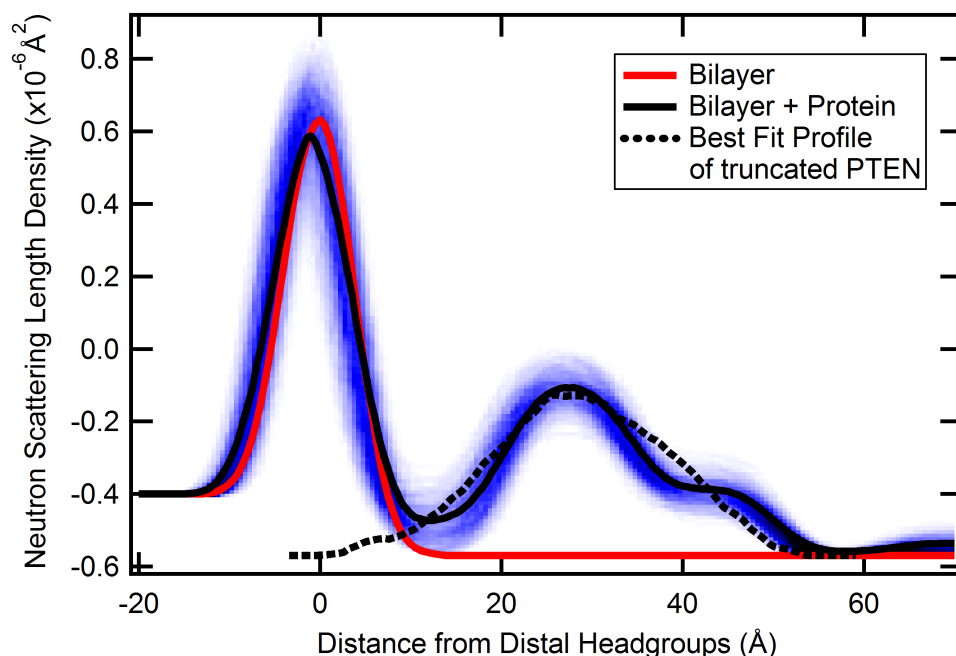
Figure 7.2: Neutron scattering length density (nSLD) profile from a slab model fit of H93R PTEN bound to a DOPC:DOPS:CHOL=70:30:3 HC18 stBLM.

Figure 7.1 depicts the reflectivity profiles for a DOPC:DOPS:CHOL = 70:30:3

bilayer on an HC18:βME = 30:70 SAM in D_2O, CM4 and H_2O contrasts; with H93R PTEN in H_2O added to the bilayer and a subsequent rinse with H_2O that removes any non-specifically bound protein. The data was analyzed using both the slab and continuous-distribution models and the analysis is described below. All the nSLD graphs include the calculated nSLD profile of the crystal structure residues at the proposed membrane-binding orientation [4] to highlight the spatial location of the truncated residues.

Slab Model

Table 7.1: Best-fit parameters for a slab model fit of H93R PTEN bound to a DOPC:DOPS:CHOL=70:30:3 HC18 stBLM.

Parameter	tBLM	tBLM+Protein
χ^2		2.7 $^{+0.3}_{-0.3}$ (1000 fits)
d tether, Å		18.8 $^{+0.5}_{-0.5}$
v.f. tether		0.58 $^{+0.01}_{-0.01}$
d lipid, Å		13.6 $^{+0.3}_{-0.3}$
Δ d lipid (protein incubation), Å	-	-0.4 $^{+1.2}_{-1.3}$
Δ d lipid (H_2O rinse), Å	-	0.2 $^{+0.3}_{-0.3}$
v.f. bilayer		0.9999 $^{+0.0001}_{-0.002}$
v.f. distal headgroup		0.60 $^{+0.06}_{-0.08}$
Δ v.f. distal headgroup (protein incubation)	-	0.01 $^{+0.1}_{-0.1}$
Δ v.f. distal headgroup (H_2O rinse)	-	0.02 $^{+0.09}_{-0.1}$
v.f. PTEN, box 1	-	0.04 $^{+0.06}_{-0.03}$
v.f. PTEN, box 2	-	0.20 $^{+0.05}_{-0.05}$
v.f. PTEN, box 3	-	0.08 $^{+0.04}_{-0.03}$
v.f. PTEN, box 4	-	0.001 $^{+0.007}_{-0.0001}$
Fraction of protein left after H_2O rinse	-	0.6 $^{+0.2}_{-0.2}$
Global-interfacial roughness, Å		6.7 $^{+0.8}_{-0.8}$

Figure 7.2 represents the 1D neutron scattering length density (nSLD) profile of H93R PTEN bound to the membrane obtained using a slab model fit of the reflectivity data. Table 7.1 contains the corresponding best-fit ($\chi^2 = 2.7 \pm 0.3$) parameters.

We have an 18.8 ± 0.5 Å sub-membrane aqueous reservoir containing $42 \pm 1\%$ of water by volume. The lipid bilayer has a volume fraction approaching 1.0, indicating an excellent defect-free bilayer preparation. Each leaflet of the bilayer has a thickness of 13.6 ± 0.3 Å. The volume fraction of the distal (with respect to the gold) lipid

headgroups is 0.60 ± 0.08 indicating 40% hydration by water.

Upon the addition of H93R PTEN, there is a minimal change in the bilayer thickness (< 1 Å) and the distal headgroup volume fraction ($< 1\%$) indicating an insignificant penetration of the protein into the bilayer. The protein's contribution to the nSLD profile was accounted for by four 15 Å slabs with volume fractions $0.04\,^{+0.06}_{-0.03}$, 0.20 ± 0.05, $0.08\,^{+0.04}_{-0.03}$ and $0.001\,^{+0.007}_{-0.001}$. The last slab has less than 1% of protein indicating that: 1) We used an appropriate number of slabs for the protein and 2) the protein extends a maximum of 45 Å from the distal lipid headgroups. After the measurement of the bilayer incubated with protein in water, the system was subsequently rinsed with water removing $40 \pm 20\%$ of the previously bound protein.

The protein nSLD profile is comparable in width to that calculated from the crystal structure (see figure 7.2), indicating that the truncated residues are located within 45 Å of the lipid headgroups.

Continuous Distribution Model
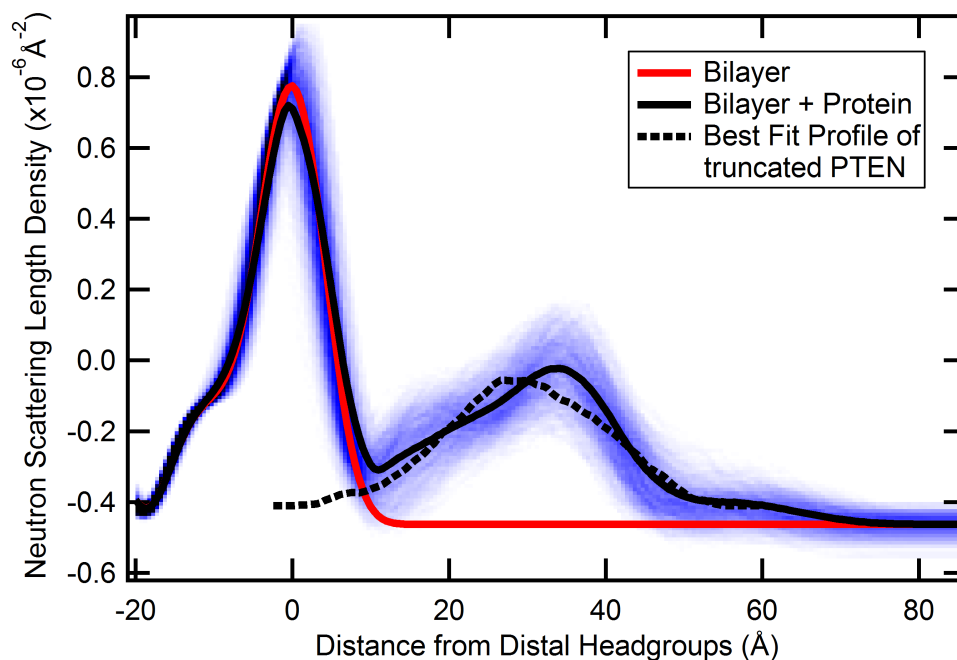
Figure 7.3: Neutron scattering length density (nSLD) profile from a continuous distribution model fit of H93R PTEN bound to a DOPC:DOPS:CHOL=70:30:3 HC18 stBLM.

Figure 7.3 depicts the nSLD profile obtained from a continuous distribution model fit of the H93R binding to PS data and table 7.2 lists the corresponding

Table 7.2: Best-fit parameters for a continuous distribution fit of H93R PTEN bound to a DOPC:DOPS:CHOL=70:30:3 HC18 stBLM.

Parameter	Value
χ^2	3.5 ± 0.5 (1500 fits)
d tether, Å	18.9 ± 0.3
v.f. tether in the inner leaflet	0.86 ± 0.14
d hydrocarbon core, Å	30.1 ± 0.3
Δ d hydrocarbon core (protein incubation), Å	0.1 ± 1.1
Δ d hydrocarbon core (H_2O rinse), Å	0.2 ± 0.3
v.f. bilayer	1.00 ± 0.00
Penetration into bilayer, Å	2.4 ± 3.3
Adsorbed protein (volume/surface area), Å	3.0 ± 0.8
Fraction of protein left after H_2O rinse	0.70 ± 0.17
Fraction of protein left after D_2O rinse	0.51 ± 0.13
Distance of protein c.o.m. from bilayer interface, Å	25.2 ± 5.0
Substrate roughness, Å	3.7 ± 0.6

best-fit ($\chi^2 = 3.5 \pm 0.5$) parameters. Once again we see that the bilayer is defect-free with a volume fraction of 1.00 ± 0.00. There is minimal penetration of the protein into the bilayer (2.4 ± 3.3 Å) and no significant change of bilayer thickness (30.1 ± 0.3 Å) upon the addition of protein. The volume of protein adsorbed per unit area is 3.0 ± 0.8 Å, 30% of which was washed away by the first rinse and a further 20% by the second rinse. The center of mass (c.o.m.) of the protein is located 25.2 ± 5.0 Å from the bilayer interface.

7.2.2 *wt* PTEN Bound to PS

Figure 7.4 depicts the reflectivity profiles for a DOPC:DOPS:CHOL = 70:30:3 bilayer on an HC18:βME = 30:70 SAM in D_2O, CM4 and H_2O contrasts, with *wt* PTEN incubating in H_2O and a subsequent rinse with H_2O. The data was analyzed using both the slab and continuous-distribution models and the analysis is described below.

Slab Model

The nSLD profile of *wt* PTEN bound to the PC:PS membrane obtained using the slab model fit is depicted in figure 7.5 with the corresponding best-fit ($\chi^2 = 2.7 \pm 0.2$) parameters listed in table 7.3.
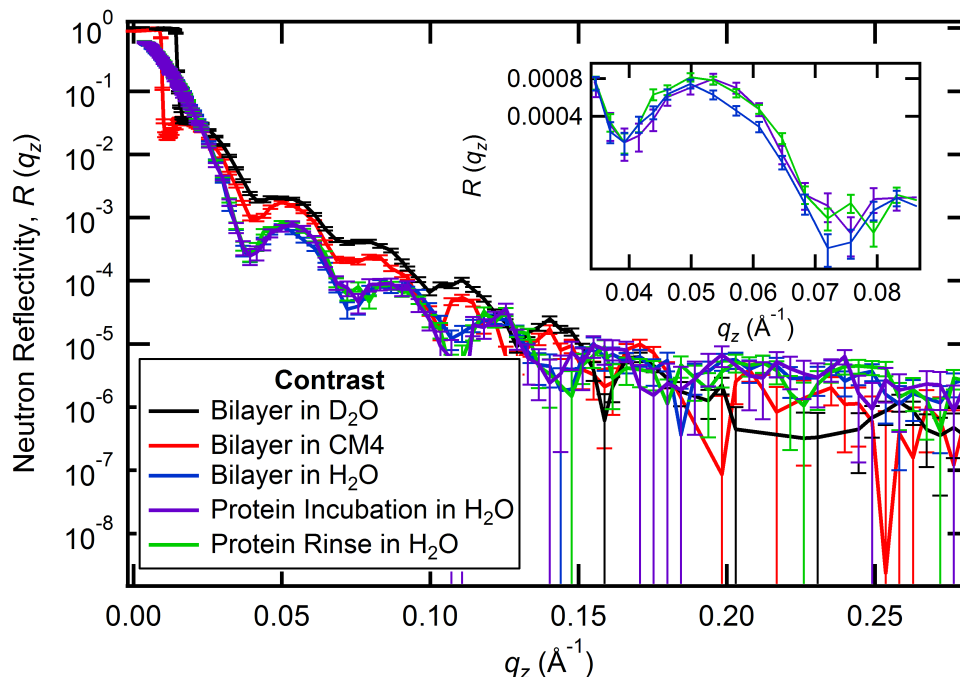
Figure 7.4: Neutron reflectivity profiles for *wt* PTEN bound to a DOPC:DOPS:CHOL=70:30:3 HC18 stBLM. **Inset:** A close-up of the water scans to show the contribution of bound PTEN.

We have a 19.8 ± 0.7 Å sub-membrane aqueous reservoir with a volume fraction of 0.60 ± 0.03. The bilayer have a volume fraction approaching 1.0 with a distal headgroup volume fraction of 0.6 ± 0.1. Each leaflet of the bilayer has a thickness of 12.2 ± 0.5 Å.

Upon the addition of protein, there is a very slight thinning of the bilayer with a change in distal leaflet thickness of -2^{+2}_{-1} Å. There is no significant change in the distal headgroup volume fraction (0.0 ± 0.2). The protein's contribution was fit with 5 boxes of 15 Å each with volume fraction 0.1 ± 0.1, 0.5 ± 0.1, 0.1 ± 0.1, $0.03^{+0.1}_{-0.03}$ and $0.001^{+0.02}_{-0.0002}$. Unlike H93R PTEN, *wt* PTEN bound to PS extends into the fourth box indicating a protein extension between 45-60 Å from the distal headgroup. A rinse of the system with water reduces the slight thinning of the bilayer seen earlier (Δd_lipid $= -0.2 \pm 0.5$ Å) and there is no change in the distal headgroup volume fraction (0.0 ± 0.2). The rinse also removes 40% of the bound protein as was the case with the H93R PTEN association with PS.

Continuous Distribution Model

Figure 7.6 depicts the nSLD profile of *wt* PTEN association with a PC:PS membrane using the continuous distribution model to fit the data. Table 7.4 lists the
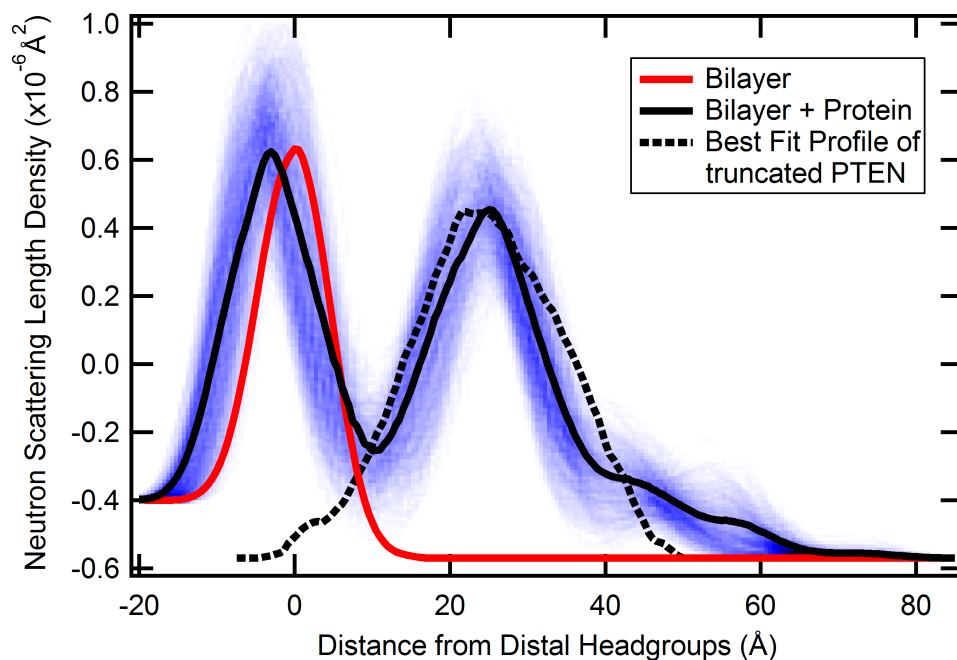
Figure 7.5: Neutron scattering length density (nSLD) profile from a slab model fit of *wt* PTEN bound to a DOPC:DOPS:CHOL=70:30:3 HC18 stBLM
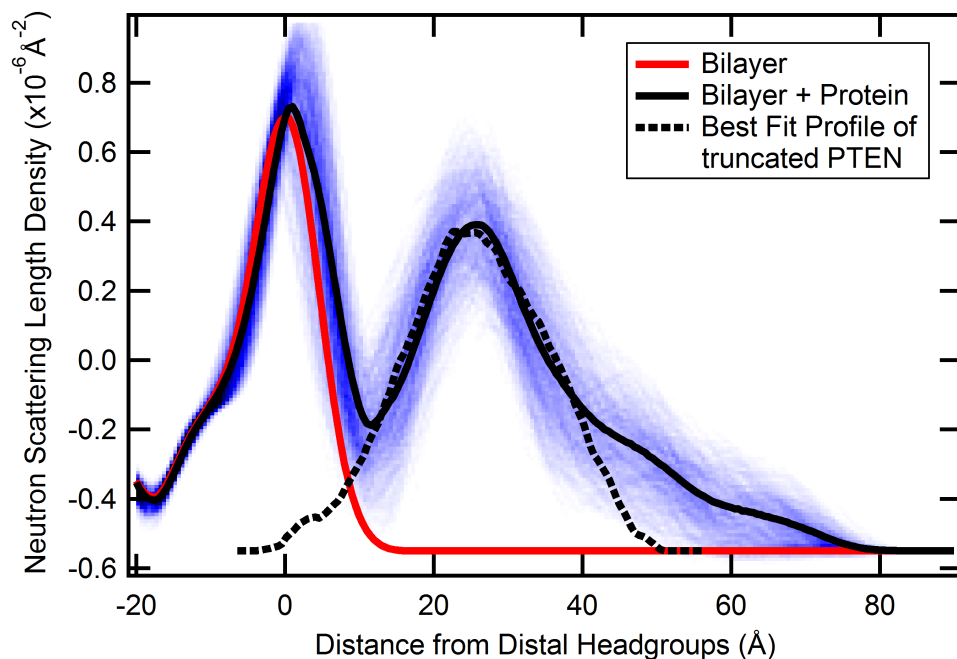
Figure 7.6: Neutron scattering length density (nSLD) profile from a continuous distribution model fit of *wt* PTEN bound to a DOPC:DOPS:CHOL=70:30:3 HC18 stBLM.

Table 7.3: Best-fit parameters for a slab model fit of *wt* PTEN bound to a DOPC:DOPS:CHOL=70:30:3 HC18 stBLM.

Parameter	tBLM	tBLM+Protein
χ^2	2.7 $^{+0.2}_{-0.2}$ (1000 fits)	
d tether, Å	19.8 $^{+0.6}_{-0.7}$	
v.f. tether	0.60 $^{+0.03}_{-0.03}$	
d lipid, Å	12.2 $^{+0.5}_{-0.5}$	
Δ d lipid (protein incubation), Å	-	-2 $^{+2}_{-1}$
Δ d lipid (H_2O rinse), Å	-	-0.2 $^{+0.5}_{-0.5}$
v.f. bilayer	0.99 $^{+0.01}$ $_{-0.01}$	0.999 $^{+0.001}_{-0.001}$
v.f. distal headgroup	0.6 $^{+0.1}_{-0.1}$	
Δ v.f. distal headgroup (protein incubation)	-	0.0 $^{+0.2}_{-0.2}$
Δ v.f. distal headgroup (H_2O rinse)	-	0.0 $^{+0.2}_{-0.2}$
v.f. PTEN, box 1	-	0.1 $^{+0.1}_{-0.1}$
v.f. PTEN, box 2	-	0.5 $^{+0.1}_{-0.1}$
v.f. PTEN, box 3	-	0.1 $^{+0.1}_{-0.1}$
v.f. PTEN, box 4	-	0.03 $^{+0.1}_{-0.03}$
v.f. PTEN, box 5	-	0.001 $^{+0.02}_{-0.0002}$
Fraction of protein left after H_2O rinse	-	0.6 $^{+0.2}_{-0.1}$
Global-interfacial roughness, Å	8.3 $^{+1}_{-0.9}$	

corresponding best-fit ($\chi^2 = 2.8 \pm 0.1$) parameters. The bilayer is defect-free with a volume fraction of 1.00 ± 0.01 and a hydrocarbon thickness of 28.8 ± 0.4 Å. Upon addition of protein, there is a negligible change in the bilayer thickness as a result of the small penetration of the protein into the bilayer (4.3 ± 2.6 Å). The volume per surface area of the adsorbed protein is 6.6 ± 1.1 Å with 35% removed by the first rinse and a further 10% by the second rinse. The protein's center of mass is located 23.6 ± 2.0 Å from the bilayer interface.

7.2.3 *wt* PTEN Bound to PS:PIP$_2$

We then proceeded to study the association of *wt* PTEN to a DOPC:DOPS:PIP$_2$:CHOL=67.5:29:3.5:3 bilayer on an HC18:βME = 30:70 SAM. Figure 7.7 depicts the reflectivity profiles for the bilayer in D$_2$O, CM4 and H$_2$O contrasts, with *wt* PTEN incubating in H$_2$O and subsequent rinses

Table 7.4: Best-fit parameters for a continuous distribution fit of *wt* PTEN bound to a DOPC:DOPS:CHOL=70:30:3 HC18 stBLM.

Parameter	Value
χ^2	2.8 ± 0.1 (1500 fits)
d tether, Å	18.8 ± 0.4
v.f. tether in the inner leaflet	0.64 ± 0.11
d hydrocarbon core, Å	28.8 ± 0.4
Δ d hydrocarbon core (protein incubation), Å	1.2 ± 1.5
Δ d hydrocarbon core (H_2O rinse), Å	0.0 ± 0.4
v.f. bilayer	1.00 ± 0.01
Penetration into bilayer, Å	4.3 ± 2.6
Adsorbed protein (volume/surface area), Å	6.6 ± 1.1
Fraction of protein left after H_2O rinse	0.65 ± 0.11
Fraction of protein left after D_2O rinse	0.55 ± 0.10
Distance of protein c.o.m. from bilayer interface, Å	23.6 ± 2.0
Substrate roughness, Å	4.5 ± 0.6
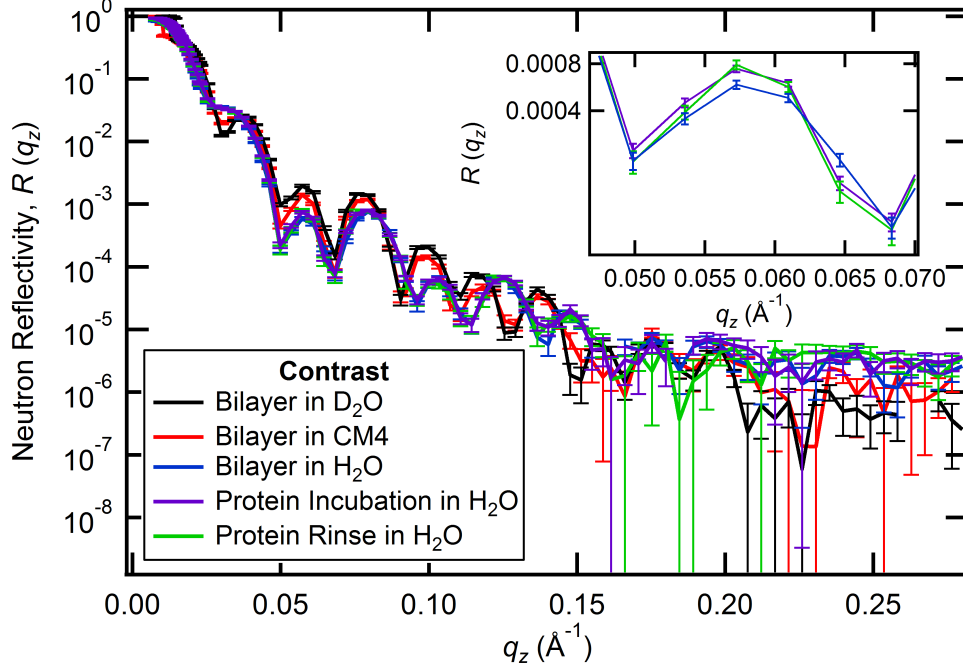
Figure 7.7: Neutron reflectivity profile for *wt* PTEN bound to a DOPC:DOPS:PIP$_2$:CHOL=67.5:29:3.5:3 HC18 stBLM. **Inset:** A close-up of the water scans to show the contribution of bound PTEN.

with H_2O, CM4 and D_2O. The data was analyzed using both the slab and continuous-distribution models which are described below.
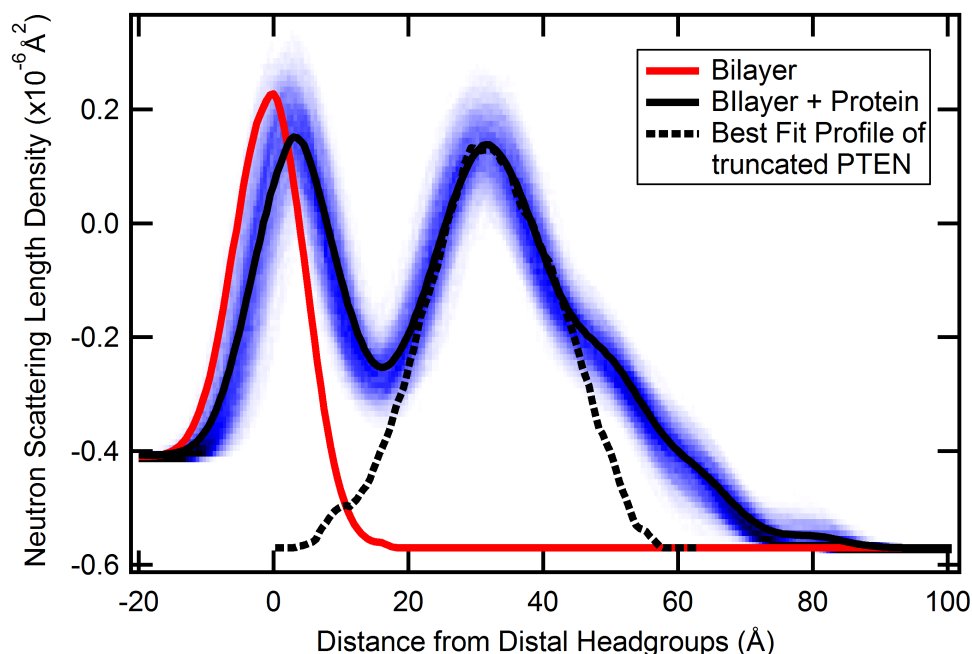
Slab Model

Figure 7.8: Neutron scattering length density (nSLD) profile from a slab model fit of *wt* PTEN bound to a DOPC:DOPS:PIP$_2$:CHOL=67.5:29:3.5:3 HC18 stBLM.

The 1D nSLD profile for *wt* PTEN bound to the PC:PS:PI(4,5)P$_2$ membrane obtained using a slab model fit of the reflectivity data is depicted in figure 7.8 and the corresponding best-fit ($\chi^2 = 4.0 \,^{+0.5}_{-0.4}$) parameters are listed in table 7.5.

This system has a $16.5 \,^{+0.6}_{-0.5}$ Å sub-membrane aqueous reservoir with a volume fraction of 0.65 ± 0.02. Each lipid of the bilayer has a thickness of 14.1 ± 0.6 Å. The bilayer had a volume fraction of $0.94 \,^{+0.02}_{-0.01}$ and while this does indicate the presence of a small number of defects, this was consistent with prior preparations of PS+PI(4,5)P$_2$ bilayers. The distal headgroups had a volume fraction of 0.5 ± 0.1.

The addition of *wt* PTEN results in a slight thickening of the bilayer with an increase of $2 \,^{+2}_{-2}$ Å. The volume fraction of the bilayer also increases by $3 \pm 2\%$ but the distal headgroup volume fraction is relatively unchanged ($-0.1 \,^{+0.2}_{-0.1}$). Once again, we had to fit the protein layer with five 15 Å slabs of volume fraction 0.12 ± 0.04, $0.33 \,^{+0.06}_{-0.05}$, 0.16 ± 0.04, $0.07 \,^{+0.04}_{-0.05}$ and $0.001 \,^{+0.03}_{-0.0004}$.

Unlike the H93R PTEN and *wt* PTEN binding to PS measurements, a water rinse leaves the amount of protein unchanged with a $0.991 \,^{+0.009}_{-0.2}$ fraction of the

115

Table 7.5: Best-fit parameters for a slab model fit of *wt* PTEN bound to a DOPC:DOPS:PIP$_2$:CHOL=67.5:29:3.5:3 HC18 stBLM.

Parameter	tBLM	tBLM+Protein
χ^2		$4.0 \, ^{+0.5}_{-0.4}$ (1000 fits)
d tether, Å		$16.5 \, ^{+0.6}_{-0.5}$
v.f. tether		$0.65 \, ^{+0.02}_{-0.02}$
d lipid, Å		$14.1 \, ^{+0.6}_{-0.6}$
Δ d lipid (protein incubation), Å	-	$2 \, ^{+2}_{-2}$
Δ d lipid (H$_2$O rinse), Å	-	$0.0 \, ^{+1}_{-1}$
Δ d lipid (D$_2$O rinse), Å	-	$0.7 \, ^{+0.4}_{-0.5}$
Δ d lipid (CM4 rinse), Å	-	$0.5 \, ^{+0.4}_{-0.4}$
v.f. bilayer		$0.94 \, ^{+0.02}_{-0.01}$
Δ v.f. bilayer	-	$0.03 \, ^{+0.02}_{-0.02}$
v.f. distal headgroup		$0.5 \, ^{+0.1}_{-0.1}$
Δ v.f. distal headgroup (protein incubation)	-	$-0.1 \, ^{+0.2}_{-0.1}$
v.f. PTEN, box 1	-	$0.12 \, ^{+0.04}_{-0.04}$
v.f. PTEN, box 2	-	$0.33 \, ^{+0.06}_{-0.05}$
v.f. PTEN, box 3	-	$0.16 \, ^{+0.04}_{-0.04}$
v.f. PTEN, box 4	-	$0.07 \, ^{+0.04}_{-0.05}$
v.f. PTEN, box 5	-	$0.0010 \, ^{+0.03}_{-0.0004}$
Fraction of protein left after H$_2$O rinse	-	$0.991 \, ^{+0.009}_{-0.2}$
Fraction of protein left after D$_2$O rinse	-	$0.7 \, ^{+0.3}_{-0.1}$
Fraction of protein left after CM4 rinse	-	$0.6 \, ^{+0.4}_{-0.2}$
Global-interfacial roughness, Å		$10.0 \, ^{+1}_{-0.9}$

protein left on the membrane. The slight thickening of the bilayer seen during the protein incubation is reversed with a change in lipid bilayer thickness of 0 ± 1 Å, compared to the neat bilayer. A subsequent D$_2$O rinse leaves a $0.7 \, ^{+0.3}_{-0.1}$ fraction of the protein untouched and a change in bilayer thickness of $0.7 \, ^{+0.4}_{-0.5}$ Å. A final CM4 rinse leaves a $0.6 \, ^{+0.4}_{-0.2}$ fraction of the protein on the bilayer and a corresponding bilayer thickness change of 0.5 ± 0.4 Å.

Continuous Distribution Model

Figure 7.9 depicts the nSLD profile based on a continuous distribution model fit of *wt* PTEN bound to a PC:PS:PI(4,5)P$_2$ bilayer. The corresponding best-fit ($\chi^2 = 4.0 \pm 0.2$) parameters are listed in table 7.6. The bilayer is of high quality with a volume fraction of 0.96 ± 0.01 and a hydrocarbon thickness of 30.2 ± 0.4 Å.
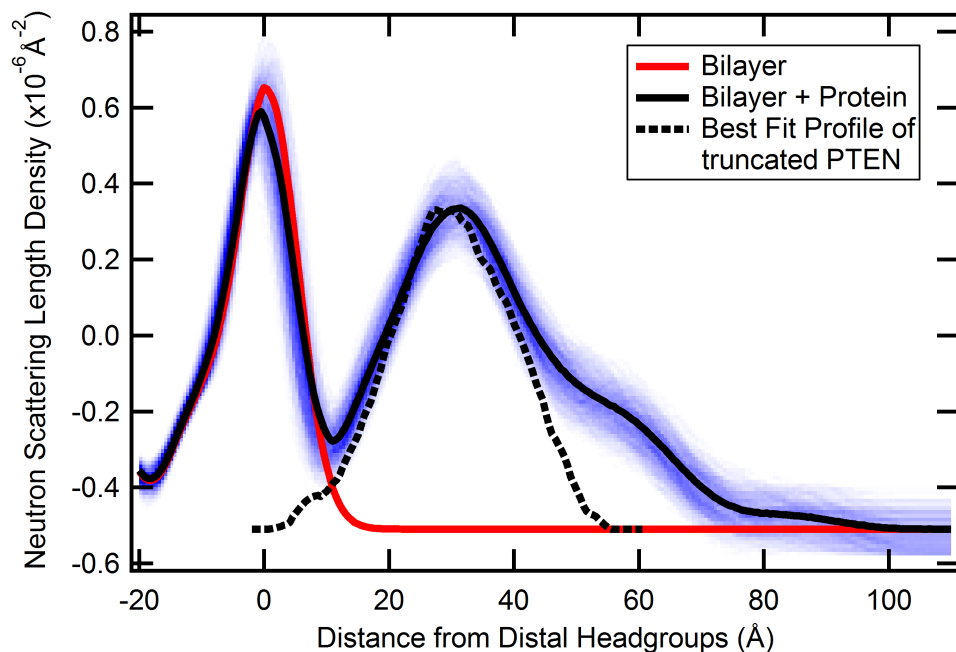
Figure 7.9: Neutron scattering length density (nSLD) profile from a continuous distribution model fit of *wt* PTEN bound to a DOPC:DOPS:PIP$_2$:CHOL=67.5:29:3.5:3 HC18 stBLM.

Table 7.6: Best-fit parameters for a continuous distribution fit of *wt* PTEN bound to a DOPC:DOPS:PIP$_2$:CHOL=67.5:29:3.5:3 HC18 stBLM.

Parameter	Value
χ^2	4.0 ± 0.2 (1500 fits)
d tether, Å	16.0 ± 0.3
v.f. tether in the inner leaflet	0.99 ± 0.11
d hydrocarbon core, Å	30.2 ± 0.4
Δ d hydrocarbon core (protein incubation), Å	-0.6 ± 1.0
Δ d hydrocarbon core (H$_2$O rinse), Å	1.0 ± 0.2
v.f. bilayer	0.96 ± 0.01
Penetration into bilayer, Å	0.5 ± 2.2
Adsorbed protein (volume/surface area), Å	7.3 ± 0.9
Fraction of protein left after H$_2$O rinse	0.99 ± 0.10
Fraction of protein left after D$_2$O rinse	0.56 ± 0.04
Fraction of protein left after CM4 rinse	0.49 ± 0.07
Distance of protein c.o.m. from bilayer interface, Å	31.2 ± 1.6
Substrate roughness, Å	4.8 ± 0.3

There is minimal penetration of the protein into the bilayer (0.5 ± 2.2 Å) and the bilayer thickness is unchanged. The volume per surface area of the adsorbed protein layer is 7.3 ± 0.9 Å. The initial rinse has no impact on the protein density, the second rinse removes 44% of the protein layer and the third rinse removes a further 7%. The center of mass of the protein is situated 31.2 ± 1.6 Å away from the bilayer interface.

7.2.4 Truncated PTEN Bound to PS:PIP$_2$
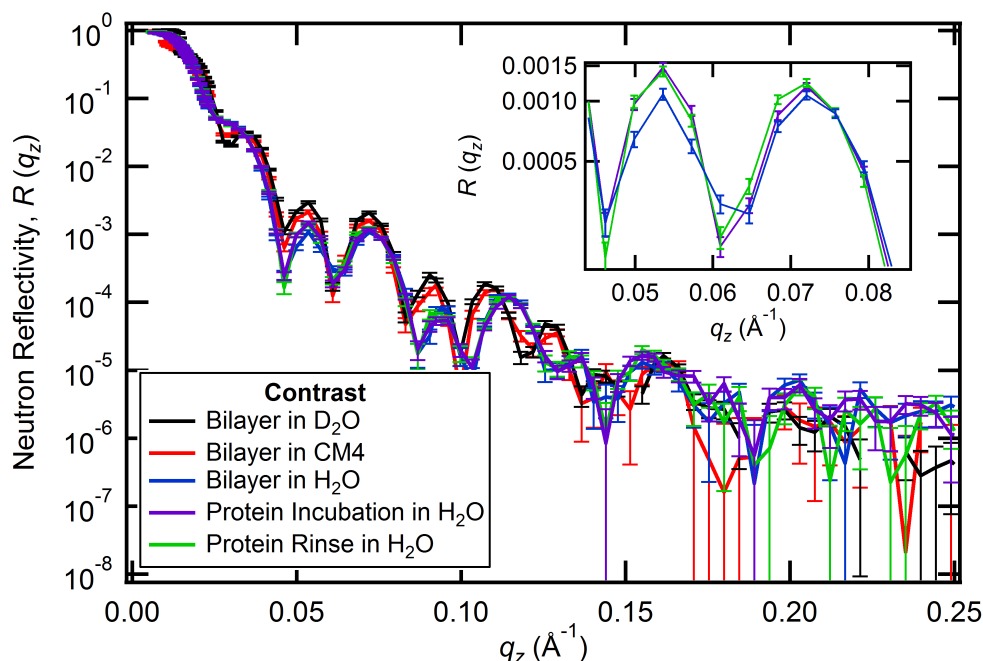
Figure 7.10: Neutron reflectivity profile for truncated PTEN bound to a DOPC:DOPS:PIP$_2$:CHOL=67.5:29:3.5:3 HC18 stBLM. **Inset:** A close-up of the water scans to show the contribution of bound PTEN.

The final system studied was the truncated crystal structure PTEN associating with a DOPC:DOPS:PI(4,5)P$_2$:chol = 67.5:29:3.5:3 bilayer on a HC18:βME = 30:70 SAM. Figure 7.10 depicts the reflectivity profiles for the bilayer in D$_2$O, CM4 and H$_2$O contrasts, with truncated PTEN incubating in H$_2$O and a subsequent rinse with H$_2$O. The data was analyzed using both the slab and continuous-distribution models which are described below.

Slab Model

The nSLD profile of the truncated PTEN bound to the PC:PS:PI(4,5)P$_2$ obtained using a slab model fit of the reflectivity data is displayed in figure 7.11 and the
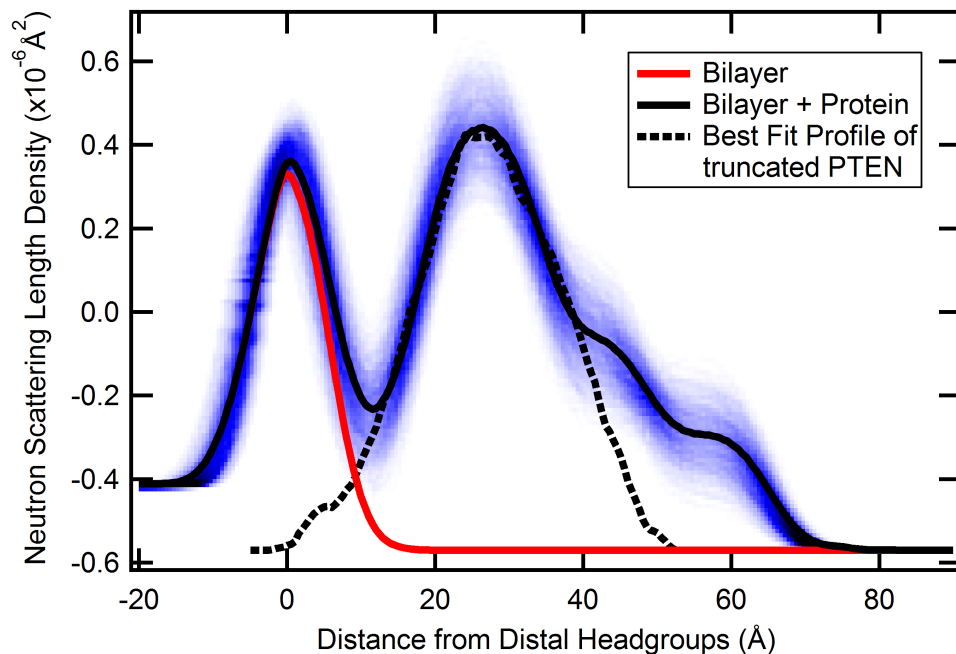
Figure 7.11: Neutron scattering length density (nSLD) profile from a slab model fit of truncated PTEN bound to a DOPC:DOPS:PIP$_2$:CHOL=67.5:29:3.5:3 HC18 stBLM.

Table 7.7: Best-fit parameters for a slab model fit of truncated PTEN bound to a DOPC:DOPS:PIP$_2$:CHOL=67.5:29:3.5:3 HC18 stBLM.

Parameter	tBLM	tBLM+Protein
χ^2	2.9 $^{+0.3}_{-0.3}$ (1372 fits)	
d tether, Å	16.0 $^{+0.8}_{-0.8}$	
v.f. tether	0.68 $^{+0.03}_{-0.03}$	
d lipid, Å	15.0 $^{+0.4}_{-0.5}$	
v.f. bilayer	0.92 $^{+0.02}_{-0.02}$	
v.f. distal headgroup	0.5 $^{+0.1}_{-0.1}$	
v.f. PTEN, box 1	-	0.11 $^{+0.08}_{-0.08}$
v.f. PTEN, box 2	-	0.46 $^{+0.09}_{-0.08}$
v.f. PTEN, box 3	-	0.23 $^{+0.09}_{-0.09}$
v.f. PTEN, box 4	-	0.12 $^{+0.07}_{-0.07}$
v.f. PTEN, box 5	-	0.0010 $^{+0.0007}_{-0.0001}$
Fraction of protein left after H$_2$O rinse	-	0.96 $^{+0.04}_{-0.1}$
Global-interfacial roughness, Å	9 $^{+2}_{-2}$	

corresponding best-fit ($\chi^2 = 2.9 \pm 0.3$) parameters are described in table 7.7.

The construct has a sub-membrane aqueous reservoir of 16.0 ± 0.8 Å and a volume fraction of 0.68 ± 0.03. The lipid bilayer has a volume fraction of 0.92 ± 0.02 with each leaflet having a thickness of 15.0 $^{+0.4}_{-0.5}$. The distal leaflet headgroup has a volume fraction of 0.5 ± 0.1.

Upon the addition of protein, there was a minimal change in the bilayer thickness or volume fraction parameters and hence the parameters were not included in the fit. The protein was fit with five 15 Å slabs of volume fraction 0.11 ± 0.08, 0.46 $^{+0.09}_{-0.08}$, 0.23 ± 0.09, 0.12 ± 0.07 and 0.001 ± 0.001. Given that the protein is missing 20% of the residues present in the *wt* including the 50 amino acid C-terminal tail, the fact that the protein's nSLD profile indicates an extent of 45-60 Å likely indicates some aggregation of the protein.

A water rinse does not change any of the bilayer parameters and a majority of the protein layer stays bound to the interface (0.96 $^{+0.04}_{-0.1}$).

Continuous Distribution Model
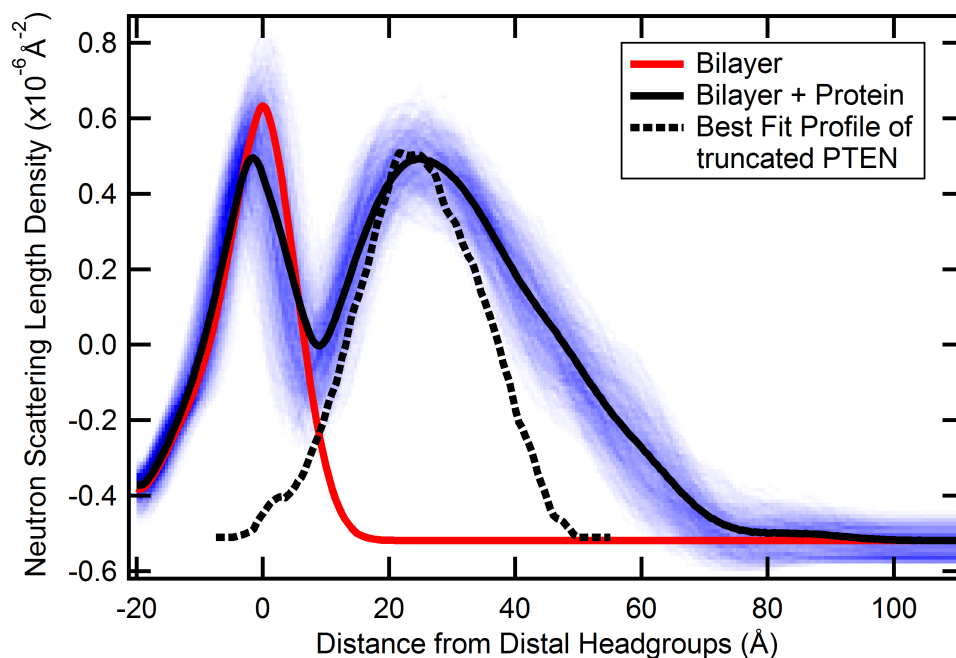
Figure 7.12: Neutron scattering length density (nSLD) profile from a continuous distribution model fit of truncated PTEN bound to a DOPC:DOPS:PIP$_2$:CHOL=67.5:29:3.5:3 HC18 stBLM.

Figure 7.12 depicts the nSLD profile of truncated PTEN bound to a PC:PS:PI(4,5)P$_2$ bilayer based on a continuous distribution model fit of the data.

Table 7.8: Best-fit parameters for a continuous distribution fit of truncated PTEN bound to a DOPC:DOPS:PIP$_2$:CHOL=67.5:29:3.5:3 HC18 stBLM.

| Parameter	Value
χ^2	3.0 ± 0.1 (1500 fits)
d tether, Å	11.6 ± 0.3
v.f. tether in the inner leaflet	0.7 ± 0.1
d hydrocarbon core, Å	29.2 ± 0.4
Δ d hydrocarbon core (protein incubation), Å	-1.1 ± 1.4
Δ d hydrocarbon core (H$_2$O rinse), Å	-0.8 ± 1.4
v.f. bilayer	0.94 ± 0.01
Penetration into bilayer, Å	2.5 ± 1.9
Adsorbed protein (volume/surface area), Å	16.6 ± 1.6
Fraction of protein left after H$_2$O rinse	0.90 ± 0.09
Distance of protein c.o.m. from bilayer interface, Å	29.7 ± 2.7
Substrate roughness, Å	4.4 ± 0.4

Table 7.8 lists the corresponding best-fit ($\chi^2 = 3.0 \pm 0.1$) parameters. The bilayer is not defect-free, but is sufficiently complete for characterizing membrane-bound PTEN with a volume fraction of 0.94 ± 0.01. The bilayer has a hydrocarbon thickness of 29.2 ± 0.4 Å which is minimally affected by the addition of truncated PTEN. The protein penetrates 2.5 ± 1.9 Å into the bilayer with a volume per surface area of 16.6 ± 1.6 Å. This latter value is significantly large and is comparable to a crystalline-like packing of the protein at the interface – another indicator that the protein is likely in an aggregated state. The center of mass of the protein is located 29.7 ± 2.7 Å from the bilayer interface and a rinse only removes 10% of the adsorbed protein layer.

7.3   Discussion

Figure 7.13 shows a comparison of the 1D nSLD profiles of the protein, with the headgroup contributions subtracted, and normalized by the amount of bound protein. Four protein-membrane systems were investigated, but since the data corresponding to the truncated PTEN bound to a PC:PS:PI(4,5)P$_2$ bilayer shows a 59.5 Å layer of protein on the membrane, we are excluding it from all further analysis due to a concern of protein aggregation.

The first result provided by such a comparison is that in all cases the protein shows no penetration into the hydrophobic core of the bilayer. Protein association is strictly interfacial with only a few Ångstroms (< 5 Å) penetration into the distal
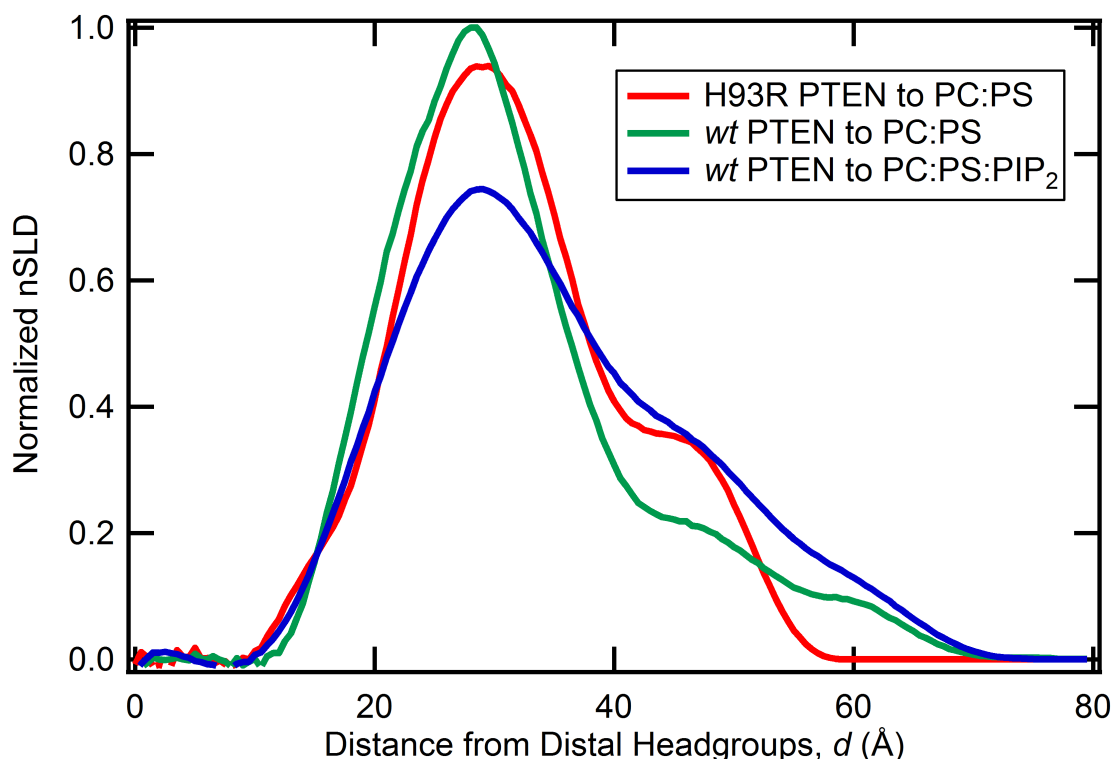
Figure 7.13: Comparison of the protein neutron scattering length density (nSLD) profiles of *wt* PTEN binding to PS, *wt* binding to PS+PI(4,5)P$_2$ and H93R PTEN binding to PS, normalized by the amount of bound protein.

Table 7.9: Comparison of the extent of the protein from the bilayer surface and the distance of the protein center-of-mass from the center-of-mass of the distal lipid headgroups for the three different protein-membrane systems studied.

System	Protein Extent	Protein-Headgroup Separation
H93R PTEN + PC:PS	45.0 Å	30.5 Å
wt PTEN + PC:PS	56.5 Å	29.1 Å
wt PTEN + PC:PS:PI(4,5)P$_2$	56.0 Å	32.3 Å

headgroup region. This is consistent with a 'scooting' model of the protein in which, upon binding, the protein skirts the bilayer surface searching for the PI(3,4,5)P$_3$ substrate.

We see small yet significant differences in the profile of membrane bound PTEN, indicating distinct membrane-bound conformations/orientations. Based on the pro-
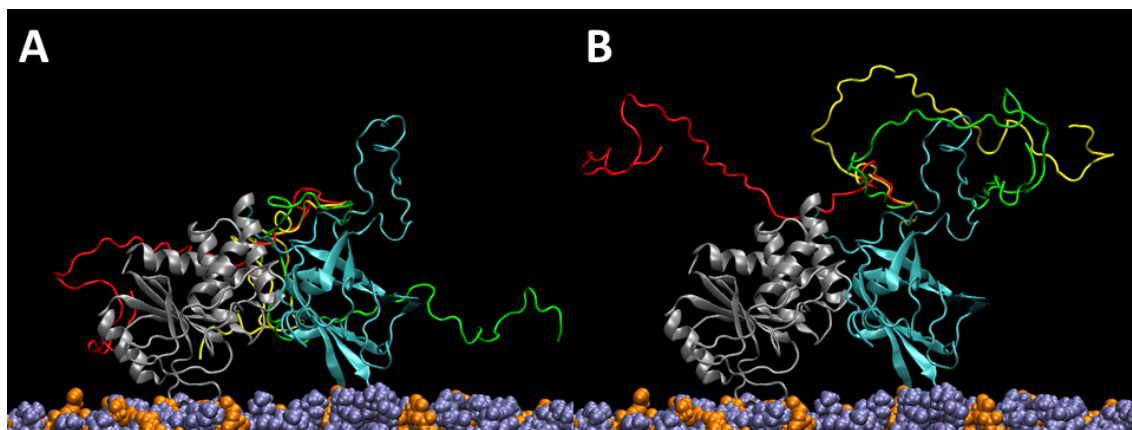
Figure 7.14: Schematic Depiction of PTEN Bound to a Lipid Bilayer.
Peptide backbone representation of (A) *wt* PTEN and (B) H93R PTEN positioned
at a DOPC:DOPS = 70:30 membrane surface that describes the most likely posi-
tioning of the core domains. PTEN only interacts interfacially with the membrane
with no significant penetration of the protein into the lipid headgroup (PC: violet,
PS: orange) region. The PTEN core domains (PD: magenta, C2: gray) are shown in
a conformation and membrane orientation predicted by the crystal structure [4]. If
we assume that the core domains are unchanged from their description in the crystal
structure, then the differences in the nSLD profiles derive from distinct organiza-
tions of the unstructured C-terminal tail. Shown here in red, yellow and green are
three distinct conformations, obtained using SASSIE [9] (see chapter 8), on each
PTEN protein core that are consistent with the observed nSLD distributions.

files, we can calculate the extent of the protein on the bilayer surface and the distance
of the center-of-mass of the protein from the center of the distal headgroups (see
table 7.9). H93R PTEN bound to PS exhibits the most compact structure with
an extension of just 45 Å from the bilayer. In comparison, *wt* PTEN bound to PS
extends an additional 11.5 Å reiterating the dramatic impact of the H93R mutation
on the protein. Figure 7.14 depicts how different conformations of the C-terminal
tail could contribute to the difference in nSLD profiles.

wt PTEN bound to PS and *wt* PTEN bound to PS+PI(4,5)P$_2$ exhibit an identi-
cal extension from the membrane but the latter is 3.5 Å removed from the headgroup
region compared to the former. There is a also a redistribution in protein contri-
bution to the nSLD for the PS+PI(4,5)P$_2$ system with a reduction in the peak at
30 Å and a greater contribution between 35-65 Å.

Earlier work using infrared (IR) spectroscopy observed an increase in α-helicity
upon *wt* PTEN association with PI(4,5)P$_2$-bearing vesicles and a "slight" decrease in
β-sheet content when bound to PS-bearing vesicles [5]. No such change was observed
for H93R association with PI(45)P$_2$ or PS [6]. While we do see differences between

wt PTEN bound to PS and PS+PI(4,5)P$_2$ membranes, the more significant result is the difference between *wt* PTEN and H93R PTEN bound to PS. Unfortunately, the given nSLD profile does not provide any information on the underlying conformation and secondary structure of the protein. As a result, we are unable to comment on the reason for the discrepancy between the membrane-bound profiles of H93R PTEN and *wt* PTEN. The idea that a conformational change of the protein, as a result of the H93R mutation, leads to altered membrane affinity is very appealing and one we plan to examine in the future. With respect to neutron reflectometry, the use of deuterated PI(4,5)P$_2$ lipids as well as specifically deuterating PTEN residues can enhance the contrast, providing us with more detailed structural information. By combining NR data with complementary techniques such as NMR measurements and molecular dynamics (MD) simulations (see chapter 9), we aim to piece together a clearer picture of the structure of PTEN, both in solution as well as in a membrane-bound state.

Chapter 8

SASSIE Analysis of Neutron Reflectivity Data

8.1   Introduction
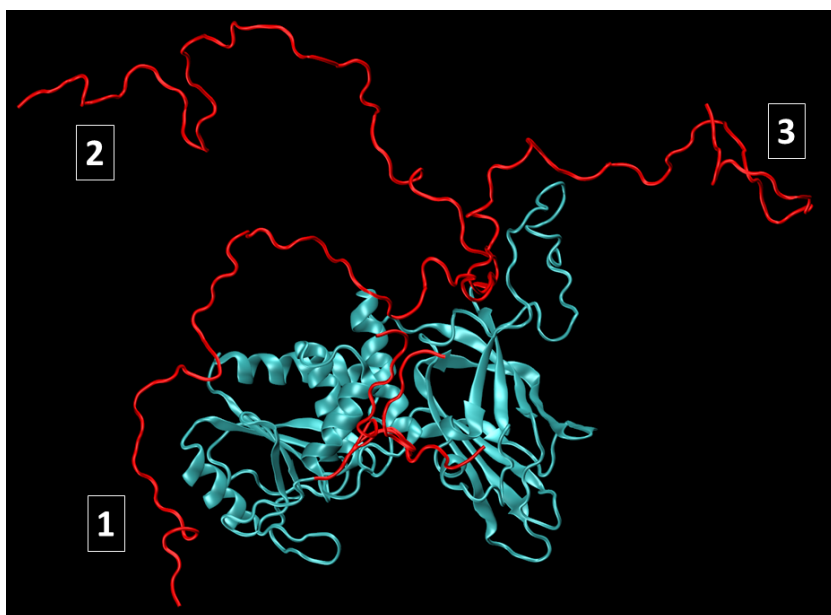
Figure 8.1: Sample SASSIE Configurations. With the core of the protein (in green) held fixed, the truncated N- and C-terminal tails (in red) were allowed to sample different dihedral angles. Three of the SASSIE generated conformations are shown here (numbered 1, 2 and 3).

Traditional neutron reflectivity analysis ends with the determination of the nSLD profile of the protein and the impact of association on the bilayer. However, as a

Table 8.1: SASSIE Parameter Set: A list of values that fully parameterize the SASSIE monomer-dihedral generation software. The flexible residues specified by the user are allowed to sample different dihedral angles in a range also specified by the user. Based on energetics, overlapping of alpha-carbons and radius of gyration cutoffs, conformations are either accepted or rejected.

Parameter	Value
Return to Last Accepted Structure	50
Low R_g cutoff	0
High R_g cutoff	400
Number of Trial Attempts	2,000 (or 20,000)
Overlap Cutoff	3
Number of Ranges	2
Max [dtheta]	30°, 30°
Low Residues	2, 352
High Residues	11, 50
Align Frames	Yes
Low Residue	200
High Residue	300
Temperature	300K
z Coordinate Filter	Yes
z Cutoff Value	-4

result of recent advances in the modeling of neutron data, if the crystal structure of the protein is known the orientation of the bound protein can be estimated [171]. In the case of the PTEN tumor suppressor, 20% of the amino acids were not included in the crystal structure, therefore complicating advanced evaluation of the neutron data. However, the development of a novel program called SASSIE [9] allowed us to account for contributions of the disordered stretches of the protein, allowing for complex orientational analysis to be performed.

We took the crystal structure of the protein, added all the missing residues and performed simulated annealing to allow the system to equilibrate. SASSIE uses importance sampling to allow residues to sample different dihedral angles using certain parameters which are listed in table 8.1. For a given residue and angle range, the program randomly picks a residue and rotates the dihedral by a random angle. Based on the residue and the user-defined temperature (300 K in our setup), only a certain range of ϕ and ψ angles are energetically favorable. This energy is calculated using the CHARMM22 all-atom protein force field [173] and based on the importance sampling criteria an angle is accepted or rejected [174, 175]. If the
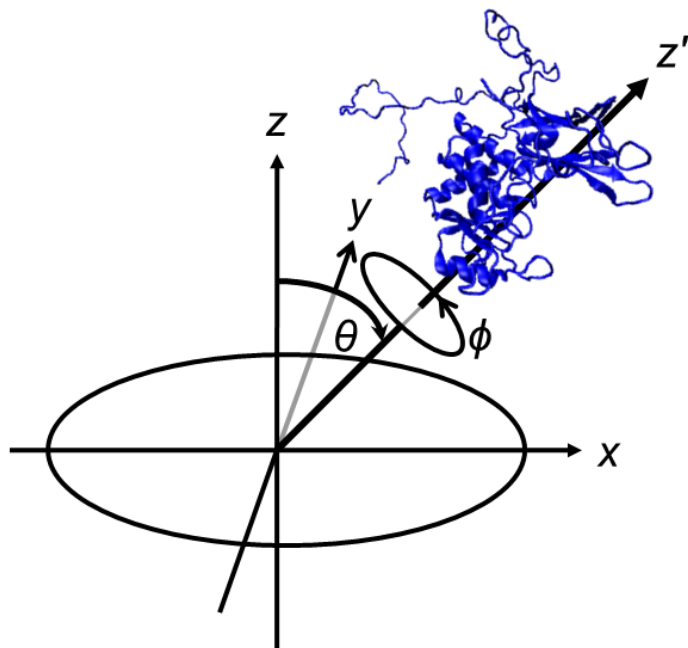
Figure 8.2: Euler Angle Based Rotation of PTEN. Each of the SASSIE generated conformations were rotated about the Euler angles θ and φ where (θ, φ) = (0°, 0°) corresponds to the proposed membrane-binding orientation of the protein [4].

rotation resulted in the overlap of any alpha-carbon atoms, the structure is rejected. Finally, a radius of gyration (R_g) is calculated. In the structure generation, we used a high R_g cutoff of 400 Å.

We used SASSIE to construct ensembles where dihedral angles corresponding to residue stretches 2-13 and 352-402 were varied. We generated 2,000 and 20,000 structures which met the acceptability criteria. Three of these structures are aligned and displayed in figure 8.1.

Each structure in the ensemble was rotated about the Euler angles θ and φ (see figure 8.2) where (θ=0°, φ=0°) corresponds to the orientation of the protein on the membrane predicted by the crystal structure [4]. For each orientation, the nSLD profile of the protein was calculated and fit to the experimental neutron reflectivity data (see figure 8.3). This yields a χ^2 'goodness of fit' parameter which can be used to evaluate the ability of the given conformation at the current orientation to reproduce the experimental results. Figure 8.4 shows the sensitivity of the χ^2 parameter. Panel (a) shows the best fit which yields a χ^2 of 0.27 while panels (b) and (c) show the impact of a 0.1 increase in χ^2.
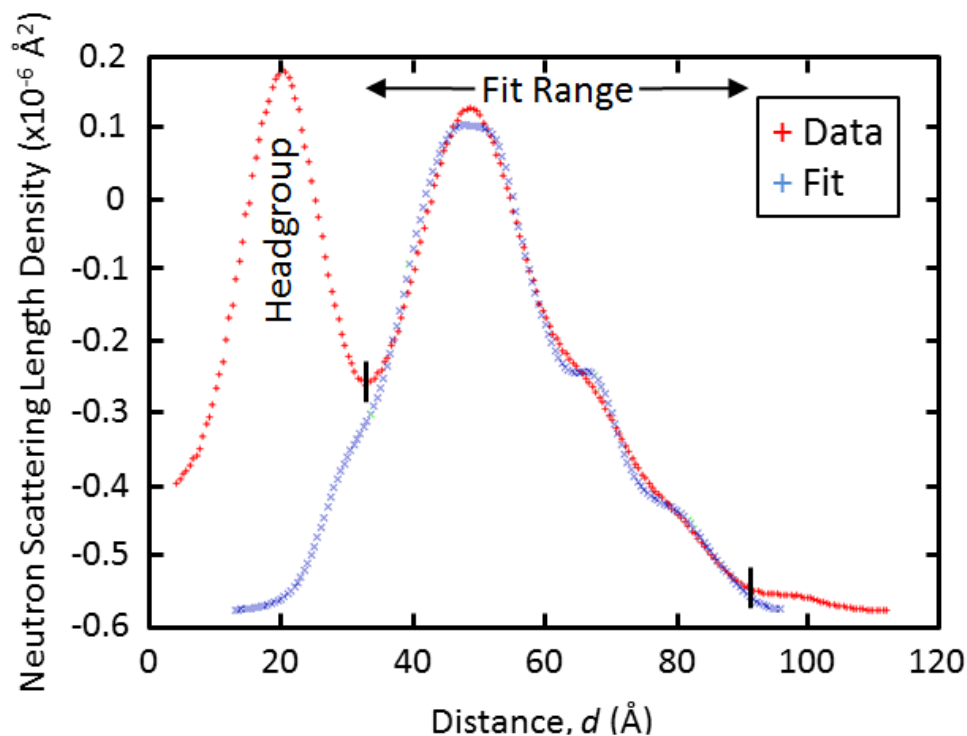
Figure 8.3: Comparison of Experimental nSLD with Theoretical nSLD.
For each orientation of a SASSIE generated conformation, a neutron scattering
length density (nSLD) profile was calculated and fit to the experimental profile.
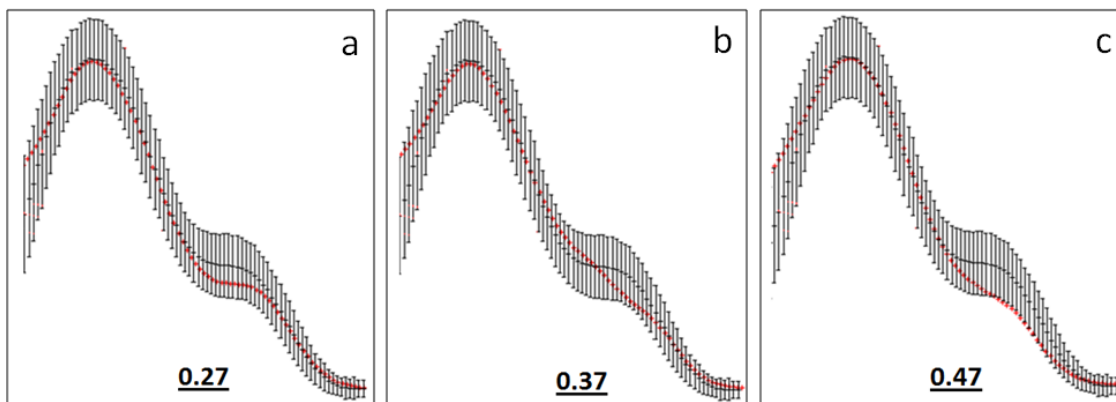
Figure 8.4: χ^2 Comparison. The χ^2 parameter is very sensitive to differences
in the experimental and calculated nSLD profiles. Panels (a), (b) and (c) illustrate
how an increase in the value of the χ^2 parameter by 0.1 corresponds to sizeable
differences in the profiles.

8.2 *wt* PTEN Bound to PS

8.2.1 Short Run
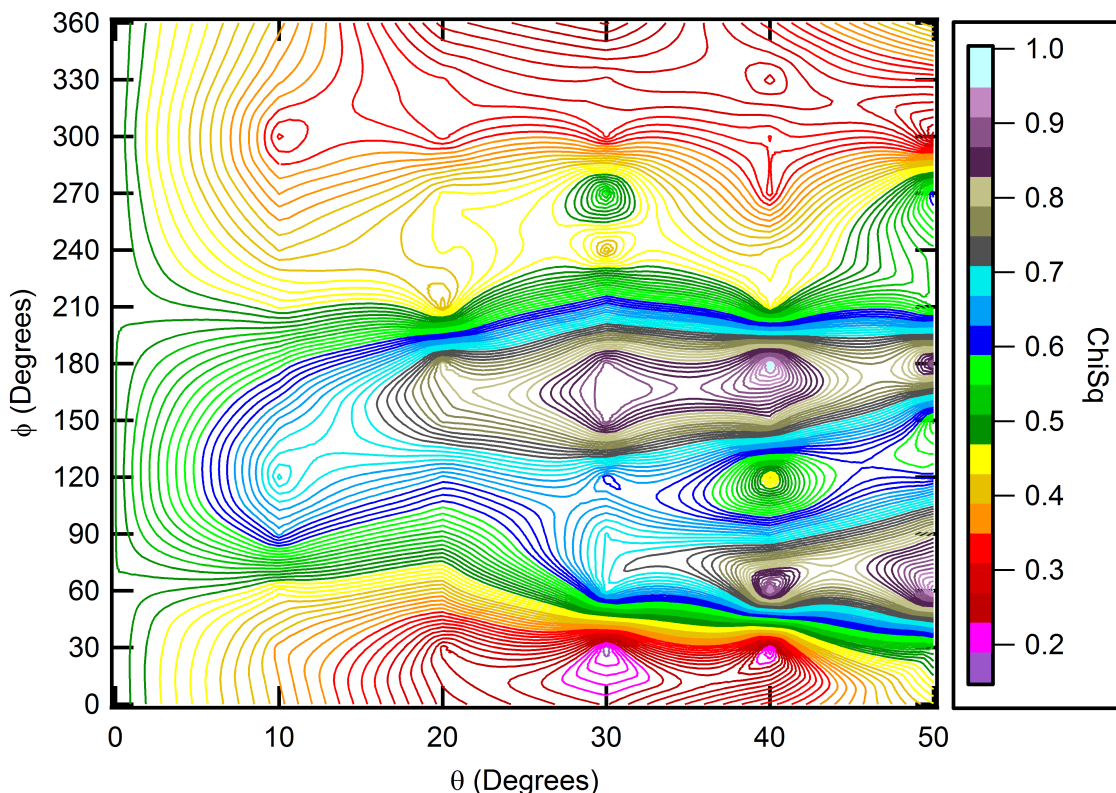
Figure 8.5: Orientation Analysis of *wt* PTEN Bound to PC:PS. χ^2 plot depicting the probability that one of the 2,000 SASSIE generated conformations could reproduce the experimental nSLD profile at a given (θ, ϕ).

For *wt* PTEN binding to PS, each of the 2,000 conformations were rotated by $0° \leq \theta \leq 50°$ and $0° \leq \phi \leq 360°$ with $10°$ increments in θ and $30°$ increments in ϕ. This allows us to create χ^2 plots where each data point represents the minimum χ^2 of 2,000 conformations at that particular θ and ϕ. For *wt* PTEN, the χ^2 plot is displayed in figure 8.5. Table 8.2 lists the top 5 configurations that best match the data.

The global minimum is centered at $(\theta=30°, \phi=30°)$ and the corresponding structure and orientation are depicted in figure 8.6. The C2 domain forms the dominant interaction with the PS-containing membrane with the loop containing the proposed binding sites able to dip into the membrane.

Table 8.2: The five configurations and orientations with the lowest χ^2 for *wt* PTEN bound to PC:PS (2,000 structures).

θ	φ	χ^2
30°	30°	0.19
40°	30°	0.203
30°	0°	0.2485
20°	30°	0.2657
20°	0°	0.2856
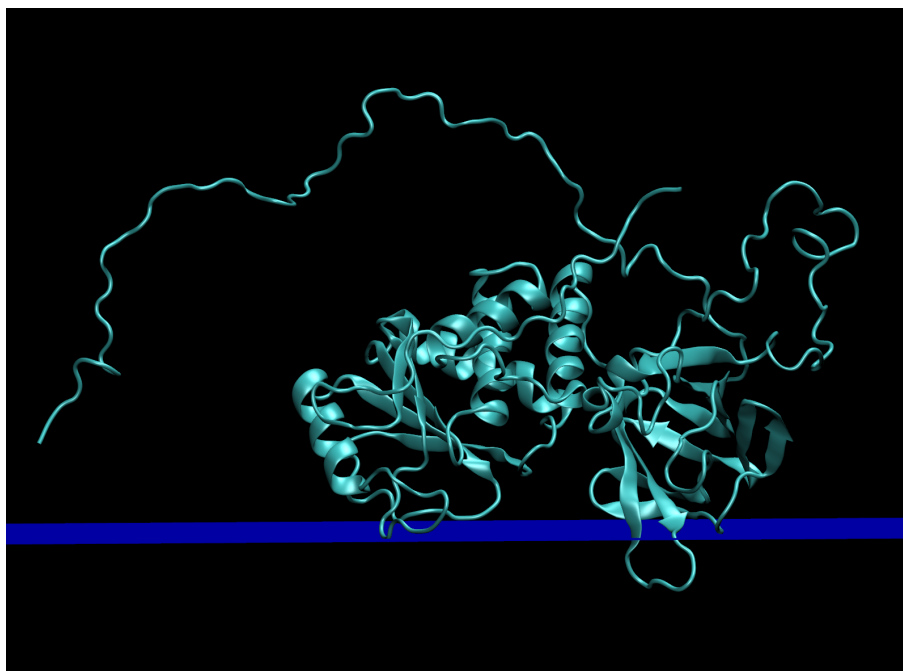
Figure 8.6: Depiction of the conformation and orientation that best matches the experimental nSLD for *wt* PTEN binding to PC:PS.

8.2.2 Long Run

An argument could be made that 2,000 conformations do not constitute a sufficient sampling of conformation space. In order to test this hypothesis, we generated 20,000 structures. Figure 8.7 compares the configuration-space encompassed by the 2,000 conformations with that of the 20,000 conformations. While the region occupied by the core of the protein is similar in both sets of structures, there is a small difference in the region distant from the membrane interface due to the flexibility of the C-terminal tail. Consequently, we proceeded to rotate the 20,000
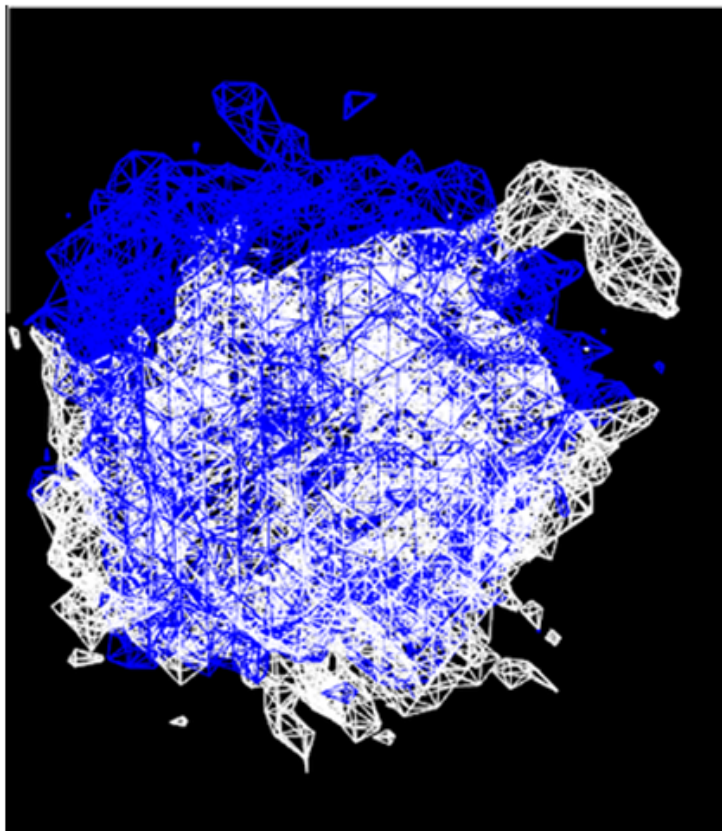
Figure 8.7: Comparison of the configuration space explored by 2,000 SASSIE configurations vs. 20,000 configurations.

conformations about the Euler angles θ and ɸ and then fit them to the experimental nSLD profile. To ensure we were not missing any minima, we used a finer grid with 5 degree increments in θ and 15 degree increments in ɸ.

Figure 8.8 depicts the χ^2 plot for the 20,000 conformations using the finer grid and table 8.3 lists the five configurations that best match the data. The plot is qualitatively very similar to the one obtained using 2,000 conformations and the best fits range in θ from 25-30° and in ɸ from 15-30°. This is evidence that the order of magnitude enhanced sampling did not make a difference in the orientational analysis and makes it unlikely that our conclusions are biased by the size of the data set.
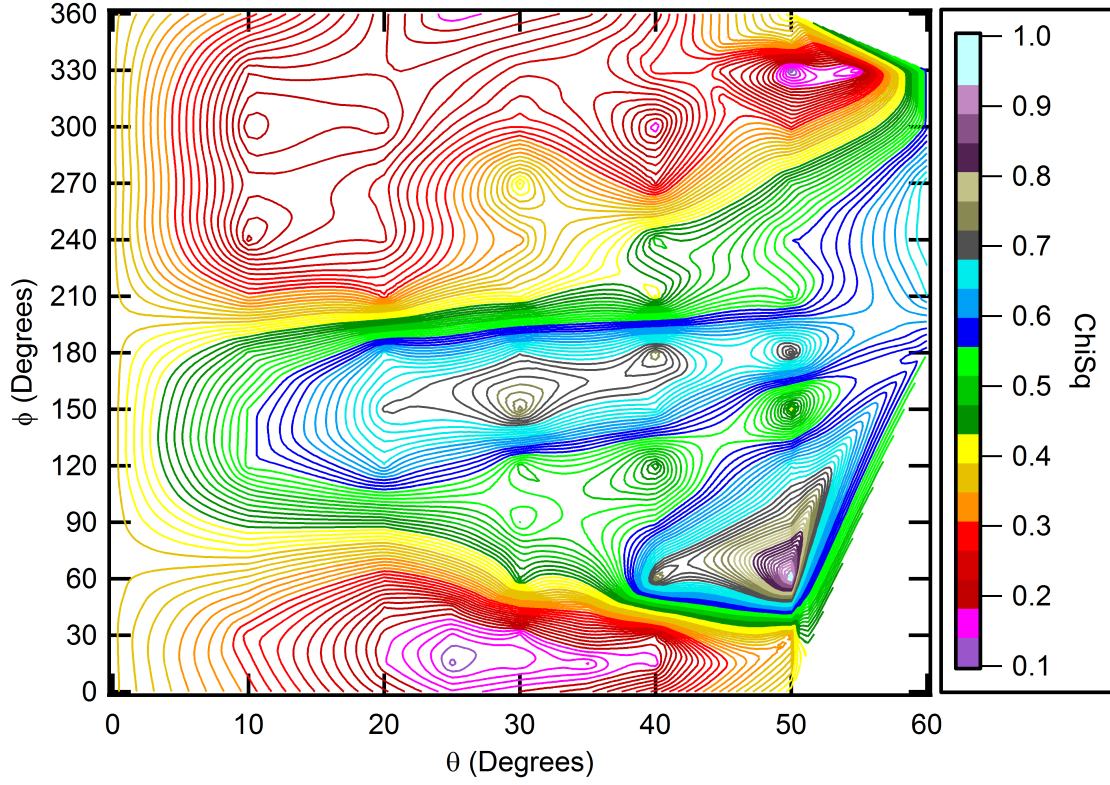
Figure 8.8: Orientation Analysis of *wt* PTEN Bound to PC:PS. χ^2 plot depicting the probability that one of the 20,000 SASSIE generated conformations could reproduce the experimental nSLD profile at a given (θ, ϕ).

Table 8.3: The five configurations and orientations with the lowest χ^2 for *wt* PTEN bound to PC:PS (20,000 structures).

θ	ϕ	χ^2
25°	15°	0.1466
30°	15°	0.1619
25°	30°	0.1668
35°	15°	0.1690
30°	30°	0.1765
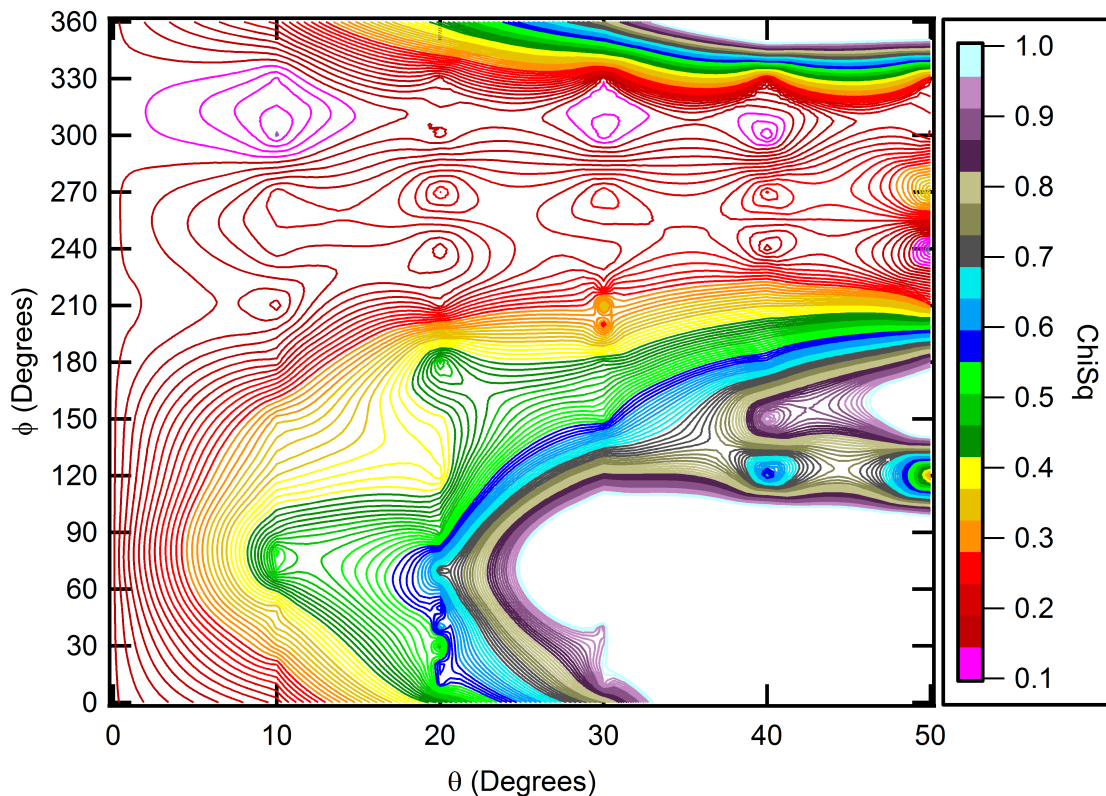
Figure 8.9: Orientation Analysis of *wt* PTEN Bound to PC:PS:PIP$_2$. χ^2 plot depicting the probability that one of the 2,000 SASSIE generated conformations could reproduce the experimental nSLD profile at a given (θ, ϕ).

Table 8.4: The three configurations and orientations with the lowest χ^2 for *wt* PTEN bound to PC:PS:PIP$_2$ (2,000 structures).

θ	ϕ	χ^2
10°	300°	0.1187
10°	330°	0.1382
0°	(any)	0.1677

8.3 *wt* PTEN Bound to PS:PIP$_2$

8.3.1 Short Run

For *wt* PTEN bound to PS+PI(4,5)P$_2$, the 2,000 structures in the ensemble were rotated by $0° \leq \theta \leq 50°$ and $0° \leq \phi \leq 360°$ with 10° increments in θ and 30°
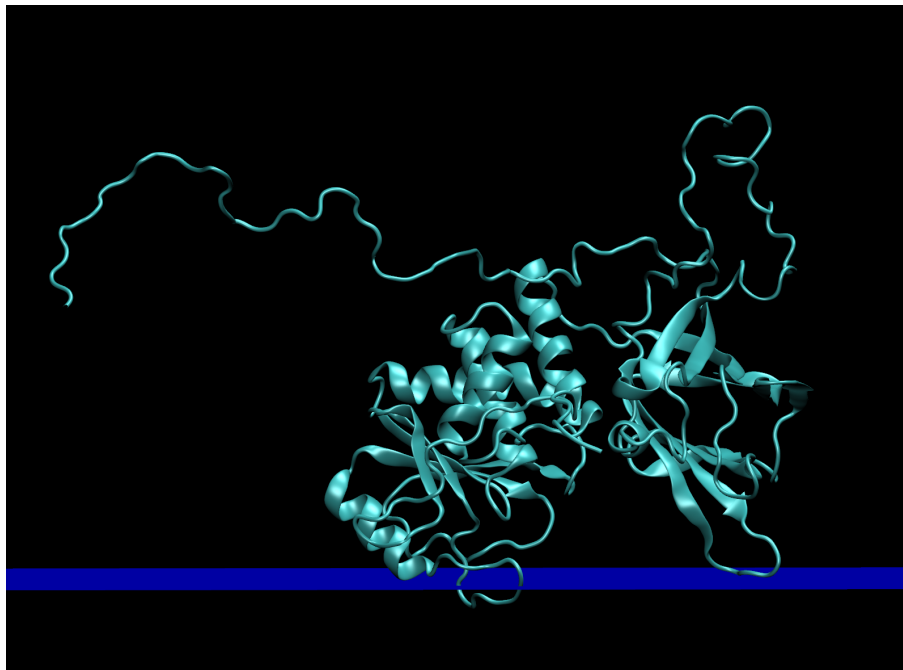
Figure 8.10: Depiction of the conformation and orientation that best matches the experimental nSLD for *wt* PTEN binding to PC:PS:PIP$_2$.

increments in ϕ. The conformations were then fit to the experimentally derived nSLD profile resulting in the χ^2 plot depicted in figure 8.9. The three configurations that best match the data are listed in table 8.4.

The global minimum is located at ($\theta=10°$, $\phi=300°$). There are two other regions of low χ^2 located at ($\theta=30°$, $\phi=300°$) and ($\theta=40°$, $\phi=300°$). However, the structures that correspond to these other minima show a large degree of penetration into the hydrophobic core of the membrane, which is something we do not observe experimentally. This leaves the minimum corresponding to ($\theta=10°$, $\phi=300°$) as the most probable orientation of the membrane bound protein which is a small deviation from the orientation predicted by the crystal structure. The configuration matching this structure and orientation is depicted in figure 8.10. Both the phosphatase domain (PD) and the C2 domain are in close proximity to the bilayer allowing for binding to PI(4,5)P$_2$ and PS to take place.

8.3.2 Long Run

To ensure we were not missing any minima by inadequate sampling of phase space, we repeated the χ^2 calculation for 20,000 structures which were rotated by $0° \leq \theta \leq 50°$ and $0° \leq \phi \leq 360°$ with $10°$ increments in θ and $30°$ increments in ϕ. The corresponding χ^2 plot is shown in figure 8.11 and the five configurations
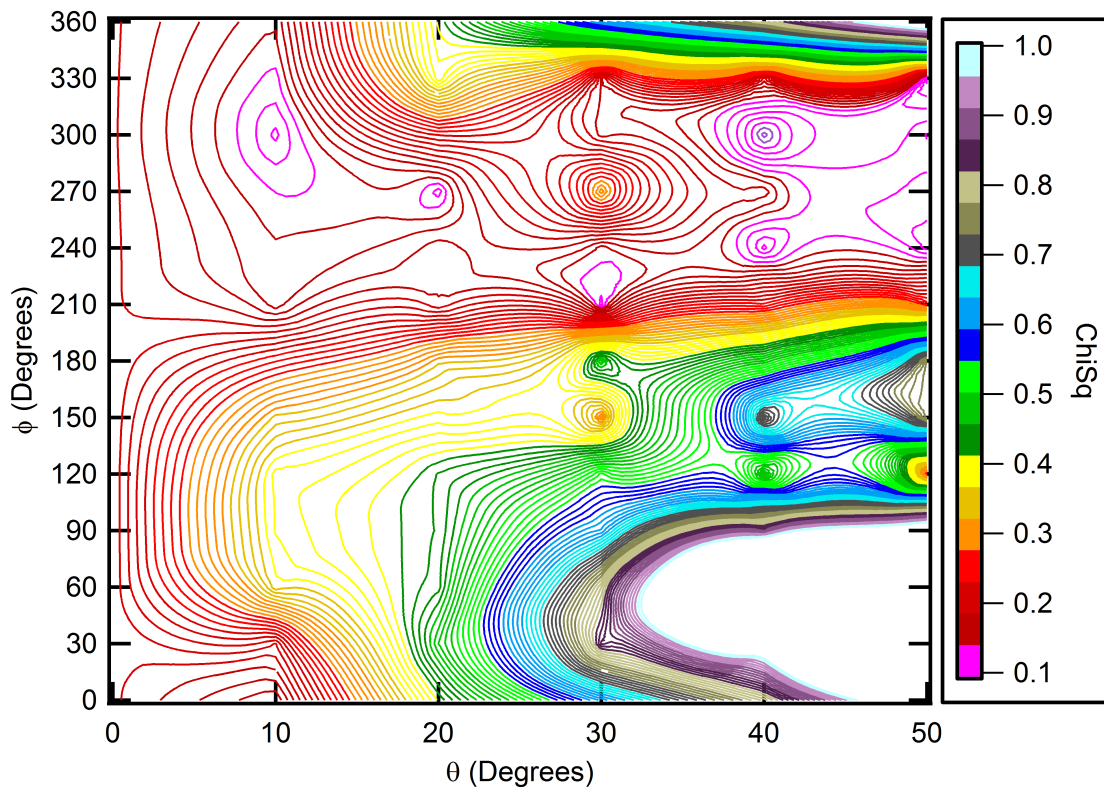
Figure 8.11: Orientation Analysis of *wt* PTEN Bound to PC:PS:PIP$_2$. χ^2 plot depicting the probability that one of the 20,000 SASSIE generated conformations could reproduce the experimental nSLD profile at a given (θ, ϕ).

Table 8.5: The five configurations and orientations with the lowest χ^2 for *wt* PTEN bound to PC:PS:PIP$_2$ (20,000 structures).

θ	ϕ	χ^2
10°	300°	0.1369
20°	270°	0.1444
10°	330°	0.1552
10°	270°	0.1595
10°	0°	0.1706

that best match the experimental data are listed in table 8.5. The global minima corresponds to θ=10° and ϕ ranging from 270-360° with ϕ=300° having the lowest χ^2, just as for the 2,000 conformations.

8.4   H93R PTEN Bound to PS
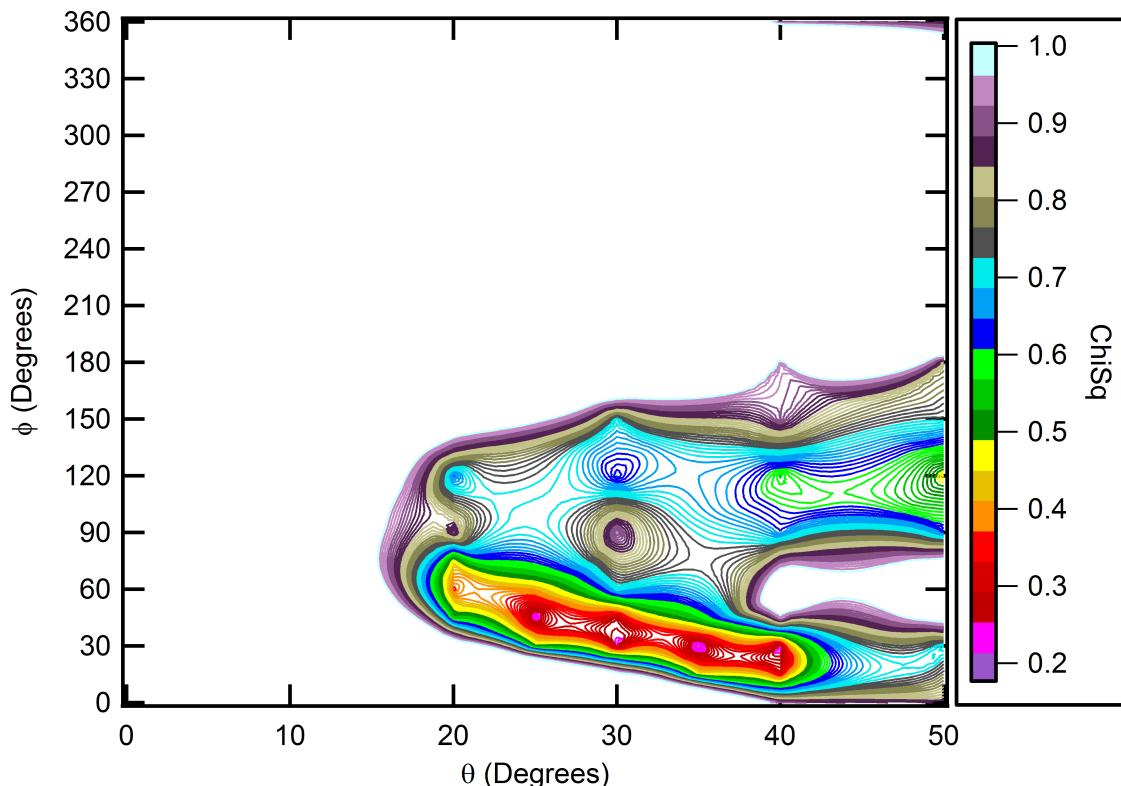
Figure 8.12: Orientation Analysis of H93R PTEN Bound to PC:PS. χ^2 plot depicting the probability that one of the 20,000 SASSIE generated conformations could reproduce the experimental nSLD profile at a given (θ, ϕ).

Finally, we performed the SASSIE analysis to find structures that best matched the neutron reflectivity data corresponding to H93R PTEN association with PS. 20000 structures were rotated by $0° \leq \theta \leq 50°$ and $0° \leq \phi \leq 360°$ with $10°$ increments in θ and $30°$ increments in ϕ. The χ^2 plot is shown in figure 8.12 and the five conformations with the lowest χ^2 are listed in table 8.6. There is a small band in orientation space with θ ranging from 25-40° and ϕ ranging from 30-45°. However, for the first time the lowest χ^2 is greater than 0.2. Figure 8.13 compares the nSLD profile of the experimental data with configuration that has the smallest χ^2. There is a 10 Å region that starts at the distal headgroup-protein interface where there is a mismatch in the fit. Given the large number of configurations in the ensemble, we believe that this indicates our underlying assumption that the core domains maintain the same conformation as in the crystal structure is incorrect.

Table 8.6: The five configurations and orientations with the lowest χ^2 for H93R PTEN bound to PC:PS (20,000 structures).

θ	ϕ	χ^2
35°	30°	0.2138
25°	45°	0.2378
40°	30°	0.2497
30°	30°	0.2595
30°	45°	0.2889
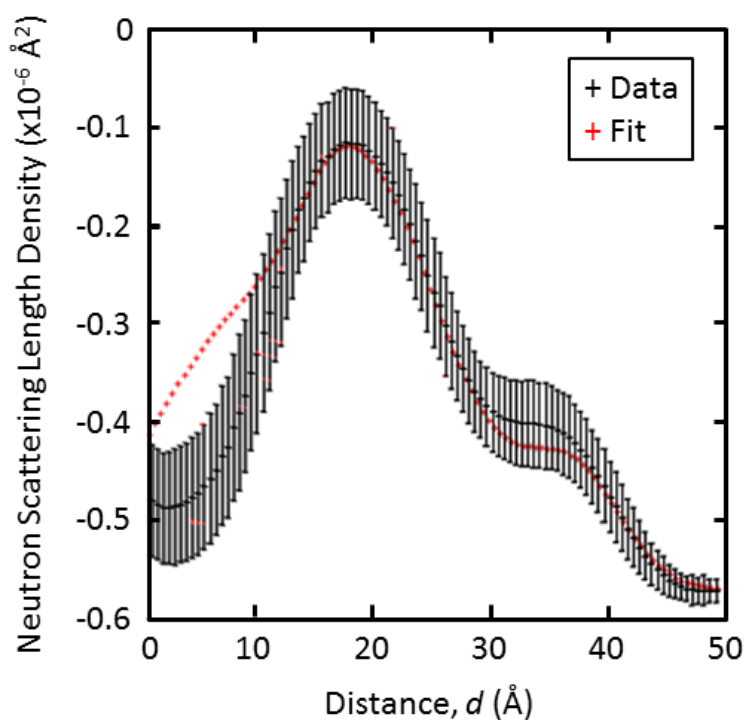
Figure 8.13: Inability of any Conformation to Perfectly Fit the nSLD Profile of H93R Bound to PC:PS (20000 structures). The figure depicts the nSLD profile with the smallest χ^2 deviation from the experimental data.

8.5 Discussion

The use of the SASSIE conformation generator in combination with the rotational analysis is a powerful tool that allows for advanced analysis of neutron reflectivity data. Given the crystal structure of a protein and assuming it is unchanged upon membrane association, the conformation and orientation of the membrane-bound

protein can be determined, even if large stretches of the protein are disordered.

By applying this methodology to the neutron reflectivity data, we determined the most probable orientation of *wt* PTEN bound to PC:PS and *wt* PTEN bound to PC:PS:PI(4,5)P$_2$ stBLMs, given the assumptions. When PTEN binds to a PC:PS membrane, the most probable orientation of the protein is at a 30° tilt in θ and 30° tilt in ϕ, with respect to the crystal structure orientation. This allows for the C2 domain which is the dominant interaction partner of PS to dip into the headgroup region and form contacts. PTEN bound to a PC:PS:PI(4,5)P$_2$ bilayer has a very slight tilt of 10° in θ and 300° in ϕ which is close to the predicted orientation. This suggests that when PTEN binds to both PS and PI(4,5)P$_2$ lipids, the two binding events at two different sites on the protein act as anchoring points that stabilize the protein with respect to the membrane, thereby allowing the protein to bind to its catalytic substrate, PI(3,4,5)P$_3$.

We have to caution that there could be changes in the secondary structure of the core domains with respect to the crystal structure upon binding which have not been accounted for. This is evident in the analysis of H93R PTEN association with a PC:PS membrane, where the flexibility of the tail is unable to provide us with a conformation that when suitably rotated compares favorably with the experimental data. There are three likely explanations for this mismatch:

1. Given the dramatic impact of the H93R mutation on the equilibrium binding kinetics of PTEN with lipid membranes and the significant loss in phosphatase activity, it is reasonable to assume a conformational or structural change of the protein. This could either be in the core domains or in the disordered N- and C-terminal tails.

2. It is possible that even with 20,000 SASSIE generated structures, we are unable to sample conformations of the tail that could explain H93R PTEN's compact structure, when compared to *wt* PTEN.

3. The SASSIE analysis performed here attempts to find structures that can describe the equilibrium conformation captured by the experimental nSLD profile. However, it may be the case that no single structure in the 20,000 structure library is adequate and we instead require an ensemble of structures. If that is the case, then SASSIE is an inefficient way of identifying these ensembles and we need to turn to more rigorous molecular dynamics simulations of PTEN.

In summary, SASSIE combined with orientational analysis helps us predict probable orientations and conformations of membrane-bound PTEN. We proceeded to set up and run all-atom molecular dynamics simulations of *wt* PTEN in solution and in a membrane-associated state to validate the SASSIE results and provide us with a more detailed understanding of equilibrium structures/ensembles and transitions between these states.

Chapter 9

Molecular Dynamics Simulations of PTEN

9.1 Introduction

So far, we have learned that PTEN is a very plastic protein with seemingly innocuous point mutations able to disrupt membrane association and alter catalytic activity. The differences in function seem to be accompanied by structural differences, as observed my comparing protein density profiles. All-atom molecular dynamics simulations are a powerful way of gaining insight into the molecular processes accompanying protein-membrane interactions, but also of studying the equilibrium conformation of PTEN in solution. Indeed, the level of detail is generally unmatched by standard experimental techniques. While they are powerful on their own, the ability of MD simulations to complement experimental data allows us to build a fuller picture of the intricate molecular interactions in biology. We aim to achieve the following objectives:

1. Model the conformational dynamics and the equilibrium structure of the tumor suppressor PTEN in explicit solvent. To date, only the crystal structure of a truncated PTEN mutant has been described [4] which is missing flexible but functionally critical regions of the protein. In addition, the solution structure may deviate from the crystal structure.

2. Model the binding mechanism and membrane-bound structure of *wt* PTEN to lipid membranes of varying composition. No structure for PTEN bound to a lipid membrane exists.

The simulations complement the experimental work by filling in the molecular level details of the binding mechanism, based on experimental constraints. In particular, by correlating the results of the simulations with our extensive surface plasmon resonance (SPR) binding affinity measurements [164], we will be able to

correlate structural changes with functional differences. And by combining our high-resolution neutron reflectivity (NR) measurement data [164] with the equilibrium structures generated by the simulation, we will be able to definitively describe the structure of membrane-bound PTEN, both as a function of lipid composition as well as PTEN mutations.

In particular, following is a list of results we would like to verify and parameters we would like to quantify in greater detail:

1. The SPR and NR results indicate that the H93R mutant shows a surprisingly large deviation from the behavior of *wt* PTEN. MD simulations may help us understand how a point mutation that is spatially separated from key residues in the binding process can have such a great impact.

2. By having an equilibrium structure of PTEN in solution and in the membrane-bound state, we can study the impact of the membrane-association on the structure of the protein. In particular, we can explore the possibility of conformational changes in the protein that allow it to bind specifically to certain lipids.

3. Assuming that the crystal structure is valid for the membrane-bound state of the protein, differences in the protein nSLD profiles (seen in chapter 7) can be explained if PTEN's orientation is a function of membrane composition. MD simulations should be able to provide equilibrium orientations of PTEN at the membrane interface, which can then be compared with the NR data for consistency.

4. The NR data are consistent with a strictly interfacial binding of PTEN to the bilayer, i.e., PTEN does not penetrate into the hydrophobic core of the membrane. Now that we have this high-level picture, we would like to use MD simulations to study the molecular details of the membrane-association mechanism, with specific focus on the basic and hydrophobic residue patches purported to be responsible for binding to the protein.

5. The SPR data showed evidence of a non 1:1 binding stoichiometry for *wt* PTEN binding to $PI(4,5)P_2$. MD simulations run for a sufficiently long amount of time (> 300 ns) may reveal the exact stoichiometry of the process – something that is difficult to determine experimentally.

6. We performed rotational analysis to help estimate the orientation of the protein from the NR data using the crystal structure of the protein. These efforts were hampered by the absence of 20% of the residues, which we tried to compensate for with the use of SASSIE. MD simulations of full length *wt* PTEN in solution should aid us in this regard. This data can be compared with that obtained directly from MD simulations of PTEN bound to lipid membranes.

7. The PI(4,5)P$_2$ binding module (PBM) is unstructured in solution but has been shown to specifically bind to PI(4,5)P$_2$ – not to PI(3,4)P$_2$, PI(3,5)P$_2$ or PI(3,4,5)P$_3$. This has led to speculation that the PBM changes conformation upon encountering a PI(4,5)P$_2$ molecule, thereby accounting for its selective behavior. This is extremely difficult to determine experimentally but is something we hope to identify in the MD simulations.

9.2 Methods

The MD simulations were carried out using the NAMD 2.8 software package [176]. The CHARMM22 [173] and CHARMM36 [177] force field parameters were used to describe the protein and the lipids (DOPC and DOPS), respectively. The parameters for the lipid PI(4,5)P$_2$ were based on the work by Lupyan et al. [178]. The simulations were performed using periodic boundary and NPT conditions at a constant temperature of 300 K using a Langevin thermostat with a damping coefficient of 1 ps^{-1} and a constant pressure of 1 atm using a Langevin piston barostat. The non-bonded van der Waals potential energy was smoothly truncated between 10 Å and 12 Å with non-bonded pairs calculated within a 13.5 Å cutoff. Full electrostatics were implemented using Particle Mesh Ewald with a grid spacing of 1 Å and the simulation was integrated every 2 fs. The trajectories were analyzed using the VMD 1.9.1 software package [179] and the MDAnalysis toolkit [180].

9.3 Systems

9.3.1 DOPC Bilayer

A 50 Å x 50 Å equilibrated DOPC bilayer patch that consisted of 36 lipids/leaflet was obtained from prior work by Kaluda et al. [177] and nine copies were stitched together to form a 150 Å x 150 Å patch. The bilayer was hydrated with TIP3 water and neutralized using sodium chloride salt. Extra salt was added to ensure the total concentration was 100 mM in order to match the experimental conditions. The system was minimized for 1,000 steps, followed by 2 ns of equilibration.

9.3.2 DOPC:DOPS=2:1 Bilayer

The *psfgen* structure building tool, a plug-in in VMD [179], was used to mutate every third lipid in the equilibrated DOPC bilayer to give a DOPC:DOPS = 2:1 membrane composition. Extra salt was added to neutralize the bilayer and to ensure the total salt concentration was 100 mM. The system was minimized for 1,000 steps, forces were applied to keep water out of the membrane for 0.5 ns followed by a 14 ns production run.

9.3.3 *wt* PTEN in Solution
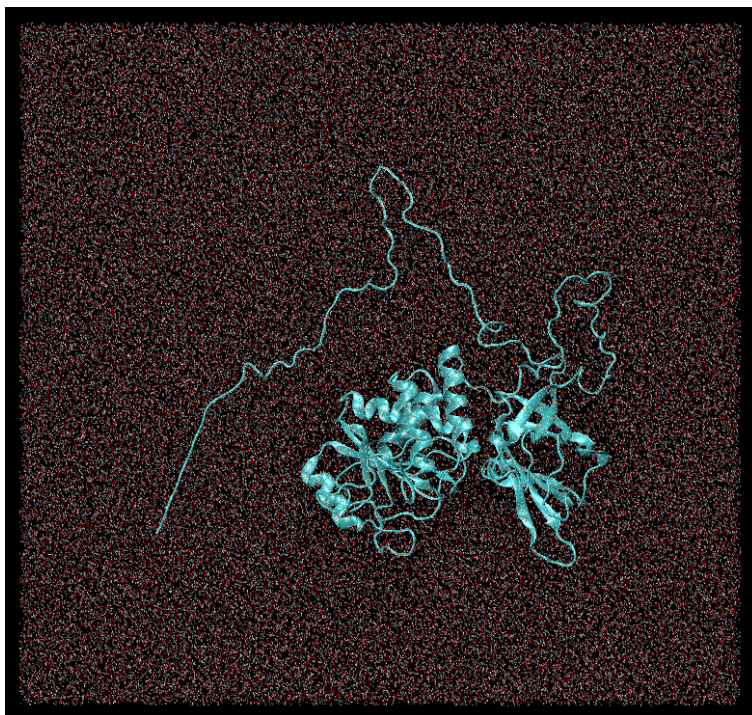
Figure 9.1: Unit cell of the *wt* PTEN in solution simulation.

The truncated PTEN crystal structure was obtained from the Protein Data Bank (PDB ID: 1D5R) [4]. Residues 1-13, 282-312 and 352-411, which were either deleted prior to crystallization or whose coordinates could not be determined, were added back to the protein's structure, along with a C-terminal Histag that was used to purify the protein for the experiments, to simulate the experimental conditions as closely as possible.

Simulated annealing was used to allow the added residues to equilibrate. PTEN was simulated in implicit solvent using a dielectric constant of 80. Amino acids included in the crystal structure were held fixed and simulations were run using a temperature ramp from 300 K to 600 K in 15 K increments over 300 ps. The system was then held at 600 K for 600 ps and ramped back down to 300 K over 300 ps. This simulated annealing cycle was repeated three times for a total of 3.6 ns of equilibration.

The SASSIE program was used to generate 2,000 structures and number 1547 was chosen as the starting candidate as the C-terminal was not fully extended away from the membrane, thereby minimizing the size of the unit cell in the simulations (see figure 9.1).

The protein was placed in a 110 Å x 200 Å x 145 Å solvation box (protein

dimensions + 25 Å in each dimension) with sodium chloride to neutralize the system and re-establish a total concentration of 100 mM. With the PTEN protein core held fixed, the system was minimized for 1000 steps. Constraints allow us to use harmonic constraint energy functions to restrict the motion of the protein core residues. We applied a 3 kcal/mol harmonic force constraint for 1 ns, followed by a 1 kcal/mol constraint for a further ns. The core was then freed and a 1 kcal/mol constraint was applied for a further 1 ns. A 300 ns production run was then initiated.

9.3.4 DOPC:DOPS=2:1 + *wt* PTEN
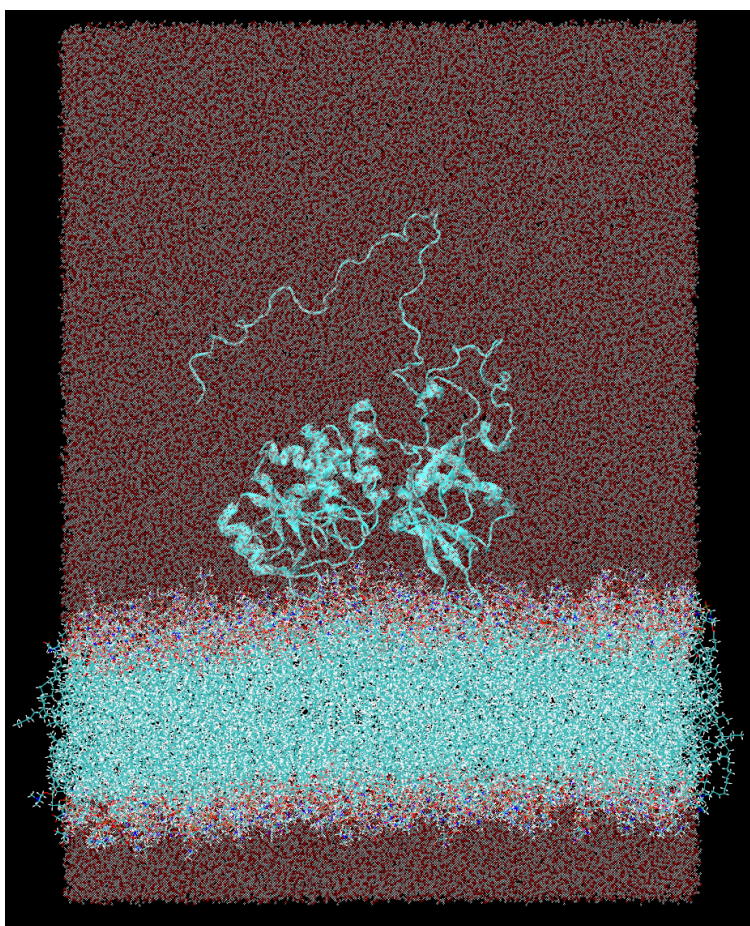
Figure 9.2: Unit cell of the *wt* PTEN binding to PC:PS simulation.

The equilibrated PTEN protein structure obtained in solution at the 9 ns simulation time point was taken without water and combined with the equilibrated DOPC:DOPS membrane from the 14 ns time point of the trajectory. The protein was centered with respect to the bilayer and shifted along the bilayer normal to create a 10 Å layer of water that separated the protein from the lipid headgroups.

An extra 40 Å of water was added along the bilayer normal to account for flexibility of the C-terminal tail. Sodium chloride was then added to neutralize the system and to ensure the total concentration was 100 mM (see figure 9.2). The entire protein was held fixed for 5 ns, followed by a 3 kcal/mol harmonic force constraint applied for 5 ns and a 1 kcal/mol constraint for a further 5 ns on the residues of the protein core. Finally, all constraints on the protein were removed and a 300 ns production run was initiated.

9.3.5 DOPC:DOPS:PI(4,5)P$_2$=65.74:32.41:1.85 + *wt* PTEN
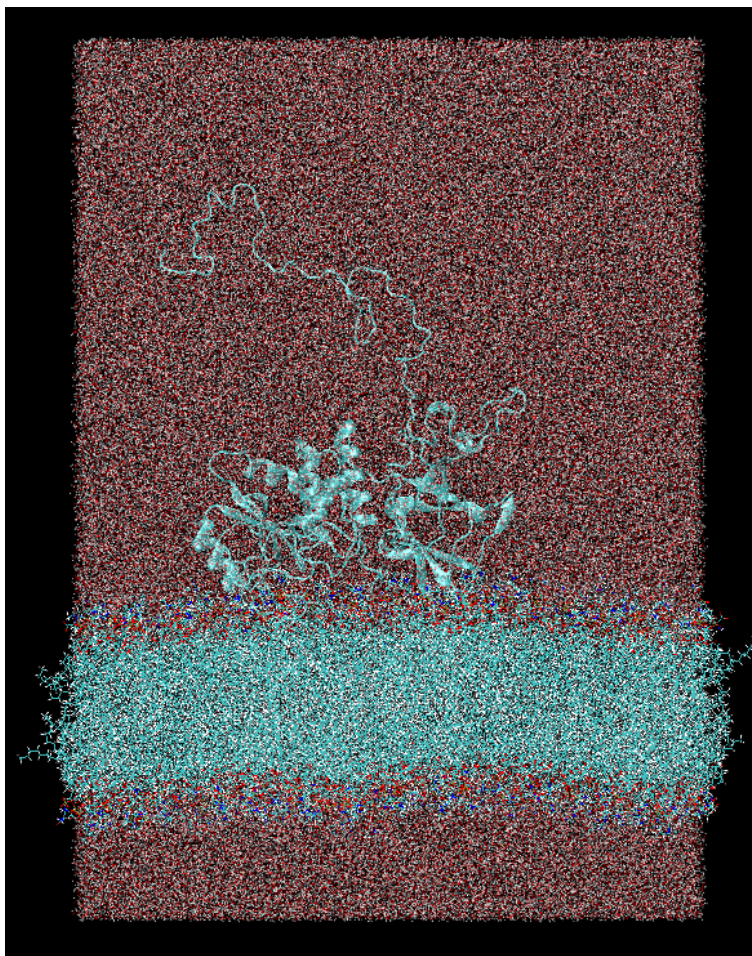
Figure 9.3: Unit cell of the *wt* PTEN binding to PC:PS:PI(4,5)P$_2$ simulation.

The equilibrated bilayer and protein from the 50 ns time point of the production run of the *wt* PTEN binding to DOPC:DOPS = 2:1 simulation was taken. On each

leaflet of the bilayer, 3 DOPC and 3 DOPS lipids were mutated to a PI(4,5)P$_2$ lipid. On the proximal (protein-facing) leaflet, one mutated DOPS lipid was chosen close to the PI(4,5)P$_2$ binding module (PBM) and one close to the PI(3,4,5)P$_3$ active site. All other mutated lipids were randomly chosen. The system (see figure 9.3) was minimized for 1,000 steps followed by a 300 ns production run was initiated.

9.4 Results

9.4.1 DOPC:DOPS=2:1 + *wt* PTEN

Determining the Boundary Between Equilibration and Production
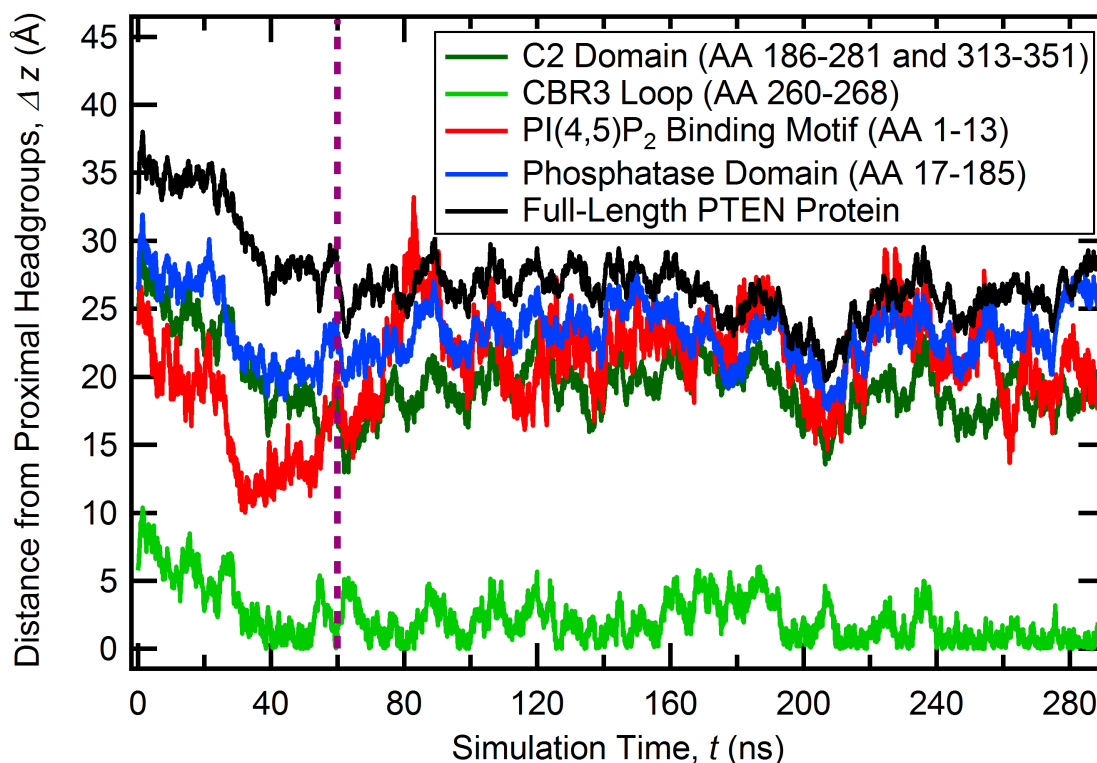
Figure 9.4: Distance between the center of mass of the different PTEN domains and the proximal (to the protein) lipid headgroups of the PC:PS membrane, over the course of the production run. The dashed purple line at the 60 ns time point corresponds to the boundary between the equilibration and production run.

Figure 9.4 depicts the distances between the center of mass of the different domains of the protein and the center of mass of the lipid headgroups proximal to the protein. A loop in the C2 domain consisting of residues 260-269 (CBR3 motif),

which has been implicated as the chief PS-binding domain [4], approaches to within 5 Å of the lipid headgroups 30 ns into the simulation – a distance at which it stays for the rest of the simulation. Since it took 60 ns for the distance between the core domains and the headgroups to equilibrate, we decided to consider the first 60 ns of the simulation as an equilibration period and the trajectory from 60 ns onwards as the production run.

Comparison of *in vitro* and *in silico* nSLD Profiles
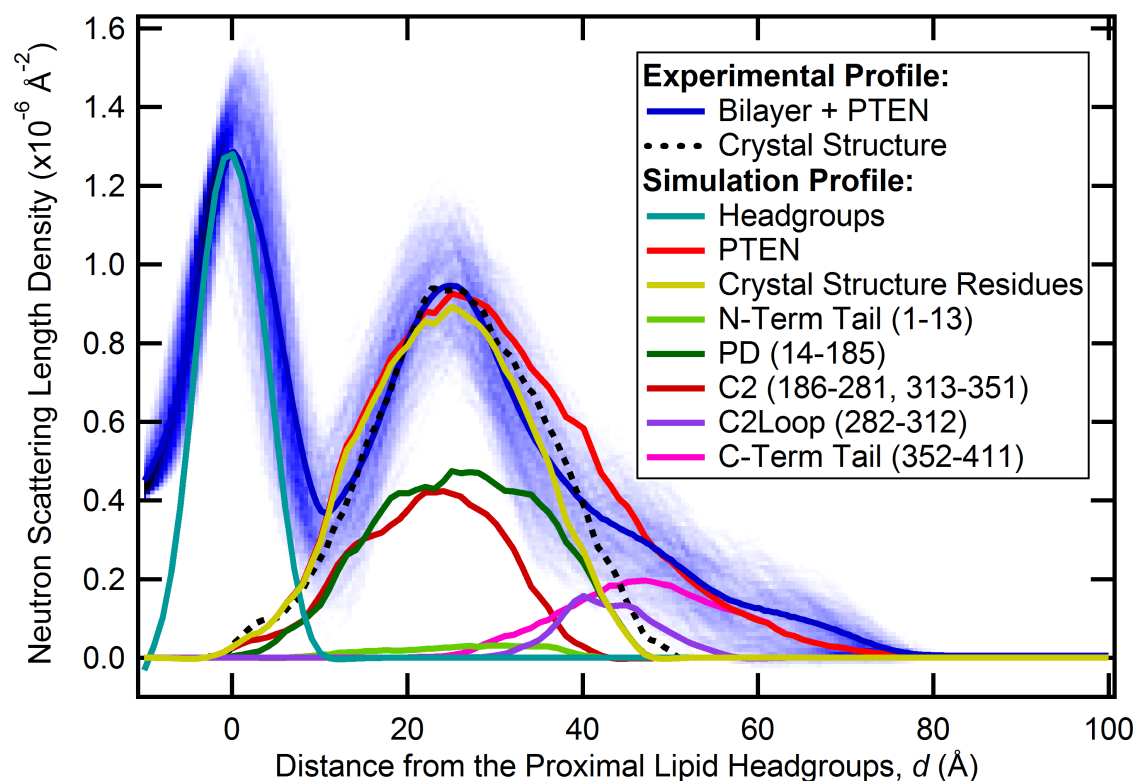
Figure 9.5: Comparison of the nSLD profile of *wt* PTEN binding to PC:PS from neutron reflectivity experiments (blue) and molecular dynamics simulations (red). MD simulations allow us to visualize the contribution of each domain to the overall nSLD profile. The yellow line shows the contribution of residues included in the crystal structure and the difference with the envelope profile confirms that the C-terminal tail is located distal to the membrane.

The reliability of the rich atomic-level detail provided by MD simulations is based on their compatibility with experimental results and their ability to make testable predictions. In the case of *wt* PTEN binding to PS-bearing bilayers, we can compare the experimental neutron scattering length density (nSLD) profiles with calculated

profiles, based on the averaged structure from the production run (see figure 9.5). Aligning the proximal lipid headgroup profiles by their maxima results in an excellent agreement of the experimental and simulation protein density envelopes. The profile of the core domains of the protein (shown in yellow) overlap with the putative crystal structure profile (shown in dotted black) reaffirming our interpretation of the NR data that the core domains are in contact with the membrane while the C-terminal tail is located distal to the bilayer. The simulation also verifies the experimental result that PTEN's association with a PS-bearing membrane is strictly interfacial with no penetration into the hydrophobic core of the bilayer. This serves to validate the simulations and allows us to perform a more detailed analysis of the data.

With respect to the nSLD data, we can now examine the contribution of each residue of the protein. The phosphatase domain (PD) and the C2 domain are located proximal to the membrane and both contain residues that interact with the lipid headgroups. The disordered N-terminal tail, which includes the $PI(4,5)P_2$ binding module (PBM), shows minimal interaction with the bilayer and has a broad profile that extends over 30 Å , indicating a high degree of flexibility in its motion. Both the C-terminal tail as well as a loop in the C2 domain (residues 282-312) were not included in the crystal structure. Consequently, there is no information on their conformation in solution or their role in membrane association. Based on the computed nSLD profile, it is clear that they are both located distal to the bilayer, do not contribute to the membrane association and are responsible for the deviation of the nSLD profile from one generated purely due to residues included in the crystal structure.

Role of the C-Terminal Tail

Figure 9.6 depicts the behavior of the C-terminal tail over the course of the simulation. The starting frame is representative of the state of the protein at the 9 ns time point in the membrane-free simulations. As observed in the nSLD profile, the tail remains distant from the membrane and shows little, if any, interaction with the protein core. This is not unexpected, as the tail has a net charge of -10 which would be electrostatically repelled by the anionic PS membrane. The tail initially extends going from a radius of gyration of 21 Å to 26 Å in 6 ns before dropping to 15 Å over the next 10 ns and eventually stabilizing at around 14 Å (see figure 9.7). This compaction is due to the formation of several loops along the length of the tail as well as an α-helix at the very end of the tail (residues 396-403).

Figure 9.8 depicts the number of hydrogen bonds formed by residues of the C-terminal tail over the course of the simulation. A hydrogen bond is considered to be formed between a donor atom (bearing the bonded hydrogen) and an acceptor atom if the distance between the two is less than 3 Å and the angle between the donor atom, the hydrogen atom involved in bonding and the acceptor atom is less

Table 9.1: Hydrogen bonds formed between the residues in the C-terminal tail for *wt* PTEN bound to a PC:PS membrane and their occupancy times.

Donor		Acceptor		Occupancy (%)
Residue	**Chain**	**Residue**	**Chain**	
SER370	Side	THR383	Main	88.48
THR382	Side	ASP368	Side	73.73
HIS406	Main	TYR379	Main	63.59
SER385	Side	ASP371	Side	57.14
ASP381	Main	LEU404	Main	54.38
THR401	Side	HIS397	Main	47.47
ASN372	Side	THR383	Main	30.88
GLN399	Main	ASP395	Main	29.03
TYR377	Main	ASP375	Side	27.19
SER362	Main	GLU358	Main	26.27
ILE400	Main	GLN396	Main	24.88
THR401	Main	HIS397	Main	17.97
LYS402	Main	SER398	Main	17.97
ASP371	Main	SER385	Side	16.59
THR382	Main	ASP381	Side	16.59
SER398	Side	GLU394	Side	16.13
ALA359	Main	HIS376	Main	15.21
SER361	Main	PRO357	Main	14.75
TYR379	Main	ASP375	Side	13.82
SER360	Side	GLU358	Side	11.98
ASP395	Main	GLU394	Side	11.98
HIS397	Main	HIS397	Side	11.52
HIS410	Main	HIS409	Side	11.06
HIS407	Main	TYR379	Main	11.06
SER361	Side	PRO357	Main	10.6

Table 9.2: Hydrogen bonds formed between the C2 domain and the C-terminal tail for *wt* PTEN bound to a PC:PS membrane

Donor		Acceptor		Occupancy (%)
Residue	**Chain**	**Residue**	**Chain**	
SER302	Side	GLU352	Side	34.56
SER355	Side	ASP301	Side	31.8
SER355	Main	SER302	Main	29.49
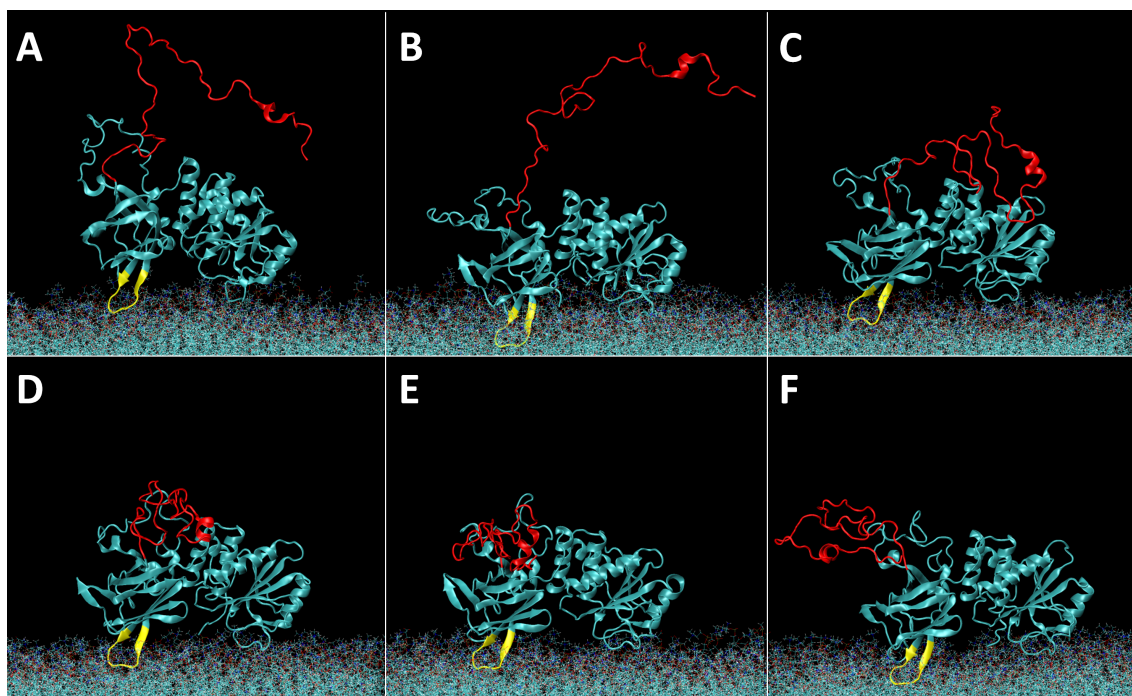
Figure 9.6: Evolution of the C-Terminal Tail over the Course of the *wt* PTEN Binding to PC:PS Simulation. A) 0 ns, B) 55 ns, C) 110 ns, D) 165 ns, E) 220 ns and F) 275 ns timesnap of the simulation. Residues 260-269, which constitute the CBR3 PS-binding motif in the C2 domain, are colored in yellow and residues 352-411, which constitute the C-terminal tail, are colored in red. The protein has been rotated by 180 degrees about the z-axis such that the phosphatase domain is on the right and the C2 domain is on the left. The C-terminal tail begins to compact by the 50 ns timepoint and stays distal to the membrane throughout the simulation.

than 60°. Within the first 50 ns, there is a large increase in the number of H-Bonds between residues of the tail from 9 to 17 and a slow saturation to an average of 19 (see table 9.2 for details). There are significant fluctuations indicating that H-Bonds are constantly being broken and formed, which reflects the disordered nature of the tail.

A salt bridge is considered to be formed if an Oxygen atom of an acidic residue is within 3.2 Å of a Nitrogen atom of a basic residue. Eight salt bridges: Arg378-Asp368, Arg378-Asp375, Arg378-Asp381, Lys402-Asp384, Lys402-Glu388, Lys402-Glu394, His406-Asp381 and His409-Glu405 are also formed that stabilize several of the loops and turns formed in the tail.

The tail does make three H-Bonds with the C2 domain (see figure 9.8) but that number stays a constant for the duration of the simulation indicating no increased interaction. Three salt bridges: Arg189-Glu353, Arg308-Glu352 and Lys349-Glu352,
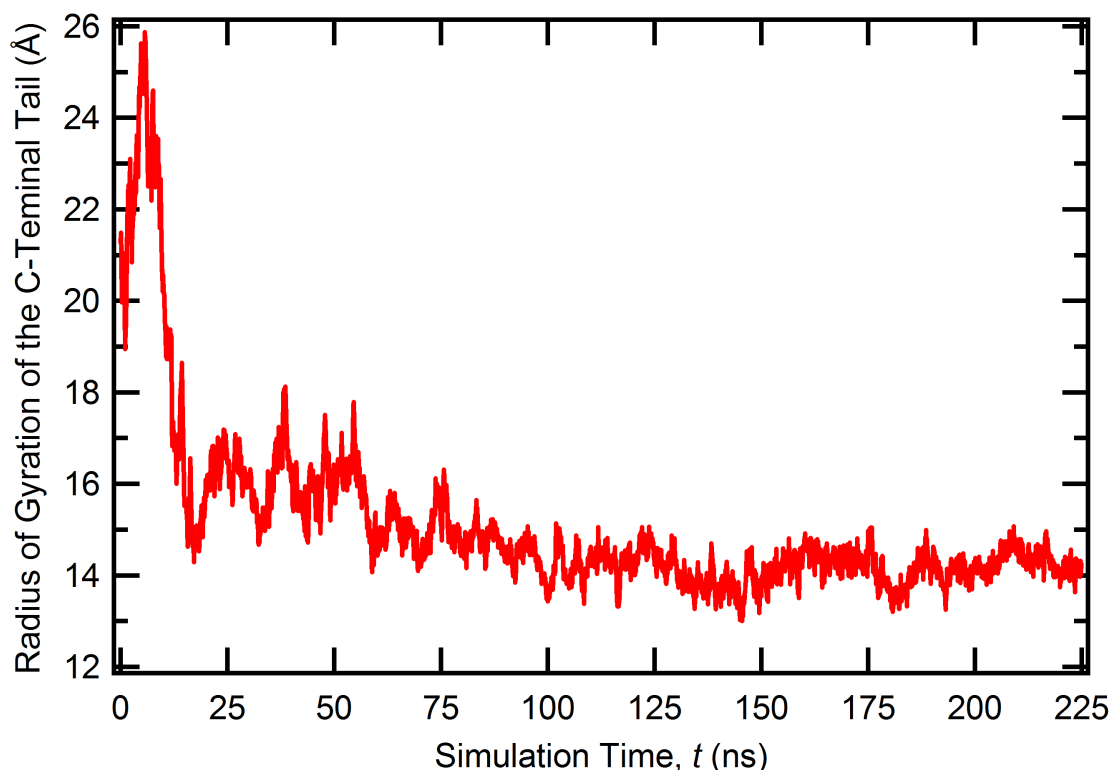
Figure 9.7: Evolution of the radius of gyration of the C-terminal tail of *wt* PTEN as it binds to the PC:PS membrane.

are also formed. However, all three H-Bonds and two of the salt bridges are formed between the tail and the disordered C-terminal loop that was truncated in the crystal structure and not with the body of the C2 domain (see table 9.2 for details).

Cluster Analysis

Given a large trajectory, it is useful to identify clusters or 'families' of structurally-related conformations to aid in the organization of the generated structures as well as to identify metastable states, their lifetimes and the transitions between them. While many clustering algorithms such as the 'neighbor' algorithm and 'K-medoids' algorithm have been formulated, the density-based 'common-nearest-neighbor' algorithm was recently identified as the most robust, especially in the identification of folded states of the protein [181]. We implemented the common-nearest-neighbor algorithm based on the instructions provided in the literature [181] and a brief description, along with the results of such an analysis, is provided below.

The algorithm has two parameters:

- *nndc*: A distance cutoff which identifies the volume about a given point in
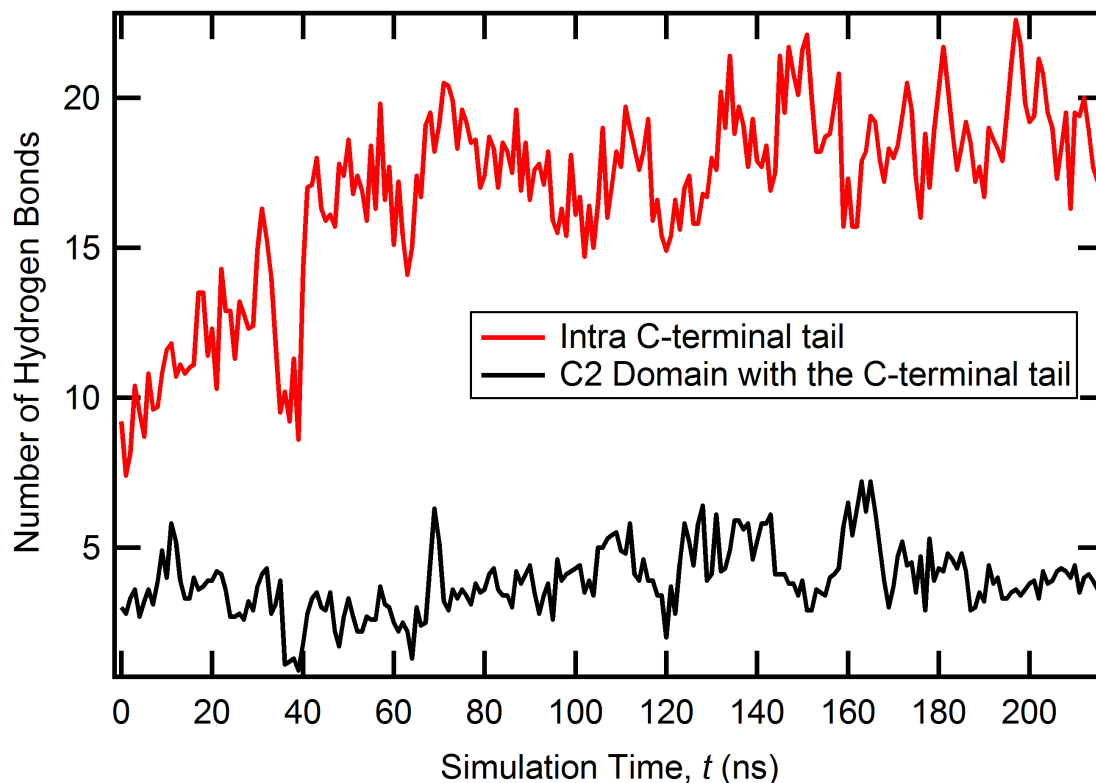
Figure 9.8: Number of hydrogen bonds formed between residues of the C-terminal tail (red) as well as between the C2 domain and the C-terminal tail (black), over the course of the production run of the simulation. A hydrogen bond is considered to be formed between a donor atom (bearing the bonded hydrogen) and an acceptor atom if the distance between the two is less than 3 Å and the angle between the donor atom, the hydrogen atom involved in bonding and the acceptor atom is less than 60°.

which a nearest neighbor can be found. To calculate this value, an RMSD matrix is calculated which consists of the RMSD of every frame of the simulation with respect to every other frame. A histogram of these RMSD values is plotted and *nndc* is identified as the RMSD value corresponding to half the probability of the first peak [see figure 9.9 (A)].

- *nnnc*: A number cutoff which is inversely proportional to the limiting density of the clusters. i.e., A small value of *nnnc* will result in a few clusters consisting of a large number of conformations and as *nnnc* is increased, new clusters are formed by splitting off from larger initial clusters. Once *nndc* is identified, we run the cluster algorithm using a range of possible *nnnc* values, 2-19 in this body of work. We then plot the number of 'large' clusters, usually consisting
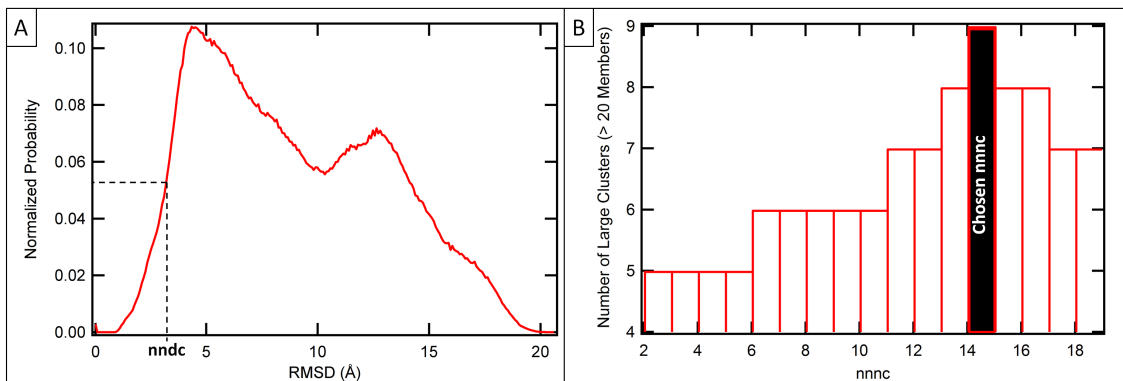
Figure 9.9: Cluster Analysis. The common-nearest-neighbor clustering algorithm makes use of two parameters: *nndc* and *nnnc*. A) *nndc* is chosen as the RMSD corresponding to half the probability of the first peak in the RMSD histogram. B) Given a value for *nndc*, the number of large clusters as a function of *nnnc* is plotted and the smallest value of *nnnc* that provides the greatest number of large clusters is chosen as the optimal *nnnc*.

of at least 1% of the total number of conformations (identified as 20 in this work), as a function of *nnnc*, as shown in figure 9.9 (B). The lowest value of *nnnc* which gives the highest number of 'large' clusters is chosen as the final *nnnc* value which is then used to identify clusters in the trajectory.

For the *wt* binding to PC:PS simulation, the parameter set used was (*nndc*=3, *nnnc*=14). The three largest clusters comprise of 67%, 7% and 6% of the trajectory population and correspond to the 76-228 ns, 39-57 ns and 24-38 ns timepoints in the simulation. The fact that the largest cluster consists of the last 152 ns of the simulation is further confirmation that the protein in the simulation has achieved and maintains an equilibrium conformation.

Orientation of the Protein

Figure 9.10 depicts the evolution of the orientation of the protein on the bilayer. The Euler angles theta (θ) and phi (ϕ) are calculated with respect to the lipids under the footprint of the protein to account for any fluctuations of the bilayer. The Euler angle psi (ψ) corresponds to the rotation of the protein about the bilayer normal – a parameter we are insensitive to in the NR measurements. (θ, ϕ) = ($0°$, $0°$) corresponds to the proposed membrane binding orientation of the protein, as described in the crystal structure [4]. There are significant fluctuations throughout the time-course of the simulations with θ having an average value of $20 \pm 8°$ and ϕ having an average value of -13 $\pm$ 5°. The average value of θ is close to the value of $30°$ predicted by the SASSIE analysis in chapter 8, given our earlier assumption that
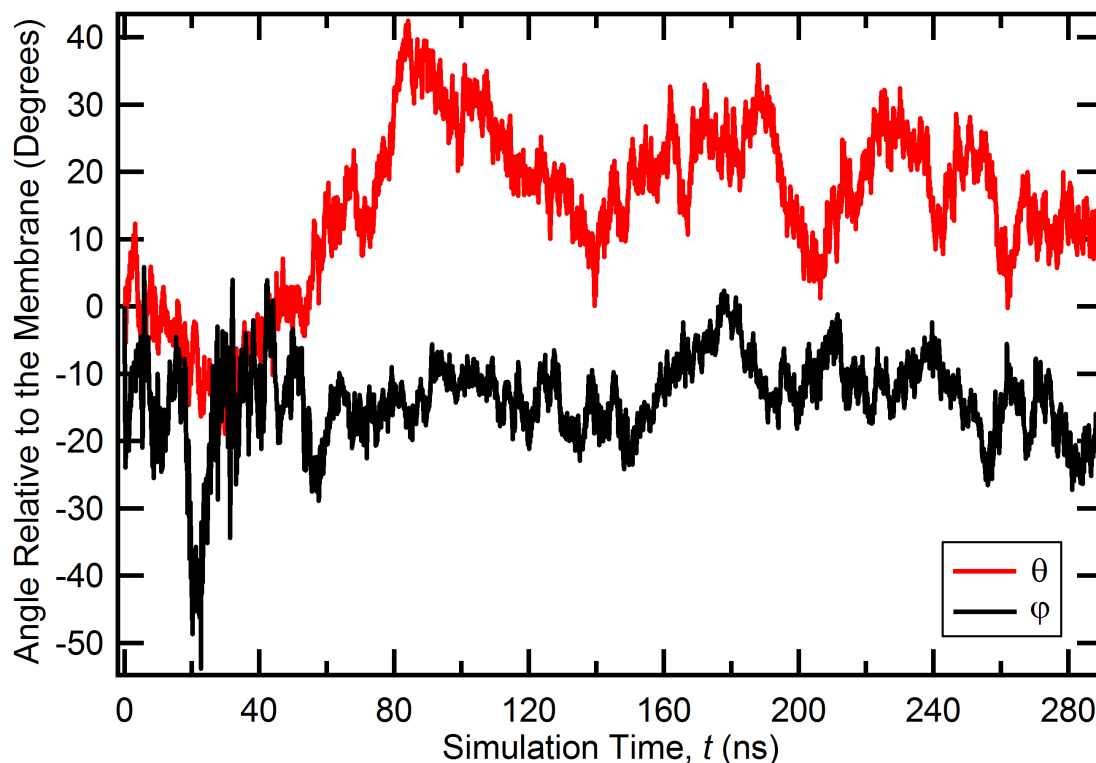
Figure 9.10: Orientation of *wt* PTEN with respect to the PS-bearing bilayer. The Euler angles θ and φ are shown in red and black respectively.

the core domains of the protein in a membrane-bound state are unchanged from the crystal structure.

Residence Time Analysis

In order to identify the PS binding sites on the protein and to compare their relative affinities, we performed residence time analysis over the entire trajectory. A lipid is considered to be interacting with a protein residue if they stay within 5 Å of each other. Given the mean-squared displacement of lipids in the distal (to the protein) leaflet (see figure 9.15), a lipid explores a circular area of radius 2.5 Å in approximately 5 ns. Consequently, we considered a lipid and residue to be 'bound' if they stayed within 5 Å of each other for at least 5 ns.

Figure 9.11 depicts the average residence time of PS lipids to every residue in the protein. In the literature [4], residues 260-269, which constitute a Lysine-rich CBR3 motif in the C2 domain, were identified as the primary PS-binding loop in PTEN. We find residues Lys260 , Asn262-Lys263 and 266-269 (Lys-Lys-Asp-Lys) partake in binding to PS of which Lysines 260 and 263 exhibit significant PS residence times.

153
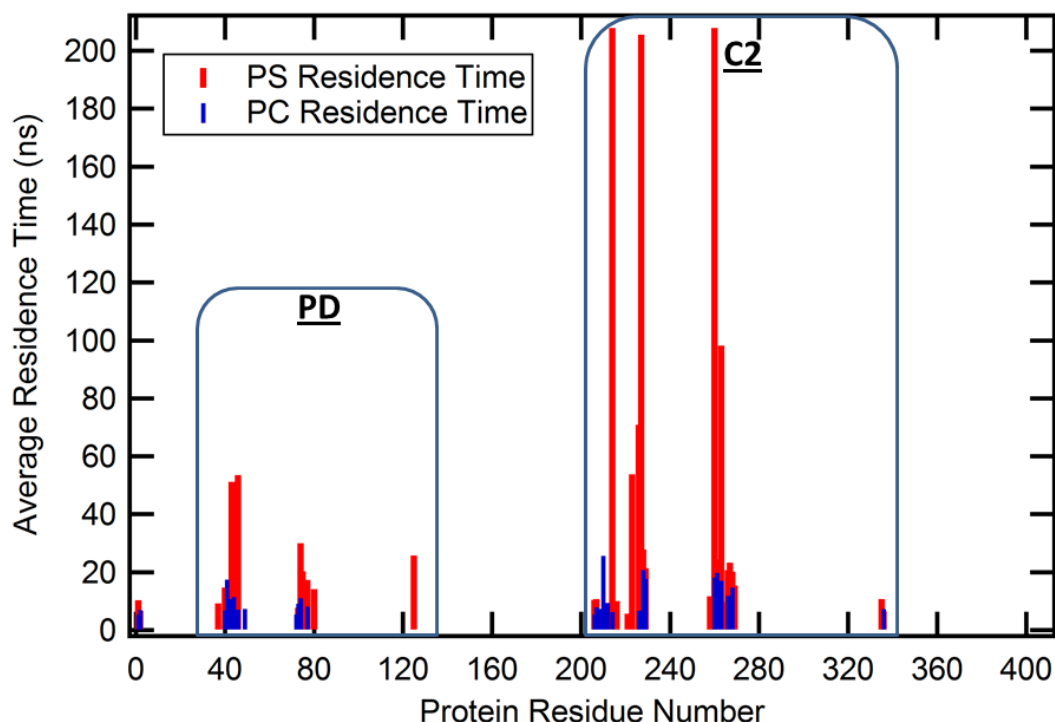
Figure 9.11: Residence time of a PS lipid (in red) to each residue of *wt* PTEN, averaged over the course of the production run of the simulation. For comparison, the residence time of PC lipids to each PTEN residue is also shown (in blue).

We also identified two other protein patches that bind, of which one consists of residues Gln214 and Val216 and the other of the basic residue Lys223 and the polar residues 226-229 (Ser-Ser-Asn-Ser), which are spatially adjacent to the CBR3 loop [see figure 9.12 (A)].

We also identified two patches in the phosphatase domain that also bind to PS, albeit weaker than those in the C2 domain. The first consists of residues 40-46 (Glu-Arg-Leu-Glu-Gly-Val-Tyr) and the second of residues 73-77 (Glu-Arg-His-Tyr-Asp) and Lys80. An analysis of the binding kinetics shows that the electrostatic field of the anionic lipids orients the protein such that the CBR3 loop is the first to interact with the membrane. It penetrates the headgroup layer allowing hydrophobic residues Met264 and Leu265 to bury into the bilayer. This brings the secondary C2 binding patches close enough to interact with the PS headgroups. Finally, the two patches in the phosphatase domain weakly associate with PS lipids [see figure 9.12 (B)].
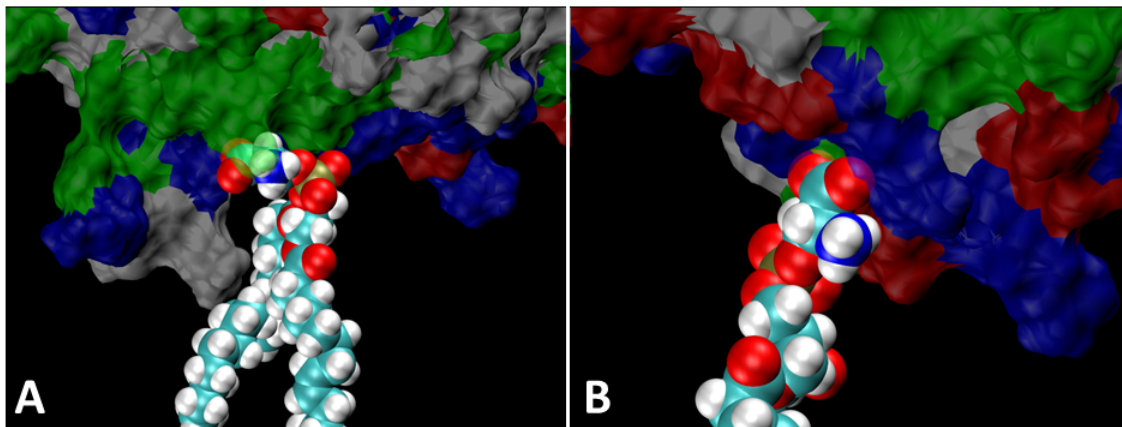
Figure 9.12: Illustration of the Binding Mechanism and Geometry of
***wt* PTEN to PS Lipids.** A) Interaction of the C2 domain with a PS lipid.
Hydrophobic residues Met264 and Leu265 penetrate the membrane while the basic
Lysines in the CBR3 motif of the C2 domain form long lasting salt bridges with
the PS lipid. B) Interaction of residues in the phosphatase domain with PS lipids.
Residues Glu43, Tyr46 and Arg74 lead the formation of short-lived electrostatic
interactions through salt bridges with PS lipids.

Flexibility of PTEN Structure

Figure 9.13 depicts the flexibility of distinct regions in the protein by plotting the
evolution of the RMSD of the protein with respect to the initial configuration. As
expected, the three disordered portions of the protein: the N-terminal tail, a C2
domain loop and the C-terminal tail, are the most flexible and find a stable RMSD
80 ns into the production run of the simulation. On the other hand, the core of
the phosphatase and C2 domains are very stable and do not change much over the
course of the simulation.

Impact of the Protein on the Bilayer

Apart from studying the effect of membrane association on the protein, we also ex-
amined the alteration in bilayer properties. We see an impact of protein binding on
the density and thickness of the bilayer. The area per lipid of the PC:PS = 2:1 mem-
brane decreased slightly from 64.6 ± 0.4 Å [see figure 9.14 (A)] to 63.8 ± 0.5 Å [see
figure 9.14 (C)] upon the addition of protein. This was accompanied by a small
increase in the hydrophobic thickness of the membrane from 30.4 ± 0.2 Å [see fig-
ure 9.14 (B)] to 30.8 ± 0.2 Å [see figure 9.14 (D)]. Neutron reflectivity measurements
(described in chapter 7) performed on a *wt* PTEN bound to a PC:PS stBLM system
had shown a negligible change in membrane thickness (given the larger uncertain-
ties in NR data as compared to MD simulation data) upon protein association,
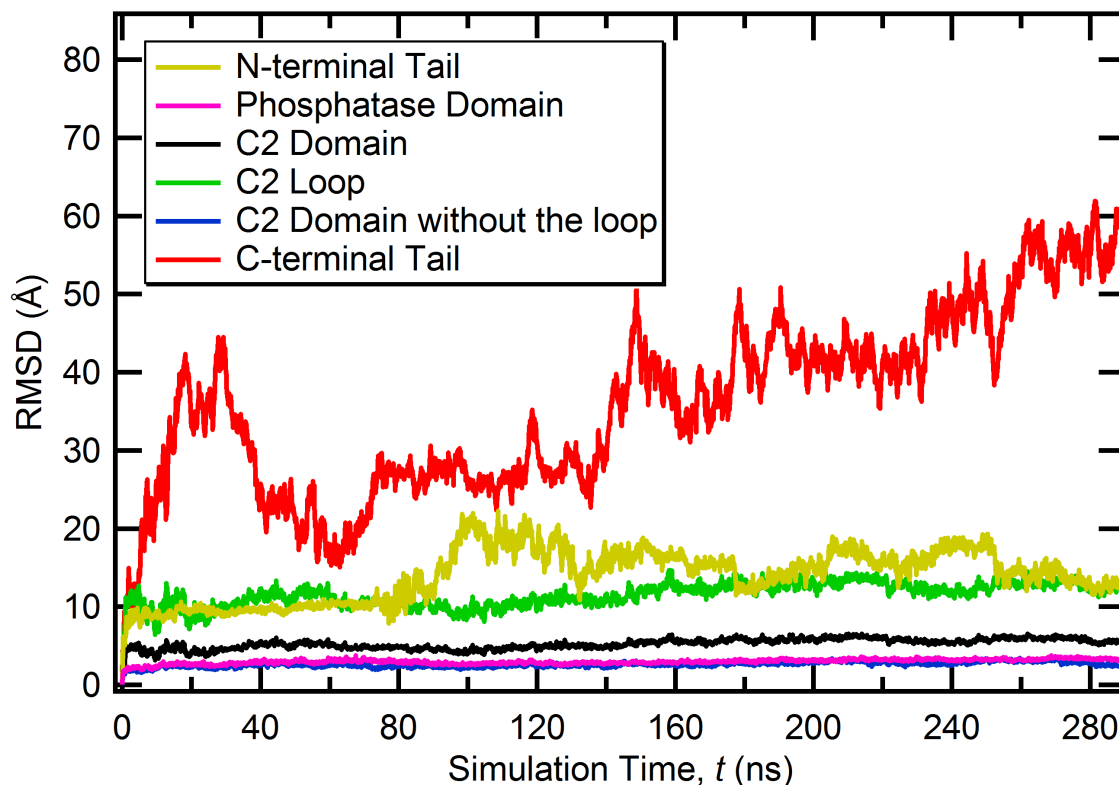
Figure 9.13: RMSD of the various regions of the protein from the starting configuration.

consistent with the simulation result.

A key measure that is very sensitive to perturbations is the fluidity of the membrane (see figure 9.15). Lipids distal to the protein have a diffusion coefficient of $7.3 \pm 0.5\ \mu m^2/s$, be they DOPC or DOPS. Proximal DOPC lipids are 40% slower with a diffusion coefficient of $4.3 \pm 0.5\ \mu m^2/s$ while proximal DOPS lipids are nearly 50% slower at $3.8 \pm 0.3\ \mu m^2/s$. If we focus on three DOPS lipids that partake in protein binding, their diffusivity is greatly hindered ($1.5 \pm 0.1\ \mu m^2/s$) as are those of adjacent DOPC lipids ($2.9 \pm 0.2\ \mu m^2/s$).

In general, the absolute values of the diffusion coefficients obtained from MD simulation data are considered to be inaccurate, mainly due to imperfect parameterization of the system. However, the relative differences between different diffusion coefficients are reliable and allow us to illustrate the adverse impact of PTEN binding on the diffusivity of lipids in the membrane, primarily due to the bound PS lipids acting as obstacles to the motion of surrounding lipids that results in hindered diffusion. There is no evidence of any clustering of PS lipids post-PTEN association, at least not on the time scale of the simulation.

156
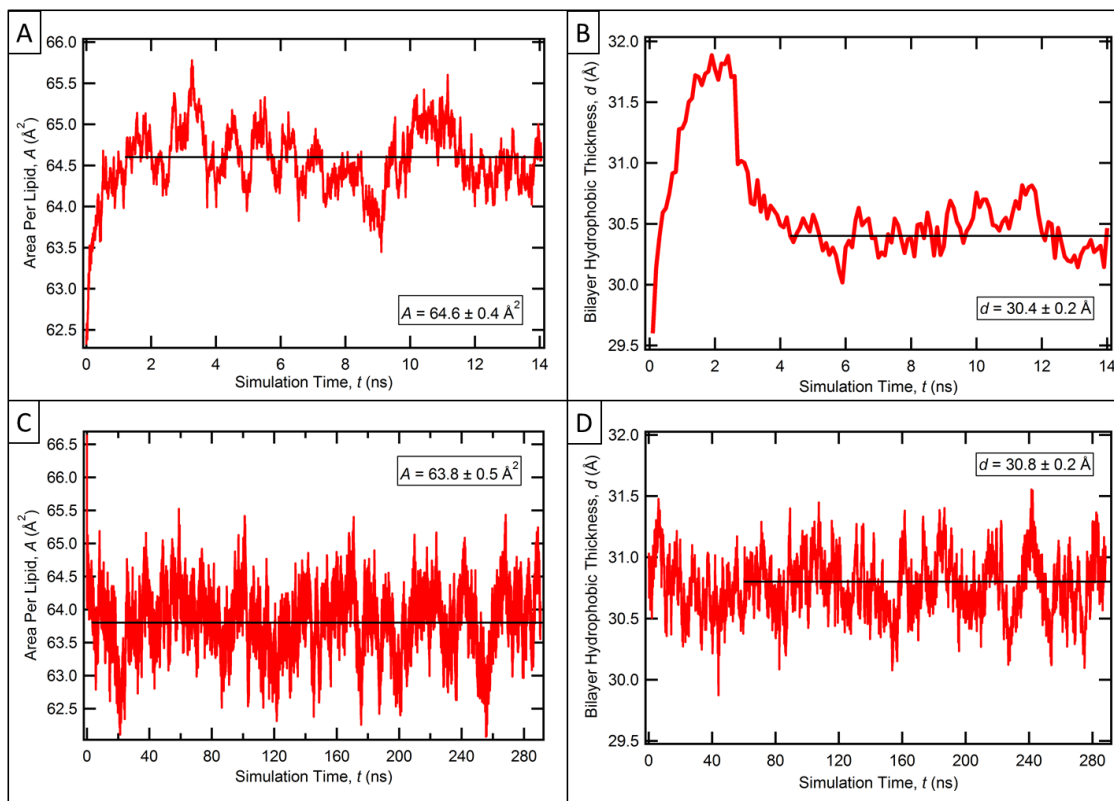
Figure 9.14: A) Evolution of the area per lipid (APL) of the PC:PS membrane (simulated without protein) over the course of the equilibration run. The APL reaches an equilibrium value of 64.6 ± 0.4 Å^2 2 ns into the simulation. B) Evolution of the hydrophobic thickness of the PC:PS bilayer that was simulated without protein. It achieves an average value of 30.4 ± 0.2 Å 4 ns into the simulation. C) Evolution of the area per lipid (APL) of the PC:PS membrane as *wt* PTEN associates with it. The average value of the APL is 63.8 ± 0.5 Å^2, lower than that of the protein-free membrane. D) Change in hydrophobic thickness of the PC:PS bilayer as *wt* PTEN associates with it. The black curve represents the first 60 ns of the simulation that was considered to be the equilibration period and was therefore excluded from detailed analysis. It achieves an average value of 30.8 ± 0.2 Å which is slightly thicker than that of the protein-free membrane.

9.4.2 *wt* PTEN in Solution

Overall, the structure of *wt* PTEN in solution is similar to the crystal structure. However, there are differences with the membrane-bound state of the protein which we sought to investigate. In particular, the C-terminal tail adopted a very distinct conformation, which is described in detail below.
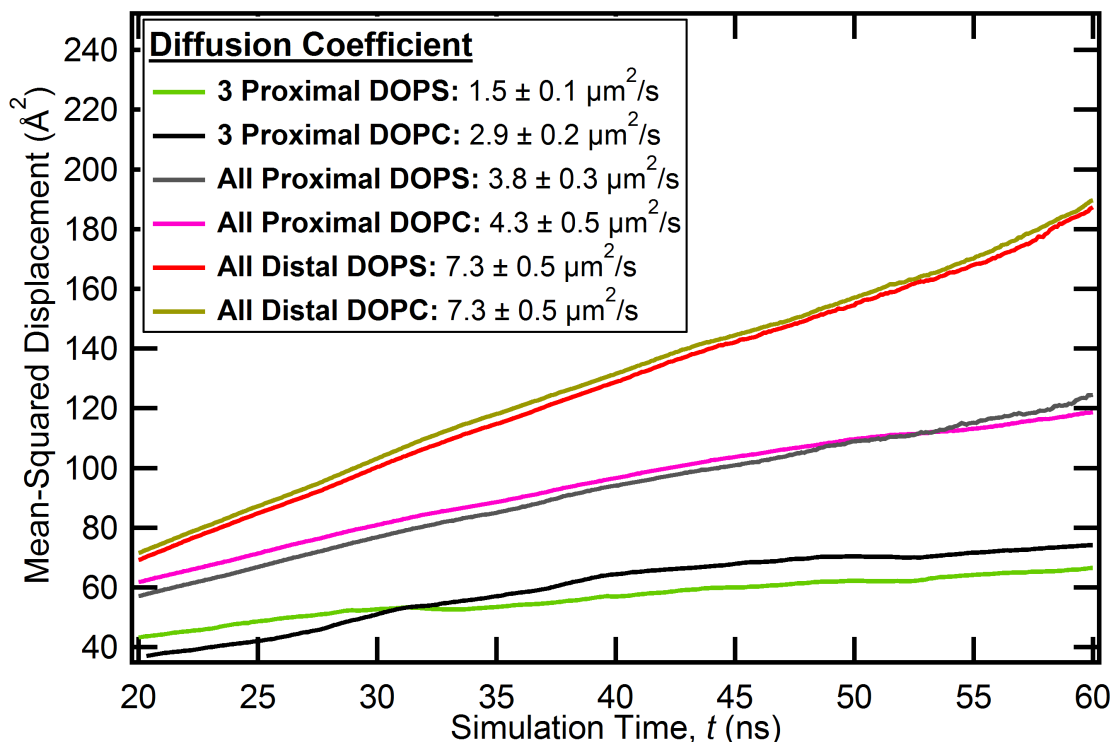
Figure 9.15: Mean-squared displacement of various lipid groups in the membrane, over the course of the *wt* PTEN binding to PC:PS molecular dynamics simulations. From the slope of each curve, the corresponding diffusion coefficient (in $\mu m^2/s$) can be calculated (see legend).

Role of the C-Terminal Tail

The disordered C-terminal tail behaves very differently in solution than in the membrane bound state (see figure 9.16). For approximately 50 ns, the tail is spatially separated from the core domains of the protein. However, it is at this time point that salt bridges are formed between Arg189-Asp368 (and briefly with Asp371), Lys221-Asp384 and Lys223-Asp386 forming the first contacts between the tail and the C2 domain. The bridge formed by Lys221 alternates between Asp384 and Asp386 while the bridge formed between Lys223 switches between Asp386 and Glu390, ensuring that for the majority of the simulation one of these contacts persists. In addition to these salt bridges, the others that are subsequently formed include Lys260-Glu394, Lys266-Glu405, Lys267-Glu390, Lys289-Glu358 and Arg308-Glu352.

Figure 9.17 depicts the number of hydrogen bonds formed between the C-terminal tail and the C2 domain (see table 9.4 for details). At the start of the simulation there are only two such bonds. At the 24 ns mark, both those bonds are broken and what follows is a linear increase in the number of hydrogen bonds
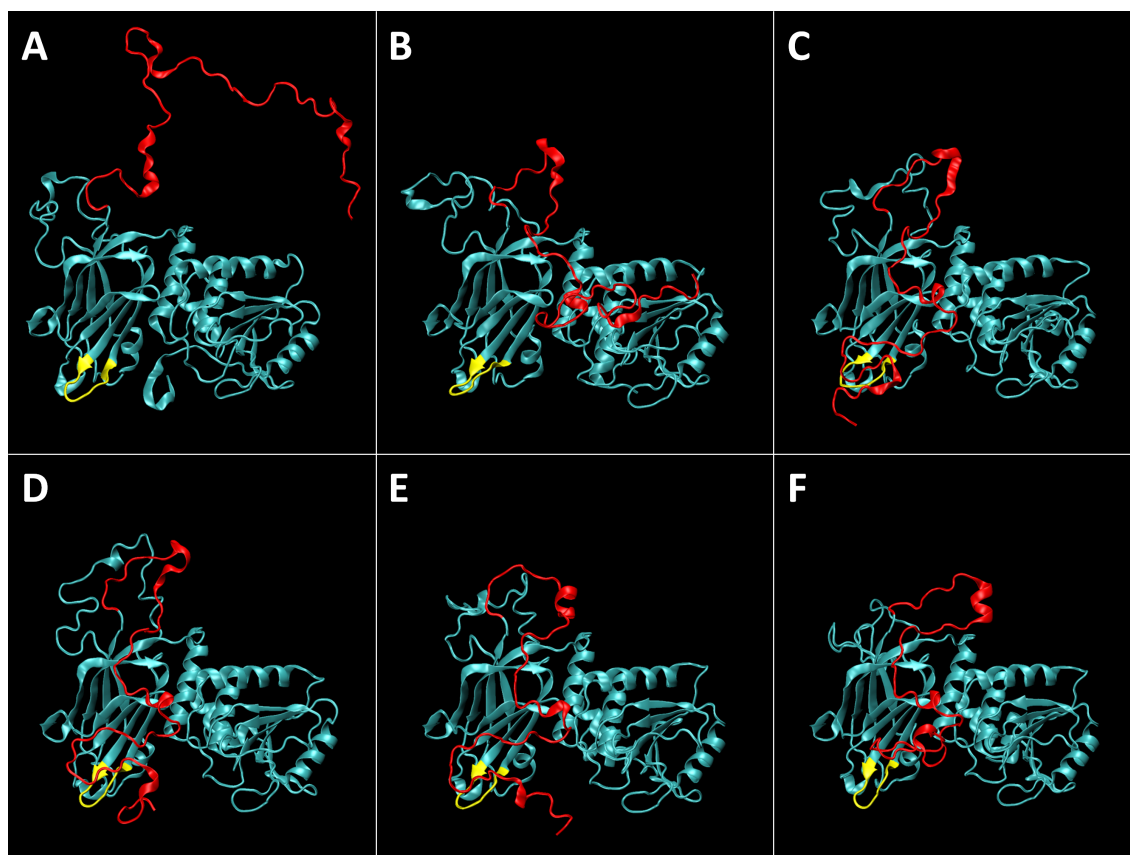
Figure 9.16: Evolution of the C-terminal Tail of the Protein, Over the Course of the *wt* PTEN in Solution Molecular Dynamic Simulations. A) 0 ns, B) 70 ns, C) 140 ns, D) 210 ns, E) 280 ns and F) 350 ns timepoint of the simulation. Residues 260-269, which constitute the CBR3 PS-binding motif in the C2 domain, are colored in yellow and residues 352-411, which constitute the C-terminal tail, are colored in red. The protein has been rotated by 180 degrees about the *z*-axis such that the phosphatase domain is on the right and the C2 domain is on the left.

formed as a result of contacts being made between the end of the C-terminal and the core of the C2 domain, stabilizing at an average of 8 H-Bonds. This implies that the initially observed salt bridges inhibit the reconfiguration of the tail and therefore need to be broken.

The various loops that form along the tail, in the state where it is bound to the surface of the C2 domain, are frequently in serine or threonine rich regions (see figure 9.18). In particular, residues Ser380, 382-383 (Thr-Thr) and Ser385, which are PEST sites that have been shown to be phosphorylated, form a loop making them solvent accessible. It is hypothesized that the phosphorylation of the C-terminal tail
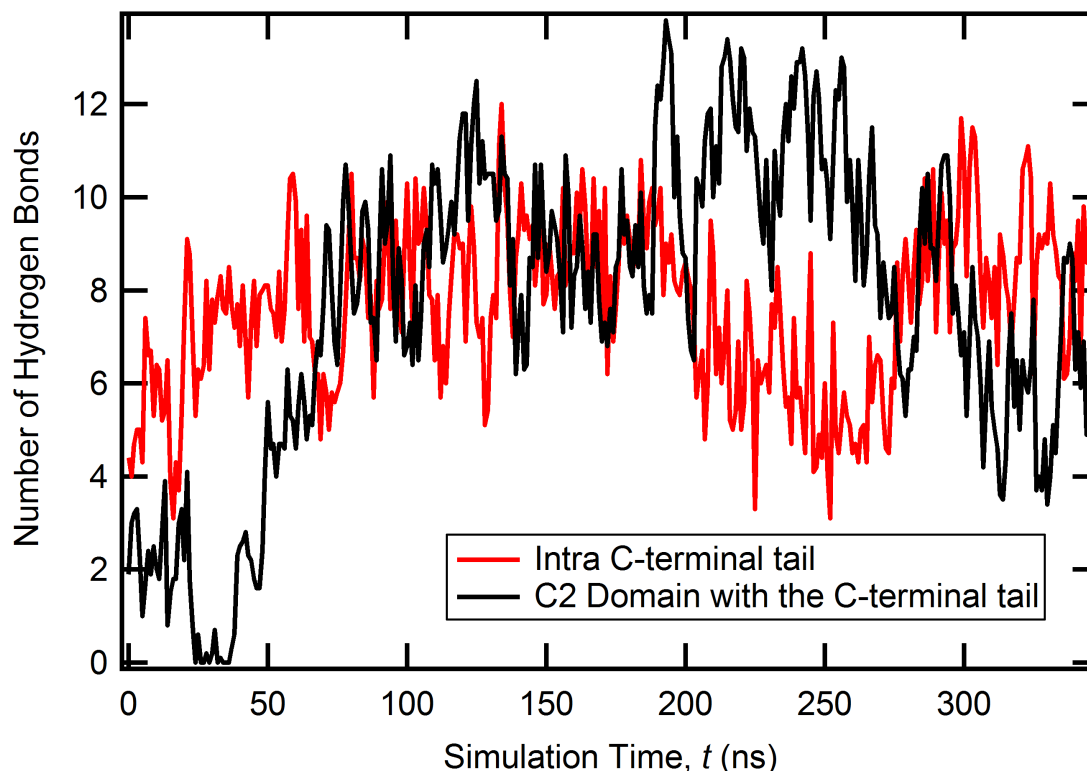
Figure 9.17: Depiction of the number of hydrogen bonds between residues of the C-terminal tail (red) as well as between the C2 domain and the C-terminal tail (black) for the *wt* PTEN in solution simulations. A hydrogen bond is considered to be formed between a donor atom (bearing the bonded hydrogen) and an acceptor atom if the distance between the two is less than 3 Å and the angle between the donor atom, the hydrogen atom involved in bonding and the acceptor atom is less than 60°.

results in an interaction between the tail and the PS-binding loop of the C2 domain, thereby preventing membrane association and locking the protein in solution [182]. This regulation of PTEN is considered critical in maintaining various pools of PTEN, only a small fraction of which is capable of membrane association [10]. In fact, a closer examination of the protein's structure in solution indicates that Lys221 and Lys223 are spatially adjacent to Thr382, Thr383 and Ser385. Phosphorylation of these PEST residues could result in salt bridging with the aforementioned Lysines, thereby increasing the lifetime of the 'closed' state [182] of PTEN. This could occur either by the increased negative charge provided by the phosphorylation resulting in enhanced association with basic residues or by a conformational change in the protein or by both.

Unlike in the membrane bound state, the number of hydrogen bonds formed

Figure 9.18: Depiction of the serines (dark green) and threonines (dark blue) along the C-terminal tail. The light green and light blue residues depict the serines and threonines, respectively, that are known phosphorylation sites (residues 370, 380, 382, 383 and 385) that are part of PEST motifs. In solution, the extended C-terminal tail interacts with the CBR3 motif of the C2 domain, thereby making the phosphorylation sites solvent accessible.

within the C-terminal tail in solution is almost constant (see figure 9.17 and table 9.3 for details) at around 8, which is far fewer than the 19 that are formed in the membrane-bound state. Three salt bridges are also created between residues within the C-terminal tail: Arg378-Glu373, Arg378-Asp381, Lys402-Glu388.

Interaction between the C-terminal tail and the CBR3 PS-binding motif

We have shown that the C-terminal tail of *wt* PTEN interacts with the C2 domain in a membrane-free environment. If we look closer at the interactions, we see that the transition of the C-terminal tail from a polymer-like state in solution to its C2-associated state follows a structured sequence of events beginning with

Table 9.3: Hydrogen bonds formed between residues of the C-terminal tail for *wt* PTEN in solution.

Donor		Acceptor		Occupancy (%)
Residue	**Chain**	**Residue**	**Chain**	
THR383	Main	TYR379	Main	41.5
SER364	Main	SER360	Main	27.09
THR363	Main	ALA359	Main	19.02
SER398	Side	GLU394	Main	15.56
GLU352	Main	GLU352	Side	14.99
ASP375	Main	ASP375	Side	13.83
SER364	Side	SER361	Main	13.83
ASP395	Main	ASP395	Side	13.26
TYR377	Main	HIS376	Side	13.26
THR382	Main	ARG378	Main	12.68
ASP381	Main	ASP381	Side	10.95
THR383	Side	TYR379	Main	10.95

Table 9.4: Hydrogen bonds formed between the C2 domain and the C-terminal tail for *wt* PTEN in solution.

Donor		Acceptor		Occupancy (%)
Residue	**Chain**	**Residue**	**Chain**	
SER226	Side	GLU390	Side	42.65
LYS260	Side	HIS397	Main	34.58
ALA192	Main	ASP368	Main	25.65
ASN228	Side	GLU390	Side	17.58
ASN228	Side	PRO391	Main	11.24

Table 9.5: Hydrogen bonds formed between the CBR3 PS-binding motif in the C2 domain and the C-terminal tail for *wt* PTEN in solution.

Donor		Acceptor		Occupancy (%)
Residue	**Chain**	**Residue**	**Chain**	
LYS260	Side	HIS397	Main	34.58
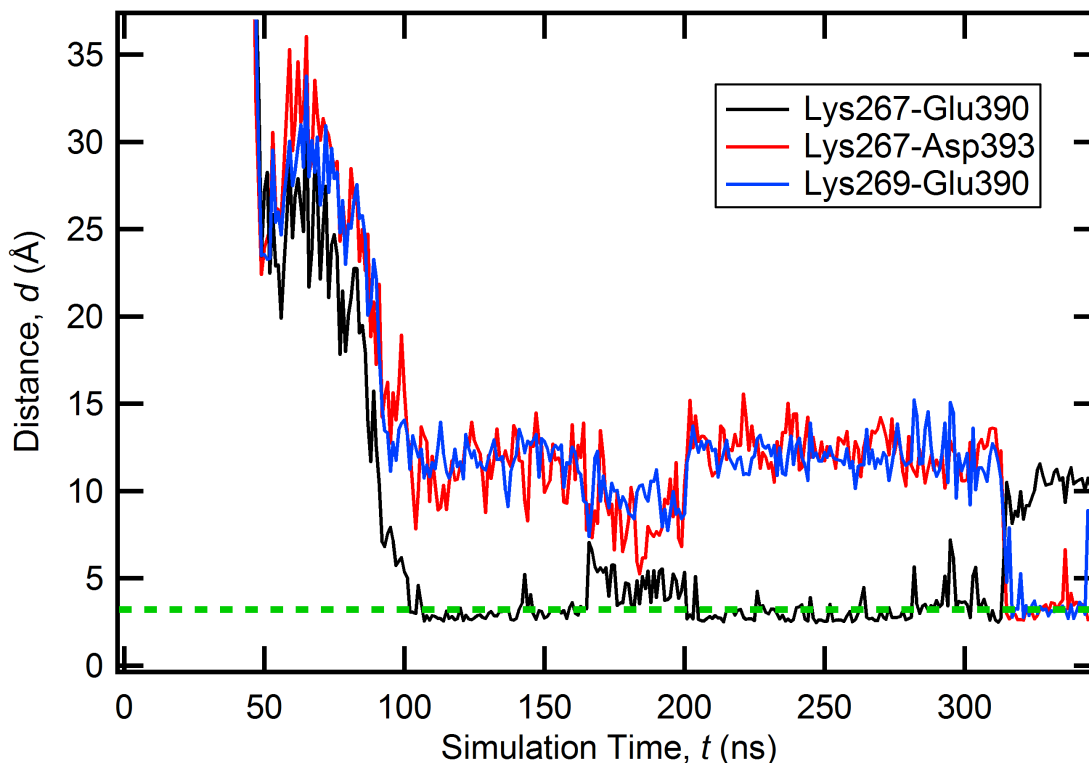
Figure 9.19: Dynamics of the formation of three salt bridges between the CBR3 PS-binding motif in the C2 domain and the C-terminal tail for *wt* PTEN in solution and bound to a membrane. A salt bridge is considered to be formed if an oxygen atom of an acidic residue is within 3.2 Å of a nitrogen atom of a basic residue (dotted green line). The distances depicted by the y-axis are between the center of mass of the oxygens in the acidic side chain and center of mass of the nitrogens in the basic side chain.

the salt bridges and hydrogen bonds described above and is followed by a zipper-like motion where the gap between the tail and the C2 domain is closed quickly (within the first 100 ns of the simulation). The tail is then stabilized in this conformation by associating with the CBR3 PS-binding motif in the C2 domain. Only one hydrogen bond (see table 9.5) partakes in this interaction but all six Lysines are involved in salt bridging indicating an electrostatically driven process. The relevant salt bridges are Lys254-Asp386, Lys260-Asp393, Lys260-Glu394, Lys263-Glu394, Lys266-Glu388, Lys266-Glu405, Lys267-Asp386, Lys267-Glu390, Lys267-Asp393, Lys269-Asp386 and Lys269-Glu390. Figure 9.19 depicts the dynamics of the formation of these salt bridges. The salt bridge between Lys267 and Glu390 is formed 102 ns into the simulation and persists till the 313 ns mark when it is broken but immediately replaced by a bridge between Lys267 and Asp393 with the Glu390

now forming a salt bridge with Lys269.

Cluster Analysis

For the *wt* in solution simulation, the parameter set used for the common-nearest-neighbor clustering algorithm (described in section 9.4.1) was (*nndc*=3, *nnnc*=6). The three largest clusters comprise of 50%, 18% and 8% of the trajectory population and correspond to the 181-357 ns, 118-181 ns and 88-118 ns timepoints in the simulation. Just as in the PS-binding simulations, the largest cluster consists of the last 177 ns of the simulation and is further confirmation that the protein in the simulation has achieved and maintains an equilibrium conformation.

Flexibility of PTEN Structure
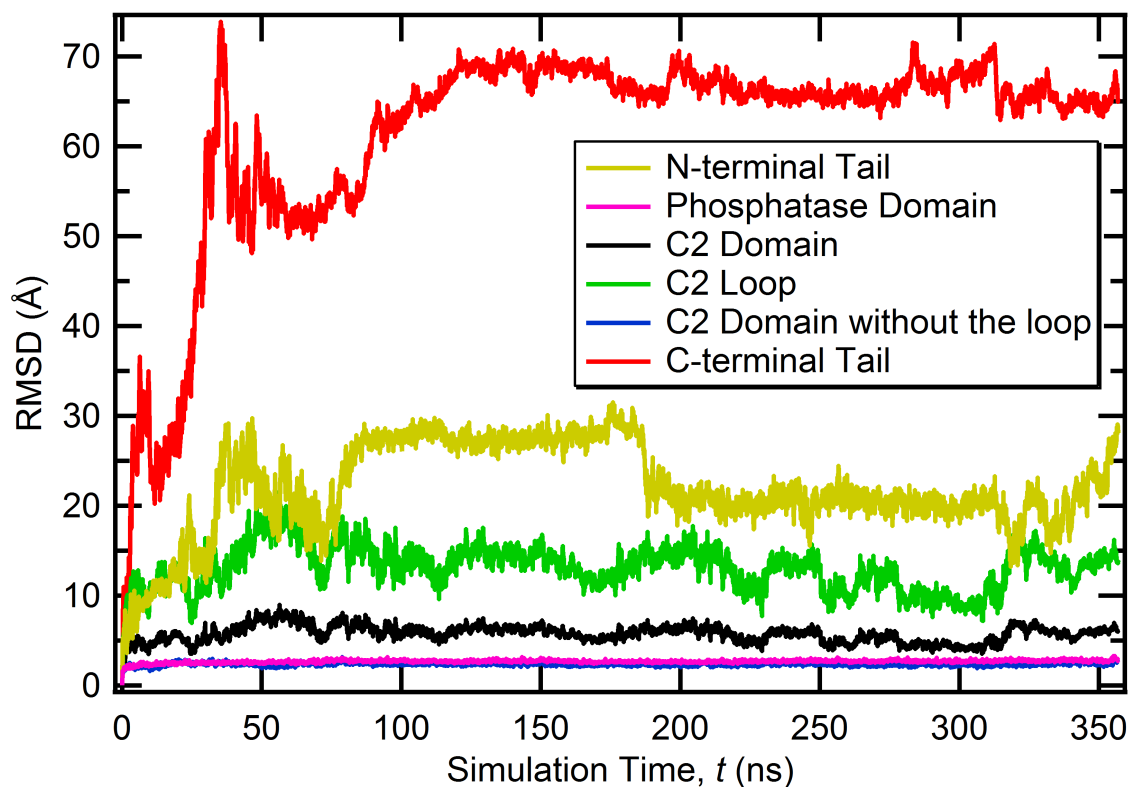
Figure 9.20: Evolution of the RMSD of various regions of the protein, with respect to the initial configuration, depicting their flexibility over the course of the production run of the molecular dynamic simulations.

Figure 9.20 illustrates the flexibility of the various regions over the course of the simulation. Just as in the PS-binding simulation, the disordered N-terminal and

C-terminal tails as well as the truncated internal C2 domain loop show the highest RMSD from the initial configuration while the core domains are relatively rigid. The only difference between the membrane-bound simulation and the solution simulation is that in the latter the N-terminal tail is more flexible possessing an averaged RMSD of 21 Å compared to 15 Å in the former.

9.4.3 DOPC:DOPS:PI(4,5)P$_2$=65.74:32.41:1.85 + *wt* PTEN

Determining the Boundary Between Equilibration and Production
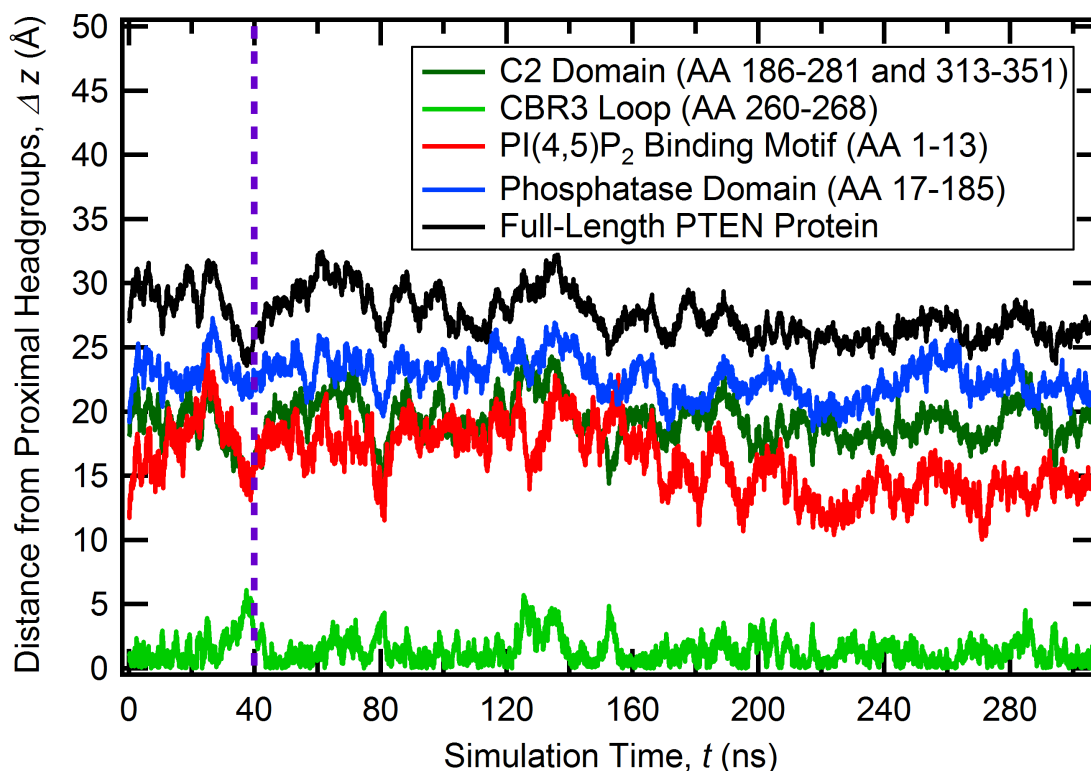
Figure 9.21: Distance between the different PTEN domains and the proximal (to the protein) lipid headgroups of the PC:PS:PI(4,5)P$_2$ membrane over the course of the simulation. The dashed line in purple at the 40 ns time point corresponds to the boundary between the equilibration and production run.

Figure 9.21 depicts the distances between the different domains of the protein and the proximal (to the protein) lipid headgroups. Table 9.6 compares these distances with those obtained from the *wt* PTEN binding to PS simulations described earlier (see section 9.4.1). Because systematic drifts were still observed during the first

Table 9.6: Comparison of the distance between center of mass of various PTEN domains and the proximal lipid headgroups when PTEN is bound to a PS-bearing membrane or a PS+PI(4,5)P$_2$-bearing membrane.

PTEN Domain	PS System	PS+PI(4,5)P$_2$ System
PI(4,5)P$_2$ Binding Module	23 ± 3 Å	16 ± 3 Å
Phosphatase Domain (PD)	24 ± 2 Å	23 ± 2 Å
C2 Domain	20 ± 2 Å	19 ± 2 Å
CBR3 Motif	3 ± 2 Å	1 ± 1 Å
Entire Protein	27 ± 2 Å	27 ± 2 Å

40 ns, that period was considered equilibration and the production run includes time points from 40 ns onwards. Most of the distances are unchanged between the two simulations except for the CBR3 PS-binding motif in the C2 domain which is slightly closer to the proximal lipid headgroups and the PI(4,5)P$_2$ binding module (PBM) which is nearly 7 Å closer indicating an interaction with the PI(4,5)P$_2$ lipids which was not present in the PC:PS simulation.

Comparison of *in vitro* and *in silico* nSLD Profiles

Figure 9.22 compares the neutron scattering length density (nSLD) profile obtained from the neutron reflectivity (NR) experiments and from the molecular dynamics (MD) simulations for *wt* PTEN binding to the PS+PI(4,5)P$_2$ membrane. At the current level of interpretation, the characteristic features in the protein's nSLD profile in the MD simulations are 8-10 Å closer to the proximal lipid headgroups than in the NR experiments. This could imply that the 300 ns simulation has not yet reached equilibrium with respect to its ability to generate the equilibrium ensemble of conformations detected by the NR measurements. Or the interpretation of the NR results could be off by assuming a coherent, in-plane structure of the bilayer where in fact there is in-plane phase segregation that's not accounted for in the model. Alternatively, it may be the case that 1.85 mol% of PI(4,5)P$_2$ in the MD simulation bilayer is unable to impact the protein's conformation in as dramatic a fashion as the 3.5 mol% in the NR experiments. In fact, control experiments have indicated that PI(4,5)P$_2$ can be over-represented by a factor of two in tBLMs prepared in the NR wet cell by rapid solvent exchange. We plan to repeat the NR measurements using vesicle fusion instead of rapid solvent exchange to improve control over membrane composition. We will also continue to run and monitor this simulation to detect any deviation from the currently observed conformations.
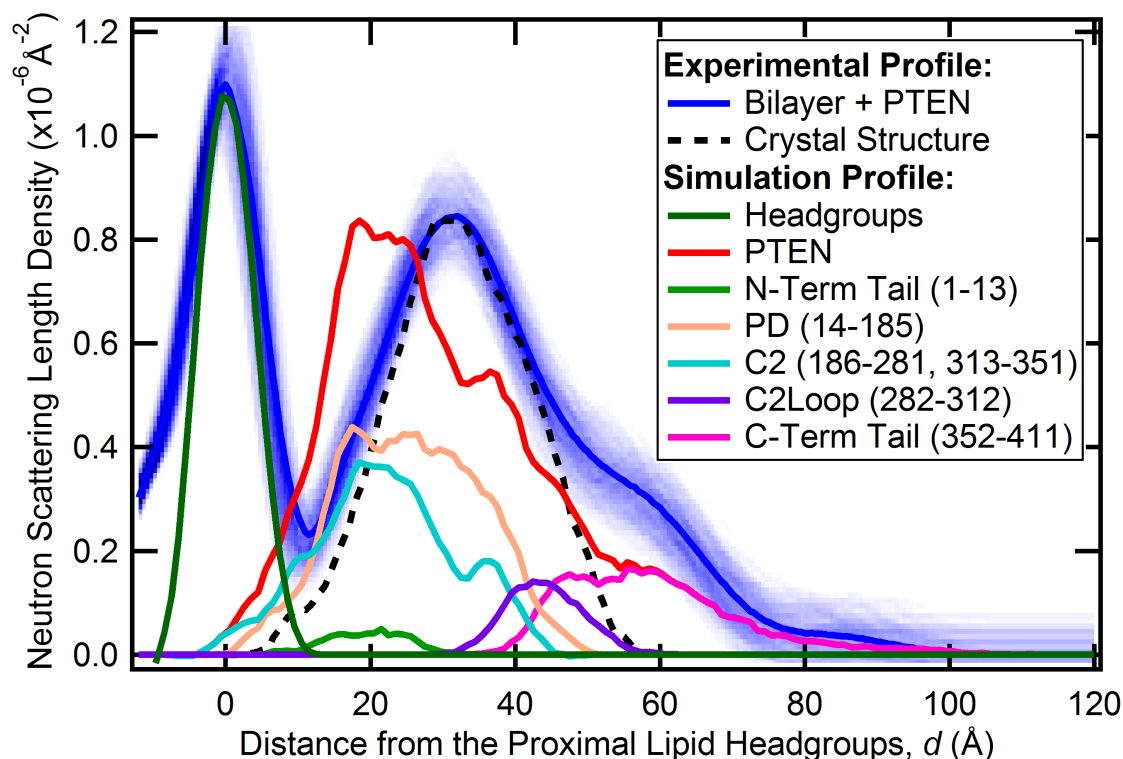
Figure 9.22: Comparison of the nSLD profile of *wt* PTEN binding to PC:PS:PIP(4,5)$_2$ from neutron reflectivity experiments (blue) and molecular dynamics simulations (red). The dotted black line shows the contribution of residues included in the crystal structure and its deviation from the overall protein envelope indicates that the C-terminal tail is located distal to the membrane.

Role of the C-Terminal Tail

Figure 9.23 shows the evolution of the protein's conformation with emphasis on the C-terminal tail. Just as in the simulation of PTEN bound to a PS-bearing membrane (see section 9.4.1), the tail initially extends before compacting within approximately 100 ns into a conformation with a radius of gyration of 14 Å by the 200 ns mark, which is identical to what was previously observed (see figure 9.24). This is expected, if electrostatic repulsion by the membrane is responsible, especially after the addition of PI(4,5)P$_2$ which is more negatively charged than a PS lipid.

We then examined the formation of hydrogen bonds by the C-terminal tail over the course of the production run. Just as in the simulation of PTEN association with a PS-bearing membrane, there are only a small number of hydrogen bonds formed between the C2 domain and the C-terminal tail (see figure 9.25) reflecting the tail's dissociation from the core domains of the protein. And once again, there are more intra-tail bonds formed in the membrane-bound state (15 H-Bonds) than
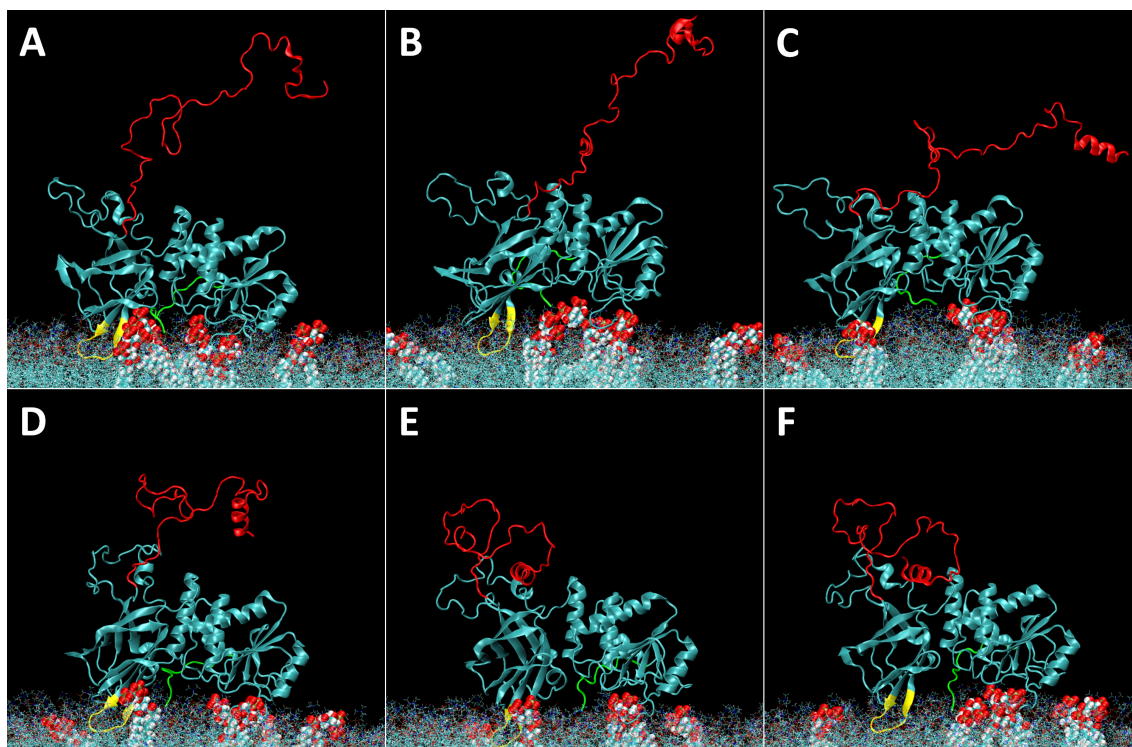
Figure 9.23: Evolution of the C-terminal Tail over the Course of the *wt* PTEN Binding to PC:PS:PI(4,5)P$_2$ Simulation. A) 0 ns, B) 60 ns, C) 120 ns, D) 180 ns, E) 240 ns and F) 300 ns timesnap of the simulation. Residues 1-13, which constitute the PI(4,5)P$_2$ binding module (PBM), are colored in green, residues 260-269, which constitute the CBR3 PS-binding motif in the C2 domain, are colored in yellow and residues 352-411, which constitute the C-terminal tail, are colored in red. The PI(4,5)P$_2$ lipids are shown in van der Waals (VDW) representation while other lipids are depicted in the 'lines' mode. The protein has been rotated by 180 degrees about the *z*-axis such that the phosphatase domain is on the right and the C2 domain is on the left.

in the solution state (8 H-Bonds) as a result of the tail's compaction.

Cluster Analysis

For the simulations of *wt* binding to membranes containing PS and PI(4,5)P$_2$, the parameter set used for the common-nearest-neighbor clustering algorithm (described in section 9.4.1) was (*nndc*=2, *nnnc*=3). The three largest clusters comprise of 32%, 6% and 4% of the trajectory population and correspond to the 181-266 ns, 156-171 ns and 171-180 ns timepoints in the simulation. Unlike the other simulations, the largest cluster accounts for less than half of the total simulation, indicating a large variability in the conformation of the protein and suggesting the need for a
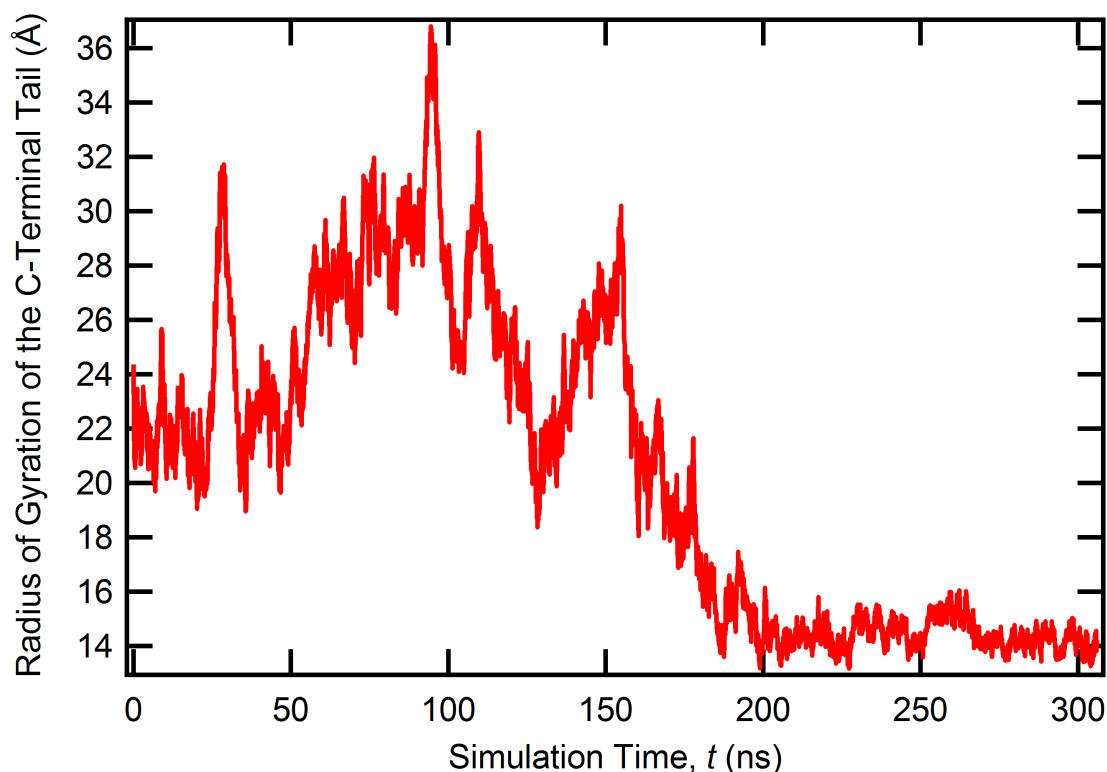
Figure 9.24: Evolution of the radius of gyration of the C-terminal tail of *wt* PTEN as it binds to a PC:PS:PIP$_2$ membrane.

longer simulation.

Orientation of the Protein

Figure 9.26 depicts the evolution of the orientation of the protein on the bilayer. The relevant Euler angles, θ and φ, are defined as before. The Euler angle θ has an average value of -3 ± 6° while the Euler angle φ has an average value of 8 ± 7°. The SASSIE analysis (see chapter 8) had predicted a minor tilt of 10° in θ and 300° in φ. Both these sets of angles imply a minimal deviation of the protein's orientation from the crystal structure prediction.

Flexibility of PTEN Structure

Figure 9.27 shows the flexibility of the various regions of the protein by depicting the root-mean-squared deviation with respect to the configuration at the 0 ns time point, with all the conformations aligned on the crystal structure residues. As expected, the disordered N-terminal and C-terminal tails as well as the disordered internal loop in the C2 domain are the most flexible. However, both the N-terminal

169
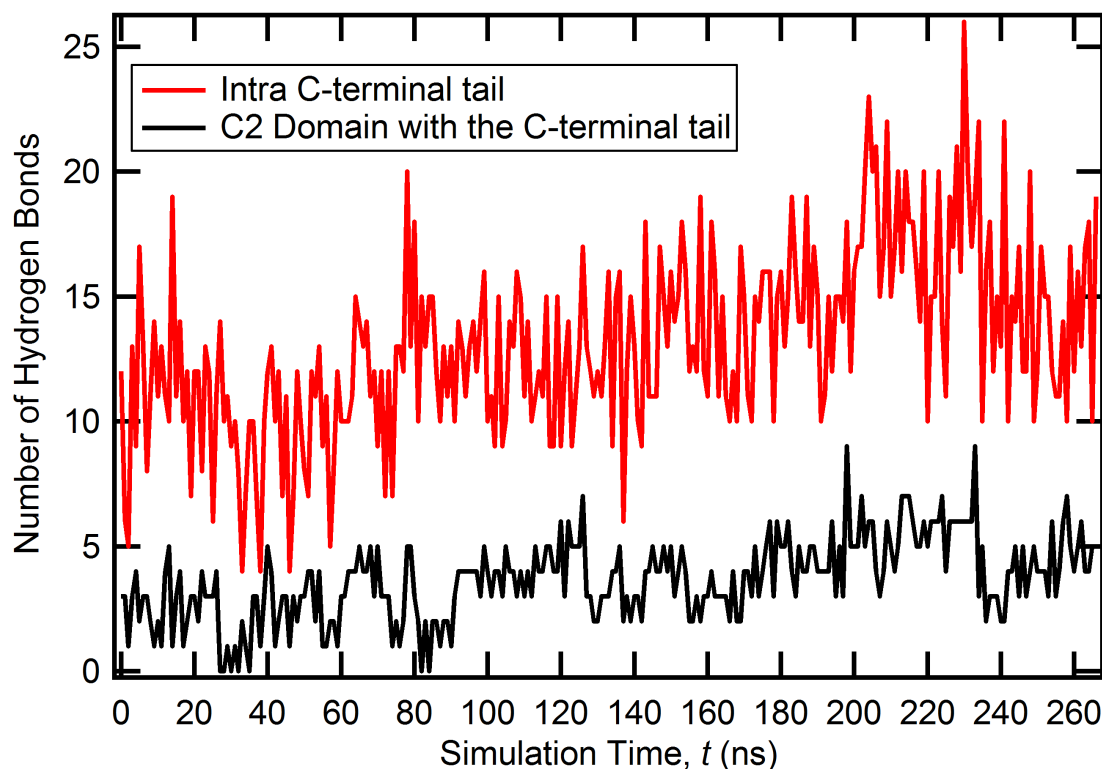
Figure 9.25: Number of hydrogen bonds formed between residues of the C-terminal tail (red) as well as between the C2 domain and the C-terminal tail (black), over the course of the production run of the simulation. A hydrogen bond is considered to be formed between a donor atom (bearing the bonded hydrogen) and an acceptor atom if the distance between the two is less than 3 Å and the angle between the donor atom, the hydrogen atom involved in bonding and the acceptor atom is less than 60°.

and C-terminal tails are more rigid than in the solution simulation. The former is because the protein is associating with PI(4,5)P$_2$ lipids while the latter is due to the aforementioned compaction and intra-tail interactions.

Impact of the Protein on the Bilayer

When *wt* PTEN was added to a PS-bearing membrane, the area per lipid decreased from 64.6 ± 0.4 Å^2 to 63.8 ± 0.5 Å^2 and the hydrophobic thickness increased slightly from 30.4 ± 0.2 Å to 30.8 ± 0.2 Å. When *wt* PTEN binds to a membrane containing both PS and PI(4,5)P$_2$, the area per lipid is further reduced to 62.9 ± 0.4 Å^2 [see figure 9.28 (A)] and the hydrophobic thickness increases to 31.1 ± 0.2 Å [see figure 9.28 (B)]. This indicates that PTEN has an ordering effect on the membrane
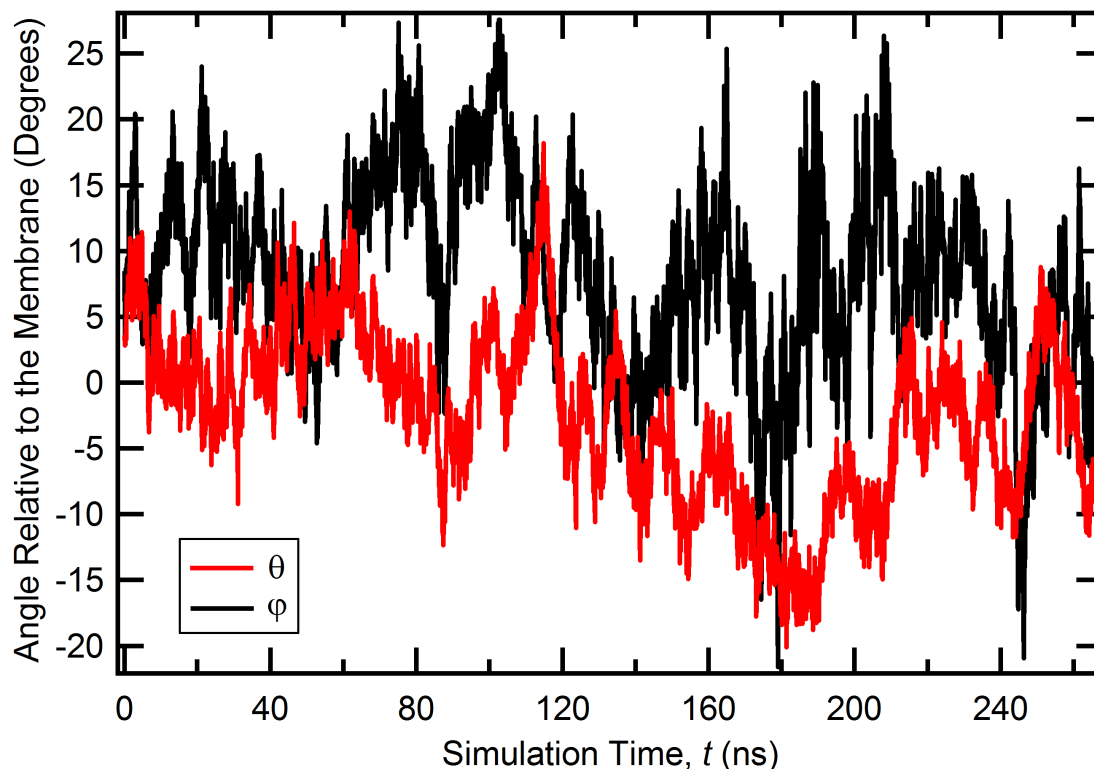
Figure 9.26: Orientation of *wt* PTEN with respect to the PS+PI(4,5)P$_2$ bilayer. The Euler angles theta (θ) and phi (ϕ) are shown in red and black respectively.

when associating with PS which is further enhanced when PI(4,5)P$_2$ is also present.

9.5 Discussion

9.5.1 Deviation from the Crystal Structure

Figure 9.29 depicts the RMSD of the core residues of the protein with respect to the crystal structure, averaged over the entire trajectory and aligned on the most stable residues in each domain (RMSD < 1 Å) for both *wt* PTEN in solution and *wt* PTEN bound to a PS membrane. We first aligned the trajectory on the PD domain and identified residues in the C2 domain there had an average RMSD from the crystal structure of less than 1 Å (176-185). We then aligned the trajectory on the C2 domain and identified residues in the PD that had an average RMSD from the crystal structure of less than 1 Å (186-199, 232-234, 240, 247, 249, 251, 275-280, 316-319 and 344-348). Finally, we aligned the trajectory on this new set of 'stable' residues (shown in green in figure 9.29) and calculated the average RMSD for all the residues of the protein that were included in the crystal structure.

171
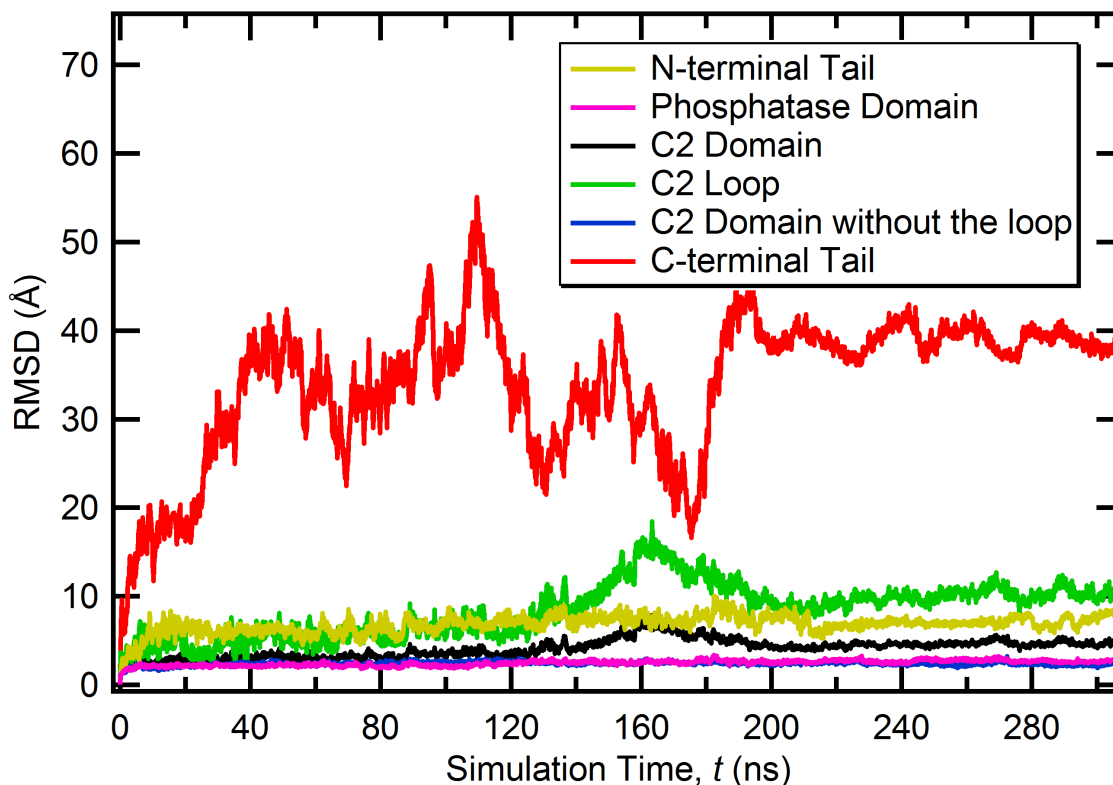
Figure 9.27: RMSD of the various regions of the protein from the starting configuration.

Overall, both models show deviation from the crystal structure, but the solution structure is less distorted than the membrane state with average RMSDs of 0.7 Å and 1.0 Å, respectively. The CBR3 loop in the C2 domain shows less deviation from the crystal structure once it binds to PS lipids than in solution. We also see a conformational change in the protein upon membrane association involving a broadening of the gap between the the membrane facing loops in the PD and C2 domain. This has the greatest impact on an α-helix in the PD domain (pα1) which shows the largest (> 4 Å) deviation from the crystal structure.

This led to a closer examination of the deviation of the equilibrium structure from the membrane binding simulations with respect to the crystal structure as shown in figure 9.30. The conformational change results in the lowering of the center of mass of the protein, thereby bringing the active site 3-4 Å closer to the plane of the membrane. This could have great physiological implications as it describes a conformational flexibility in the protein that does not significantly alter the secondary structure but allows for easier access of the catalytic site to the PI(3,4,5)P$_3$ substrate. It could also aid the hydrophobic residues in the CBR3 loop to penetrate into the headgroup region of the bilayer without forcing the PD to do so as well.
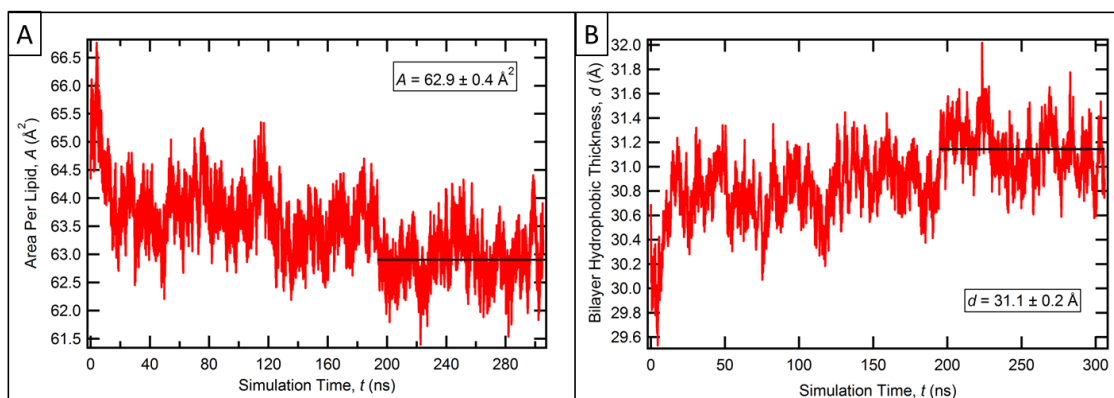
Figure 9.28: A) Evolution of the area per lipid (APL) of the PC:PS:PI(4,5)P$_2$ membrane as *wt* PTEN associates with it. The average value of the APL is 62.9 ± 0.4 Å^2, lower than that of the protein-free membrane. B) Change in hydrophobic thickness of the PC:PS:PI(4,5)P$_2$ bilayer as *wt* PTEN associates with it. The black curve represents the first 40 ns of the simulation that was considered to be the equilibration period and was therefore excluded from detailed analysis. It achieves an average value of 31.1 ± 0.2 Å which is slightly thicker than that of the protein-free membrane.

Since we do not observe such a structural deviation for *wt* PTEN in solution, we conclude that this is a membrane driven effect caused by association of the protein with the bilayer which in turn is driven by electrostatic interactions with PS lipids.

9.5.2 Difference in C-Terminal Tail Conformation

Figure 9.31 provides a comparison of the equilibrium structures of *wt* PTEN in solution and on the membrane. Aligning the core phosphatase and C2 domains allows for a comparison of the structural differences between the two structures. We have already examined the conformational change of the protein (figure 9.30), but figure 9.31 also highlights the dramatically different conformations of the C-terminal tail. In solution, the tail associates stably with the C2 domain through multiple hydrogen bonds. In contrast, on the membrane the tail stays in solution and forms no contacts with the body of the protein. Given that the C-terminal tail has a net charge of -10, it is repelled by the anionic bilayer, thereby preventing any membrane association.

   Figure 9.32 shows the packing of the C-terminal tail with the C2 domain in solution. Such an interaction reduces the exposed hydrophobic surface area by approximately 500 Å^2. This corresponds to a free energy gain of nearly 12.5 kcal/mol [183] indicating that it is energetically favorable for the tail, in the absence of the anionic membrane, to associate with the body of the C2 domain rather than with itself.
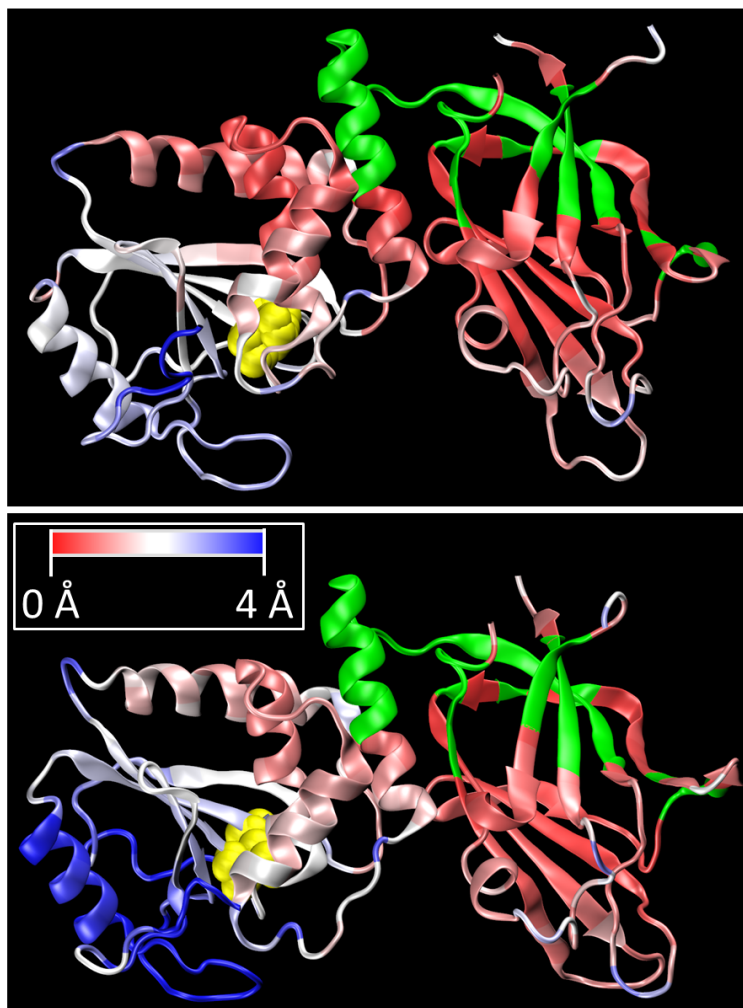
Figure 9.29: Comparison of the RMSD of the amino acids of the protein with respect to the crystal structure for A) *wt* PTEN in solution and B) *wt* PTEN bound to a PC:PS membrane, averaged over the simulations and with respect to the crystal structure. The protein was aligned on the most rigid residues (RMSD < 1 Å) in each domain (shown in green).

When PTEN binds to the membrane, the electrostatic repulsion from anionic lipids forces the tail into a compact state in solution, distal to the membrane. The entropic gain, combined with the intra-tail interactions must be able to compensate for some of the hydrophobic free energy no longer accessible in the membrane-bound state.

This alteration in the state of the disordered tail based on its interaction with a PS-bearing lipid bilayer has never before been observed. The fact that the tail is in close proximity to the PS-binding loop in the C2 domain suggests a molecular mechanism for the regulation of PTEN activity wherein phosphorylation of the

Figure 9.30: Conformational Change of the Protein upon Binding to a PC:PS Membrane. This figure overlays the crystal structure of PTEN (in red) with the equilibrium structure obtained from the MD simulations of *wt* PTEN binding to PC:PS membranes (in white). The proteins are aligned on the PD to highlight the relative motion of the C2 domain with respect to the PD.

PEST sites along the C-terminal tail result in an interaction between anionic residues on the tail and basic residues of the PS-binding loop. This would then prevent membrane association and lock the protein in a 'closed' inactive state in solution. This model explains the reason for different pools of PTEN *in vivo*, only a small percentage of which is capable of membrane association [10]. Given that we see the tail adopting a conformation that brings it close to the PS binding loop, it will be interesting to phosphorylate the tail and study this mechanism of PTEN regulation.

Contact maps allow us to identify residues that interact with one another and compare the longevity of those associations. The graph plots the Cα-Cα distance for each amino acid pair, averaged over the simulation, with darker colors indicating residues that are spatially adjacent to one another. Figure 9.33 compares the contact map of the C2 domain with the C-terminal tail for both *wt* PTEN in solution and in a membrane-bound state. In solution, several contacts are formed but the two
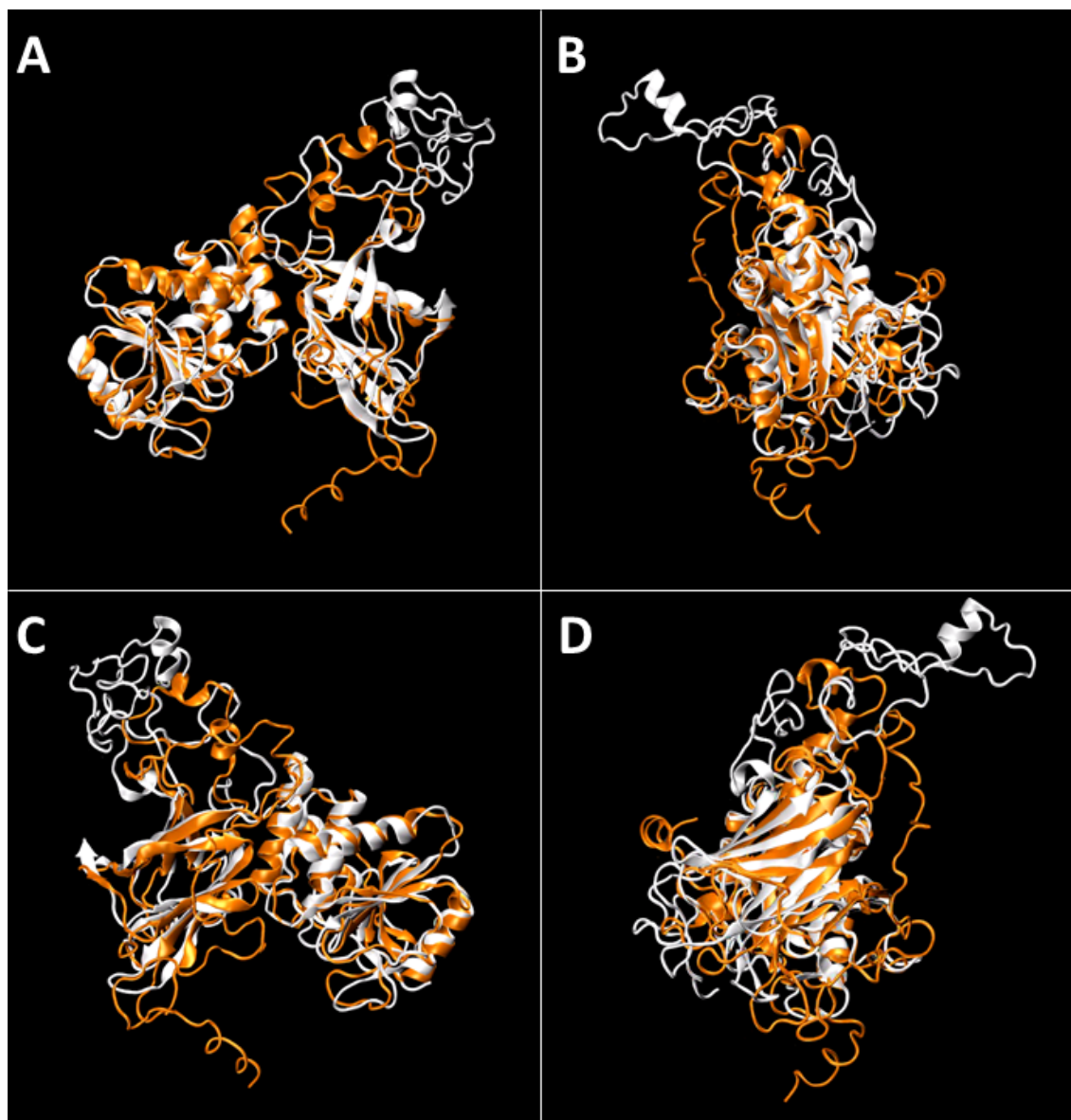
Figure 9.31: Comparison of the equilibrium state of *wt* PTEN in solution (orange) and bound to a PC:PS membrane (white). Each frame is a 90° rotation of the protein about the bilayer normal (vertical z-axis) to allow for visualization of the differences in three-dimensions.

primary ones are residues 220-226 with 373-383 and 246-251 with 371-377. In terms of secondary structure, this results in loops being formed that bring some amount of order to the otherwise disordered tail thereby allowing it to stably associate with the C2 domain. On the membrane, there is no interaction between the core of the C2 domain and the C-terminal tail. Instead, there are a few contacts formed

176
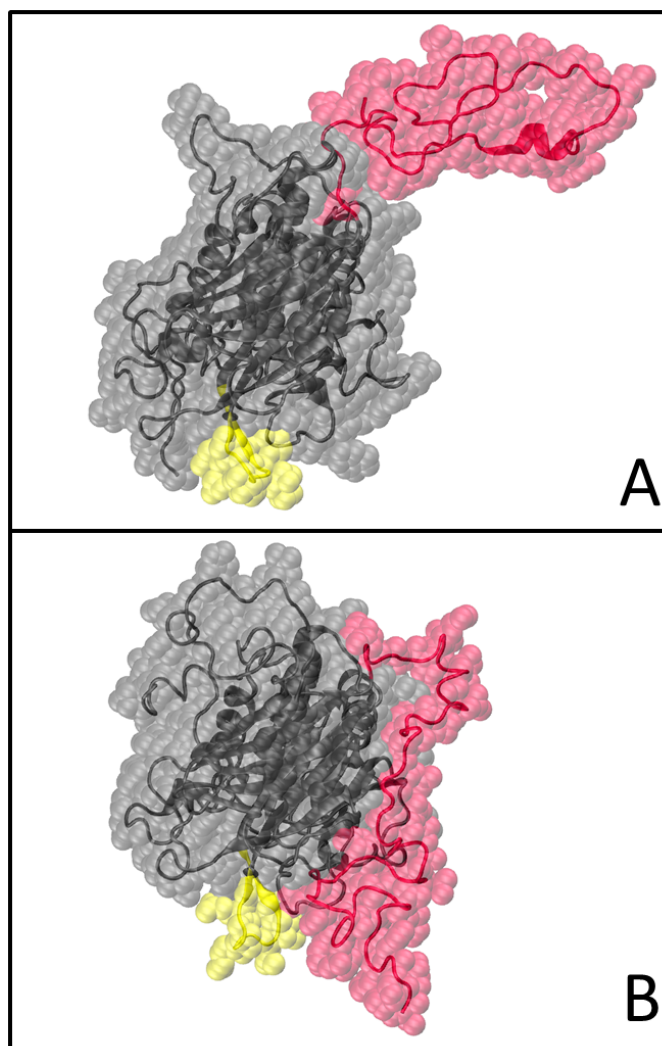
Figure 9.32: Comparison of the Packing of the C-Terminal Tail. A) In the membrane-bound state, the C-terminal tail forms minimal contacts with the body of the protein and mainly forms intra-tail bonds. B) In solution, the C-terminal tail associates with the body of the C2 domain including the CBR3 PS-binding loop [Color code: CBR3 loop in yellow, C-terminal tail in red and all other residues in gray].

between residues 302-307 in the disordered loop and residues 352-362 at the start of the tail. There are no common hydrogen bonds formed between residues in the C2 domain and the C-terminal tail in the two simulations. However, Arg189 partakes in a salt bridge with Glu353 in the PC:PS simulation and with Asp368 in the solution simulation and a Arg308-Glu352 salt-bridge is also observed in both.

Figure 9.34 depicts the intra-tail interactions for *wt* PTEN in solution and *wt*
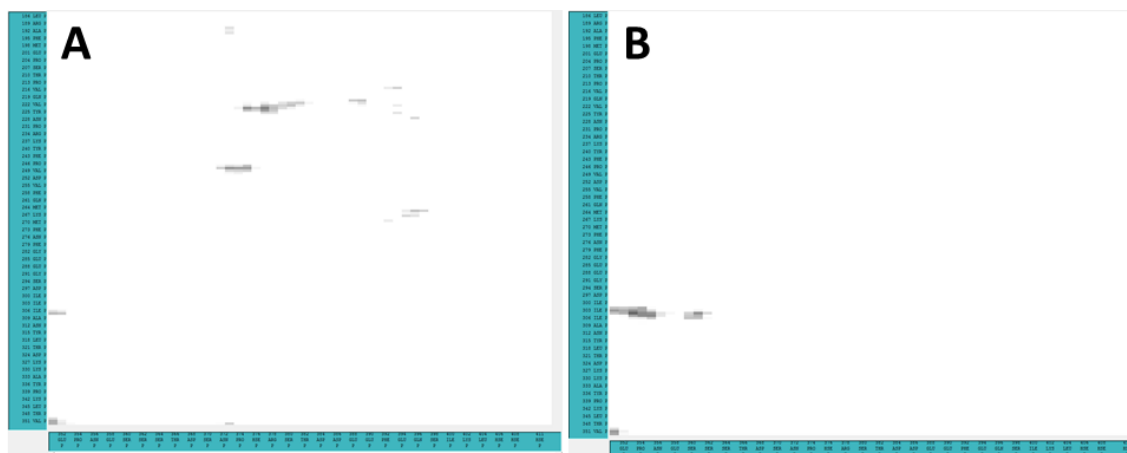
Figure 9.33: Comparison of contact maps, which depict distances between C2 domain residues and the C-terminal tail residues, averaged over the length of the production run of the simulations for A) *wt* PTEN in solution and B) *wt* PTEN binding to a PC:PS membrane. Black: 0.0 Å separation, white: ≥ 10.0 Å and a linear gray scale is used in between.
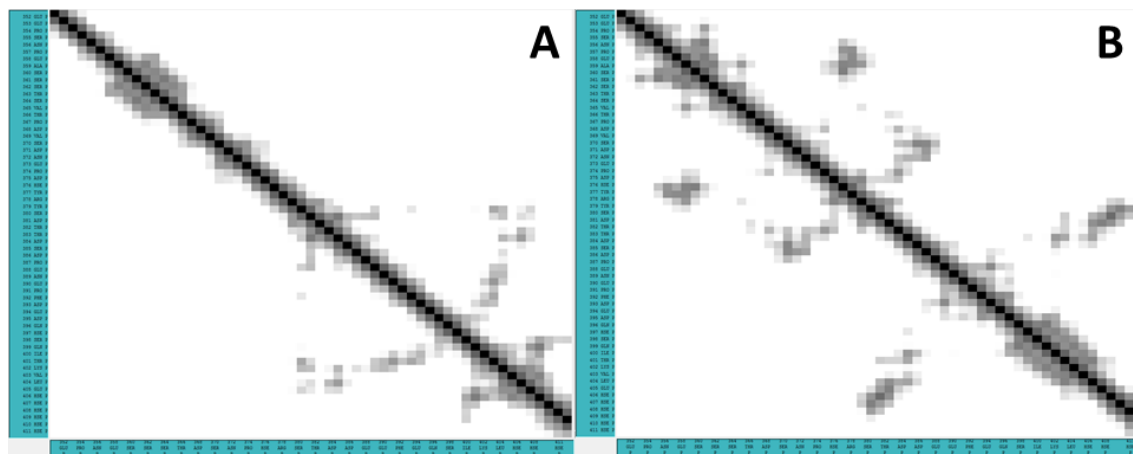
Figure 9.34: Comparison of contact maps, which depict distances between residues in the C-terminal tail, averaged over the length of the production run of the simulations for A) *wt* PTEN in solution and B) *wt* PTEN binding to a PC:PS membrane. Black: 0.0 Å separation, white: ≥ 10.0 Å and a linear gray scale is used in between.

bound to a PC:PS membrane. In solution, residues 380-395 interact with 399-403 at the very end of the tail. On the membrane, residues 381-387 form contacts with residues 400-401, similar to the interaction in solution. But we also observe two other stable interactions: 1) 354-361 with 374-380 and 2) 367-377 with 382-387. Each of these contacts consist of two groups of at least six residues. In combination with the hydrogen bonding data that exhibited large fluctuations, a picture emerges

of transient loops being formed in the tail that result in some amount of compaction in a highly dynamic, interconverting fashion.

There are three hydrogen bonds formed between residues in the C-terminal tail that are common to the solution and membrane-bound simulations: Tyr377 (with Asp375 on the membrane, His376 in solution), Thr382 (with Asp381 on the membrane, Arg378 in solution), Asp381 (with Leu404 on the membrane, with Asp381 in solution). There are also three common salt bridges formed: Arg378 (with Asp368, Asp375 and Asp381 on the membrane, with Glu373 and Asp 381 in solution), Lys402 (with Asp384, Glu388 and Glu394 on the membrane, with Glu388 in solution).

9.5.3 Secondary Structure Comparison

Table 9.7: Comparison of the equilibrium secondary structure composition of the truncated PTEN in the crystal structure, *wt* PTEN in solution, *wt* PTEN bound to a PC:PS membrane and *wt* PTEN bound to a PC:PS:PI(4,5)P$_2$ membrane. The 'rigid' residues are defined as those that were included in the crystal structure while 'flexible' refers to all the truncated residues. The values were normalized by the number of residues considered rigid (307) or flexible (104).

System	Alpha (%)		Beta (%)		Coil (%)	
	Rigid	Flexible	Rigid	Flexible	Rigid	Flexible
Crystal Structure	21.5	–	31.3	–	14.7	–
Solution	23.6±0.9	13±5	30±1	0±0	17±2	46±6
PS	23±1	8±3	30±1	0±0	16±2	52±5
PS+PIP$_2$	23.5±0.9	8±3	29±1	0±0	17±2	44±6

Apart from describing probable mechanisms for PTEN interaction with bilayers and equilibrium structures of the protein in solution and on the membrane, simulations also allow us to generate data that can be compared with experiments. Circular Dichroism (CD) is a commonly used technique that estimates the secondary structure composition of proteins. Table 9.7 (derived from figure 9.35) lists the α-helical, β-sheet and random coil content of the truncated PTEN mutant in the crystal structure, *wt* PTEN in solution, *wt* PTEN bound to the PC:PS membrane and *wt* PTEN bound to the PC:PS:PI(4,5)P$_2$ membrane. The rigid residues are defined as those that were included in the crystal structure (14-281 and 313-351) and the flexible residues are those that were truncated or could not be resolved (1-13, 282-312 and 352 to 411).

Compared to the truncated mutant, all the other systems have increased α-helicity, both in the rigid and flexible residues, increased propensity for forming coils
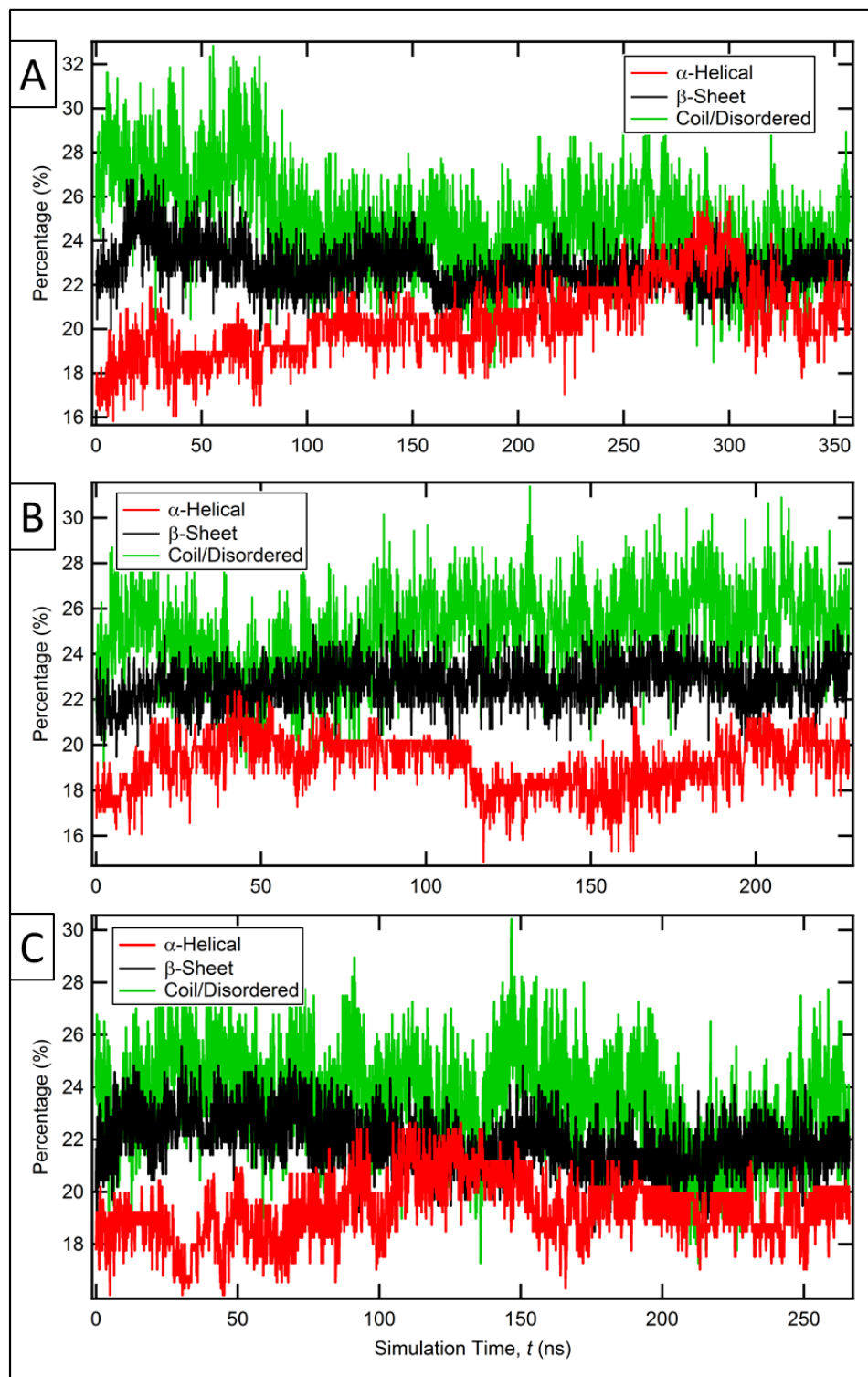
Figure 9.35: Evolution of the secondary structure composition of *wt* PTEN in:
A) Solution, B) Bound to a PC:PS membrane and C) Bound to a PC:PS:PI(4,5)P$_2$
membrane.

180

and a slightly reduced β-sheet structure. It is important to note that in none of the simulations were any β-sheets observed in the flexible regions of the protein. Upon binding to a PS-bearing membrane, there is a negligible change in the secondary structure of the protein – a fact that was experimentally observed using infrared spectroscopy (FTIR) to study *wt* PTEN binding to PS-bearing vesicles [5]. On the whole, the structural composition of *wt* PTEN, be it in solution, bound to a PS-bearing membrane or to a PS+PI(4,)P$_2$-bearing membrane is very similar.
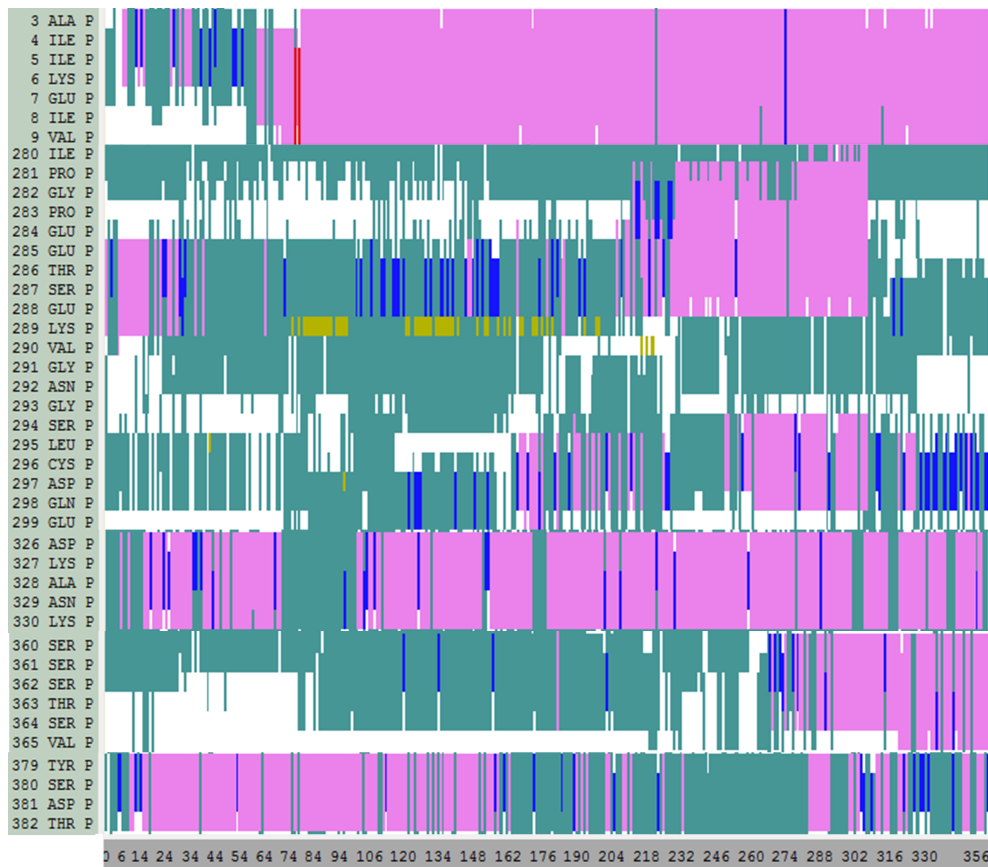
Figure 9.36: Evolution of the secondary structure of individual residues showing conformational changes during the course of the *wt* PTEN in solution simulations. Color coding: Turn (dark green), β-sheet (yellow), isolated bridge (light green), α-helix (pink), 3-10 helix (blue), π-helix (red).

However, just because the average number of α-helices or β-sheets remains a constant it does not imply that conformational changes are absent. The formation of an α-helix in one part of the protein could negate the disruption of an α-helix at some other position, leaving the net number of α-helices unchanged. Consequently, we examined the conformational evolution of each residue in each of the three simulations.
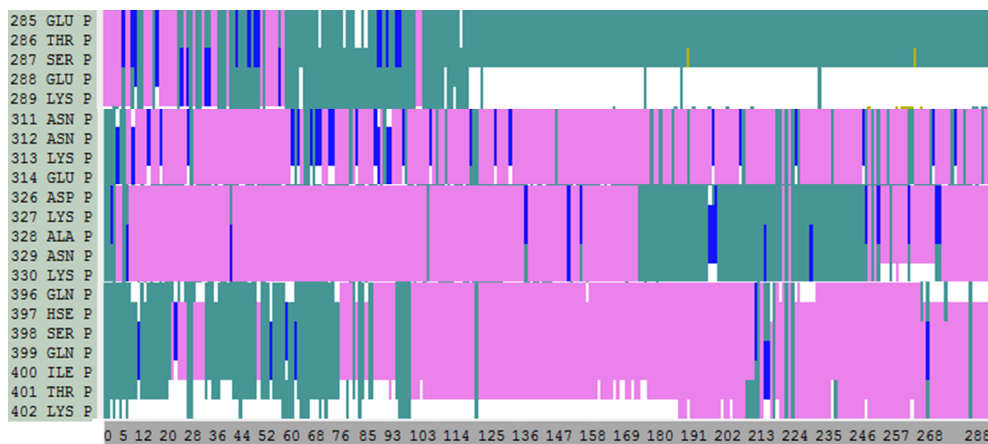
Figure 9.37: Evolution of the secondary structure of individual residues showing conformational changes during the course of the *wt* PTEN bound to PS simulations. Color coding: Turn (dark green), β-sheet (yellow), isolated bridge (light green), α-helix (pink), 3-10 helix (blue), π-helix (red).
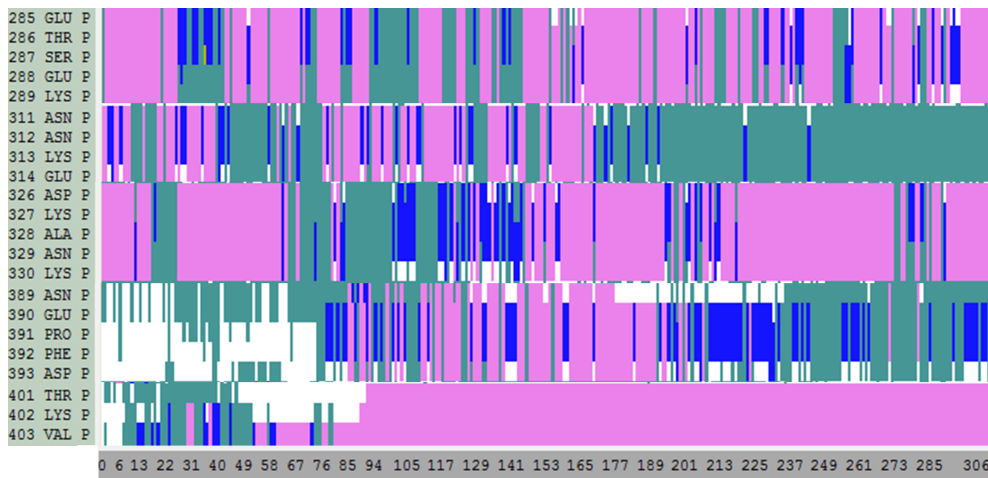
Figure 9.38: Evolution of the secondary structure of individual residues showing conformational changes during the course of the *wt* PTEN bound to PS+PI(4,5)P$_2$ simulations. Color coding: Turn (dark green), β-sheet (yellow), isolated bridge (light green), α-helix (pink), 3-10 helix (blue), π-helix (red).

For *wt* PTEN in solution (see figure 9.36), residues 3-9 which are part of the PI(4,5)P$_2$ binding module (PBM) in the disordered N-terminal tail form an α-helix in the first 60 ns which persists for the duration of the simulation. Residues 280-288 and 294-298 which are part of the internal loop in the C2 domain that was truncated during the determination of the crystal structure alternate between α-helical, turn and random coil configurations. Residues 326-330, 360-365 and 379-

382, all part of the C2 domain, which are defined as turns in the crystal structure seem to gain some α-helical content on average, especially towards the latter half of the simulation. Of all these changes, the formation of an α-helix in the PBM is the most significant as it shows the ability of the disordered N-terminal tail to change conformation which may assist in the specific detection of and association with PI(4,5)P$_2$ lipids.

During the association of *wt* PTEN with a PS-bearing membrane (see figure 9.37), the phosphatase domain remains unchanged from the crystal structure. However in the C2 domain, residues 285-289 lose their α-helicity to form turns or random coils, while residues 311-314 and 326-330 gain α-helicity from an initial turn configuration. These reflect the impact of membrane association on the secondary structure of PTEN. Finally, we also notice that the residues 396-402, which are at the very tip of the C-terminal tail, evolve from a turn configuration to an α-helix.

When *wt* PTEN associates with a membrane bearing both PS and PI(4,5)P$_2$ lipids (see figure 9.38), the same set of residues that were affected upon binding to PS: 285-289, 311-314 and 326-330 are also affected in this case as well. The only difference is that the α-helicity of the terminal portion of the C-terminal tail is restricted to residues 401-403 unlike the 396-402 range that was observed earlier.

To summarize, the simulations of *wt* PTEN in solution give us insights into the secondary structure of the disordered residues that were excluded from the truncated PTEN mutant. Upon association with an anionic membrane, there is a conformational change that sees a widening of the protein between the pα1 helix in the PD and the CBR3 loop in the C2 domain which repositions α-helices in the PD and switches turns to α-helices (and vice-versa) in the C2 domain.

9.6 Conclusions

Molecular dynamics simulations are a powerful tool to gain in-depth knowledge of molecular interactions. The reliability of their predictions, however, is often a source of debate which can be avoided by cross-validating them with experimental results. In the case of the PTEN tumor suppressor, the crystal structure of a truncated PTEN mutant when combined with binding kinetics information from SPR and structural information from NR allows us to confidently describe the interactions and associations, both within the protein as well as between the protein and lipid bilayers. Our results show two very distinct organization schemes for the C-terminal tail in solution and on the membrane, of which the solution conformation obstructs the binding interface and blocks the CBR3 loop at times. The accompanying extension of the tail makes PEST sites solvent accessible. Consequently, if this structure were to be locked in by phosphorylation, that would suggest a mechanism to regulate the activity of the PTEN tumor suppressor, supporting the two-state model where phosphorylated PTEN is locked in solution in a 'closed' state and upon de-

phosphorylation transforms into an 'open' state that is able to interact with the lipid bilayer [10]. This model, if true, would have significant biological implications as it would provide a mechanism by which dephosphorylation of $PI(3,4,5)P_3$ to $PI(4,5)P_2$ can be controlled, thereby regulating the PTEN-PI3K/Akt signaling pathway and adversely impacting cell growth and survival. A fine balance would exist between the open and closed conformations, with the phosphorylation and dephosphorylation of PTEN by some yet to be determined agent(s) responsible for keeping it in check. We also observe a conformational change of the protein upon membrane association which could allow the active site easier access to the $PI(3,4,5)P_3$ substrate, both by bringing the active site closer to the lipid headgroups and by increasing the accessible area of the protein. The interpretation of the NR results of *wt* PTEN binding to a membrane bearing PS and $PI(4,5)P_2$ suggest an equilibrium structure of the protein that is 8 Å further away from the lipid headgroups than is observed in the PS-binding simulations or the PS+$PI(4,5)P_2$ binding simulations. Further investigations of the reasons for this discrepancy are in progress.

Chapter 10

Summary and Future Outlook

Let us summarize the key results presented in this work:

1. Sparsely tethered bilayer lipid membranes (stBLMs) enable quantitative binding studies with SPR that show:

   - Synergy between PS and PI(4,5)P$_2$.
   - An increased affinity to PS of the H93R, C124S and truncated PTEN mutants that have presumably different reasons:
     - H93R PTEN might undergo a conformational change as a result of the mutation and/or altered interaction between the phosphatase and C2 domains.
     - C124S PTEN might interact with PS but not with PI(4,5)P$_2$ in the obstructed catalytic site.
     - The absence of unfavorable interactions between the C-terminal tail and the CBR3 PS-binding motif of the C2 domain in the truncated PTEN mutant.
   - Non-competitive and independent association of PTEN with PI(4,5)P$_2$ and PI(3,4,5)P$_3$ with higher affinity for PI(3,4,5)P$_3$ than PI(4,5)P$_2$.

2. Neutron reflectivity (NR) and molecular dynamics (MD) simulations show independently that:

   - PTEN association with the lipid bilayer is strictly interfacial with no significant penetration into the lipid headgroup region.
   - The C-terminal tail with a net charge of -10 is repelled by anionic lipids and is located distal to the membrane.

3. The MD simulations also show us that:

- The C-terminal tail is fundamentally different in its organization in a solution-state compared to a membrane-bound state. This suggests a molecular mechanism for PTEN regulation.

- There is a conformational change in the protein upon membrane association that lowers the center of mass of the protein, thereby providing easier access for the catalytic site to the PI(3,4,5)P$_3$ substrate.

- The CBR3 motif is indeed the dominant PS-binding region on the protein but it acts in concert with spatially adjacent residues in the C2 domain.

While answering pressing mechanistic and regulatory questions, the simulations also suggest future work that needs to be done, both in terms of experiments as well as further simulations. In particular, following are simulations that we either plan to start or have already initiated:

1. **Study H93R PTEN in solution and in a membrane-bound state.** While we have SPR data showing that the H93R mutation results in dramatically altered catalytic activity, membrane binding affinities and protein nSLD profile on the membrane, we have yet to ascertain if the mutation alters the structure of the protein and the mechanism behind such an effect.

2. **Validate the Open/Closed regulatory model.** We would first like to study the impact of introducing the closed state of the protein (that was observed in the solution simulation) to a PS-bearing membrane. Does the tail get repelled by the membrane, thereby breaking its contacts with the CBR3 motif and allowing the protein to associate with the bilayer? We would also like to phosphorylate the C-terminal tail of the protein at the identified PEST sites and see if the open configuration of the protein transitions to the closed configuration. Does such a closed conformation stay locked in this position, even in close proximity to a PS-bearing membrane?

3. **Determine the stoichiometry of PTEN binding to PI(4,5)P$_2$.** SPR experiments suggest that the PTEN association with PI(4,5)P$_2$ does not follow a 1:1 stoichiometry. We have initiated simulations of a system identical to the that in the experiments with the aim to validate this observation and to provide us with more quantitative information. So far, the slow diffusion of PI(4,5)P$_2$ in the membrane is affecting our ability to study this situation. We hope to rectify this by increasing the PI(4,5)P$_2$ concentration (currently 1.85 mol%) as well as by running the existing simulation for a longer period of time.

In terms of future NR experiments, the simulations provide us with information on the suitability of various residues for deuteration, especially along the C-terminal tail, to add contrast thereby aiding the experimental detection of their averaged position, with respect to the membrane. Either phosphorylating the PEST sites or

substituting the serines and threonines with glutamic acid to mimic phosphorylation will allow us to compare the affinity of the closed state with the open state to membranes using SPR. If the open/closed model is indeed accurate, we would expect to see a dramatically greater affinity for the open state to the membrane.

To summarize, we have taken great strides forward in understanding the tumor suppressor role of PTEN and the ability of point mutations to disrupt the protein's biological function. We hope that the progress we have made is merely the start of a renewed effort to ultimately counteract the loss of PTEN's activity, thereby preventing the uncontrolled proliferation of cells leading to cancer.

Bibliography

[1] "GLOBOCAN 2008 (IARC) Section of Cancer Information." `http://globocan.iarc.fr/factsheets/populations/factsheet.asp?uno=900`. [Online; accessed 1-April-2012].

[2] R. J. Shaw and L. C. Cantley, "Ras, PI(3)K and mTOR signalling controls tumour cell growth.," *Nature*, vol. 441, pp. 424–30, May 2006.

[3] M. S. Greenblatt, W. P. Bennett, M. Hollstein, and C. C. Harris, "Mutations in the p53 tumor suppressor gene: clues to cancer etiology and molecular pathogenesis.," *Cancer Res.*, vol. 54, pp. 4855–78, Sept. 1994.

[4] J. O. Lee, H. Yang, M. M. Georgescu, A. Di Cristofano, T. Maehama, Y. Shi, J. E. Dixon, P. Pandolfi, and N. P. Pavletich, "Crystal structure of the PTEN tumor suppressor: implications for its phosphoinositide phosphatase activity and membrane association.," *Cell*, vol. 99, pp. 323–34, Oct. 1999.

[5] D. A. Redfern, R. E. Redfern, M. L. M. Furgason, M. Munson, A. H. Ross, and A. Gericke, "PTEN phosphatase selectively binds phosphoinositides and undergoes structural changes.," *Biochemistry*, vol. 47, pp. 2162–71, Feb. 2008.

[6] R. E. Redfern, M.-C. Daou, L. Li, M. Munson, A. Gericke, and A. H. Ross, "A mutant form of PTEN linked to autism," *Protein Sci.*, vol. 19, pp. 1948–1956, 2010.

[7] D. Vaknin, K. Kjaer, J. Als-Nielsen, and M. Lösche, "Structural properties of phosphatidylcholine in a monolayer at the air/water interface," *Biophys. J.*, vol. 59, pp. 1325–1332, June 1991.

[8] P. Shekhar, H. Nanda, M. Lösche, and F. Heinrich, "Continuous distribution model for the investigation of complex molecular architectures near interfaces with scattering techniques," *J. Appl. Chem.*, vol. 110, p. 102216, 2011.

[9] J. E. Curtis, S. Raghunandan, H. Nanda, and S. Krueger, "SASSIE : A program to study intrinsically disordered biological molecules and macromolecular ensembles using experimental scattering restraints," *Comp. Phys. Comm.*, vol. 183, no. 2, pp. 382–389, 2012.

[10] A. H. Ross and A. Gericke, "Phosphorylation keeps PTEN phosphatase closed for business.," *P. Natl. Acad. Sci. USA*, vol. 106, pp. 1297–8, Feb. 2009.

[11] J. Li, C. Yen, D. Liaw, K. Podsypanina, S. Bose, S. I. Wang, J. Puc, C. Miliaresis, L. Rodgers, R. McCombie, S. H. Bigner, B. C. Giovanella, M. Ittmann, B. Tycko, H. Hibshoosh, M. H. Wigler, and R. Parsons, "PTEN: a putative protein tyrosine phosphatase gene mutated in human brain, breast, and prostate cancer," *Science*, vol. 275, no. 5308, pp. 1943–1947, 1997.

[12] P. A. Steck, M. A. Pershouse, S. A. Jasser, W. K. Yung, H. Lin, A. H. Ligon, L. A. Langford, M. L. Baumgard, T. Hattier, T. Davis, C. Frye, R. Hu, B. Swedlund, D. H. Teng, and S. V. Tavtigian, "Identification of a candidate tumour suppressor gene, MMAC1, at chromosome 10q23.3 that is mutated in multiple advanced cancers.," *Nat. Gen.*, vol. 15, pp. 356–62, Apr. 1997.

[13] D. M. Li and H. Sun, "TEP1, encoded by a candidate tumor suppressor locus, is a novel protein tyrosine phosphatase regulated by transforming growth factor beta," *Cancer Res.*, vol. 57, pp. 2124–2129, 1997.

[14] T. Maehama and J. E. Dixon, "The tumor suppressor, PTEN/MMAC1, dephosphorylates the lipid second messenger, phosphatidylinositol 3,4,5-trisphosphate.," *J. Biol. Chem.*, vol. 273, pp. 13375–8, May 1998.

[15] M. Tamura, "Inhibition of Cell Migration, Spreading, and Focal Adhesions by Tumor Suppressor PTEN," *Science*, vol. 280, pp. 1614–1617, June 1998.

[16] F. Vazquez, S. Ramaswamy, N. Nakamura, and W. R. Sellers, "Phosphorylation of the PTEN tail regulates protein stability and function.," *Mol. Cell Biol.*, vol. 20, pp. 5010–8, July 2000.

[17] X. Wu, K. Hepner, S. Castelino-Prabhu, D. Do, M. B. Kaye, X. J. Yuan, J. Wood, C. Ross, C. L. Sawyers, and Y. E. Whang, "Evidence for regulation of the PTEN tumor suppressor by a membrane-localized multi-PDZ domain containing scaffold protein MAGI-2," *P. Natl. Acad. Sci. USA*, vol. 97, pp. 4233–4238, 2000.

[18] Y. Wu, D. Dowbenko, S. Spencer, R. Laura, J. Lee, Q. Gu, and L. A. Lasky, "Interaction of the tumor suppressor PTEN/MMAC with a PDZ domain of MAGI3, a novel membrane-associated guanylate kinase," *J. Biol. Chem.*, vol. 275, pp. 21477–21485, 2000.

[19] J. A. Engelman, J. Luo, and L. C. Cantley, "The evolution of phosphatidylinositol 3-kinases as regulators of growth and metabolism.," *Nat. Rev. Gen.*, vol. 7, pp. 606–19, Aug. 2006.

[20] N. Chalhoub and S. J. Baker, "PTEN and the PI3-Kinase Pathway in Cancer," *Ann. Rev. Pathol.*, vol. 4, pp. 127–150, 2009.

[21] A. Bellacosa, C. C. Kumar, A. Di Cristofano, and J. R. Testa, "Activation of AKT kinases in cancer: implications for therapeutic targeting.," *Adv. Cancer Res.*, vol. 94, pp. 29–86, Jan. 2005.

[22] L. Li and A. H. Ross, "Why is PTEN an important tumor suppressor?," *J. Cell Biochem.*, vol. 102, pp. 1368–74, Dec. 2007.

[23] L. C. Trotman and P. P. Pandolfi, "PTEN and p53: who will get the upper hand?," *Cancer Cell*, vol. 3, pp. 97–9, Feb. 2003.

[24] T. Tamguney and D. Stokoe, "New insights into PTEN.," *J. Cell Sci.*, vol. 120, pp. 4071–9, Dec. 2007.

[25] T. Virolle, E. D. Adamson, V. Baron, D. Birle, D. Mercola, T. Mustelin, and I. de Belle, "The Egr-1 transcription factor directly activates PTEN during irradiation-induced signalling.," *Nat. Cell Biol.*, vol. 3, pp. 1124–8, Dec. 2001.

[26] L. Patel, I. Pass, P. Coxon, C. Downes, S. A. Smith, and C. H. Macphee, "Tumor suppressor and anti-inflammatory actions of PPARγ agonists are mediated via upregulation of PTEN," *Curr. Biol.*, vol. 11, pp. 764–768, May 2001.

[27] V. Stambolic, D. MacPherson, D. Sas, Y. Lin, B. Snow, Y. Jang, S. Benchimol, and T. Mak, "Regulation of PTEN Transcription by p53," *Molec. Cell*, vol. 8, pp. 317–325, Aug. 2001.

[28] F. Edwin, R. Singh, R. Endersby, S. J. Baker, and T. B. Patel, "The tumor suppressor PTEN is necessary for human Sprouty 2-mediated inhibition of cell proliferation.," *J. Biol. Chem.*, vol. 281, pp. 4816–22, Feb. 2006.

[29] Y. H. Shen, L. Zhang, Y. Gan, X. Wang, J. Wang, S. A. LeMaire, J. S. Coselli, and X. L. Wang, "Up-regulation of PTEN (phosphatase and tensin homolog deleted on chromosome ten) mediates p38 MAPK stress signal-induced inhibition of insulin signaling. A cross-talk between stress signaling and insulin signaling in resistin-treated human endothelial cell," *J. Biol. Chem.*, vol. 281, pp. 7727–36, Mar. 2006.

[30] K. A. Waite, M. R. Sinden, and C. Eng, "Phytoestrogen exposure elevates PTEN levels.," *Hum. Mol. Gen.*, vol. 14, pp. 1457–63, June 2005.

[31] D. Xia, H. Srinivas, Y.-H. Ahn, G. Sethi, X. Sheng, W. K. A. Yung, Q. Xia, P. J. Chiao, H. Kim, P. H. Brown, I. I. Wistuba, B. B. Aggarwal, and J. M.

Kurie, "Mitogen-activated protein kinase kinase-4 promotes cell survival by decreasing PTEN expression through an NF kappa B-dependent pathway.," *J. Biol. Chem.*, vol. 282, pp. 3507–19, Feb. 2007.

[32] L. M. L. Chow and S. J. Baker, "PTEN function in normal and neoplastic growth.," *Cancer Lett.*, vol. 241, pp. 184–96, Sept. 2006.

[33] L. Mahimainathan, F. Das, B. Venkatesan, and G. G. Choudhury, "Mesangial cell hypertrophy by high glucose is mediated by downregulation of the tumor suppressor PTEN.," *Diabetes*, vol. 55, pp. 2115–25, July 2006.

[34] K. Hettinger, F. Vikhanskaya, M. K. Poh, M. K. Lee, I. de Belle, J.-T. Zhang, S. A. G. Reddy, and K. Sabapathy, "c-Jun promotes cellular survival by suppression of PTEN.," *Cell Death Differ.*, vol. 14, pp. 218–29, Feb. 2007.

[35] M. M. Georgescu, K. H. Kirsch, T. Akagi, T. Shishido, and H. Hanafusa, "The tumor-suppressor activity of PTEN is regulated by its carboxyl- terminal region," *P. Natl. Acad. Sci. USA*, vol. 96, pp. 10182–10187, 1999.

[36] L. Odriozola, G. Singh, T. Hoang, and A. M. Chan, "Regulation of PTEN activity by its carboxyl-terminal autoinhibitory domain.," *J. Biol. Chem.*, vol. 282, pp. 23306–15, Aug. 2007.

[37] A. M. Al-Khouri, Y. Ma, S. H. Togo, S. Williams, and T. Mustelin, "Cooperative phosphorylation of the tumor suppressor phosphatase and tensin homologue (PTEN) by casein kinases and glycogen synthase kinase 3beta.," *J. Biol. Chem.*, vol. 280, pp. 35195–202, Oct. 2005.

[38] S. J. Miller, D. Y. Lou, D. C. Seldin, W. S. Lane, and B. G. Neel, "Direct identification of PTEN phosphorylation sites," *FEBS Letters*, vol. 528, pp. 145–153, Sept. 2002.

[39] J. Torres and R. Pulido, "The tumor suppressor PTEN is phosphorylated by the protein kinase CK2 at its C terminus. Implications for PTEN stability to proteasome-mediated degradation.," *J. Biol. Chem.*, vol. 276, pp. 993–8, Jan. 2001.

[40] F. Okahara, H. Ikawa, Y. Kanaho, and T. Maehama, "Regulation of PTEN phosphorylation and stability by a tumor suppressor candidate protein.," *J. Biol. Chem.*, vol. 279, pp. 45300–3, Oct. 2004.

[41] Z. Li, X. Dong, Z. Dong, W. Liu, N. Deng, Y. Ding, L. Tang, T. Hla, R. Zeng, L. Li, and D. Wu, "Regulation of PTEN by Rho small GTPases.," *Nat. Cell Biol.*, vol. 7, pp. 399–404, Apr. 2005.

[42] M. Raftopoulou, S. Etienne-Manneville, A. Self, S. Nicholls, and A. Hall, "Regulation of cell migration by the C2 domain of the tumor suppressor PTEN.," *Science*, vol. 303, pp. 1179–81, Feb. 2004.

[43] M. P. Myers, I. Pass, I. H. Batty, J. Van der Kaay, J. P. Stolarov, B. A. Hemmings, M. H. Wigler, C. P. Downes, and N. K. Tonks, "The lipid phosphatase activity of PTEN is critical for its tumor supressor function.," *P. Natl. Acad. Sci. USA*, vol. 95, pp. 13513–8, Nov. 1998.

[44] M. Tamura, J. Gu, T. Takino, and K. M. Yamada, "Tumor Suppressor PTEN Inhibition of Cell Invasion, Migration, and Growth: Differential Involvement of Focal Adhesion Kinase and p130Cas," *Cancer Res.*, vol. 59, pp. 442–449, Jan. 1999.

[45] L. C. Trotman, X. Wang, A. Alimonti, Z. Chen, J. Teruya-Feldstein, H. Yang, N. P. Pavletich, B. S. Carver, C. Cordon-Cardo, H. Erdjument-Bromage, P. Tempst, S.-G. Chi, H.-J. Kim, T. Misteli, X. Jiang, and P. P. Pandolfi, "Ubiquitination regulates PTEN nuclear import and tumor suppression.," *Cell*, vol. 128, pp. 141–56, Jan. 2007.

[46] X. Wang, L. C. Trotman, T. Koppie, A. Alimonti, Z. Chen, Z. Gao, J. Wang, H. Erdjument-Bromage, P. Tempst, C. Cordon-Cardo, P. P. Pandolfi, and X. Jiang, "NEDD4-1 is a proto-oncogenic ubiquitin ligase for PTEN.," *Cell*, vol. 128, pp. 129–39, Jan. 2007.

[47] K. Okumura, M. Mendoza, R. M. Bachoo, R. A. DePinho, W. K. Cavenee, and F. B. Furnari, "PCAF modulates PTEN activity.," *J. Biol. Chem.*, vol. 281, pp. 26562–8, Sept. 2006.

[48] J. Kwon, S.-R. Lee, K.-S. Yang, Y. Ahn, Y. J. Kim, E. R. Stadtman, and S. G. Rhee, "Reversible oxidation and inactivation of the tumor suppressor PTEN in cells stimulated with peptide growth factors.," *P. Natl. Acad. Sci. USA*, vol. 101, pp. 16419–24, Nov. 2004.

[49] S.-R. Lee, K.-S. Yang, J. Kwon, C. Lee, W. Jeong, and S. G. Rhee, "Reversible inactivation of the tumor suppressor PTEN by H2O2.," *J. Biol. Chem.*, vol. 277, pp. 20336–42, June 2002.

[50] N. R. Leslie, D. Bennett, Y. E. Lindsay, H. Stewart, A. Gray, and C. P. Downes, "Redox regulation of PI 3-kinase signalling via inactivation of PTEN.," *EMBO J.*, vol. 22, pp. 5501–10, Oct. 2003.

[51] J. H. Seo, Y. Ahn, S.-R. Lee, C. Yeol Yeo, and K. Chung Hur, "The major target of the endogenously generated reactive oxygen species in response to insulin

stimulation is phosphatase and tensin homolog and not phosphoinositide-3 kinase (PI-3 kinase) in the PI-3 kinase/Akt pathway.," *Mol. Biol. Cell*, vol. 16, pp. 348–57, Jan. 2005.

[52] Y. Takahashi, F. C. Morales, E. L. Kreimann, and M.-M. Georgescu, "PTEN tumor suppressor associates with NHERF proteins to attenuate PDGF receptor signaling.," *EMBO J.*, vol. 25, pp. 910–20, Feb. 2006.

[53] F. Vazquez, S. R. Grossman, Y. Takahashi, M. V. Rokas, N. Nakamura, and W. R. Sellers, "Phosphorylation of the PTEN tail acts as an inhibitory switch by preventing its recruitment into a protein complex.," *J. Biol. Chem.*, vol. 276, pp. 48627–30, Dec. 2001.

[54] F. Vazquez and P. Devreotes, "Regulation of PTEN Function as a PIP3 Gatekeeper Through Membrane Interaction," *Cell Cycle*, vol. 5, pp. 1523–1527, 2006.

[55] Y. E. Whang, X. Wu, H. Suzuki, R. E. Reiter, C. Tran, R. L. Vessella, J. W. Said, W. B. Isaacs, and C. L. Sawyers, "Inactivation of the tumor suppressor PTEN/MMAC1 in advanced human prostate cancer through loss of expression.," *P. Natl. Acad. Sci. USA*, vol. 95, pp. 5246–50, Apr. 1998.

[56] A. Perren, L. P. Weng, A. H. Boag, U. Ziebold, K. Thakore, P. L. Dahia, P. Komminoth, J. A. Lees, L. M. Mulligan, G. L. Mutter, and C. Eng, "Immunohistochemical evidence of loss of PTEN expression in primary ductal adenocarcinomas of the breast.," *Am. J. Pathol.*, vol. 155, pp. 1253–60, Oct. 1999.

[57] O. Gimm, A. Perren, L. P. Weng, D. J. Marsh, J. J. Yeh, U. Ziebold, E. Gil, R. Hinze, L. Delbridge, J. A. Lees, G. L. Mutter, B. G. Robinson, P. Komminoth, H. Dralle, and C. Eng, "Differential nuclear and cytoplasmic expression of PTEN in normal thyroid tissue, and benign and malignant epithelial thyroid tumors.," *Am. J. Pathol.*, vol. 156, pp. 1693–700, May 2000.

[58] M. B. Lachyankar, N. Sultana, C. M. Schonhoff, P. Mitra, W. Poluha, S. Lambert, P. J. Quesenberry, N. S. Litofsky, L. D. Recht, R. Nabi, S. J. Miller, S. Ohta, B. G. Neel, and A. H. Ross, "A role for nuclear PTEN in neuronal differentiation.," *J. Neurosci.*, vol. 20, pp. 1404–13, Feb. 2000.

[59] T. Sano, H. Lin, X. Chen, L. A. Langford, D. Koul, M. L. Bondy, K. R. Hess, J. N. Myers, Y.-K. Hong, W. K. A. Yung, and P. A. Steck, "Differential Expression of MMAC/PTEN in Glioblastoma Multiforme: Relationship to Localization and Prognosis," *Cancer Res.*, vol. 59, pp. 1820–1824, Apr. 1999.

[60] Z. Lian and A. Di Cristofano, "Class reunion: PTEN joins the nuclear crew.," *Oncogene*, vol. 24, pp. 7394–400, Nov. 2005.

[61] F. Liu, S. Wagner, R. B. Campbell, J. A. Nickerson, C. A. Schiffer, and A. H. Ross, "PTEN enters the nucleus by diffusion," *J. Cell Biochem.*, vol. 96, pp. 221–34, Oct. 2005.

[62] A. Gil, A. Andrés-Pons, E. Fernández, M. Valiente, J. Torres, J. Cervera, and R. Pulido, "Nuclear localization of PTEN by a Ran-dependent mechanism enhances apoptosis: Involvement of an N-terminal nuclear localization domain and multiple nuclear exclusion motifs.," *Mol. Biol. Cell*, vol. 17, pp. 4002–13, Sept. 2006.

[63] M. T. V. Diepen, M. Parsons, C. P. Downes, N. R. Leslie, R. Hindges, and B. J. Eickholt, "MyosinV controls PTEN function and neuronal cell size," *Nat. Cell Biol.*, vol. 11, no. 10, pp. 1191–1197, 2009.

[64] J.-H. Chung, M. E. Ginn-Pease, and C. Eng, "Phosphatase and tensin homologue deleted on chromosome 10 (PTEN) has nuclear localization signal-like sequences for nuclear import mediated by major vault protein.," *Cancer Res.*, vol. 65, pp. 4108–16, May 2005.

[65] Y. Lindsay, D. McCoull, L. Davidson, N. R. Leslie, A. Fairservice, A. Gray, J. Lucocq, and C. P. Downes, "Localization of agonist-sensitive PtdIns(3,4,5)P3 reveals a nuclear pool that is insensitive to PTEN expression," *J. Cell Sci.*, vol. 119, pp. 5160–8, Dec. 2006.

[66] K. Okumura, M. Zhao, R. A. Depinho, F. B. Furnari, and W. K. Cavenee, "Cellular transformation by the MSP58 oncogene is inhibited by its physical interaction with the PTEN tumor suppressor," *P. Natl. Acad. Sci. USA*, vol. 102, pp. 2703–2706, Feb. 2005.

[67] A. G. Li, L. G. Piluso, X. Cai, G. Wei, W. R. Sellers, and X. Liu, "Mechanistic insights into maintenance of high p53 acetylation by PTEN.," *Molec. Cell*, vol. 23, pp. 575–87, Aug. 2006.

[68] R. B. Campbell, F. Liu, and A. H. Ross, "Allosteric activation of PTEN phosphatase by phosphatidylinositol 4,5-bisphosphate.," *J. Biol. Chem.*, vol. 278, pp. 33617–20, Sept. 2003.

[69] G. McConnachie, I. Pass, S. Walker, and C. Downes, "Interfacial kinetic analysis of the tumour suppressor phosphatase, PTEN: evidence for activation by anionic phospholipids.," *Biochem. J.*, vol. 371, pp. 947–955, 2003.

[70] S. M. Walker, N. R. Leslie, N. M. Perera, I. H. Batty, and C. P. Downes, "The tumour-suppressor function of PTEN requires an N-terminal lipid-binding motif.," *Biochem. J.*, vol. 379, pp. 301–7, Apr. 2004.

[71] Y. Okamura, "Another story of arginines in voltage sensing: the role of phosphoinositides in coupling voltage sensing to enzyme activity.," *J. Gen. Physiol.*, vol. 134, pp. 1–4, July 2009.

[72] M. Iijima, Y. E. Huang, H. R. Luo, F. Vazquez, and P. N. Devreotes, "Novel mechanism of PTEN regulation by its phosphatidylinositol 4,5-bisphosphate binding motif is critical for chemotaxis.," *J. Biol. Chem.*, vol. 279, pp. 16606–16613, Apr. 2004.

[73] M. Rahdar, T. Inoue, T. Meyer, J. Zhang, F. Vazquez, and P. N. Devreotes, "A phosphorylation-dependent intramolecular interaction regulates the membrane association and activity of the tumor suppressor PTEN.," *P. Natl. Acad. Sci. USA*, vol. 106, pp. 480–5, Jan. 2009.

[74] J. Puc, M. Keniry, H. S. Li, T. K. Pandita, A. D. Choudhury, L. Memeo, M. Mansukhani, V. V. V. S. Murty, Z. Gaciong, S. E. M. Meek, H. Piwnica-Worms, H. Hibshoosh, and R. Parsons, "Lack of PTEN sequesters CHK1 and initiates genetic instability.," *Cancer Cell*, vol. 7, pp. 193–204, Feb. 2005.

[75] W. H. Shen, A. S. Balajee, J. Wang, H. Wu, C. Eng, P. P. Pandolfi, and Y. Yin, "Essential role for nuclear PTEN in maintaining chromosomal integrity," *Cell*, vol. 128, pp. 157–70, Jan. 2007.

[76] C. H. Kwon, X. Zhu, J. Zhang, L. L. Knoop, R. Tharp, R. J. Smeyne, C. G. Eberhart, P. C. Burger, and S. J. Baker, "PTEN regulates neuronal soma size: a mouse model of Lhermitte-Duclos disease.," *Nat. Gen.*, vol. 29, pp. 404–11, Dec. 2001.

[77] S. Marino, P. Krimpenfort, C. Leung, H. A. G. M. van der Korput, J. Trapman, I. Camenisch, A. Berns, and S. Brandner, "PTEN is essential for cell migration but not for fate determination and tumourigenesis in the cerebellum," *Development*, vol. 129, pp. 3513–3522, July 2002.

[78] M. Groszer, R. Erickson, D. D. Scripture-Adams, R. Lesche, A. Trumpp, J. A. Zack, H. I. Kornblum, X. Liu, and H. Wu, "Negative regulation of neural stem/progenitor cell proliferation by the Pten tumor suppressor gene in vivo.," *Science*, vol. 294, pp. 2186–9, Dec. 2001.

[79] J. Zhang, J. C. Grindley, T. Yin, S. Jayasinghe, X. C. He, J. T. Ross, J. S. Haug, D. Rupp, K. S. Porter-Westpfahl, L. M. Wiedemann, H. Wu, and L. Li,

"PTEN maintains haematopoietic stem cells and acts in lineage choice and leukaemia prevention.," *Nature*, vol. 441, pp. 518–22, May 2006.

[80] O. H. Yilmaz, R. Valdez, B. K. Theisen, W. Guo, D. O. Ferguson, H. Wu, and S. J. Morrison, "PTEN dependence distinguishes haematopoietic stem cells from leukaemia-initiating cells.," *Nature*, vol. 441, pp. 475–82, May 2006.

[81] M. Groszer, R. Erickson, D. D. Scripture-Adams, J. D. Dougherty, J. Le Belle, J. A. Zack, D. H. Geschwind, X. Liu, H. I. Kornblum, and H. Wu, "PTEN negatively regulates neural stem cell self-renewal by modulating G0-G1 cell cycle entry.," *P. Natl. Acad. Sci. USA*, vol. 103, pp. 111–6, Jan. 2006.

[82] H. Feilotter, M. Nagai, A. Boag, C. Eng, and L. Mulligan, "Analysis of PTEN and the 10q23 region in primary prostate carcinomas," *Oncogene*, vol. 16, pp. 1743–1748, 1998.

[83] X. Li, H. Zheng, H. Takahashi, S. Masuda, X. Yang, and Y. Takano, "PTEN expression and mutation in colorectal carcinomas.," *Oncol. Rep.*, vol. 22, pp. 757–764, 2009.

[84] C. Castaneda, H. Cortes-Funes, H. Gomez, and E. Ciruelos, "The phosphatidyl inositol 3-kinase/AKT signaling pathway in breast cancer.," *Cancer Metastasis Rev.*, vol. 29, pp. 751–759, 2010.

[85] S. Pesche, A. Latil, F. Muzeau, O. Cussenot, G. Fournier, M. Longy, C. Eng, and R. Lidereau, "PTEN/MMAC1/TEP1 involvement in primary prostate cancers," *Oncogene*, vol. 16, pp. 2879–2883, 1998.

[86] J. Risinger, A. Hayes, A. Berchuck, and J. Barrett, "PTEN/MMAC1 mutations in endometrial cancers," *Cancer Res.*, vol. 57, pp. 4738–4738, 1997.

[87] T. Kohno, M. Takahashi, R. Manda, and J. Yokota, "Inactivation of the PTEN/MMAC1/TEP1 gene in human lung cancers," *Genes Chromosomes Cancer*, vol. 22, pp. 152–156, 1998.

[88] Y. Tohma, C. Gratas, W. Biernat, A. Peraud, M. Fukuda, Y. Yonekawa, P. Kleihues, and H. Ohgaki, "PTEN (MMAC1) mutations are frequent in primary glioblastomas (de novo) but not in secondary glioblastomas," *J Neuropathol Exp Neurol.*, vol. 57, pp. 684–689, 1998.

[89] R. Levine, C. Cargile, M. Blazes, B. van Rees, R. Kurman, and L. Ellenson, "PTEN mutations and microsatellite instability in complex atypical hyperplasia, a precursor lesion to uterine endometrioid carcinoma," *Cancer Res.*, vol. 58, pp. 3254–3258, 1998.

[90] G. Maxwell, J. Risinger, C. Gumbs, H. Shaw, R. Bentley, J. Barrett, A. Berchuck, and P. Futreal, "Mutation of the PTEN tumor suppressor gene in endometrial hyperplasias," *Cancer Res.*, vol. 58, pp. 2500–2503, 1998.

[91] K. Yoshinaga, H. Sasano, T. Furukawa, H. Yamakawa, M. Yuki, S. Sato, A. Yajima, and A. Horii, "The PTEN, BAX, and IGFIIR Genes Are Mutated in Endometrial Atypical Hyperplasia," *Cancer Sci.*, vol. 89, pp. 985–990, Oct. 1998.

[92] H. Sun, T. Enomoto, M. Fujita, H. Wada, K. Yoshino, K. Ozaki, T. Nakamura, and Y. Murata, "Mutational analysis of the PTEN gene in endometrial carcinoma and hyperplasia," *Am. J. Clin. Pathol.*, vol. 115, pp. 32–38, 2001.

[93] H. Tashiro, M. S. Blazes, R. Wu, K. R. Cho, S. Bose, S. I. Wang, J. Li, R. Parsons, and L. H. Ellenson, "Mutations in PTEN are frequent in endometrial carcinoma but rare in other common gynecological malignancies," *Cancer Res.*, vol. 57, no. 18, pp. 3935–3940, 1997.

[94] J. Risinger, K. Hayes, G. Maxwell, M. Carney, R. Dodge, J. Barrett, and A. Berchuck, "PTEN mutation in endometrial cancers is associated with favorable clinical and pathologic characteristics.," *Clin. Cancer Res.*, vol. 4, pp. 3005–3010, 1998.

[95] D. Stokoe, "PTEN," *Curr. Biol.*, vol. 11, no. 13, p. R502, 1999.

[96] A. Di Cristofano and P. P. Pandolfi, "The multiple roles of PTEN in tumor suppression.," *Cell*, vol. 100, pp. 387–90, Feb. 2000.

[97] C. Eng, "Genetics of Cowden syndrome: through the looking glass of oncology," *Int. J. Oncol.*, vol. 12, no. 3, pp. 701–711, 1998.

[98] L. Salmena, A. Carracedo, and P. P. Pandolfi, "Tenets of PTEN tumor suppression.," *Cell*, vol. 133, pp. 403–14, May 2008.

[99] M. Rutter, A. Bailey, P. Bolton, and A. Le Couteur, "Autism and known medical conditions: myth and substance (review)," *J. Child Psychol. Psychiatry*, vol. 35, pp. 311–322, 1994.

[100] L. Boccone, V. Dessi, A. Zappu, S. Piga, M. Piludu, M. Rais, C. Massidda, S. De Virgiliis, A. Cao, and G. Loudianos, "BannayanRileyRuvalcaba syndrome with reactive nodular lymphoid hyperplasia and autism and a PTEN mutation," *Am. J. Med. Gen.*, vol. 140A, pp. 1965–1969, 2006.

[101] M. G. Butler, M. J. Dasouki, X. P. Zhou, Z. Talebizadeh, M. Brown, T. N. Takahashi, J. H. Miles, C. H. Wang, R. Stratton, R. Pilarski, and C. Eng,

"Subset of individuals with autism spectrum disorders and extreme macrocephaly associated with germline PTEN tumour suppressor gene mutations," *J. Med. Genet.*, vol. 42, pp. 318–321, 2005.

[102] J. D. Buxbaum, G. Cai, P. Chaste, G. Nygren, J. Goldsmith, J. Reichert, H. Anckarsäter, M. Rastam, C. J. Smith, J. M. Silverman, E. Hollander, M. Leboyer, C. Gillberg, A. Verloes, and C. Betancur, "Mutation screening of the PTEN gene in patients with autism spectrum disorders and macrocephaly.," *Am. J. Med. Gen.*, vol. 144B, pp. 484–91, June 2007.

[103] A. Goffin, L. H. Hoefsloot, E. Bosgoed, A. Swillen, and J. P. Fryns, "PTEN mutation in a family with Cowden syndrome and autism.," *Am. J. Med. Gen.*, vol. 105, pp. 521–4, Aug. 2001.

[104] G. E. Herman, E. Butter, B. Enrile, M. Pastore, T. W. Prior, and A. Sommer, "Increasing Knowledge of PTEN Germline Mutations : Two Additional Patients With Autism and Macrocephaly," *Am. J. Med. Gen.*, vol. 143A, pp. 589 – 593, 2007.

[105] K. L. McBride, E. A. Varga, M. T. Pastore, T. W. Prior, K. Manickam, J. F. Atkin, and G. E. Herman, "Confirmation study of PTEN mutations among individuals with autism or developmental delays/mental retardation and macrocephaly.," *Autism Res.*, vol. 3, pp. 137–41, June 2010.

[106] A. Orrico, L. Galli, S. Buoni, A. Orsi, G. Vonella, and V. Sorrentino, "Novel PTEN mutations in neurodevelopmental disorders and macrocephaly," *Clin. Genet.*, vol. 75, pp. 195–198, 2009.

[107] M. A. Parisi, M. B. Dinulos, K. A. Leppig, V. P. Sybert, C. Eng, and L. Hudgins, "The spectrum and evolution of phenotypic findings in PTEN mutation positive cases of Bannayan-Riley-Ruvalcaba syndrome," *J. Med. Genet.*, vol. 38, pp. 52–58, 2001.

[108] T. Kohno, M. Takahashi, T. Fukutomi, K. Ushio, and J. Yokota, "Germline mutations of the PTEN/MMAC1 gene in Japanese patients with Cowden disease," *Jpn. J. Cancer Res.*, vol. 89, pp. 471–474, 1998.

[109] C. Eng, "PTEN: one gene, many syndromes," *Hum. Mutat.*, vol. 22, pp. 183–198, 2003.

[110] D. J. McGillivray, G. Valincius, D. J. Vanderah, W. Febo-Ayala, J. T. Woodward, F. Heinrich, M. Lösche, and J. J. Kasianowicz, "Molecular-scale structural and functional characterization of sparsely tethered bilayer lipid membranes," *Biointerphases*, vol. 2, no. 1, pp. 21–33, 2007.

[111] B. A. Cornell, V. L. Braach-Maksvytis, L. G. King, P. D. Osman, B. Raguse, L. Wieczorek, and R. J. Pace, "A biosensor that uses ion-channel switches.," *Nature*, vol. 387, pp. 580–3, June 1997.

[112] D. Magde, E. L. Elson, and W. W. Webb, "Thermodynamic fluctuations in a reacting system: measurement by fluorescence correlation spectroscopy," *Phys. Rev. Lett.*, vol. 29, pp. 705–708, 1972.

[113] E. L. Elson and D. Magde, "Fluorescence correlation spectroscopy. I. Conceptual basis and theory.," *Biopolymers*, vol. 13, pp. 1–27, 1974.

[114] D. Magde, E. L. Elson, and W. W. Webb, "Fluorescence correlation spectroscopy. II. An experimental realization.," *Biopolymers*, vol. 13, pp. 29–61, 1974.

[115] R. Rigler, U. Mets, J. Widengren, and P. Kask, "Fluorescence correlation spectroscopy with high count rate and low background analysis of translational diffusion.," *Eur. Biophys. J.*, vol. 22, pp. 169–175, 1993.

[116] M. Göppert-Mayer, "Uber Elementarakte mit zwei Quantensprüngen [Translation: About elementary events with two quantal jumps]," *Ann. Phys. (Leipzig)*, vol. 9, pp. 273–294, 1931.

[117] P. Schwille and E. Haustein, "Fluorescence Correlation Spectroscopy: An Introduction to its Concepts And Applications," *The Biophysics Textbook Online*, 2002.

[118] S. Sorscher and M. Klein, "Profile of a focussed collimated laser beam near the focal minimum characterized by fluorescence correlation spectroscopy," *Rev. Sci. Instrum.*, vol. 51, no. 1, 1980.

[119] A. Benda, M. Beneš, V. Marecek, A. Lhotsky, W. Hermens, and M. Hof, "How to determine diffusion coefficients in planar phospholipid systems by confocal fluorescence correlation spectroscopy," *Langmuir*, vol. 19, pp. 4120–4126, May 2003.

[120] S. Shenoy, R. Moldovan, J. Fitzpatrick, D. J. Vanderah, M. Deserno, and M. Lösche, "In-plane homogeneity and lipid dynamics in tethered bilayer lipid membranes (tBLMs)," *Soft Matter*, vol. 6, pp. 1263–1274, 2010.

[121] W. Knoll, "Interfaces and thin films as seen by bound electromagnetic waves.," *Ann. Rev. Phys. Chem.*, vol. 49, pp. 569–638, Jan. 1998.

[122] R. Schasfoort and A. Tudos, eds., *Handbook of Surface Plasmon Resonance*. Cambridge: The Royal Society of Chemistry, 2008.

[123] S. Ushioda and Y. Sasaki, "Raman scattering mediated by surface-plasmon polariton resonance," *Phys. Rev. B*, vol. 27, pp. 1401–1404, Jan. 1983.

[124] W. N. Hansen, "Electric fields produced by propagation of plane coherent electromagnetic radiation in a stratified medium," *J. Opt. Soc.*, vol. 58, no. 3, pp. 380–390, 1968.

[125] W. Press, B. P. Flannery, S. Teukolsky, and W. T. Vetterling, *Numerical Recipes*. Cambridge, U.K.: Cambridge University Press: Cambridge, U.K., 1986.

[126] D. J. Vanderah, V. Silin, and H. Weetall, "SPR Studies of the Nonspecific Adsorption Kinetics of Human IgG and BSA on Gold Surfaces Modified by Self-Assembled Monolayers (SAMs)," *J. Colloid. Interf. Sci.*, vol. 185, pp. 94–103, Jan. 1997.

[127] Y. Liu and P. Daum, "Relationship of refractive index to mass density and self-consistency of mixing rules for multicomponent mixtures like ambient aerosols," *Aerosol Science*, vol. 39, pp. 974–986, 2008.

[128] "Refractive index database." `http://refractiveindex.info/?group=LIQUIDS&material=Glycerol`. [Online; accessed 10-January-2010].

[129] "Luxpop: Thin film and bulk index of refraction and photonics calculations." `http://www.luxpop.com/`. [Online; accessed 10-January-2010].

[130] J. A. De Feijter, J. Benjamins, and F. A. Veer, "Ellipsometry as a tool to study the adsorption behavior of synthetic and biopolymers at the air-water interface," *Biopolymers*, vol. 17, pp. 1759–1772, July 1978.

[131] J. Daillant and A. Gibaud, eds., *X-ray and Neutron Reflectivity: Principles and Applications*. Springer, Berlin Heidelberg, 2009.

[132] L. G. Parratt, "Surface studies of solids by total reflection of x rays," *Phys. Rev.*, vol. 95, pp. 359–369, 1954.

[133] B. Kirby, P. Kienzle, B. Maranville, N. Berk, J. Krycka, F. Heinrich, and C. Majkrzak, "Phase-sensitive specular neutron reflectometry for imaging the nanometer scale composition depth profile of thin-film materials," *Curr. Opin. Colloid In.*, vol. 17, pp. 44–53, Feb. 2012.

[134] D. M. Hawkins, "The problem of overfitting.," *J. Chem. Inf. Comput. Sci*, vol. 44, no. 1, pp. 1–12, 2004.

[135] E. Catmull and R. Rom, "A class of local interpolating splines," in *Computer Aided Geometric Design* (R. E. Barnhill and R. F. Reisenfeld, eds.), vol. 1, pp. 317–326, Academic Press, New York, 1974.

[136] D. J. Vanderah, D. J. McGillivray, G. Valincius, F. Heinrich, J. W. F. Robertson, W. Febo-Ayala, I. Ignatjev, M. Lösche, and J. J. Kasianowicz, "Structure of functional Staphylococcus aureus alpha-hemolysin channels in tethered bilayer lipid membranes.," *Biophys. J.*, vol. 96, pp. 1547–53, Feb. 2009.

[137] E. Barsoukov and J. Macdonald, eds., *Impedance Spectroscopy: Theory, Experiment, and Applications.* John Wiley & Sons, Inc., Hoboken, NJ, 2005.

[138] H. Fricke, "The Theory of Electrolytic Polarization," *Philos. Mag.*, vol. 14, pp. 310–318, 1932.

[139] K. S. Cole and R. H. Cole, "Dispersion and Absorption in Dielectrics. I. Alternating-Current Characteristics," *J. Chem. Phys.*, vol. 9, pp. 341–351, 1941.

[140] B. Franklin, W. Brownrigg, and Farish, "Of the Stilling of Waves by means of Oil. Extracted from Sundry Letters between Benjamin Franklin, LL.D.F.R.S. William Brownrigg, M.D.F.R.S. and the Reverend Mr. Farish," *Philos. Trans.*, vol. 64, pp. 445–460, 1774.

[141] I. Langmuir, "The constitution and fundamental properties of solids and liquids. II. Liquid," *J. Am. Chem. Soc.*, vol. 39, pp. 1848–1906, 1917.

[142] C. M. Knobler and R. C. Desai, "Phase Transitions in Monolayers," *Ann. Rev. Phys. Chem.*, vol. 43, pp. 207–236, Oct. 1992.

[143] H. Mohwald, "Phospholipid and phospholipid-protein monolayers at the air/water interface.," *Ann. Rev. Phys. Chem.*, vol. 41, pp. 441–76, Jan. 1990.

[144] M. Lipp, K. Lee, J. Zasadzinski, and A. Waring, "Phase and morphology changes in lipid monolayers induced by SP-B protein and its amino-terminal peptide," *Science*, vol. 273, no. 5279, pp. 1196–1199, 1996.

[145] A. Bouchet, F. Lairion, and E. A. Disalvo, "Role of guanidinium group in the insertion of l-arginine in DMPE and DMPC lipid interphases.," *BBA*, vol. 1798, no. 3, pp. 616–623, 2010.

[146] M. Lösche, E. Sackmann, and H. Mohwald, "A fluorescence microscopic study concerning the phase diagram of phospholipids," *Ber. Bunsenges. Phys. Chem.*, vol. 87, pp. 848–852, 1983.

[147] P. C. Ke and C. A. Naumann, "Single Molecule Fluorescence Imaging of Phospholipid Monolayers at the Air-Water Interface," *Langmuir*, vol. 17, pp. 3727–3733, June 2001.

[148] I. Langmuir, "The mechanism of the surface phenomena of flotation," *Trans. Faraday Soc.*, vol. 15, pp. 62–74, 1920.

[149] K. B. Blodgett, "Films built by depositing successive monomolecular layers on a solid surface," *J. Am. Chem. Soc.*, vol. 57, pp. 1007–1022, 1935.

[150] P. Mueller, D. O. Rudin, H. I. Tien, and W. C. Wescott, "Reconstitution of cell membrane structure in vitro and its transformation into an excitable system," *Nature*, vol. 194, pp. 979–980, 1962.

[151] H. T. Tien, S. Carbone, and E. A. Dawidowicz, "Formation of 'black' lipid membranes by oxidation products of cholesterol," *Nature*, vol. 212, pp. 718–719, 1966.

[152] O. Purrucker, H. Hillebrandt, K. Adlkofer, and M. Tanaka, "Deposition of highly resistive lipid bilayer on silicon-silicon dioxide electrode and incorporation of gramicidin studied by AC impedance spectroscopy," *Electrochimica Acta*, vol. 47, pp. 791–798, 2001.

[153] M. Przybylo, J. Sýkora, J. Humpolíckova, A. Benda, A. Zan, and M. Hof, "Lipid diffusion in giant unilamellar vesicles is more than 2 times faster than in supported phospholipid bilayers under identical conditions.," *Langmuir*, vol. 22, pp. 9096–9, Oct. 2006.

[154] F. Heinrich, T. Ng, D. J. Vanderah, P. Shekhar, M. Mihailescu, H. Nanda, and M. Lösche, "A new lipid anchor for sparsely tethered bilayer lipid membranes.," *Langmuir*, vol. 25, pp. 4219–29, Apr. 2009.

[155] N. Kahya, D. Scherfeld, K. Bacia, and P. Schwille, "Lipid domain formation and dynamics in giant unilamellar vesicles explored by fluorescence correlation spectroscopy.," *J. Struct. Bio.*, vol. 147, no. 1, pp. 77–89, 2004.

[156] M. A. Deverall, S. Garg, K. Lüdtke, R. Jordan, J. Rühe, and C. A. Naumann, "Transbilayer coupling of obstructed lipid diffusion in polymer-tethered phospholipid bilayers," *Soft Matter*, vol. 4, no. 9, p. 1899, 2008.

[157] L. Zhang and S. Granick, "Lipid diffusion compared in outer and inner leaflets of planar supported bilayers.," *J. Chem. Phys.*, vol. 123, no. 21, p. 211104, 2005.

[158] J. Leathes, "Condensing effect of cholesterol on monolayers," *Lancet*, vol. 208, pp. 853–856, Apr. 1925.

[159] R. Demel, L. Van Deenen, and B. Pethica, "Monolayer interactions of phospholipids and cholesterol," *BBA-Biomembranes*, vol. 135, pp. 11–19, Feb. 1967.

[160] M. C. Phillips, "The Physical State of Phospholipids and Cholesterol in Monolayers, Bilayers, and Membranes," in *Prog. Surf. Sci.*, pp. 139–221, Academic Press, New York, 1972.

[161] Y. K. Levine and M. H. Wilkins, "Structure of oriented lipid bilayers.," *Nat. New Biol.*, vol. 230, pp. 69–72, Mar. 1971.

[162] W.-C. Hung, M.-T. Lee, F.-Y. Chen, and H. W. Huang, "The condensing effect of cholesterol in lipid bilayers.," *Biophys. J.*, vol. 92, pp. 3960–7, June 2007.

[163] S. Das, J. E. Dixon, and W. Cho, "Membrane-binding and activation mechanism of PTEN.," *P. Natl. Acad. Sci. USA*, vol. 100, pp. 7491–6, June 2003.

[164] S. Shenoy, P. Shekhar, F. Heinrich, M.-C. Daou, A. Gericke, A. H. Ross, and M. Lösche, "Membrane Association of the PTEN Tumor Suppressor: Molecular Details of the Protein-Membrane Complex from SPR Binding Studies and Neutron Reflection," *PLoS ONE*, vol. 7, p. e32591, Apr. 2012.

[165] K. Narayan and M. Lemmon, "Determining selectivity of phosphoinositide-binding domains," *Methods*, vol. 39, no. 2, pp. 122–133, 2006.

[166] J. Wang, A. Gambhir, G. Hangyás-Mihályné, D. Murray, U. Golebiewska, and S. McLaughlin, "Lateral sequestration of phosphatidylinositol 4,5-bisphosphate by the basic effector domain of myristoylated alanine-rich C kinase substrate is due to nonspecific electrostatic interactions.," *J. Biol. Chem.*, vol. 277, pp. 34401–12, Sept. 2002.

[167] K. A. Hinchliffe, A. Ciruela, and R. F. Irvine, "PIPkins, their substrates and their products: new functions for old enzymes," *BBA-Mol. Cell Biol. L.*, vol. 1436, pp. 87–104, Dec. 1998.

[168] D. J. Vanderah, D. J. McGillivray, G. Valincius, F. Heinrich, R. Budvytyte, Y. Sokolov, J. E. Hall, and M. Lösche, "Soluble amyloid beta-oligomers affect dielectric membrane properties by bilayer insertion and domain formation: implications for cell toxicity.," *Biophys. J.*, vol. 95, no. 10, pp. 4845–61, 2008.

[169] D. J. Vanderah, D. J. McGillivray, G. Valincius, F. Heinrich, J. W. F. Robertson, W. Febo-Ayala, I. Ignatjev, M. Lösche, and J. J. Kasianowicz, "Structure of functional Staphylococcus aureus alpha-hemolysin channels in tethered bilayer lipid membranes.," *Biophys. J.*, vol. 96, pp. 1547–53, Feb. 2009.

[170] M. S. Kent, J. K. Murton, D. Y. Sasaki, S. Satija, B. Akgun, H. Nanda, J. E. Curtis, J. Majewski, C. R. Morgan, and J. R. Engen, "Neutron Reflectometry Study of the Conformation of HIV Nef Bound to Lipid Membranes," *Biophys. J.*, vol. 99, no. 6, pp. 1940–1948, 2010.

[171] H. Nanda, S. Datta, F. Heinrich, M. Lösche, J. E. Curtis, A. Rein, and S. Krueger, "Electrostatic Interactions and Binding Orientation of HIV-1 Matrix Studied by Neutron Reflectivity," *Biophys. J.*, vol. 99, no. October, pp. 2516–2524, 2010.

[172] C. M. Pfefferkorn, F. Heinrich, A. J. Sodt, A. S. Maltsev, R. W. Pastor, and J. C. Lee, "Depth of α-Synuclein in a Bilayer Determined by Fluorescence, Neutron Reflectometry, and Computation," *Biophys. J.*, vol. 102, pp. 613–621, Feb. 2012.

[173] A. D. MacKerell, D. Bashford, Bellott, R. L. Dunbrack, J. D. Evanseck, M. J. Field, S. Fischer, J. Gao, H. Guo, S. Ha, D. Joseph-McCarthy, L. Kuchnir, K. Kuczera, F. T. K. Lau, C. Mattos, S. Michnick, T. Ngo, D. T. Nguyen, B. Prodhom, W. E. Reiher, B. Roux, M. Schlenkrich, J. C. Smith, R. Stote, J. Straub, M. Watanabe, J. Wiórkiewicz-Kuczera, D. Yin, and M. Karplus, "All-Atom Empirical Potential for Molecular Modeling and Dynamics Studies of Proteins," *J. Phys. Chem. B*, vol. 102, no. 18, pp. 3586–3616, 1998.

[174] D. McQuarrie, ed., *Statistical Mechanics.* Harper and Row, New York, 1976.

[175] D. Frenkel and B. Smit, eds., *Understanding Molecular Simulation.* Academic Press, San Diego, 1996.

[176] J. C. Phillips, R. Braun, W. Wang, J. Gumbart, E. Tajkhorshid, E. Villa, C. Chipot, R. D. Skeel, L. Kalé, and K. Schulten, "Scalable molecular dynamics with NAMD," *J. Comp. Chem.*, vol. 26, no. 16, pp. 1781–1802, 2005.

[177] J. B. Klauda, R. M. Venable, J. A. Freites, J. W. OConnor, D. J. Tobias, C. Mondragon-Ramirez, I. Vorobyov, A. D. MacKerell, and R. W. Pastor, "Update of the CHARMM All-Atom Additive Force Field for Lipids: Validation on Six Lipid Types," *J. Phys. Chem. B*, vol. 114, no. 23, pp. 7830–7843, 2010.

[178] D. Lupyan, M. Mezei, D. E. Logothetis, and R. Osman, "A Molecular Dynamics Investigation of Lipid Bilayer Perturbation by PIP 2," *Biophys. J.*, vol. 98, pp. 240–7, Jan. 2010.

[179] W. Humphrey, A. Dalke, and K. Schulten, "VMD: Visual Molecular Dynamics," *J. Molec. Graphics*, vol. 14, pp. 33–38, 1996.

[180] N. Michaud-Agrawal, E. J. Denning, T. B. Woolf, and O. Beckstein, "MD-Analysis: A toolkit for the analysis of molecular dynamics simulations," *J. Comp. Chem.*, vol. 32, no. 10, pp. 2319–2327, 2011.

[181] B. Keller, X. Daura, and W. F. van Gunsteren, "Comparing geometric and kinetic cluster algorithms for molecular simulation data.," *J. Chem. Phys.*, vol. 132, p. 074110, Feb. 2010.

[182] A. Gericke, M. Munson, and A. H. Ross, "Regulation of the PTEN phosphatase.," *Gene*, vol. 374, pp. 1–9, June 2006.

[183] C. Chothia, "The nature of the accessible and buried surfaces in proteins.," *J. Mol. Bio.*, vol. 105, pp. 1–14, July 1976.